

A SPECTROSCOPIC INVESTIGATION OF PROTON
TRANSFER AND BJERRUM DEFECT
ACTIVITY IN AMORPHOUS ICE

By

MARK EDWIN FISHER

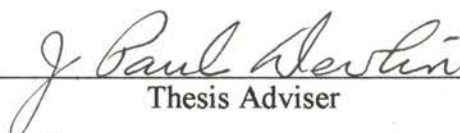
Bachelor of Science
Cameron University
Lawton, Oklahoma
1985

Master of Science
Oklahoma State University
1989

Submitted to the Faculty of the Graduate College
of the Oklahoma State University
in partial fulfillment of the requirements
for the Degree of
DOCTOR OF PHILOSOPHY
August, 2002

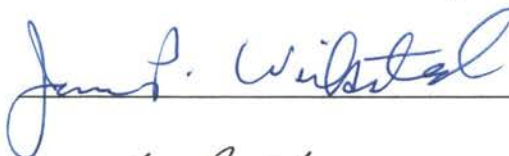
A SPECTROSCOPIC INVESTIGATION OF PROTON
TRANSFER AND BJERRUM DEFECT
ACTIVITY IN AMORPHOUS ICE

Thesis Approved:

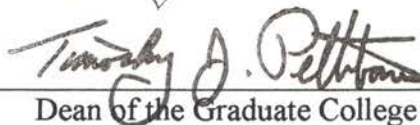


Thesis Adviser









Dean of the Graduate College

PREFACE

Isotopic scrambling of D₂O isolated in a matrix of H₂O has been observed as a consequence of the action of mobile protons and Bjerrum L-defects as they pass through sites in the ice lattice occupied by a number of spectroscopically distinguishable deuterated species and reaction products. Kinetic studies were enabled by collection of spectra over time at a given reaction temperature. The results of these studies provides insight into the glass transition in amorphous ice.

I wish to thank all who assisted in me with this work. In particular, I wish to thank Dr. J. Paul Devlin, my major advisor, for his direction, insight, encouragement, and patience. I also wish to thank my committee members, Dr. Donald Thompson, Dr. Mark Rockley, Dr. James Wicksted, and Dr. Gilbert Mains who served on my committee until his retirement.

I also wish to thank the National Science Foundation for funding this work.

I also wish to thank my employer, Nomadics, Inc., for their support during the final stages of thesis writing.

Last but not least, I wish to thank my wife Lisa for her encouragement and support. I could not have completed this work without her.

TABLE OF CONTENTS

Chapter	Page
I. LITERATURE REVIEW	1
Introduction	1
An Overview of the Phases and Structure of Ice	3
The Phase Diagram of Ice.....	5
Proton Disorder in Ice	8
The Structure of Hexagonal Ice	10
The Structure of Cubic Ice	28
The Structure of Amorphous Ice	33
Investigation of the Glass Transition in Amorphous Solid Water.....	38
Defects in the Ice Structure	40
Ionic Defects	41
Orientational Defects	44
The Infrared Spectrum of Ice	46
The Mid-Infrared Spectrum of the Isotopomers of H ₂ O Decoupled in Ice.....	49
Studies of Defect Activity in Ice	53
Conductivity Studies	55
Studies of the Dielectric Constant and Dielectric Relaxation of Ice	57
The Theory of Defect Activity in Ice	61
Spectroscopic Studies of Defect Activity	64
The Trapping of Mobile Protons in Shallow Traps	68
Statement of the Problem	70
II. EXPERIMENTAL SETUP, SAMPLE PREPARATON, AND DATA COLLECTION.....	72
An Overview of the Experimental Setup	72
Sample Preparation	77
Proton Enrichment of Samples	78
Collection of Data for Kinetic Studies	80

Chapter	Page
III. DATA ANALYSIS AND MODEL DEVELOPMENT	82
Band Fitting	82
Background Correction	84
Isolated HOD Spectrum	86
Determination of Sample Concentrations	88
Spectrum of D ₂ O	96
Spectrum of Vibrationally Coupled HOD	103
Fitting of Spectral Data Kinetic Runs	109
Kinetic Model Development	109
IV. RESULTS AND CONCLUSIONS	133
Results From Preparation of Spectra For Kinetic Study.....	133
Results of Kinetic Study	135
Conclusions and Summary.....	174
REFERENCES	176

LIST OF TABLES

Table	Page
I. Structural Data for Some Crystalline Phases of Ice	9
II. Average Molecular Geometry for Hexagonal Ice Structure Shown in Figure 5.....	22
III. Average Hydrogen Bond Geometry for Hexagonal Ice Structure Shown in Figure 5.....	22
IV. Results of Deposition Experiments Performed by Blackman and Lisgarten.....	30
V. Comparison of X-Ray Diffraction Results for Ice I_h and Ice I_a at 77 K.....	36
VI. Infrared Absorption Frequencies for Vapor Phase and H_2O and D_2O Ice I_h	48
VII. Ratio of Integrated Intensities for OD Band Complex to H_2O Combination Band as a Function of HOD Concentration	91
VIII. Total Integrated Intensity of OD Band Complex During a Kinetic Run	94
IX. Total OD Concentration for Samples	95
X. Refined V_3 to V_1 Intensity Ratios for D_2O	99
XI. Refined FWHM for V_3 and V_1 of D_2O and Isolated HOD in Wavenumbers.....	100
XII. Refined Positions of Peak Maxima for D_2O and Isolated HOD in Wavenumbers.....	101
XIII. Ratio of V^- to V^+ for (HOD) _{cp}	105
XIV. Positions of Band Maxima in Wavenumbers for Samples After Irradiation.....	106
XV. FWHM of Bands in Wavenumbers for Samples After Irradiation.....	107
XVI. Change in Isotopomer Concentrations Before and After UV Photolysis of 2-Naphthol.....	134

Table

Page

XVII. Change in Isotopomer Concentrations During Heating of Samples To Temperature for Collection of First Spectrum of Kinetic Run.....	136
--	-----

LIST OF FIGURES

Figure	Page
1. The pT phase diagram of ice.....	7
2. The tetrahedral coordination and six possible orientations of a water molecule in ice.....	11
3. Oxygen atom positions in ice I _h	14
4. The ice I _h structure showing the disorder in the proton positions.....	16
5. Average atomic arrangement in one oxygen tetrahedron of hexagonal ice based on the half-hydrogen model.....	21
6. The best estimate of the atomic arrangement of one oxygen tetrahedron of hexagonal ice from a compilation of all available data.....	27
7. Oxygen atom positions in ice I _c	31
8. Structure of an amorphous ice cluster.....	36
9. Schematic representation of formation of an ionic defect pair.....	42
10. The formation and migration of Bjerrum defects in ice.....	45
11. The librational modes of water (ice).....	50
12. The O-D stretching band complex for D ₂ O decoupled in H ₂ O ice I _c	54
13. AC and DC conductivity data from 263 K to 182 K.....	56
14. Static relative permittivity and dielectric relaxation time at 263 K as a function of [HF] in ice.....	59
15. The dielectric constant of ice I _h as a function of frequency at 263 K.....	60
16. Action of ionic and orientational defects in ice.....	62

Figure	Page
17. Spectra illustrating the conversion of D ₂ O to HOD.....	65
18. The mechanism of proton conduction in ice.....	66
19. Orientation of substrate during spectral analysis and sample deposition.....	76
20. Photolysis of 2-Naphthol.....	81
21. Baseline corrected data set	85
22. Subtraction of water background and baseline to yield OD stretch band complex.....	87
23. 80K isolated HOD spectra for several HOD concentrations	89
24. Isolated HOD peak position as a function of temperature	90
25. Percent OD calibration line.....	91
26. Calibration line for molar concentration of OD oscillators	92
27. Goodness of fit for ν_3 to ν_1 ratio for D ₂ O.....	98
28. Pure component spectra derived from samples before irradiation	102
29. Goodness of fit for ν^+ to ν^- ratio of (HOD) _{cp}	104
30. Pure component spectra derived from samples after irradiation	108
31. Proposed isotopic exchange mechanism.....	110
32. Conversion of D ₂ O to (HOD) _{cp}	114
33. Conversion of (HOD) _{cp} to D ₂ O.....	115
34. Conversion of (HOD) _{cp} to (HOD) _{pc}	116
35. Conversion of (HOD) _{pc} to (HOD) _{cp}	117
36. Conversion of (HOD) _{cp} to (HOD) _{nn}	118
37. Conversion of (HOD) _{nn} to (HOD) _{cp}	119

Figure	Page
38. Conversion of (HOD) _{nn} to (HOD) _{is} series 1.....	120
39. Conversion of (HOD) _{nn} to (HOD) _{is} series 2.....	121
40. Conversion of (HOD) _{is} to (HOD) _{nn} series 1.....	122
41. Conversion of (HOD) _{is} to (HOD) _{nn} series 2.....	123
42. Conversion of (HOD) _{is} to (HOD) _{nn} series 3.....	124
43. Conversion of (HOD) _{pc} to (HOD) _{is} series 1.....	125
44. Conversion of (HOD) _{pc} to (HOD) _{is} series 2.....	126
45. Conversion of (HOD) _{is} to (HOD) _{pc} series 1.....	127
46. Conversion of (HOD) _{is} to (HOD) _{pc} series 2.....	128
47. A simplified reaction mechanism.....	129
48. Fit to experimental data for kinetic run 1 at 102 K.....	137
49. Fit to experimental data for kinetic run 1 at 105 K.....	138
50. Fit to experimental data for kinetic run 1 at 108 K.....	139
51. Fit to experimental data for kinetic run 1 at 110 K.....	140
52. Fit to experimental data for kinetic run 1 at 112 K.....	141
53. Fit to experimental data for kinetic run 1 at 115 K.....	142
54. Fit to experimental data for kinetic run 3 at 118 K.....	143
55. Fit to experimental data for kinetic run 1 at 120 K.....	144
56. Fit to experimental data for kinetic run 3 at 122 K.....	145
57. Fit to experimental data for kinetic run 3 at 125 K.....	146
58. Calculated isotopomer concentrations from fit to experimental data for run 1 at 102 K.....	148

Figure	Page
59. Calculated isotopomer concentrations from fit to experimental data for run 1 at 105 K.....	149
60. Calculated isotopomer concentrations from fit to experimental data for run 1 at 108 K.....	150
61. Calculated isotopomer concentrations from fit to experimental data for run 1 at 110 K.....	151
62. Calculated isotopomer concentrations from fit to experimental data for run 1 at 112 K.....	152
63. Calculated isotopomer concentrations from fit to experimental data for run 1 at 115 K.....	153
64. Calculated isotopomer concentrations from fit to experimental data for run 3 at 118 K.....	154
65. Calculated isotopomer concentrations from fit to experimental data for run 1 at 120 K.....	155
66. Calculated isotopomer concentrations from fit to experimental data for run 3 at 122 K.....	156
67. Calculated isotopomer concentrations from fit to experimental data for run 3 at 125 K.....	157
68. Estimated mobile proton concentration versus time for run 1 at 102 K.....	158
69. Estimated mobile proton concentration versus time for run 1 at 105 K.....	159
70. Estimated mobile proton concentration versus time for run 1 at 108 K.....	160
71. Estimated mobile proton concentration versus time for run 1 at 110 K.....	161
72. Estimated mobile proton concentration versus time for run 1 at 112 K.....	162
73. Estimated mobile proton concentration versus time for run 1 at 115 K.....	163
74. Estimated mobile proton concentration versus time for run 3 at 118 K.....	164
75. Estimated mobile proton concentration versus time for run 1 at 120 K.....	165
76. Estimated mobile proton concentration versus time for run 3 at 122 K.....	166

Figure	Page
77. Estimated mobile proton concentration versus time for run 3 at 125 K.....	167
78. Arrhenius plot for proton hopping reactions.....	172
79. Arrhenius plot for L-defect activity.....	173

CHAPTER I

LITERATURE REVIEW

Introduction

Water, one of the simplest molecules capable of forming hydrogen bonds, is one of the most fascinating substances ever studied by scientists. Water possesses many unusual physical, chemical, and biological properties, many of which are essential for the existence of life. Water is a logical starting point for the investigation of fundamental properties of hydrogen bonded systems because it is one of the simplest molecules that forms hydrogen bonds. This is one reason that water has been the focus of numerous experimental and theoretical studies. The solid phases of water (ice) have been widely investigated (1). Ice has been used as a model for studying the behavior of protons in hydrogen bonds, a problem that is of interest in the physical, chemical, and biological sciences (2). In spite of the widespread interest in ice and the number of studies that have focused on it, many of the details regarding the structure and behavior of ice at the molecular level are not well understood.

An important property of hydrogen bonds is that they enable the transfer of protons between hydrogen-bonded molecules. In solid hydrogen bonded materials such as ice, a considerable amount of data suggests that the proton transfer mechanism involves the motion of ionic and orientational (Bjerrum) point defects. It has been postulated that

point defect activity is an important part of the mechanism in a number of important physical and biological processes including protonic conductivity and dielectric relaxation in ice and ice-like substances such as clathrate hydrates (1), proton transfer in the vision process and in photosynthesis (3, 4), proton transport through biomembranes (5) and along fast-ion conductors (6), charge separation in clouds leading to electrical storms (7), and proton ordering in certain phases of ice (8, 9). Of interest in the present study is data suggesting that low-temperature phase transformations in hydrogen bonded solids such as ice may depend on the concentration and mobility of orientational defects within these systems at a given temperature (10). It is conceivable that techniques for controlling ice formation in systems where ice formation is undesirable could be developed if the mechanism of low-temperature phase transformations in ice and ice-like substances were better understood. Possible applications of this information exist in the field of cryobiology where controlling the crystallization of water in biological systems at low temperature is important (11), and in the prevention of costly blockages of high-pressure natural gas pipelines by the formation of clathrate hydrates (12).

In recent years, there has been a steady increase in the amount of information concerning point defect activity and the defect structure of ice at the molecular level. One experimental method that has been used to investigate defect activity in ice involves the use of vibrational spectroscopy to monitor isotopic exchange caused by defect activity. Techniques exist which make it possible to isolate intact, deuterated water molecules (D_2O) in thin films of protiated ices and clathrate hydrates without an appreciable degree of isotopic exchange between the D_2O molecules and the H_2O lattice. This is accomplished by rapidly condensing separate molecular beams of D_2O and H_2O vapors

onto a cold substrate at a temperature where orientational and ionic defects are inactive (or are immobilized after traveling very short distances, limiting isotopic exchange). After preparing the sample, it is then heated to a temperature where defects are active. Conversion of the intact D_2O into isolated HOD through a series of steps involving the passage of ionic and orientational defects through a D_2O site in the lattice is then monitored spectroscopically. By monitoring the change in concentration of spectroscopically distinguishable isotopic species with respect to time and over a range of temperatures, defect kinetics can be investigated. This technique has been used to study defect activity in cubic ice (ice I_C) (13, 14, 15, 16) and for the clathrate hydrate of ethylene oxide (17). In this study, the technique has been applied to the study of defect activity in amorphous solid water (ice I_a), a solid phase of water that is similar in some respects to liquid water.

An Overview of the Phases and Structure of Ice

Pure materials can exist in several physical forms. The most stable equilibrium form of a material depends on the temperature and pressure of the system. The relationship between the different phases can be expressed thermodynamically by the Gibbs free energy (G),

$$G = U - TS + pV \quad (1.1)$$

where (G) is a minimum for a system in equilibrium at a given temperature (T) and pressure (p). At low temperatures and pressures, the internal energy (U) of the system is the major factor that determines the most stable equilibrium form of the substance.

Hence, at low temperatures the most stable form of a substance will be one in which the

bonding between adjacent molecules is strongest (the internal energy is minimized, typical of solid phases). At higher temperatures, the entropy (S) of the system becomes important, leading to more disordered forms being the most stable (liquid phases), even though the internal energy is greater. At even higher temperatures, the vapor phase becomes the most stable as long as the pressure remains low. At higher pressures, the pV term increases in magnitude, and the most stable form will be one in which the volume of the substance is minimized to counteract the increase in pressure.

Under certain conditions, it is possible for a phase of a substance to exist that appears to be stable but is not in thermodynamic equilibrium at a given temperature and pressure. In other words, a phase of a substance can exist that has a higher Gibbs free energy than the phase that results when the system is at thermodynamic equilibrium (at a given temperature and pressure). Phases of a substance that appear to be stable but are not at thermodynamic equilibrium are referred to as being metastable. A metastable phase will convert to a more stable phase when the constraints preventing the metastable phase from achieving thermodynamic equilibrium are removed.

In ice, the bonding between molecules (hydrogen bonding) is a dipole-dipole interaction of the form $O-H\cdots O$ where the proton of $O-H$ interacts electrostatically with a lone pair of electrons on the oxygen atom of another water molecule. This interaction is highly directional, with the minimum energy configuration usually occurring when all three atoms participating in the hydrogen bond are linear (18). Because of the directional nature of hydrogen bonds, the solid phases of most hydrogen-bonded substances are highly ordered, forming geometrically well-defined structures. Another important property of hydrogen bonds is their unusual adaptability. Although hydrogen

bonds are highly directional, they are flexible enough to allow the molecules in hydrogen-bonded solids to assume conformations in which hydrogen bonds between neighboring molecules deviate from linearity when structural constraints (such as those imposed when ice is exposed to high pressure) force such deviations. Because of the unusual adaptability of hydrogen bonds, water forms more solid phases than any other known substance.

The Phase Diagram of Ice

At least twelve phases of ice have been prepared and studied in the laboratory, but evidence for the existence of only three of these phases in nature has been reported. The only phase of ice for which naturally occurring samples have been recovered is hexagonal ice (ice I_h). Hexagonal ice occurs in great abundance in the oceans, in the atmosphere, and on the surface of the earth. It is the solid phase of water that is commonly recognized and referred to as 'ice' in ordinary conversation. The two remaining phases of ice that exist in nature are the amorphous (ice I_a) and cubic (ice I_c) phases. Evidence for the existence of these two phases of ice in the upper levels of the atmosphere and in outer space (19, 20, 21) has been reported, but naturally occurring samples of these phases have not been recovered. Of the three phases of ice that are known to exist in nature, all three exist in low-pressure environments. These are referred to as the low-pressure phases of ice. The low-pressure phases of ice (hexagonal, cubic, and amorphous) are of particular interest in this study, and each will be reviewed in detail in this chapter.

A number of phases of ice can be formed at high pressures and low temperatures. These phases of ice are normally prepared by exposing hexagonal ice to pressures in excess of approximately 2 kbar at temperatures low enough to prevent melting.

Hexagonal ice has a very open structure that gives it a density less than that of liquid water (22). This open structure begins to collapse when exposed to pressures in excess of 2 kbar, resulting in phases of ice in which the water molecules are more closely packed than in hexagonal ice. At least nine different phases of ice have been prepared in the laboratory by exposing hexagonal ice to high pressures and low temperatures, with the phase formed depending on the temperature and pressure of the system. These phases are referred to as the high-pressure phases of ice.

Before discussing the low-pressure phases of ice in detail, a brief discussion of the high-pressure phases of ice is in order. Figure 1 is the pressure / temperature phase diagram for most of the known phases of ice. The evolution of the phase diagram of ice to its present form has taken close to a century. The first investigations of high-pressure phases of ice were made by Tammann (23) in 1900 when he first discovered ices II and III. In 1912, Bridgman (24) studied ice up to 18 kbar and discovered ices V and VI. In these studies, Bridgman was probably the first to observe a metastable phase in the region of ice V, but it was not until 1935 that Bridgman (25) later confirmed the existence of this phase of ice known as ice IV. In 1937 Bridgman (26) expanded his investigation to 45 kbar and discovered ice VII. In 1967 Whalley added ice VIII (27) to the phase diagram, followed by ice IX (28) a year later in 1968. Not shown in Figure 1 is ice X (29), first reported in 1984. Ice X is an extremely high-pressure form that exists at pressures in excess of 440 kbar. Its structure has not been determined. In spite of the fact that a number of these phases have been known to exist for quite some time, it has not been possible to directly measure the stable (or metastable) equilibrium lines between all the

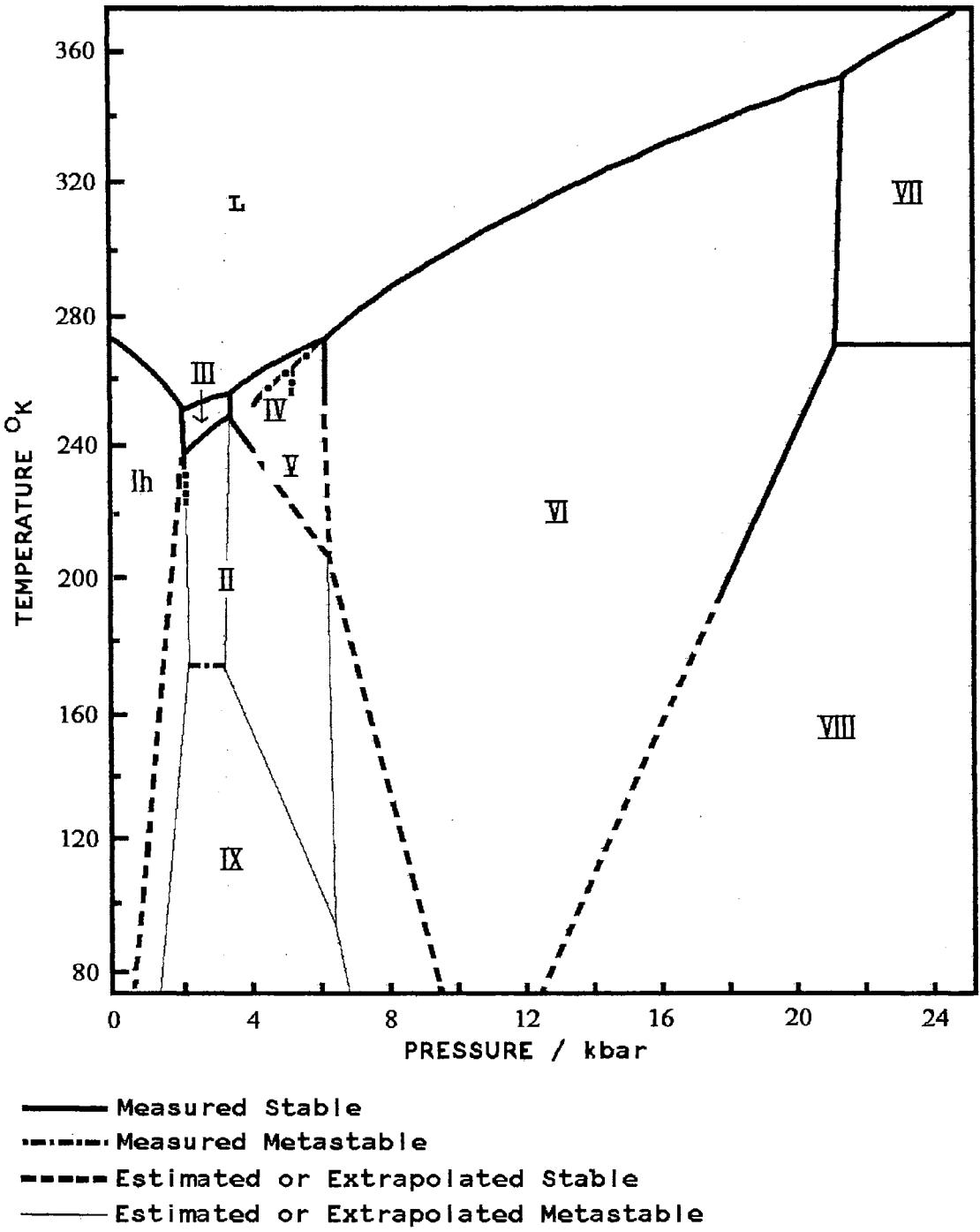


Figure 1. The pT phase diagram of ice, from reference 1.

phases. Evidence for the existence of other high pressure phases of ice have been reported in the literature (30), but these phases have not been completely investigated. Table 1 is a summary of some of the known structural data for the crystalline phases of ice. The determination of ice structures and properties is a complex process. It has not been possible to completely determine any of these structures on the basis of results from any one experimental technique. Scattering methods, spectroscopy, and theoretical calculations have all been used in the determination of ice structures (31). Because of the unusual adaptability of the hydrogen bond network in ice to its environment and the large number of ice structures that are possible because of this extraordinary adaptability, it is difficult to predict whether more phases of ice exist, and even more difficult to predict their structures (32).

Not shown in Figure 1 are the low-pressure phases of ice (except for ice I_h). These phases (cubic ice, high and low density amorphous ice, and possibly others) all occur in the lower temperature portion of the ice I_h region of the phase diagram. The relative stabilities of these phases have been a topic of debate in the chemical literature for a number of years. The relative stability of each of the known low-pressure phases will be discussed in detail later in this review.

Proton Disorder in Ice

All of the phases of ice that have been studied and characterized in the literature up to this point have two common features. The first feature is that all the known phases of ice are composed of intact water molecules (the concentration of ionic defects in pure ices

TABLE 1
 STRUCTURAL DATA FOR SOME CRYSTALLINE PHASES OF ICE
 FROM REFERENCE 31

Ice Polymorph	No. of nearest neighbors and distances (Å) of H-bonds	No. of next nearest neighbors and distances less than 3.6 Å	Hydrogen order	O—O—O angles (degrees)	Density (g cm ⁻³)
Ice I _h	4, 2.76	—	Disordered	109	0.931
Ice I _c	4, 2.75	—	Disordered	109.5	0.93
Ice II	4, 2.77-2.84	9, 3.24-3.60	Ordered	81-128	1.18
Ice III	4, 2.75-2.80	1, 3.45	Disordered	87-144	1.16
Ice IX (III)	4, 2.75-2.80	1, 3.45	Partial	87-144	1.16
Ice IV	4, 2.79-2.92	9, 3.14-3.29	Disordered†	88-128	1.27
Ice V	4, 2.76-2.80	7, 3.28-3.49	Disordered†	84-128	1.23
Ice VI	4, 2.80-2.82	17, 3.44-3.46	Disordered†	76-128	1.31
Ice VII	4, 2.90	4, 2.90	Disordered	109.5	1.50
Ice VIII	4, 2.88	5, 2.74-3.14	Ordered	109.5	1.50

† May be some partial ordering at low temperatures

is very small). The second feature is that the structures of the various phases of ice are dominated by water molecules that are coordinated to four neighboring water molecules (see Table 1) (21). This is due to the fact that most water molecules in ice participate in four hydrogen bonds: two bonds in which a water molecule donates its protons to two neighboring water molecules, and two bonds in which it accepts protons from two neighboring water molecules. From Figure 2 it can be seen that the requirement of tetrahedral hydrogen bonding can be satisfied by a given water molecule in six different ways. In each of the six different orientations, the molecular axis of the central water molecule points in a different direction. Hence, a possibility for orientational disorder exists in each of the phases of ice. Since each of the six orientations shown in Figure 2 results in a different arrangement of protons in the crystal, orientational disorder in ice can also be viewed in terms of disorder in the proton positions. As can be seen from Table 1, most of the known phases of pure crystalline ice exhibit disorder in the position of their protons. There is controversy as to whether or not the protons in some of these phases are partially ordered, especially at low temperatures (33). Ice II (34) and ice VIII (1) are the only known phases of pure ice in which the protons are fully ordered. The protons in ice IX (35) are almost completely ordered. All of the known low pressure forms of pure ice appear to exhibit disorder in the positions of their protons, although Suga (8) (9) has reported ordered proton domains in KOH doped ice I_h .

The Structure of Hexagonal Ice

As previously mentioned, the only naturally occurring phase of ice on earth is hexagonal ice. Hexagonal ice is most easily prepared by cooling a bulk sample of liquid

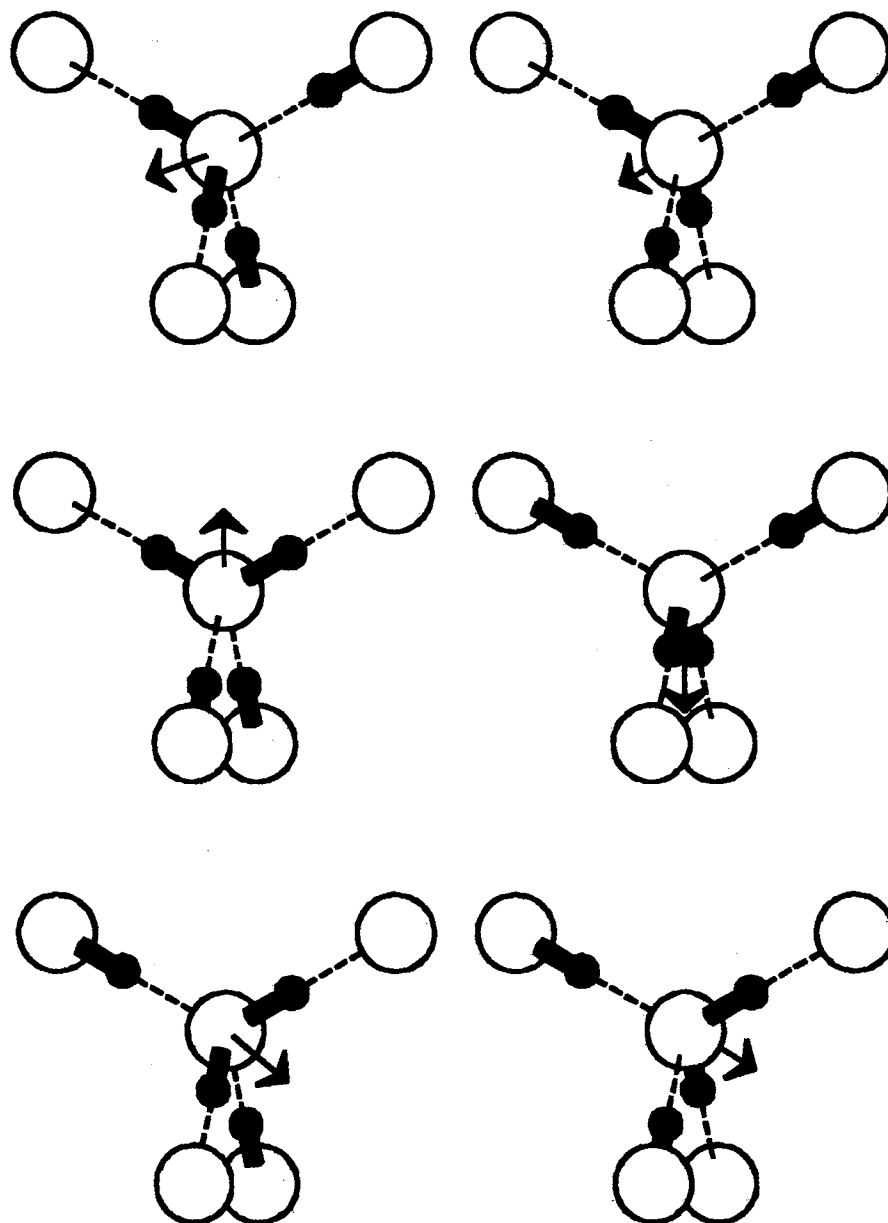


Figure 2. The tetrahedral coordination and six possible orientations of a water molecule in ice.

water to a temperature below its freezing point, or by quenching water vapor onto a cold substrate held at a temperature above approximately -100°C (1). All of the early structural studies on ice focused on hexagonal ice, partly due to the fact that it could be handled at lower pressures and at higher temperatures than the other phases of ice. It was not until the 1960's that the structures of other phases of ice were first determined. A period of approximately 50 years elapsed from the time the first structural studies were published until the structure was known with reasonable certainty. Hexagonal ice is one of the most thoroughly disordered crystalline substances ever studied, and as such the structure of hexagonal ice has proven to be very difficult to determine. Some of the finer aspects of the structure still remain unresolved.

The most common experimental method of determining crystal structure is by diffraction techniques (x-ray, electron, and neutron). X-ray diffraction was the first diffraction technique to be employed in structural analysis, and hexagonal ice was one of the first substances to be studied by x-ray diffraction. Since x-rays are scattered mostly by the electron distribution in a crystal, and since the electron density is greatest around the oxygen nucleus in a water molecule, the oxygen atom positions in ice are much easier to determine using x-ray diffraction than the proton positions. Hydrogen atoms scatter x-rays to some extent, but this scattering is very difficult to detect experimentally, even in ordered crystals. The potential for orientational disorder in ice further complicates the problem. These difficulties led to a great deal of disagreement in the early literature as to the actual location of the protons in ice I_h . In 1922, Bragg (36) analyzed x-ray diffraction data gathered by Rinne (37), St. John (38), and Dennison (39) and concluded that the oxygen atoms in ice I_h were distributed in a tetrahedral arrangement with hexagonal

symmetry, with the oxygen atom positions in the crystal lying in crinkled sheets that are normal to the unit cell c-axis (see Figure 3). The hydrogen atom positions could not be determined in these experiments. It was not until 1948 that the scattering of x-rays by hydrogen atoms was first detected (1). Up until that point, the hydrogen atom positions were left to speculation.

One interesting ice I_h structure that was reported in the early literature was proposed by Barnes in 1929 (40). Barnes proposed that the protons in hexagonal ice were located at the center of a line joining the oxygen atoms of two neighboring water molecules. This type of structure would be essentially that of an ionic crystal composed of H^+ and O^{2-} ions, not intact water molecules. Several problems with this assumption were first discussed in the literature in 1933 by Kinsey and Sponsler (41). They argued that if this assumption were true, then ice I_h should have properties similar to that of other ionic crystals; it clearly does not. The melting point of most ionic crystals is several hundred degrees higher than ice I_h , and molten ionic crystals are good conductors while liquid water is not. In addition, a mean value for the static dielectric constant of ice I_h at $0^\circ C$ is reported as 97.1 (1). A dielectric constant of this magnitude suggests the presence of permanent dipoles in the ice I_h structure; ionic crystals are not composed of permanent dipoles. These arguments raised serious doubts as to the validity of Barnes proposed structure. Additional evidence that the water molecules in ice remain intact (as opposed to H^+ and O^{2-} ions suggested by Barnes structure) comes from a comparison of the infrared and Raman spectra of water vapor, liquid water, and ice. The spectra of water vapor, liquid water, and hexagonal ice are all similar, suggesting that the internal structure

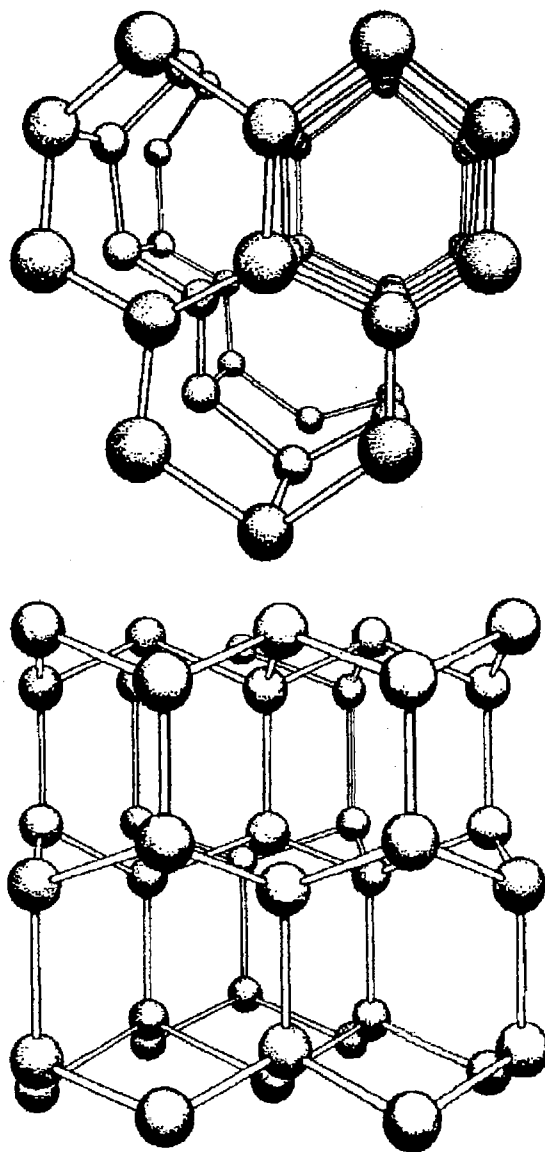


Figure 3. Oxygen atom positions in ice I_h .
Top: view along the c-axis,
bottom: view perpendicular to
the c-axis. From Reference 32.

of the water molecule is similar in all three phases. The similarities in the spectra of ice to that of the liquid and vapor phases of water led Bernal and Fowler (42) to suggest ice I_h structures in which the structure of the water molecule in ice was similar to the structure of the vapor phase molecule. Several different structures meeting this requirement were proposed by Bernal and Fowler in 1933. Although each of the structures proposed by Bernal and Fowler were quite different, they were all similar in that it was assumed that the water molecules in the lattice remained intact, and that the water molecules were oriented so that each proton on a water molecule was directed towards a lone pair electron hybrid orbital on a neighboring water molecule. Instead of the protons being located at the center of lines connecting neighboring oxygen atoms (as proposed by Barnes), Bernal and Fowler suggested that the protons were located on a lines between pairs of oxygen atoms at a position approximately 1 Å from one oxygen atom and 1.76 Å from the other, with each oxygen atom having exactly two protons at a distance of 1 Å from it. The possibility of orientational disorder in ice I_h was pointed out by Bernal and Fowler in the discussion of their proposed ice structures. They concluded that it was likely that ice I_h was 'crystalline only in the position of its molecules but glass-like in their orientations'. Figure 4 illustrates the orientational disorder in hexagonal ice proposed by Bernal and Fowler.

The conclusion that ice I_h is crystalline only in the positions of its molecules but glass-like in their orientations was later substantiated through work done by Pauling in 1935 (43). Based on the findings of Debye relating to the dielectric properties of ice I_h (44), Pauling pointed out that the dielectric constant of ice I_h above 200 K is similar to that of liquid water, implying that the water molecules in ice I_h at these temperatures have.

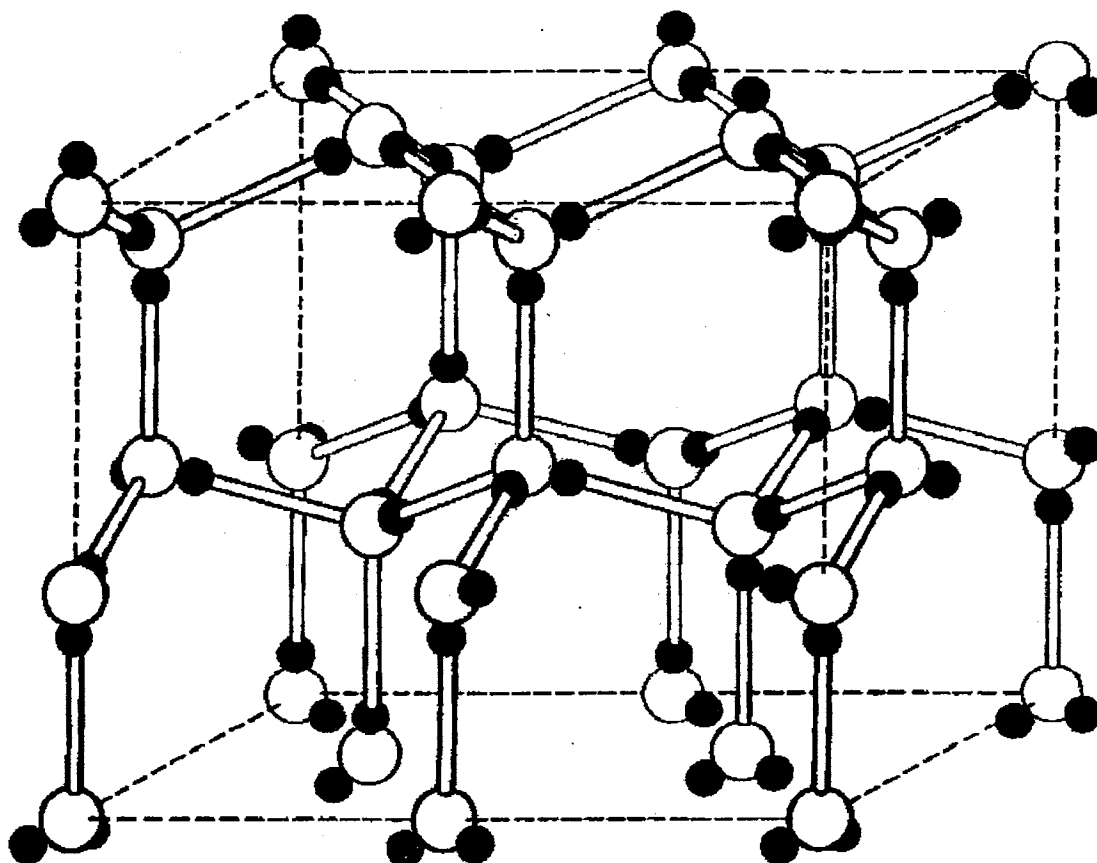


Figure 4. The ice I_h structure showing the disorder in the proton positions.
From Reference 22.

the ability to readily change their orientations, thus enabling the water molecules in ice I_h to assume any one of the many possible configurations proposed by Bernal and Fowler.

Pauling proposed a statistical model for the structure of ice I_h based on four assumptions, which are now commonly referred to as the Bernal - Fowler rules. The four assumptions that form the basis for Pauling's statistical model (the Bernal - Fowler rules) are as follows:

- (i). Water molecules in the ice structure remain intact, with each oxygen atom attached to two hydrogen atoms, with a bond length of 0.95 \AA .
- (ii). Each water molecule is oriented so that its two hydrogen atoms are directed towards the lone-pair electron hybrid orbitals of two of the four oxygens that surround it tetrahedrally (each water molecule is tetrahedrally hydrogen bonded to four neighboring water molecules).
- (iii). Adjacent water molecules are oriented so that only one hydrogen atom lies between each pair of oxygen atoms.
- (iv). Under ordinary conditions ice I_h can exist in any one of a large number of configurations with respect to the distribution of the hydrogen atoms in relationship to the oxygen atoms.

An interesting feature of Pauling's model was that at higher temperatures the ice structure could change from one configuration to another by either of two routes. The first route was through the rotation of a water molecule by approximately 120° about one of its four hydrogen bonds. The second route was through the movement (i.e., 'hopping') of a proton from one end of a hydrogen bond to the other end of the hydrogen bond (from a potential minimum 0.95 \AA from one oxygen atom to a potential minimum located 0.95 \AA away from an adjacent oxygen atom). Pauling proposed that as the temperature of the crystal is decreased, at some temperature the rotation of the water molecules and the hopping of protons ceases, and the proton configuration in the crystal becomes 'frozen'

into the configuration it happens to be in at the time. If it is assumed that the proton positions in the crystal are completely disordered at the temperature where this configuration becomes frozen in, the measured residual entropy of the crystal at 0 K will be equal to the entropy due to proton disorder, assuming entropy from all other sources is negligible at 0 K. Pauling calculated the residual entropy for the statistical model of hexagonal ice using the expression

$$S_0 = k \ln W \quad (1.2)$$

where (S_0) is the residual entropy at 0 K, (k) is the Boltzmann constant, and (W) is the number of possible configurations accessible to the crystal. Pauling calculated the number of configurations accessible to the crystal, each equally probable, using the following argument. From Figure 2 it can be seen that each water molecule can have six possible orientations, giving 6^N configurations for a crystal having N molecules if the proper formation of bonds is neglected (a bond was defined to be properly formed if exactly one proton lies between adjacent oxygen atoms). There are $2N$ O—H.....O bonds in the crystal, and the probability for a given molecule that the bond is made properly is $(2/4)$, so the possible number of configurations must be reduced by a factor of $(2/4)^{2N}$. This gives the number of possible configurations (W) that obey the model as

$$W = (2/4)^{2N} * 6^N = (1/4)^N * 6^N = (6/4)^N \quad (1.3)$$

which gives a value for the residual entropy (S_0) of

$$S_0 = Nk \ln (6/4) = 0.805 \text{ cal mol}^{-1} \text{ deg}^{-1} \quad (1.4)$$

which is in excellent agreement with the experimentally determined value of 0.82 ± 0.05 cal mol⁻¹ deg⁻¹ determined by Flubacher (45).

When diffraction techniques are used to determine crystal structure, the sampling of the crystal is over the instantaneous configurations of the crystal in time and space, provided that the interaction time of the radiation is short compared to the rate of atomic motion (i. e., the scattering center does not move appreciably over the period of sampling) and the coherence length of the radiation is shorter than the size of the coherently scattering sample. If these conditions are met, the diffraction pattern observed is that of the time and space averaged structure of the crystal. Since the statistical models proposed by Pauling and by Bernal and Fowler are based on the assumption that there is exactly one proton between each neighboring pair of oxygen atoms, and that there are two equally probable proton positions between each pair of oxygen atoms, it would be expected that a specific proton position in the unit cell of ice I_h will be occupied by a proton in half of the unit cells in the sample. Because of this feature, the statistical models of Pauling and of Bernal and Fowler are often referred to as 'half-hydrogen' models. If the 'half-hydrogen' model is correct, then the experimentally determined time and space averaged crystal structure of ice I_h would be one in which the hydrogen atoms are distributed so that each of the two possible proton sites between oxygen atoms is occupied by a proton 50% of the time. The atomic positions predicted by the half-hydrogen model of Pauling have been confirmed experimentally from neutron diffraction data. Neutron diffraction is a technique that is more sensitive to scattering by protons than is x-ray diffraction, and as such is useful in determining the positions of protons. There is a small drawback to using this technique to determine the structure of ices. Atoms like hydrogen and deuterium have a nuclear spin, and the scattering of neutrons depends on the relative orientation of the neutron spin and the spin of the nucleus. Since the orientation of the nuclear spin is

different from atom to atom, so is the interaction of neutrons with these atoms. This spin incoherence results in diffuse scattering. This is an undesirable effect that is very strong in protiated ices, but is weak in deuterated ices (28). In addition, if the protons in ice are replaced by deuterons, the scattering of neutrons by oxygen atoms and deuterium atoms is almost equal (1). For these reasons, most neutron diffraction studies of ice have been performed on deuterated ices. The hydrogen atom positions in deuterated ice I_h were first established experimentally in 1949 by Wollan (46) from neutron powder data. A few years later, single crystal neutron diffraction studies performed by Peterson and Levy were able to more accurately determine the structure of D_2O hexagonal ice (47). More recently, in an effort to refine the structure determined by Peterson and Levy, Kuhs and Lehmann (48) investigated the structure of H_2O and D_2O ice I_h in a series of experiments over a range of temperatures using high resolution neutron diffraction. The average atomic arrangement determined in these studies for one oxygen tetrahedron of ice I_h based on the half-hydrogen model is shown in Figure 5. Table 2 is a compilation of the data of Kuhs and Lehmann and also of Peterson and Levy, giving the average molecular geometry for the half-hydrogen model of hexagonal ice, while Table 3 gives the average hydrogen bond geometry determined by the same workers (the atomic notation used in Table 2 and Table 3 refers to the labeling of atoms used in Figure 5). The possibility of oxygen atom disorder and bent hydrogen bonds, which will be discussed later in this section, was not included at this stage of refinement. From this data it can be seen that the intermolecular distances increase as a function of temperature in both D_2O and H_2O ice I_h . Over the same temperature range, the intramolecular geometry of the molecules remains virtually unchanged. The intermolecular distances parallel and oblique to the crystallographic c-

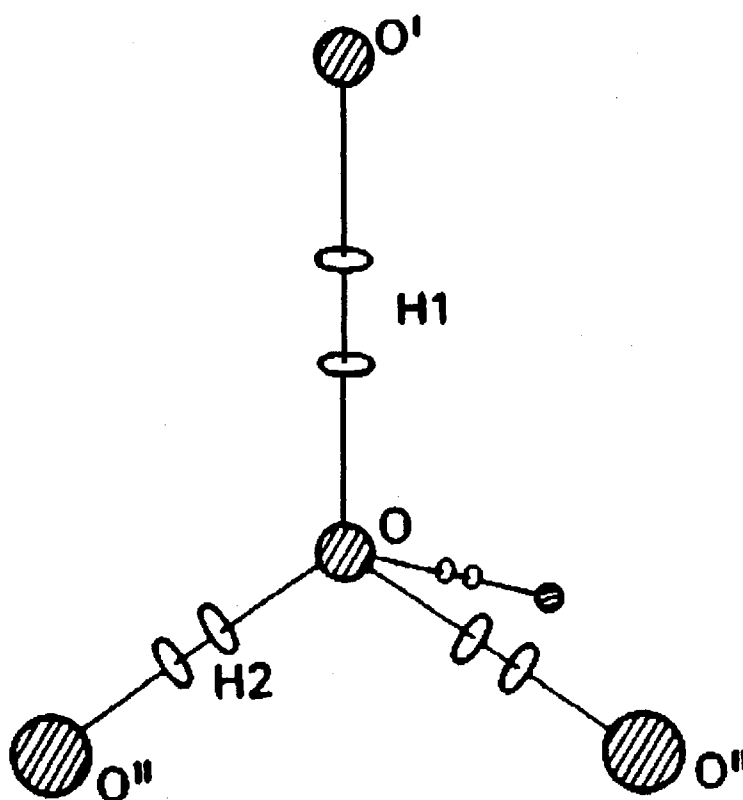


Figure 5. Average atomic arrangement in one oxygen tetrahedron of hexagonal ice based on the half-hydrogen model. Angles and distances are given in Table 2 and Table 3. From Reference 31.

TABLE 2

AVERAGE MOLECULAR GEOMETRY FOR HEXAGONAL ICE STRUCTURE
SHOWN IN FIGURE 5 (DISTANCES IN Å, ANGLES IN DEGREES)

	H ₂ O			D ₂ O		
	60 K†	123 K†	223 K†	60 K†	123 K†	223 K‡
O—H1	1.005(2)	1.009(2)	1.000(4)	1.003(1)	1.002(1)	1.000(9)
O—H2	1.005(1)	1.005(1)	0.997(2)	0.999(1)	1.001(1)	1.007(5)
H1—H2	1.638(3)	1.643(3)	1.632(5)	1.633(1)	1.634(1)	1.635(12)
H2—H2	1.645(2)	1.641(2)	1.628(4)	1.634(2)	1.636(1)	1.648(9)
H1—O—H2	109.15(13)	109.42(14)	109.52(24)	109.31(6)	109.30(6)	109.10(30)
H2—O—H2	109.79(13)	109.53(14)	109.43(24)	109.63(6)	109.65(6)	109.86(26)

† Data from Kuhs and Lehman (48).

‡ Data from Peterson and Levy (47).

TABLE 3

AVERAGE HYDROGEN BOND GEOMETRY FOR HEXAGONAL ICE
STRUCTURE SHOWN IN FIGURE 5 (DISTANCES IN Å, ANGLES IN DEGREES)

	H ₂ O			D ₂ O		
	60 K†	123 K†	223 K†	60 K†	123 K†	223 K‡
O—O'	2.748(1)	2.752(1)	2.760(1)	2.754(1)	2.755(1)	2.752(8)
O—O''	2.749(1)	2.752(1)	2.759(2)	2.753(1)	2.755(1)	2.765(1)
O'—H1	1.743(2)	1.743(1)	1.758(3)	1.752(1)	1.753(1)	1.751(10)
O''—H2	1.744(1)	1.747(1)	1.763(2)	1.754(1)	1.754(1)	1.759(6)
O—H1—O'	180.00	180.00	180.00	180.00	180.00	180.00
O—H2—O''	179.73(20)	179.93(21)	179.76(37)	179.99(9)	179.96(10)	176.8(2)
O'—O—O''	109.32(2)	109.37(2)	109.36(4)	109.30(1)	109.32(1)	109.55(15)
O''—O—O''	109.62(2)	109.57(2)	109.58(4)	109.64(1)	109.62(1)	109.40(2)

† Data from Kuhs and Lehmann (48).

‡ Data from Peterson and Levy (47).

axis are virtually identical, but the O—O—O angles are larger than when two of the oxygen atoms are in the hexagonal plane. This leads to a slight compression along the c-axis. The protons (or deuterons) appear in the structure as symmetrical pairs of half-atom positions located at each of the two possible proton (deuteron) positions on each bond. The average occupancy of these positions is 50%, a result that is consistent with the statistical distribution of protons proposed by Pauling. The angle between protons is nearly that of a perfect tetrahedron ($109^{\circ} 28'$) indicating that the protons lie near the line connecting the oxygen atoms of adjacent water molecules, forming nearly linear hydrogen bonds. The statistical model of Pauling does not require that the protons lie directly on this line even though the statistical mean positions are on the line (19). Kuhs and Lehmann also reported a significant scattering density, which increases with temperature at the midpoint of the oxygen - oxygen bond, indicating that the hydrogen atoms were present at the middle of the hydrogen bond an observable part of the time. It could not be determined if the proton actually moved across the midpoint of the bond toward a neighboring oxygen atom.

Unit cell parameters for ice I_h have been measured in a number of x-ray diffraction studies. A number of inconsistencies were noted in the values published for these parameters in the early literature. Consequently, more detailed measurements of unit cell parameters for ice I_h were performed (49, 50, 51, 52). These studies all confirmed the general arrangement of oxygen atoms in hexagonal ice determined in the earlier studies. At 77 K, the distance between oxygen - oxygen nearest neighbors is 0.275 nanometers, and the unit cell lattice parameters are $a = b = 0.448$ nanometers, and $c = 0.731$ nanometers (53). The lattice parameters for hexagonal D_2O ice are very similar to those of H_2O ice,

differing by less than 0.1% (37). Using simple trigonometry, it can be shown that the ratio of the lattice parameters (c/a) should equal $(8/3)^{1/2} = 1.633$ if the lattice of hexagonal ice is perfectly tetrahedral. Experimental values of (c/a) in the literature range from 1.627 to 1.632, indicating that the oxygen atom positions in ice I_h may not be perfectly tetrahedral. The x-ray measurements of Brill and Tippe (52) indicate that the distances between oxygen-oxygen nearest neighbors parallel to the c -axis are about 0.001 nanometer shorter than the oblique oxygen-oxygen distances, and very slight distortions in the O—O—O angles (0.05°) from perfect tetrahedra may also occur.

Electron diffraction experiments have also been performed on hexagonal ice. The electron diffraction results of Shimaoka (54) are essentially in agreement with the neutron diffraction results of Kuhs and Lehmann. For this reason, the electron diffraction results will not be discussed in detail in this review.

Since protons have a large magnetic moment, nuclear magnetic resonance (NMR) techniques can be used to obtain information on the positions of the protons in hexagonal ice. Since the degree of broadening of the proton resonance line in a steady applied magnetic field is inversely proportional to the cube of the equilibrium separation of the two protons in a water molecule, either the H—O—H bond angle or the O—H bond length can be calculated if one of these values is known. Rabideau (55), Whalley (56), and Baianu (57) have all measured the equilibrium separation of the protons in ice, and have obtained a value for $r_{H\dots H}$ of 1.58(1) Å. Using a value of 0.98 Å for the O—H bond length and 1.58 Å for $r_{H\dots H}$, a best estimate of $107(1)^\circ$ for the H—O—H bond angle has been calculated (28). A direct measurement of the intramolecular angle is not available at the present time. The equilibrium separation of protons in hexagonal ice

determined by NMR studies is significantly smaller than the value predicted by crystallographic data when the half-hydrogen model assuming tetrahedral bond angles is assumed.

In addition to the disorder in the proton positions in hexagonal ice, evidence for disorder in the oxygen atom positions in ice has been reported. It has been proposed that the proton disorder in ice results in local environments in which the oxygen atoms are forced out of their ordered positions resulting in small variations in the O—O distances. Spectroscopic evidence for oxygen disorder in hexagonal ice was first suggested in 1964 by Bertie and Whalley (58). They explained the full width at half height (FWHH) of the uncoupled O—H stretch band in terms of the variations in the in O—O distances as a result of static oxygen atom disorder induced by the proton disorder in hexagonal ice. The FWHH of the uncoupled O—H stretch band in hexagonal ice decreases with temperature down to about 100 K and remains fairly constant at temperatures below 100 K (59). If this effect is due to oxygen atom disorder, it would indicate that the magnitude of the disorder in the oxygen atom positions decreases with temperature down to about 100 K, at which point the disorder becomes frozen in. As the magnitude of the disorder decreases, so does the range of hydrogen bond strengths resulting in a decrease in the FWHH of the band. The range of hydrogen bond strengths is usually explained in terms of the variation in O—O distances as a result of oxygen disorder, but hydrogen bond bending could also contribute to the range of hydrogen bond strengths (31). Additional evidence for oxygen atom disorder comes from crystallographic data. Mean square displacement data obtained from crystallographic measurements include disorder components, while the same data obtained spectroscopically does not. By comparing mean square displacement

data from high-resolution neutron diffraction studies with that obtained from spectroscopic measurements, Kuhs and Lehmann (31) were able to calculate the mean square displacements of hydrogen and oxygen atoms in hexagonal ice. The disorder observed was small (only a fraction of the thermal root mean square displacement) and went undetected in earlier crystallographic studies done at lower resolution. A crude estimate of the displacement of the oxygen atom from its position in the half-hydrogen model of ice was placed at approximately $0.06(2)$ Å. When oxygen atom disorder was considered in the refinement of the structure, it was found that the O—H bond length was shorter than that calculated for the half-hydrogen model (approximately 0.98 Å as opposed to a value of approximately 1.005 Å for the half-hydrogen model). This value is in better agreement with the O—H bond length determined using other experimental techniques. The hydrogen bond length obtained when oxygen atom disorder was allowed is approximately 1.80 Å, which is about 0.05 Å longer than the value of 1.75 Å obtained using the half-hydrogen model.

In summary, the structure of hexagonal ice has been fairly well established by using a number of different techniques, although some of the finer details of the structure still remain unresolved. The best estimate of the structure of hexagonal ice based on all available data is shown in Figure 6. The idealized hydrogen bond directions predicted by the half-hydrogen model are shown as dotted lines in the figure, while the actual hydrogen bonds are represented by the dashed lines. At the present time, the hydrogen bond angle cannot be measured experimentally and the hydrogen bond angle is not accurately known, but it is not believed to be exactly linear. This is because the H—O—H angle in a water molecule is not perfectly tetrahedral because of distortions induced by repulsions between

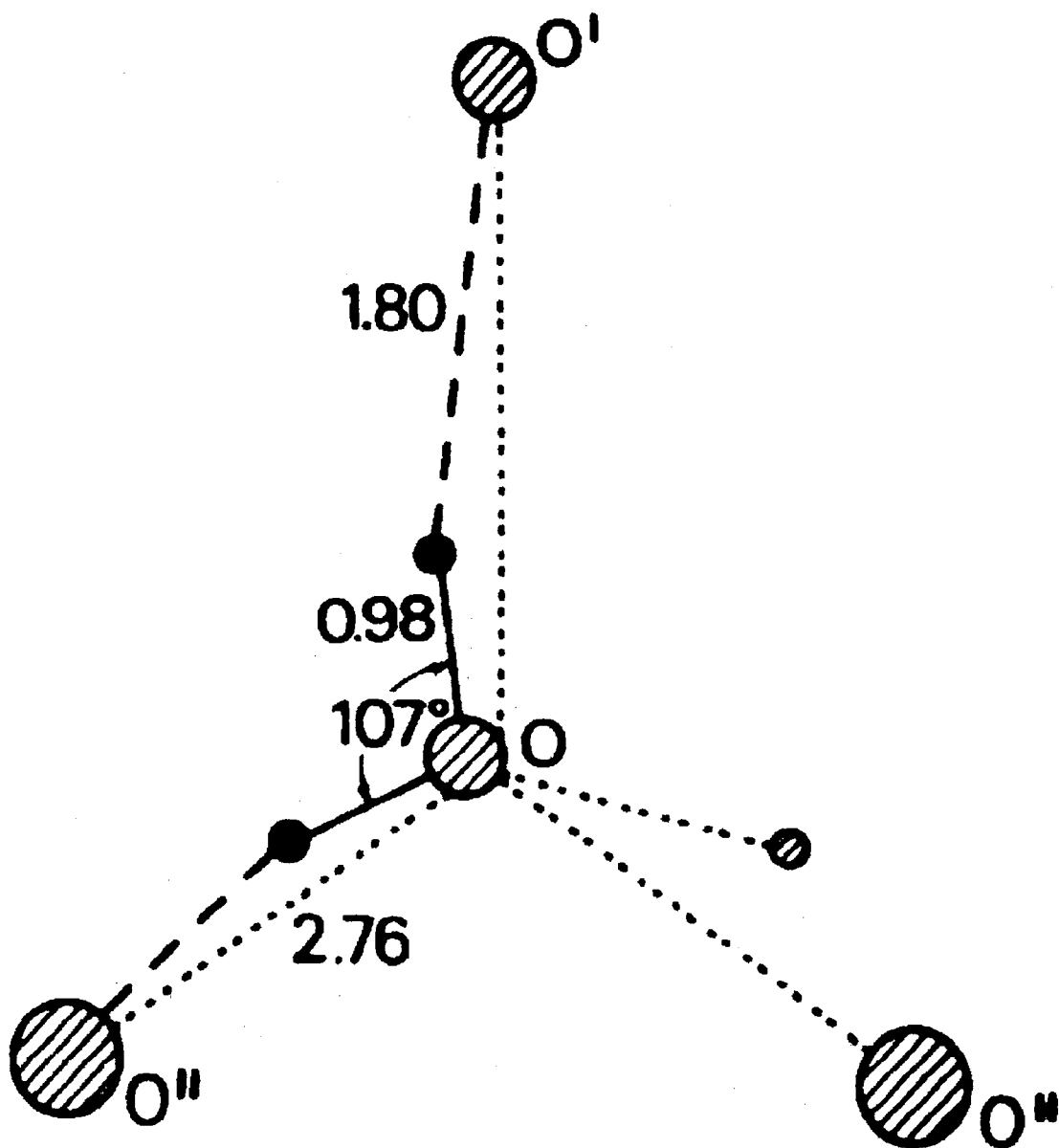


Figure 6. The best estimate of the atomic arrangement of one oxygen tetrahedron of hexagonal ice from a compilation of all available data. Distances are in Å and angles are in degrees. From Reference 31.

the two lone pairs of electrons in the water molecule. Therefore, it is not possible for the H atoms to lie perfectly on the O—O bond axis. The O—O—O angles are not exactly known because of a small amount of oxygen atom disorder, but are not far from tetrahedral. Not shown in Figure 6 is the proton disorder in pure hexagonal ice, the existence of which has been well established.

The Structure of Cubic Ice

Cubic ice (ice I_c) was first prepared in the laboratory shortly after the turn of this century. Dewar (60) recognized that he had prepared a new phase of ice in his laboratory in 1905, but at that time it was impossible to determine its structure. It was shown approximately 50 years later that the phase Dewar had prepared was cubic ice. In 1935, Burton and Oliver (61) studied the x-ray diffraction patterns of ice prepared by condensing water vapor onto a cold copper rod at low temperatures. For samples deposited at temperatures above 193 K, the diffraction pattern was that of hexagonal ice. For samples deposited at temperatures below 193 K they obtained diffraction patterns different from that of hexagonal ice, and at temperatures below 158 K diffraction patterns similar to that of liquid water were obtained. They concluded that the diffraction pattern obtained for samples deposited below 158 K was due to a vitreous or amorphous solid, and at temperatures between 158 K and 193 K a semi-crystalline or crystalline solid different from hexagonal ice was obtained. The phases observed by Burton and Oliver were later studied by Konig (62) in 1943. From electron diffraction data of vapor deposited thin films of ice deposited over a range of temperatures, Konig observed a diffraction pattern of diffuse rings (characteristic of an amorphous substance) for samples deposited at 103

K. Upon heating the sample to 133 K, the diffraction pattern changed from one of diffuse rings to one of sharp rings characteristic of a cubic structure, and upon further heating to approximately 193 K the diffraction pattern slowly changed to one consistent with a hexagonal structure. Electron diffraction experiments conducted by Blackman and Lisgarten (63) later confirmed that three different phases of ice could be formed by condensing water vapor onto a cooled substrate. The phase formed was found to depend on the temperature of the substrate and the rate of deposition, and was independent of the substrate material used in the experiment. The results of these experiments are recorded in Table 4. When the substrate temperature was held between 133 K and 153 K, the phase formed produced a diffraction pattern consistent with a cubic structure. The structure of cubic ice has been studied by Honjo and Shimaoka (64) and Shimaoka (54) using electron diffraction. The oxygen atom positions of cubic ice (ice I_c) are shown in Figure 7. It is a face-centered cubic unit cell with oxygen atom positions, which correspond to the diamond structure. The structure of cubic ice is very similar to that of hexagonal ice (see Table 1). Both ices are composed of layers of hexagonal rings of water molecules, with the rings being of chair configuration. The main difference between the two structures is in the way the layers are connected. When viewed along the c -axis, the layers are eclipsed in hexagonal ice (top structure in Figure 3) and staggered in cubic ice (top structure in Figure 7). The unit cell parameters for ice I_c are $a = b = c = 6.350 \text{ \AA}$ at 143 K, which gives essentially the same volume per molecule as in hexagonal ice. The distance between nearest neighbor oxygen atoms is 2.75 \AA as opposed to 2.76 \AA for hexagonal ice. The nearest neighbor environment in cubic ice is virtually identical to that of hexagonal ice, with the differences in environment beginning at the second nearest

TABLE 4
RESULTS OF DEPOSITION EXPERIMENTS
PERFORMED BY BLACKMAN
AND LISGARTEN

Temperature of Substrate	Type of Ice Formed
93 K to 133 K	amorphous
133 K to 153 K	cubic
153 K to 173 K	hexagonal + cubic
> 173 K	hexagonal

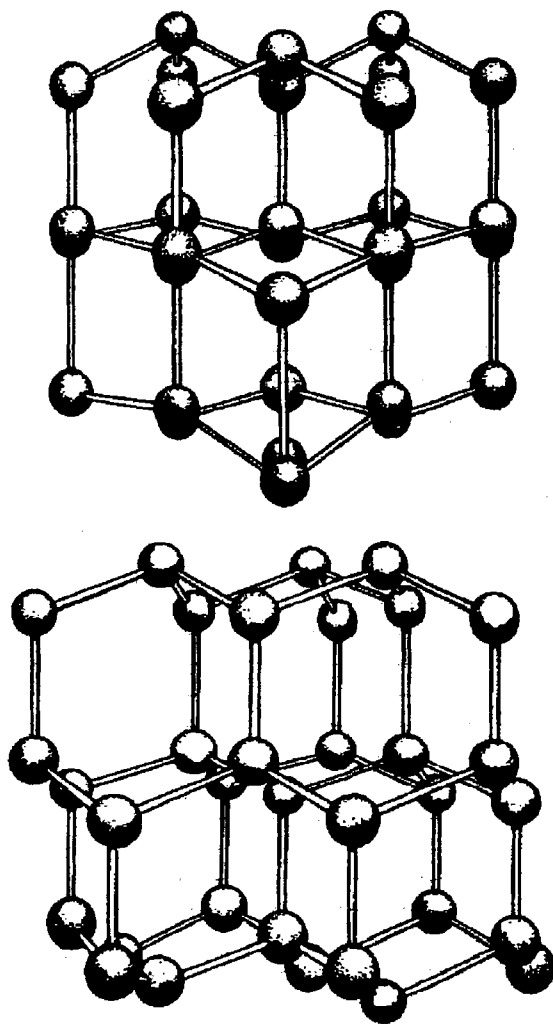


Figure 7. Oxygen atom positions in ice Ic.
Top: view along the c-axis,
bottom: view perpendicular to
the c-axis. From Reference 32.

neighbor molecules in the structure. The electron diffraction results of Honjo and Shimaoka (64) reveal that the proton positions in ice I_C are disordered in a manner consistent with Pauling's statistical half-hydrogen model. The infrared spectrum (55) and dielectric properties (65) of cubic and hexagonal ice are virtually identical, which is further evidence of the similarity of the environments of the water molecules in these ices. Cubic ice can be prepared in several ways. The direct formation of thin films of ice I_C by vapor deposition over the temperature range of approximately 125 K to 175 K has already been mentioned. Ice I_C can also be prepared by heating vapor deposited amorphous ice or pressure amorphized ice to near 140 K and holding it at this temperature for several minutes (66). Larger quantities of cubic ice can also be prepared from several of the high-pressure phases of ice. Whalley and co-workers (67) prepared bulk samples of cubic ice by first preparing ice III and then cooling it to liquid nitrogen temperature. Upon decreasing the pressure to atmospheric and warming the sample to 157 K for a minute or so, the ice III transforms to cubic ice. This is essentially the procedure followed by Dewar in 1905 when he prepared what he recognized as a new phase of ice. Whalley (67, 68) was able to show that ices II, III, IV, V, VI, and VII all transform to cubic ice when recovered at 77 K and atmospheric pressure followed by heating to temperatures around 160 K. It appears that if a metastable solid phase of water can be recovered at 77 K and atmospheric pressure, cubic ice can be made from that phase by heating it to approximately 160 K.

Ice I exists in large quantities on the earth, in the solar system (69), and possibly in interstellar space (70). Some of this ice probably exists as ice I_C . Although no naturally occurring samples of cubic ice have been recovered, the existence of cubic ice in nature

has been inferred by several workers and reported in the literature. Minerals such as diamond and sphalerite, which have internal structure similar to cubic ice, are known to form octahedral crystals. Several natural phenomena have been explained based on the assumption that cubic ice crystals in the upper atmosphere exist as octahedra rather than cubes. It has been proposed that Scheiner's halo, a very rare halo that has only been observed six times since it was first observed in 1677, is caused by octahedral crystals of cubic ice in the upper atmosphere (21). It has also been suggested that some natural polycrystalline snowflakes grow from ice nuclei in the upper atmosphere that are octahedral crystals of cubic ice (71). This idea comes from the fact that many polycrystalline snow crystals are composed of twinned hexagonal ice crystals that have their c-axes oriented at about 70° to each other. This is the angle that would be expected between c-axes if hexagonal ice grew on the faces of cubic ice octahedra so that the c-axes of the hexagonal crystals were perpendicular to the faces of the octahedra.

The Structure of Amorphous Ice

When water vapor is slowly deposited onto a very cold substrate, the vapor phase molecules quickly lose their energy to the substrate and stick close to the point where they strike the substrate. If the temperature of the substrate is high enough, the molecules will have enough energy to move over the surface of the growing ice film and seek out positions of minimum potential energy before becoming frozen into position. When the molecules are able to achieve the positions of lowest potential energy, crystalline phases of ice (hexagonal ice or cubic ice) are formed. However, if the temperature of the substrate is low enough the molecules stick to the surface before they are able to relax to the

minimum energy crystalline structure. In this case, amorphous (non-crystalline) ice is formed. Amorphous solid water, or vitreous ice (denoted as ice I_{as} , I_v , or I_a) was first reported by Burton and Oliver (61) in 1935. When water vapor was deposited at temperatures below approximately 158 K, Burton and Oliver obtained a material with an x-ray diffraction pattern resembling that of liquid water. The electron diffraction studies of Blackman and Lisgarten (63) discussed in the section on cubic ice also indicated the formation of an amorphous phase of ice when water vapor was deposited onto a substrate at temperatures less than approximately 130 K. It was suggested as early as 1952 by Pryde and Jones (72) that the amorphous ice prepared in these and other earlier studies was not pure amorphous ice because of the large variance in thermal properties reported in the literature. This was later confirmed by Olander and Rice (73). By comparing the x-ray diffraction pattern of amorphous ice samples prepared at around 20 K to those prepared at higher temperatures (over 77 K), Olander and Rice concluded that samples prepared at higher temperatures contained an appreciable concentration of crystalline ice nuclei and were much less stable towards crystallization than samples prepared at temperatures less than 77 K. They concluded that to insure purely amorphous samples of ice the vapor must be deposited slowly (sample growth less than or equal to 0.1 mm / hr) and at temperatures less than 77 K (preferably less than 55 K). Amorphous ice prepared in this way (slow vapor deposition at temperatures less than 77 K) has a density of approximately 0.94 g cm^{-3} (66). A high-density phase with a density of 1.17 g cm^{-3} can also be prepared at 77 K by pressurizing hexagonal ice to 12 kbar (74) or low-density amorphous ice to 5 kbar (75). This metastable phase can then be recovered at 77 K and atmospheric pressure. The high-density phase prepared by this method converts to low-

density amorphous ice upon heating to approximately 128 K. The x-ray diffraction pattern of low-density amorphous ice prepared by this method was shown by Bosio and co-workers (76, 77) to be identical to that of vapor deposited amorphous ice. Bosio also argued that the high-density phase of amorphous ice reported by Rice and co-workers (75) that was prepared by vapor deposition at 10 K was not actually a new phase (high density amorphous ice), but was a result of the deposition process. Bosio proposed that at 10 K, a significant number of water molecules stick to the surface of the sample before achieving tetrahedral hydrogen bonding. This leads to interstitial packing with extra molecules frozen in voids, and hence an increase in density.

A molecular level simulation of the formation of amorphous ice has been performed by Zhang and Buch (78). Using classical molecular dynamics and a TIPS II potential, the condensation of water molecules onto a cluster of amorphous ice was simulated. These clusters were then used as models for amorphous ice. A typical calculated structure is shown in Figure 8. In these calculated structures, the distribution of ring structure sizes is wide, ranging from 3-membered to 7-membered polygons. This distribution is very similar to that found in liquid water (79). For the largest cluster calculated (296 molecules), a water molecule forms on the average 3.7 hydrogen bonds, a finding which is consistent with the x-ray diffraction results. In addition, the distribution of oxygen-oxygen first and second neighbor distances is very similar to the x-ray results (66). These computational results support the conclusion drawn from the x-ray diffraction results (Table 5) that amorphous ice can be described as a continuous, random, tetrahedral network of water molecules.

TABLE 5

COMPARISON OF X-RAY DIFFRACTION RESULTS FOR
ICE I_h AND ICE I_a AT 77 K. FROM REFERENCE 66.

	Density, g cm ⁻³	Coordination Number	O-O Distance, Angstroms	RMS Variation, Angstroms
Ice I _h	0.93 (2)	4.0 (2)	2.751 (3)	0.091 (3)
Ice I _a	0.94 (2)	3.8 (3)	2.76 (1)	0.114 (3)

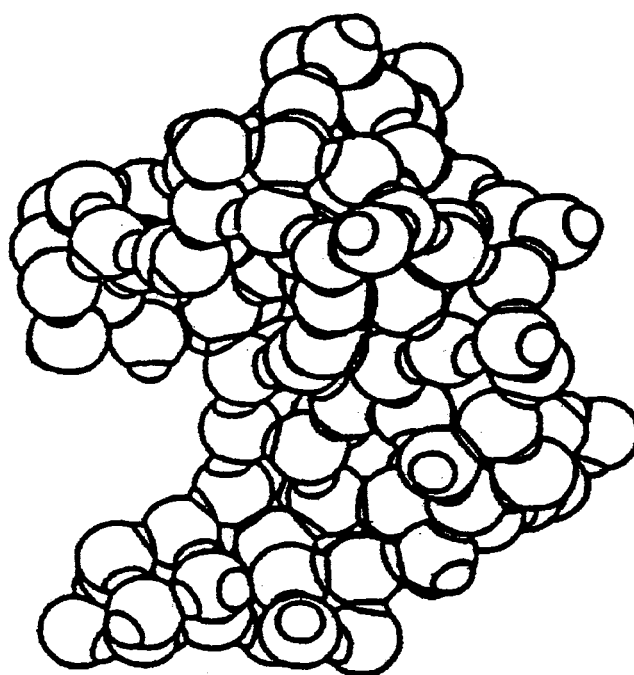


Figure 8. Structure of an amorphous ice cluster. From Reference 78.

Cubic ice (ice I_C) and amorphous ice (ice I_a) are metastable in the lower temperature portion of the ice I_h region of the phase diagram. Both of these phases are metastable in the lower temperature portion of the ice I_h region of the phase diagram. Ice I_C (cubic ice) occurs in the lower temperature part of the ice I_h region of the phase diagram and, although it has been argued that ice I_C is more stable than ice I_h at low temperatures, ice I_C appears to be metastable with respect to ice I_h . Ice I_C transforms slowly and irreversibly to ice I_h at temperatures above about 176 K (80) at a rate that depends on the temperature and thermal history of the sample. Ice I_a (amorphous ice) is a metastable phase that also occurs in the lower temperature segment of the ice I_h region of the phase diagram. The phase behavior of ice I_a is complex, exhibiting behavior that is dependent upon the method of preparation, thermal history, heating rates, and other experimental parameters related to a given type of experiment (81). This complexity has led to discrepancies in the literature relating to the behavior of ice I_a , particularly in the temperature range of 120 - 160 K. Ice I_a is metastable with respect to ice I_C , transforming irreversibly to ice I_C beginning at temperatures above approximately 130 K, with the rate of transformation depending on the temperature and thermal history of the sample.

Johari has induced transformation of polycrystalline hexagonal ice to a high-density amorph by application of a uniaxial pressure of approximately 10 kbar (82). Calorimetric and diffraction measurements performed on samples prepared in this way were performed. Johari concluded that the high-density amorph prepared in this way was not a homogeneously random structure, but was a mixture of highly strained microcrystalline

high-pressure phases of ice that transform to low-density amorphous ice when heated to near 130K.

Investigation of the Glass Transition in Amorphous Solid Water

Direct observation of the glass transition in amorphous solid water has proven to be elusive, and has led to considerable controversy (83). Values of the glass transition temperature reported in the literature vary widely, and appear to depend on the cooling rate during sample preparation, the heating rate at which measurements of the glass transition are made, the history of the sample, and sample preparation method. For example, the glass transition temperature has been reported as 124 K for low density amorphous ice warmed at 10 K per hour (84), and as 136 K for vapor deposited amorphous solid water (ASW) heated at a rate of 1800 K per hour (85).

Because of the structural disorder inherent in ASW, a larger number of proton configurations exist in the ice lattice relative to that observed in crystalline ice phases. Upon heating, the the higher entropy disordered structure formed upon rapid quenching relaxes to a lower energy state, with a corresponding release in energy. Hallbrucker and Mayer have reported a calorimetric study of hyperquenched glassy water (86). They report a release of heat beginning at 120 K that continues to 155 K. At 155 K, the amorphous sample crystallizes. Hallbrucker and Mayer attribute this exotherm to relaxation of the high energy quenched state to a lower enthalpy state. The magnitude of the exotherm and the temperature range over which the annealing occurs is larger for samples with a greater difference in the heating and cooling rates for the sample. Faster

cooling rates generate samples with larger entropy, which translates into a greater change in enthalpy upon annealing.

The mechanism for structural relaxation responsible for the exotherms observed upon heating of ASW is strongly debated. One viewpoint is that the exotherm observed is due to structural changes primarily in the proton system, with no translational diffusion of water molecules (i.e., is not due to a true glass transition). This would imply that ASW is a non-diffusive glass. This viewpoint assumes that the oxygen atom network remains intact (with only minor changes in oxygen atom positions) during the relaxation process. This viewpoint suggests that the actual glass transition temperature lies well above the ASW crystallization temperature, making it impossible to observe the glass transition directly.

The second point of view presumes that near the glass transition temperature the onset of molecular translational diffusion occurs, characteristic of a liquid state. This viewpoint implies that the liquid state is metastable for significant periods of time in the presence of nucleating ice crystals, at a temperature nearly 100 K below the homogeneous nucleation temperature of water (which, if correct, is surprising).

Recently, it has been reported that ice I_a undergoes a reversible glass transition at approximately 135 K to a phase that is presumably liquid, and this liquid phase then converts irreversibly to ice I_c at approximately 150 K (87, 88). Evidence for molecular diffusion in amorphous solid water has also been suggested by Kay (89). Samples were prepared by sequential vapor deposition of H_2O , D_2O , and $H_2^{18}O$ on Au(111) and Ru(001) substrates. Samples prepared in this way consist of layers of the various isotopic species. The samples were then heated at a rate of 0.5 K/s from 85K to a temperature

sufficient to desorb the film completely from the substrate. The desorption rate was measured over time with a quadrupole mass spectrometer. Before the phase transition to crystalline ice, no isotopic mixing between layers was observed, but complete mixing was observed after the phase transition. In one experiment, only H₂O (the top layer in this experiment) was desorbed below 154 K, but above this temperature H₂O, D₂O, and HOD are all detected, suggesting that all species were then present in the top layer. The diffusion rates for the isotopic species from the bulk to the topmost layer were a factor of 10⁶ greater than expected based on extrapolations from data for diffusion in ice at 273 to 233 K. Hence, the conclusion was drawn that translational diffusion of water molecules was required in order to explain the discrepancy in diffusion rates.

It will be proposed in the work reported here that the endothermic relaxation observed upon heating ASW is facilitated by the onset of rapid mobility of non-diffusive Bjerrum point defects in ASW (90). The current work will suggest that Bjerrum point defects, which will be discussed in detail in the next section, become active in ASW near the glass transition temperature. These defects also become mobile in cubic and hexagonal ice at near the same temperature (approximately 130 K) (14). Data will be presented suggesting that this model (Bjerrum defect activity) is consistent with the viewpoint that the observed relaxation in ASW upon heating occurs without the onset of molecular translational diffusion.

Defects in the Ice Structure

As has been previously discussed, an ice crystal that strictly obeys Pauling's statistical model for ice, and hence the Bernal - Fowler rules, is referred to as an 'ideal' ice

crystal. Real ice crystals contain various types of defects and as a result do not strictly obey the Bernal - Fowler rules. For instance, the second Bernal - Fowler rule states that all of the water molecules in ice are tetrahedrally hydrogen-bonded; at the surface of an ice crystal this is impossible to accomplish. Real ice crystals can also contain defects referred to as vacancies. This type of defect occurs when a water molecule is missing from the ice lattice, again destroying the tetrahedral network. Other types of defects exist in ice, several of which are important in the present study. These defects will be reviewed in detail in the following paragraphs.

Ionic Defects

One of the Bernal - Fowler rules states that water molecules remain intact in the ice structure. However, if a proton were to jump from the water molecule at one end of a hydrogen bond to the water molecule at the other end of the bond, a defect referred to as an ionic defect occurs. The exact nature of the ions formed in ice from such a process is not known, but they are assumed to be either H^+ and OH^- , or H_3O^+ and OH^- (1). The reaction can be represented by



where the ions are always formed in pairs. Whether or not there are two potential minima along the O-H...O bond is uncertain (91, 92), but at best the two ions are metastable towards recombination. There is a finite probability that a proton jump could occur along neighboring bonds that would separate the ions by a water molecule before recombined. This situation is illustrated in Figure 9. Once the defects are separated by a water molecule, they are stable in the sense that they cannot immediately recombine even though

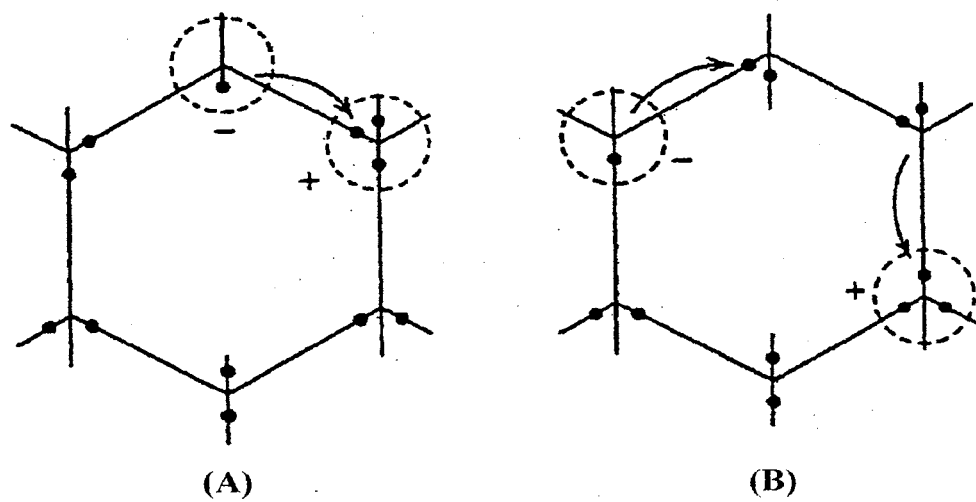


Figure 9. Schematic representation of formation of an ionic defect pair. From Reference 22.

there is an electrostatic attraction between them (22). Subsequent proton jumps could lead to either recombination of the ions if two ions of opposite signs meet, or to diffusive separation of the ions. It should be noted that although individual protons are restrained to movement along the bond on which they sit, the ionic defects can still migrate through the crystal.

For a pure ice crystal in thermal equilibrium, the concentration of ionic defects in the crystal is given by

$$n_+ = n_- = n_s \exp(-H_{\pm}^f / 2kT), \quad 1.6$$

where (n_s) is the number of intact water molecules per unit volume in the crystal, (H_{\pm}^f) is the enthalpy of formation for a single separated defect pair, (k) is the Boltzmann constant, and (T) is the temperature. The enthalpy of formation for the defect pair is composed of two parts: the enthalpy involved in proton transfer along the bond, and the enthalpy due to the separation to the two ion states against their electrostatic attraction. It is not easy to measure the concentration of ionic defects in ice, but it has been estimated that this concentration is less than in liquid water at the same temperature by a factor of between 10^{-2} and 10^{-5} (22). It has also been determined that the positive ion states in ice are much more mobile than the negative ion states (88). In the case of the positive ion state mobility, an excess proton is being transferred between two essentially neutral molecules. In the case of negative ion state (OH^-) mobility, the ion state migrates by transfer of a proton between two negatively charged OH^- units, which would have a higher energy barrier to proton motion relative to the mobility of the positive ion state (22).

Orientalional Defects

The third rule of Bernal and Fowler states that in an ideal ice crystal only one proton lies between oxygen-oxygen nearest neighbors. Bjerrum (94) proposed that in a real ice crystal there are water molecules that are oriented in violation of the third Bernal - Fowler rule so that there are either zero or two protons between oxygen-oxygen nearest neighbors. The existence of these 'orientational defects' was proposed by Bjerrum to account for the dielectric properties of ice by some mechanism other than by the migration of ionic defects. When two protons lie between oxygen-oxygen nearest neighbors, the defect that results is referred to as a D-defect (from the German word 'doppelt', which means 'doubled'), and the defect which results when there are no protons between oxygen-oxygen nearest neighbors is referred to as an L-defect (from the German word 'leer', meaning 'empty'). These defects are formed in pairs by a 120° rotation of a single water molecule about one of its hydrogen bonds, leading to one doubly occupied bond (D-defect) and one unoccupied bond (L-defect). Since the newly formed pair of defects lie on adjacent bonds, the probability is high that the molecule will rotate back to its original position, eliminating the pair of defects. However, there is a finite probability that the two defects will diffuse farther apart by successive rotations of neighboring water molecules. The formation of a pair of orientational defects and their subsequent migration is described in Figure 10. When L and D-defects meet each other in the lattice, they may recombine with each other and be eliminated. Hence, at a given temperature an equilibrium exists in which there will be a well-defined and equal concentration of L and D-defects in the crystal. It has been estimated that the number of molecules in ice involved in orientational

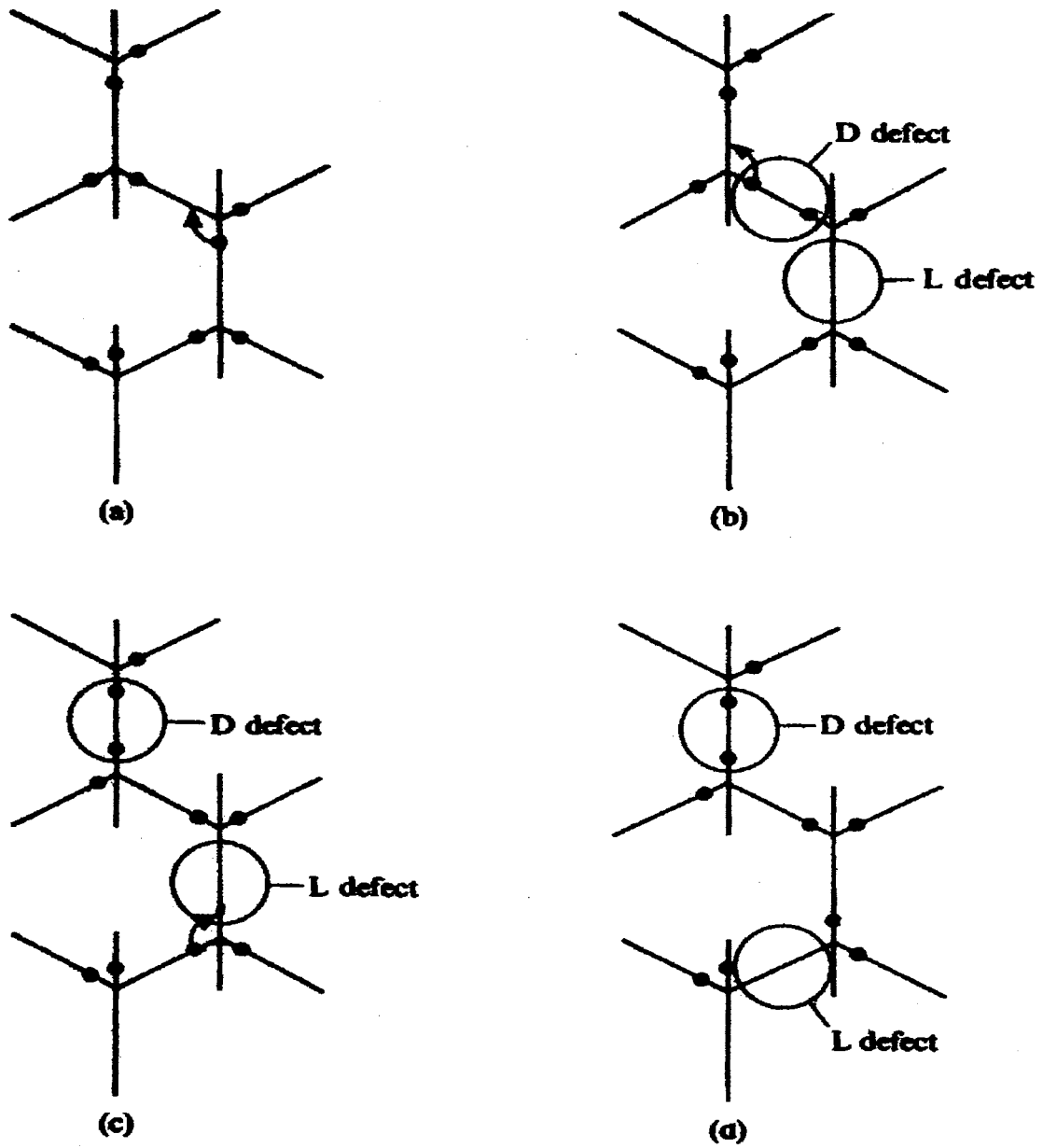


Figure 10. The formation and migration of Bjerrum defects in ice.
From Reference 1.

defects is approximately 1 molecule in 6×10^6 at just below 0° , and the frequency of rotation of the hydrogen atoms is about $5 \times 10^4 \text{ s}^{-1}$ (1). It is generally recognized that L-defects in pure ice are more mobile than D-defects (95). The enthalpy of formation of an L and D-defect pair at 263 K is approximately $16 \text{ kcal mole}^{-1}$ (22).

The Infrared Spectrum of Ice

When electromagnetic radiation interacts with a material, the oscillating electric field of the electromagnetic wave causes the atoms in the material to vibrate about their equilibrium positions. If these vibrations produce a change in the electric dipole moment of the individual molecules which make up the material, radiation is absorbed or emitted as the atoms take up different vibrational energy levels. If the material is a polar gas, the radiation may also be absorbed or emitted due to the molecular dipoles rotating in the applied electric field. If electronic excitations are ignored, changes in the energy state of a molecule are then caused by vibrational and rotational excitations of the molecules. Radiation that causes vibrational and rotational excitation of molecules is primarily in the infrared region, in the wavenumber range extending from 10 cm^{-1} to about $13,000 \text{ cm}^{-1}$. Infrared radiation responsible for rotational excitations of molecules is generally below about 600 cm^{-1} , and the radiation responsible for vibrational excitations is generally above about 600 cm^{-1} . The infrared spectrum of water vapor is composed of absorptions due to rotational as well as vibrational excitations (1). In ice, since the water molecules strongly interact with other water molecules in the ice lattice, the free rotation of water molecules possible in the gas phase is not possible in ice. Hence, the vibrational spectrum of ice consists of broad bands with no rotational structure.

Making accurate, detailed assignments of ice spectra is very difficult. As previously mentioned, the bands in ice spectra are typically broad (due in part to proton disorder in ice) and overlap considerably. The effects of Fermi resonance in ice further complicate the making of accurate band assignments (96). Fermi resonance can sometimes occur when two vibrational modes (normally a fundamental and an overtone) are accidentally nearly degenerate, which is the case for ν_1 and $2\nu_2$ in ice. This resonance can give rise to unusual band shapes that are not simple sums of the component bands. In addition, the overtone (which is normally weak in intensity) can gain intensity at the expense of the intensity of the fundamental. Because of the complexity of the ice spectrum, only the major points of interest related to the present study will be reviewed in this chapter. For a more thorough review of ice spectra, see the review of Rice and Sceats in reference (97).

The infrared absorption frequencies of the vapor phase and H_2O and D_2O ice I_h are given in Table 6. The bands are broad, and are shifted considerably compared to the vapor phase values due to strong hydrogen bonding in ice. The frequencies for ice I_c are very nearly equal to the frequencies for ice I_h , again reflecting the high degree of similarity in the hexagonal and cubic ice structures (22). The band frequencies are shifted to slightly higher frequencies in amorphous ice, which reflects an increase in the O-H bond strength due to weaker hydrogen bonding in ice I_a . In addition, the bands in amorphous ice are much broader than in ice I_h or ice I_c because of the disorder in oxygen atom positions in ice I_a (98). In all three of these phases of H_2O ice, ν_1 , ν_3 , and the ν_2 overtone contribute to a broad, complex band system in the mid-infrared ice spectrum at near 3200 cm^{-1} . This complex peak is shifted to near 2400 cm^{-1} in D_2O ice.

TABLE 6
INFRARED ABSORPTION FREQUENCIES FOR VAPOR
PHASE AND H₂O AND D₂O ICE I_h.

	H ₂ O Vapor	H ₂ O Ice	D ₂ O Ice
ν_1	3652	3143	2347
ν_2	1595	1640	1210
ν_3	3756	3252	2440

In addition to the intramolecular vibrational modes discussed in the previous paragraph, an ice crystal has translational and librational modes that are due to intermolecular interactions between neighboring water molecules in the ice lattice. The translational modes produce weak bands in the far infrared region between 152 cm^{-1} and 175 cm^{-1} , and another band near 60 cm^{-1} . The bands near 150 cm^{-1} have been assigned to hindered translations of water molecules produced by hydrogen-bond stretching motions, while the 60 cm^{-1} band has been assigned to hydrogen-bond bending motions (99). The frequency shift for the translational modes upon changing from H_2O to D_2O ice I_h is close to $(18/20)^{1/2}$ (22). The librational modes are due to hindered rotations of water molecules. These modes correspond to twisting, wagging, and rocking motions of coordinated water molecules, and are illustrated in Figure 11. The frequency of the absorptions due to librational modes in H_2O ice I_h are in the far to mid-infrared region, producing a broad band between approximately 500 cm^{-1} and $1,050\text{ cm}^{-1}$ (100).

The Mid-Infrared Spectrum of the Isotopomers of H_2O Decoupled in Ice

Haas and Hornig (101) prepared a series of hexagonal ice samples by depositing room temperature mixtures of H_2O and D_2O vapor of varying compositions onto a cooled AgCl substrate held at approximately 190 K . When H_2O and D_2O vapor are mixed at room temperature, isotopic exchange occurs readily, meaning that the mixtures that were deposited contained appreciable amounts of HOD . For samples in which the concentration of HOD was small (5% or less), the sample was essentially HOD isolated in either a H_2O or D_2O matrix. In these samples, it was observed that the O-D stretching band complex collapsed to a sharp, relatively narrow (with a width of 20 cm^{-1}),

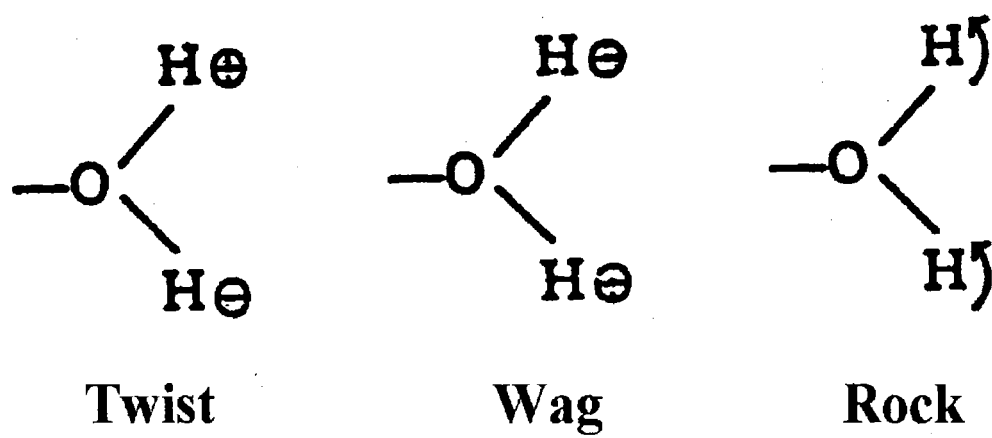


Figure 11. The librational modes of water (ice).

structureless peak at near 2416 cm^{-1} . Upon increasing the concentration of HOD in the samples (to 18% HOD), two bands appeared at near $2,393\text{ cm}^{-1}$ and $2,442\text{ cm}^{-1}$. These features were attributed to coupled vibrations of neighboring HOD molecules. Hence, Haas and Hornig concluded that the broadening of the bands in the O-H (or O-D) stretching complex in ice was not due to hydrogen bonding, but rather to a mixture of intramolecular and intermolecular dynamical coupling of O-H (or O-D) oscillators.

The in-phase coupled vibrational band of the O-D \cdots O-D pair absorbs more intensely and lower in frequency than the out-of-phase coupled vibration. Whalley and Klug (102) have reported the value for the frequency of the in-phase coupled vibration in ice I_c as $2,396\text{ cm}^{-1}$, while the frequency of the out-of-phase coupled vibration is about $2,439\text{ cm}^{-1}$. The half-width of the in-phase component is approximately 23 cm^{-1} , while the value is about 22 cm^{-1} for the out-of-phase component. It would be expected that these bands would be broader and shifted to higher frequency in amorphous ice. The ratio of the intensity of the in-phase component to the out-of-phase component is reported as 1.66 ± 0.02 for cubic ice.

Techniques have been developed by which it is possible to prepare samples of D_2O isolated (decoupled) in H_2O ice, with only a small amount of isotopic exchange taking place during sample preparation (103, 104, 105). The procedure involves the co-condensation of a vapor beam of H_2O with a vapor beam of D_2O onto a cooled infrared window. By varying the flow rates of the beams, it is possible to control the ratio of D_2O to H_2O in the samples. The temperature of the substrate during deposition, along with the flow rates, determines which phase of ice is prepared. At temperatures between

approximately 175 K and 273 K, ice I_h is deposited, and at temperatures between about 125 K and 175 K, ice I_c is deposited. At lower temperatures (less than 77 K), it is possible to prepare ice I_a . It is necessary to keep the flow rates of the vapor beams low enough to insure that the temperature of the substrate is not elevated considerably during deposition. After the samples are prepared, the temperature of the sample can then be elevated to a point where isotopic exchange begins, and the exchange process can be followed spectroscopically.

Devlin and co-workers have assigned the vibrational frequencies in the O-D stretching region for D_2O , HOD, and neighbor-coupled HOD (written as $(HOD)_{cp}$) decoupled in H_2O ice I_c (15). Using spectral subtraction techniques, it is possible to separate the O-D stretching band complex into its individual component peaks. This is accomplished as follows. The H_2O ice background is first subtracted from the band complex. From the resulting spectrum, the absorption due to HOD present as a contaminant formed during deposition is subtracted, leaving the spectrum of decoupled D_2O , assuming that little or no $(HOD)_{cp}$ is present in the sample. The spectrum of decoupled HOD, which is needed to obtain the decoupled D_2O spectrum, can be obtained in two ways. The first method involves preparing a normal sample of D_2O decoupled in H_2O , and then allowing complete isotopic scrambling of the D_2O into HOD by raising the sample to a temperature at which the scrambling process is rapid and complete. If this is not possible to accomplish, which is the case in ice I_a , the decoupled HOD spectrum can be obtained directly by depositing at the appropriate temperature the vapor of a 4% mixture of HOD in H_2O . The spectrum of $(HOD)_{cp}$ is more difficult to obtain. Samples prepared as described in the previous paragraph contain very little $(HOD)_{cp}$. However,

techniques exist which enable the concentration of $(\text{HOD})_{\text{cp}}$ in a sample to be increased by converting some of the D_2O in the sample into $(\text{HOD})_{\text{cp}}$ (14, 16). After generating an appreciable concentration of $(\text{HOD})_{\text{cp}}$ in the sample, the spectrum of $(\text{HOD})_{\text{cp}}$ can then be obtained by subtracting the absorptions due to decoupled D_2O and HOD in the sample. A sample of the results of this separation procedure are illustrated in Figure 12 for ice I_c .

The fact that the individual component spectra can be obtained is important to the present study in that it enables changes in the concentrations of D_2O , HOD , and $(\text{HOD})_{\text{cp}}$ to be monitored spectroscopically as the defect activity in ice brings about isotopic scrambling in the sample.

Studies of Defect Activity in Ice

Pauling's statistical model allowed the configuration of an ice crystal to change either by the rotation of water molecules about a hydrogen bond, or by proton hopping along hydrogen bonds. Neither of these configurational changes can occur in an ideal ice crystal without violating the Bernal - Fowler rules unless the orientation of other water molecules in the lattice change simultaneously to accommodate the change in configuration. Such changes in configuration are unlikely energetically, and would produce no change in the net dipole moment of the crystal. The electrical properties of ice cannot be explained by such changes in configuration. However, the presence of defects in ice would allow isolated changes in the configuration of the crystal, which would result in a change in the net dipole moment of the crystal. It has been postulated that ionic and orientational defect activity in ice is directly responsible for many of the electrical

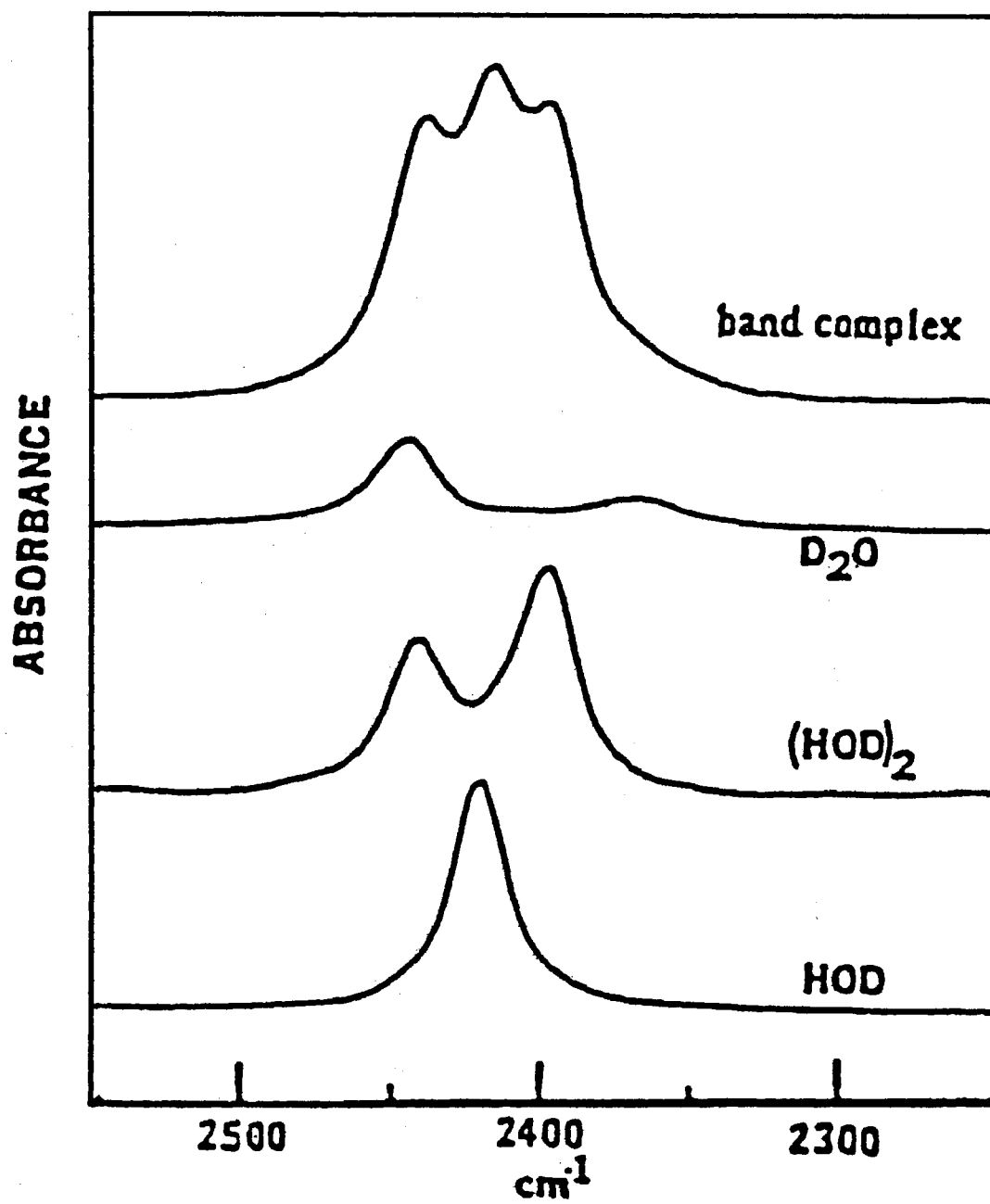


Figure 12. The O-D stretching band complex for D₂O decoupled in H₂O ice I_c.

properties of ice. In addition, it has already been mentioned that orientational defects may play a role in the phase transformation mechanism in hydrogen-bonded systems (10).

Conductivity Studies

Figure 13 shows the results of studies performed by Camp (106) on the ac and dc conductivity measurements of ice I_h at a variety of temperatures. These studies suggest that the dc conductivity remained fairly constant at higher temperatures, but eventually started to decrease as the temperature was lowered. The ac conductivity followed a pattern opposite of the dc conductivity, with the conductivity steadily decreasing as the temperature was lowered, and eventually becoming nearly constant at lower temperatures. The symmetry of the dc and ac conductivities implies that there are two fundamental processes in ice that contribute to the conductivity. It has been proposed that these two processes might be ionic and orientational defect motion. Furthermore, it has been proposed that the ac conductivity is due primarily to orientational defect activity, while the dc conductivity is due primarily to ionic defect activity.

Both the dc and ac conductivity of ice decrease with decreasing temperature. The dc conductivity has been reported as $(1.1 \pm 0.5) \times 10^{-8} \text{ ohm}^{-1} \text{ m}^{-1}$ at 263 K, with an activation energy of about 8 kcal mole^{-1} at temperatures above 213 K (107). The ac conductivity has been reported as $(4.47 \pm 0.14) \times 10^{-5} \text{ ohm}^{-1} \text{ m}^{-1}$ at 273 K, with an activation energy of about $13 \text{ kcal mole}^{-1}$ for temperatures above 223 K (106). The conductivity in ice has been shown to be purely protonic, with no appreciable contribution from electrons (108). Ionic impurities can have a drastic effect on the conductivity of ice.

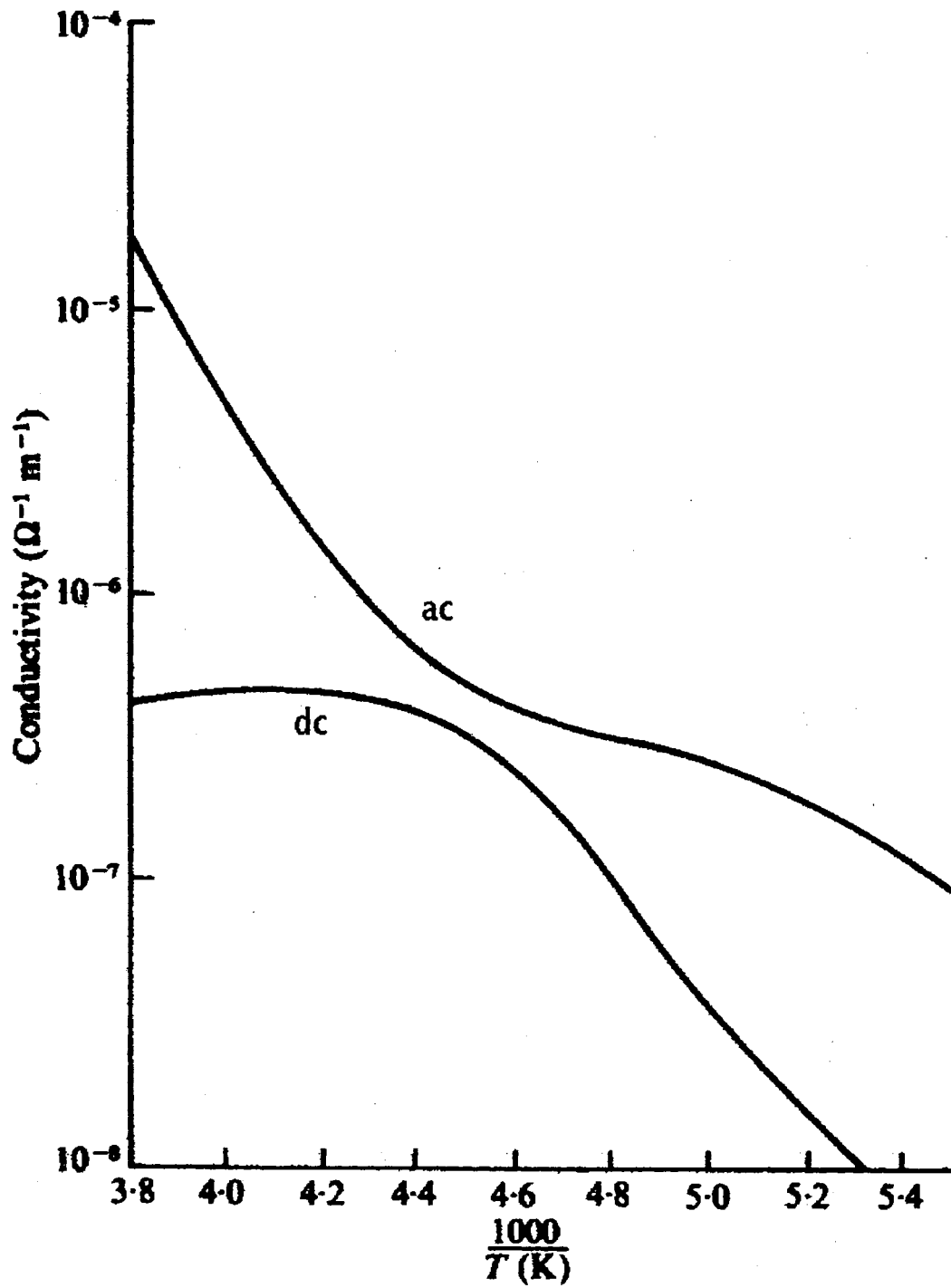


Figure 13. AC and DC conductivity data from 263 K to 182 K. Adapted from Reference 32.

The dc conductivity of HF doped ice increases as the square root of the concentration of HF over the range 10^{-5} to 10^{-2} mol liter $^{-1}$ (109).

Studies of the Dielectric Constant and Dielectric Relaxation of Ice

Studies on doped ice crystals have yielded insight into the nature of the major and minor charge carriers in ice. For every HF molecule built into the ice lattice, there is a deficiency of one proton for bonding. Therefore, when an ice crystal is doped with HF, there is an increase in the number of L-defects in the crystal. In addition to the L and D-defects present due to thermal activation in the crystal, each HF molecule in the lattice results in an additional L-defect. Hence, the number of additional L-defects is proportional to the concentration of HF in the crystal. The addition of HF in the crystal also produces ionic defects in the crystal due to the reaction



The F^- ion should be immobile in the crystal and not affect the electrical properties, but the H_3O^+ ion has a considerable effect on the electrical properties of ice. The dissociation constant for the above reaction is given by the law of mass action as

$$K' = \frac{n^+ n_{\text{F}^-}}{n n_{\text{HF}}} \quad 1.8$$

where (n^+) is the concentration of H_3O^+ , (n_{F^-}) is the concentration of F^- , (n) is the concentration of water molecules in the lattice, and (n_{HF}) is the concentration of HF in the lattice. (K') is a constant, and (n) is large and remains effectively constant. For high concentrations of HF, the concentration of (n^+) due to HF ionization is large compared to (n^+) due to the normal ionization of H_2O in the crystal. Hence, it can be argued that the

contribution to (n^+) from H_2O ionization can be neglected. This being the case, it can be assumed that (n^+) is approximately equal to (n_{F^-}) . Therefore, when the HF concentration is large, it can be said that (n^+) is proportional to $(n_{HF})^{1/2}$ (i.e., the concentration of H_3O^+ increases as the square root of the HF concentration). Hence, as the concentration of HF is increased in the crystal, the concentration of L-defects should eventually dominate over the increase in the concentration of H_3O^+ , since the concentration dependence of L-defects is linear (first power) and the concentration dependence of H_3O^+ varies as the square root (1). This can be observed experimentally in studies of the static relative permittivity (dielectric constant) and dielectric relaxation time for HF doped ice performed by Steinmann (110) on ice I_h at 263 K (refer to Figure 14). Steinmann found that between the two minima in ϵ_s , the dielectric relaxation time (τ) varied inversely as the square root of [HF]. At higher concentrations, (τ) varied proportionally as the reciprocal of [HF]. It can be argued that at high concentrations of HF (above the second minimum in the curve), the L-defects dominate. At the second minimum, the concentration of orientational defects and ionization defects must be such that there is no polarization of the ice. Under these condition, the doped ice behaves much like a good conductor, which explains the drop in the relative permittivity near the second minimum. In the region between the two minima, the ionization defects dominate. At the first minimum, the ice again behaves as a poor conductor. At lower concentrations, the orientational defects again dominate. Extrapolating to zero HF concentration, the majority carriers in pure ice at 263 K should be orientational defects.

The dielectric constant of ice as a function of frequency has been measured (refer to Figure 15) (22). The static dielectric constant is large, with a value near 100. This

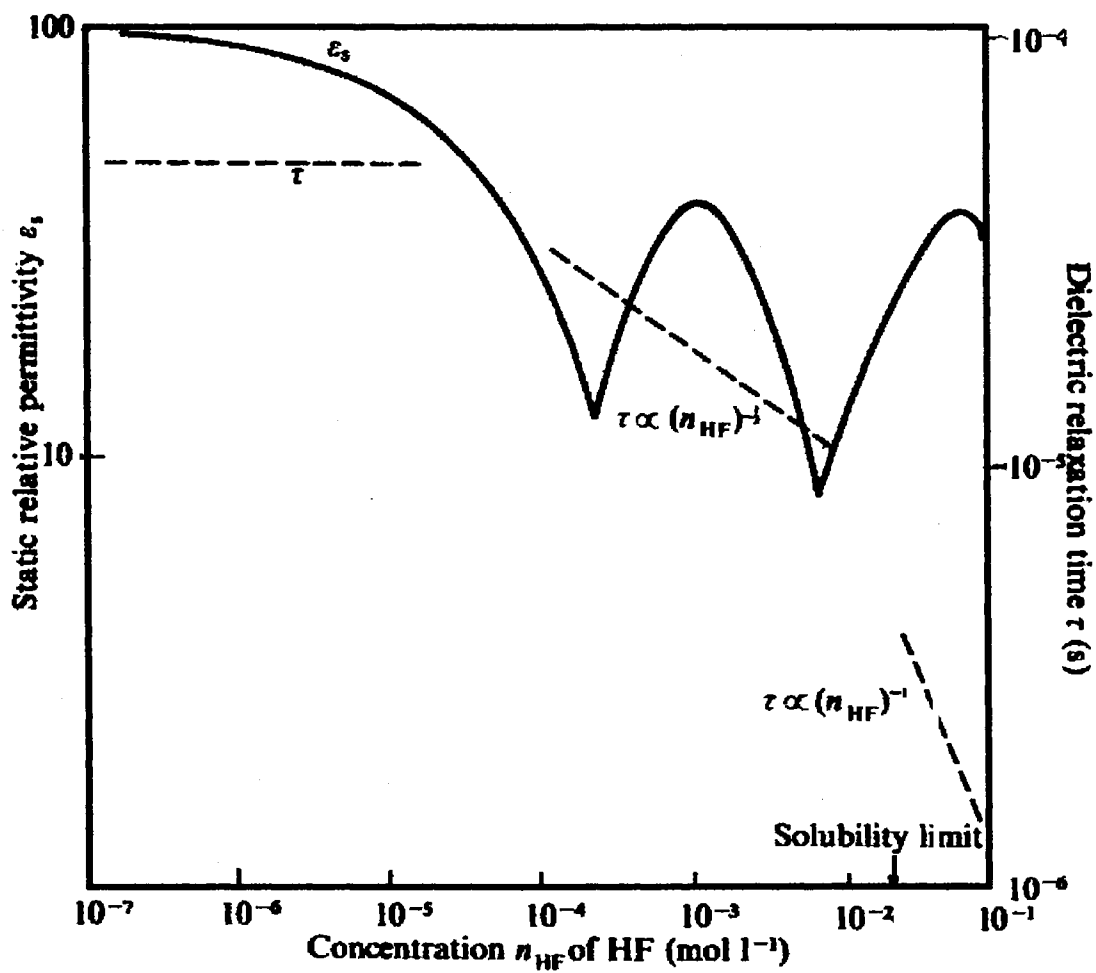


Figure 14. Static relative permittivity and dielectric relaxation time at 263 K as a function of [HF] in ice. From Reference 1.

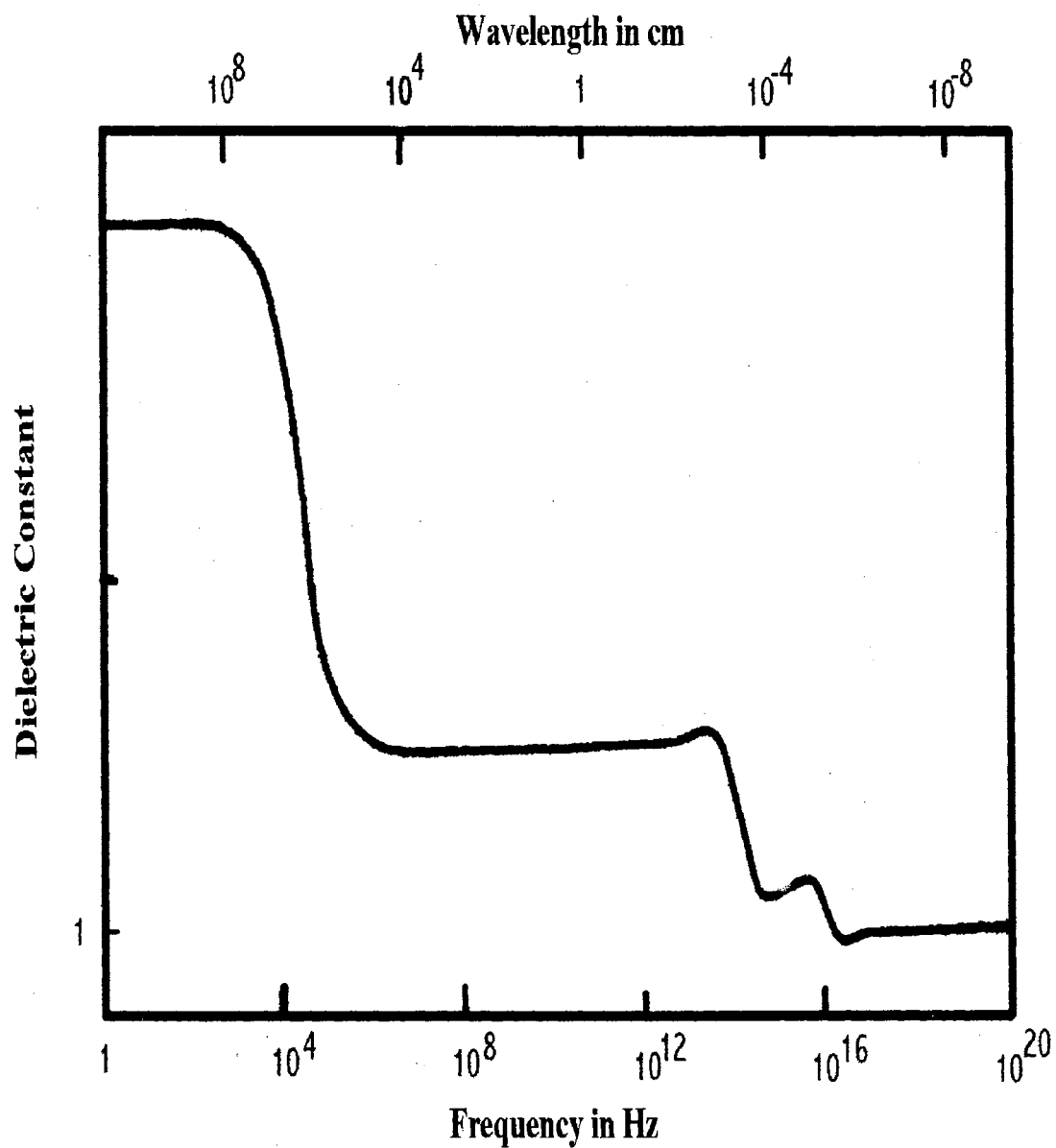


Figure 15. The dielectric constant of ice I_h as a function of frequency at 263 K. From Reference 22.

large value for the dielectric constant is consistent with the orientation of molecular dipoles preferentially in the direction of the electric field. The frequency at which the value of ϵ falls to a value of 3.2 can be associated with the inverse relaxation time for reorientation of molecular dipoles in the ice crystal. This frequency is highly dependent on the temperature and purity of the ice (22). Orientational and ionic defect activity is also highly dependent on the temperature and purity of ice. The conclusion could then be drawn that the reorientation of dipoles in the ice crystal is a result of point defect motion in ice.

The Theory of Defect Activity in Ice

Many of the theories that explain the experimentally observed conductivity and relaxation phenomena in ice depend on defect activity as a critical part of the theory. This theory has developed through the contributions of many workers including Bjerrum (94), Granicher (109), Onsager and Dupuis (111), and Jaccard (112, 113, 114). These theories are based on a two-step mechanism for proton transfer in ice. The first step is the transfer of a proton from a H_3O^+ ion to the next water molecule, and the second step involves the rotation of the water molecule. Hence, the mechanism involves both ionic and orientational defect activity.

The fact that both ionic and orientational defect motion is necessary for proton conduction in ice can be explained as follows. The motion of a D-defect along a chain of bonds (Figure 16a) leads to a configuration where all the bonds are polarized so that it is impossible for another D-defect to move along the same bonds in the same direction (Figure 16b). It is also impossible for an L-defect to move along the same bonds in the

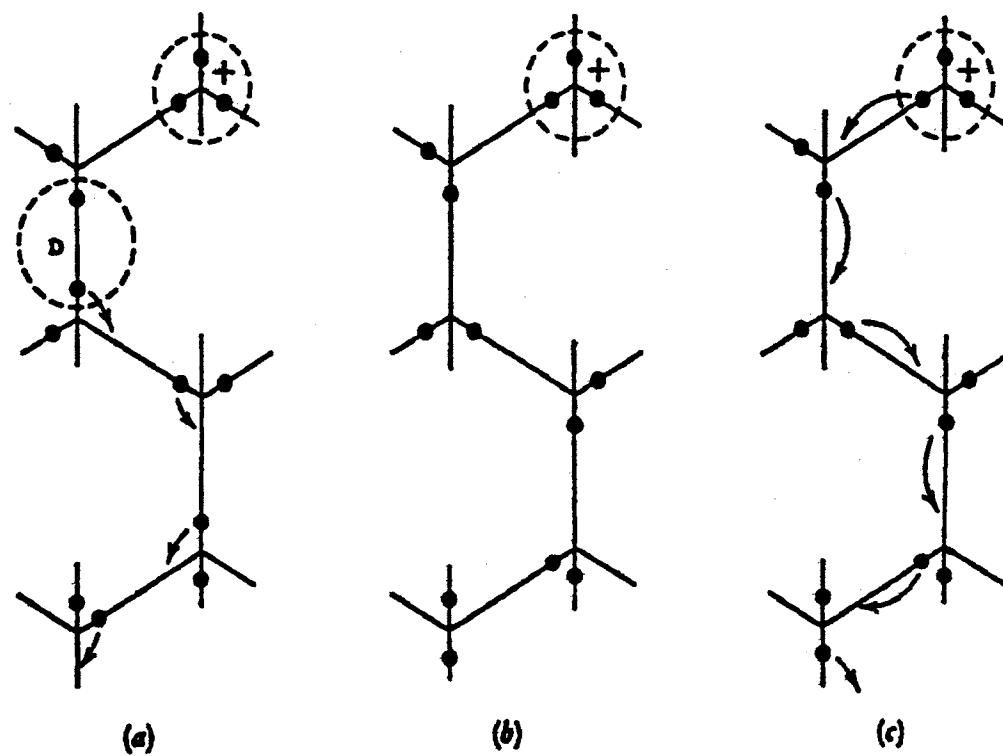


Figure 16. Action of ionic and orientational defects in ice.

opposite direction. Therefore, it is impossible for orientational defects alone to carry a steady proton current. However, the chain can be reset to its original configuration by the passage of a positive ionic defect (i.e., a H_3O^+ ion) along the chain in the same direction as the D-defect. The chain could also be reset by the passage of a negative ionic defect (i.e., an OH^- ion) in the opposite direction of the D-defect passage (22). Hence, both ionic and orientational defect activity is necessary to explain the static electrical conductivity of protons in ice by this theory.

According to theory, either orientational or ionic defects can be the majority charge carrier depending on the temperature and purity of the ice. Experimental results support this idea. The ac conductivity of ice I_h can be described as both the ionic and orientational defects contributing to the conductivity in parallel, which means that the majority carrier determines the ac conductivity. By definition, the majority charge carrier is the defect whose product of concentration times mobility is greater. The dc conductivity of ice I_h can be described as both ionic and orientational defects contributing to the conductivity in series, which means that the minority carrier determines the dc conductivity (1). As was previously discussed, the majority carrier at high temperatures (263 K) has been shown to be the orientational defects (110), meaning that the ac conductivity of ice I_h at high temperatures is largely due to orientational defects acting as the majority charge carrier. At low temperatures, it has been suggested that the ionization defects may become the majority charge carriers in pure ice (1), implying that the low-temperature dc conductivity in pure ice I_h is again determined by orientational defects, if orientational defects are indeed the minority charge carriers at low temperatures.

Spectroscopic Studies of Defect Activity

As previously mentioned, samples of D_2O decoupled in H_2O ice are an effective probe into defect activity in ice. Devlin and co-workers have made spectral assignments for the bands of the isotopomers of H_2O decoupled in H_2O ice in the O-D stretching region, and have used the spectral data to probe defect activity in the samples (10, 13, 14, 15). For pure ice I_C , it was found that upon warming the sample to between 135 K and 160 K, it was possible to follow the isotopic exchange spectroscopically (13). The rate of exchange at a given temperature was studied by collecting spectra at several time intervals as the isotopic scrambling of the sample proceeded. Upon completion of the collection of data, the spectrum of the O-D stretching region was separated as previously described into the individual spectra of the various isotopomers that make up the spectrum of the O-D stretching band complex. By comparing the changes in concentration of the individual component spectra (i.e., the concentrations of D_2O , HOD, and $(HOD)_{cp}$) with time, the rate of exchange could be followed. With time, the concentration of D_2O decreased, with bands that were attributed to $(HOD)_{cp}$ and HOD growing in intensity (Figure 17).

A mechanism was proposed which explained the spectroscopic data in terms of defect activity. The proposed mechanism was the two-step process that is illustrated in Figure 18. The first figure contains an isolated D_2O molecule. Note that the deuterons of this molecule cannot be separated by a rotation of the molecule, but only by the passage of a proton through the D_2O site. In the middle figure, the effect of the passage of the proton through the D_2O site is illustrated. This step produces neighbor-coupled HOD molecules, as can be seen in the middle figure. This mechanism does not allow deuterons

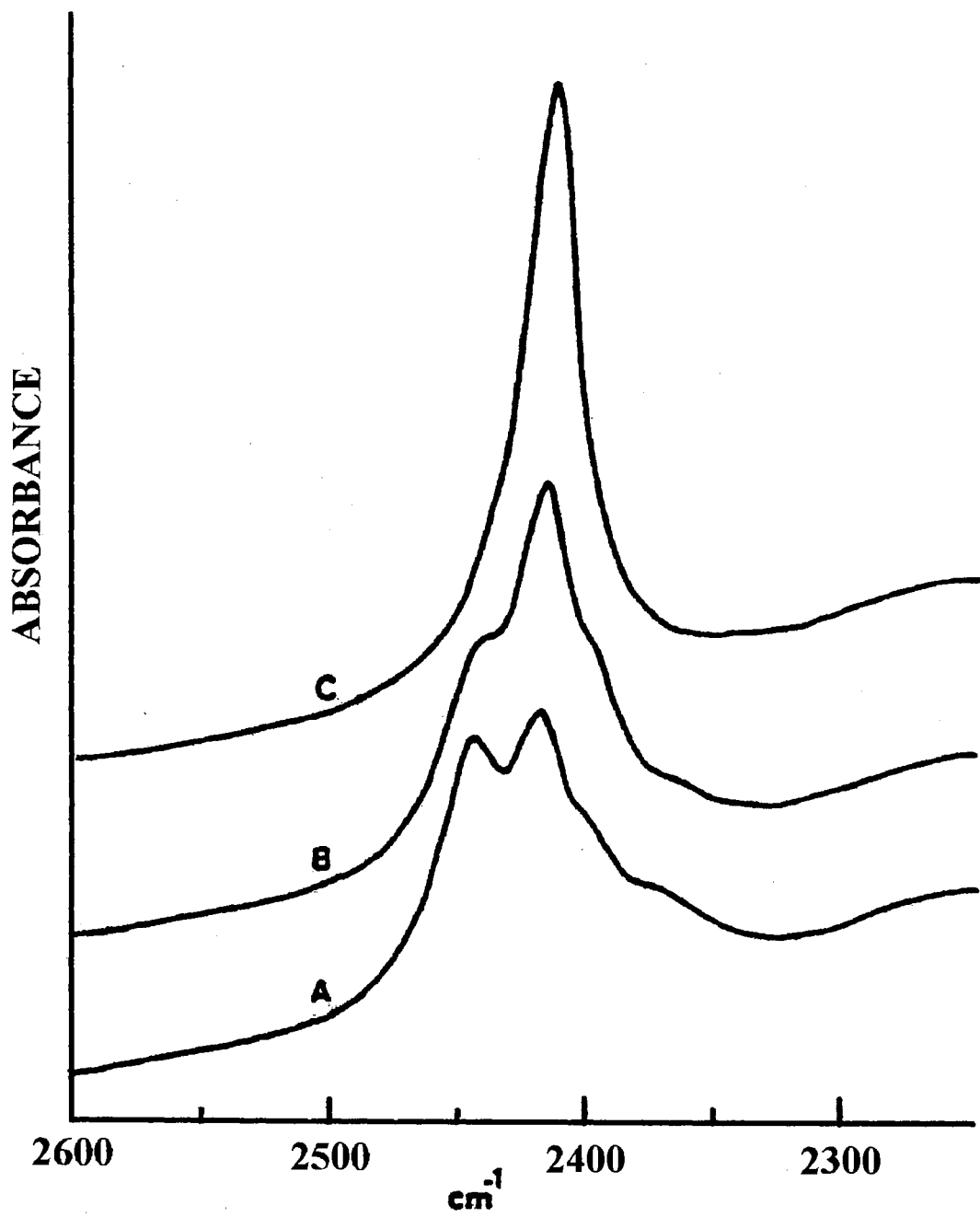


Figure 17. Spectra illustrating the conversion of D₂O to HOD.

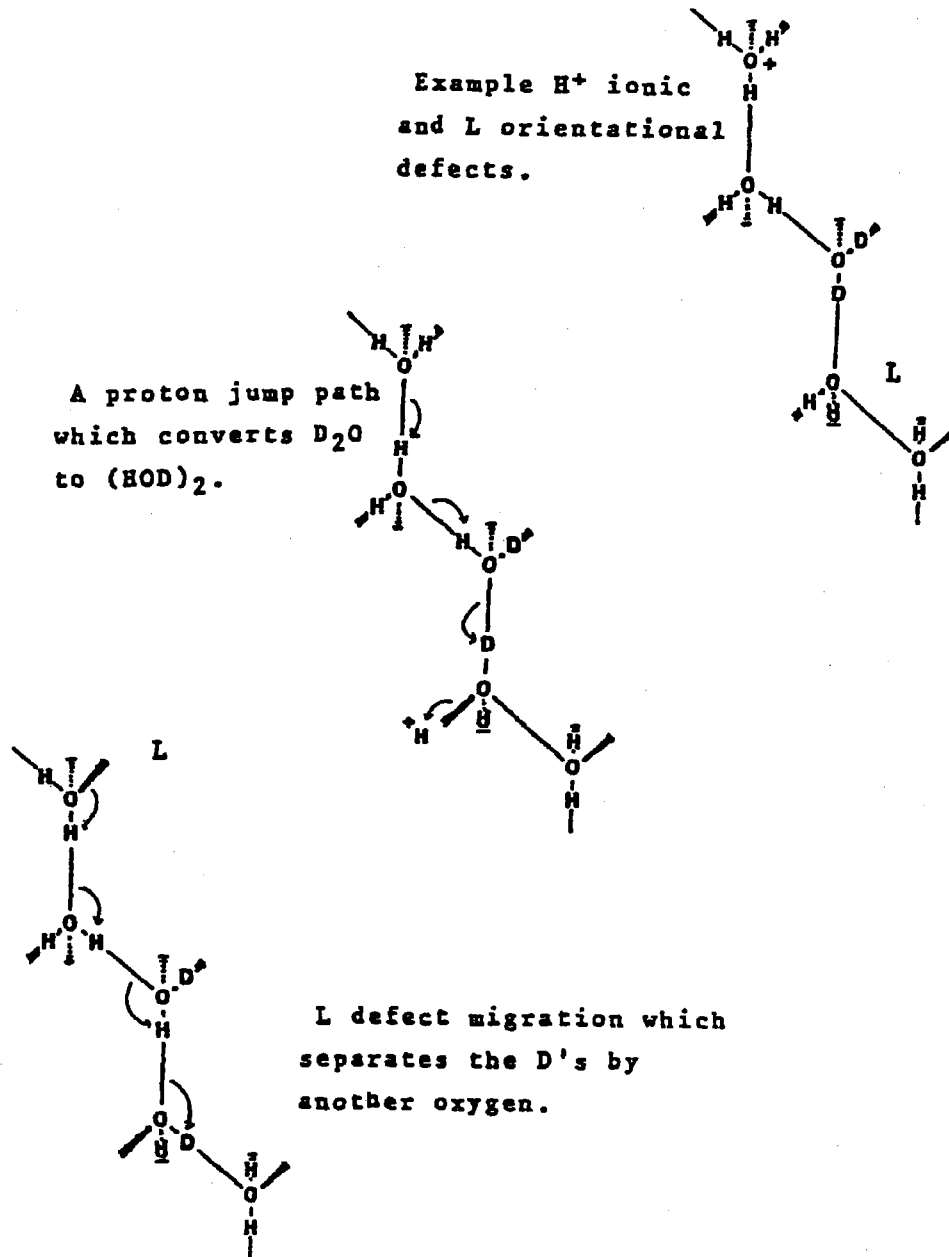
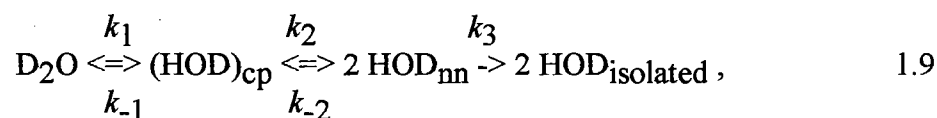


Figure 18. The mechanism of proton conduction in ice.

to separate any farther by the passage of another proton because the passage of another proton through the site in the same direction is not possible. However, the passage of an L-defect through the site will separate the deuterons by an oxygen molecule, as can be seen in the bottom figure. This results in the formation of two HOD nearest neighbor molecules (HOD_{nn}). The deuterons can then be further separated by successive passages of ionic and orientational defects.

The rates and energies of proton transfer and orientational defect migration in ice I_c were determined by Collier, Ritzhaupt, and Devlin (13) using the two-step mechanism described in the previous paragraph. The rates of reaction were fit to the differential equations describing the reaction



where the k 's are the rate constants for the forward or reverse reactions. Again, HOD_{nn} represents $(\text{HOD})_{\text{cp}}$ uncoupled by the passage of an L-defect but not yet separated by the passage of a proton. The rate constants k_1 and k_{-1} are for the forward and reverse proton transfer steps respectively, while k_2 and k_{-2} are the rate constants for the forward and reverse turn steps corresponding to the passage of an L-defect. The values of the k 's were determined for data collected at several temperatures. The Arrhenius activation energies for the proton transfer and turn steps were then determined from the slope of a plot of $\ln k$ against $1/T$. The Arrhenius activation energies for the proton transfer step and the turn step were reported as $9.5 \pm 0.7 \text{ kcal mole}^{-1}$ and $12.0 \pm 0.4 \text{ kcal mole}^{-1}$ respectively, at temperatures near 150 K. The minor differences in the rate constants for the two

processes suggest that the mobility of ionic defects and orientational defects at this temperature are very similar. Hence, these results indicate that there is no majority charge carrier at temperatures near 150 K. This finding conflicts with the results of ac and dc conductivity studies that predict ionic defects are the majority carrier at these temperatures.

The Trapping of Mobile Protons in Shallow Traps

The passage of a proton through a D_2O molecule in the ice lattice results in the formation of $(HOD)_{cp}$. In the absence of orientational defect activity, the $(HOD)_{cp}$ formed will remain as $(HOD)_{cp}$, since the passage of an orientational defect through the site is necessary to uncouple the $(HOD)_{cp}$. In the case of ice I_c , orientational defects are inactive below 130 K, which means that any proton mobility in ice below 130 K would result in the formation of $(HOD)_{cp}$ from D_2O that was isolated in the sample. In pure ice below 130 K, the mobile proton concentration is effectively zero, so the formation of $(HOD)_{cp}$ in pure cubic ice below 130 K does not occur. It is possible to generate mobile protons in ice below 130 K by several methods. If these protons are generated at temperatures below 110 K, it has been observed that the protons become associated with shallow traps.

Nanosecond time-resolved conductivity studies of pulse-ionized ice have been performed by Kunst and Warman (115). It was proposed that for a brief period of time following the ionizing pulse mobile protons were in pseudo-equilibrium with protons associated with shallow traps. These traps were believed to be L-defects.

The dissociative ionization of cubic ice induced by 488 nm radiation from a CW argon ion laser has been studied by Devlin (116). It was found that at 90 K, D₂O molecules isolated in H₂O ice were converted to (HOD)_{cp}, with the isotopic exchange being considerable after several hours. Of interest was the fact that the Raman spectrum of the sample a few millimeters away from the irradiation site was essentially the same before and after irradiation, indicating that the protons generated by irradiation were trapped locally before migrating a significant distance.

Radiolysis of cubic ice samples at 90 K with 1.7 MeV electrons has been observed to convert isolated D₂O in the samples to (HOD)_{cp}, with little isolated HOD forming during the radiolysis (16). This would indicate that radiolysis of this type produces mobile protons but not mobile orientational defects, since the (HOD)_{cp} formed during radiolysis by the mobile protons was not decoupled by the passage of orientational defects through the site of the (HOD)_{cp}. It was observed that the conversion of D₂O to (HOD)_{cp} stopped when the irradiation was stopped, but upon warming the sample to near 130 K the conversion to (HOD)_{cp} resumed, with the conversion being rapid. By comparison, in pure unirradiated ice at 130 K, isotopic exchange proceeds very slowly. The fact that the conversion to (HOD)_{cp} resumed upon warming was explained by the fact that some of the mobile protons that were generated at 90 K fell into shallow traps (i.e., L-defects), and upon heating to 130 K the trapped protons were released from the traps causing the conversion of (HOD)_{cp} to resume. Similar behavior was observed for amorphous samples, but due to the broader infrared bands of the amorphous samples it was difficult to determine if the D₂O was converted to (HOD)_{cp} or isolated HOD. It was observed that proton mobility in amorphous ice and cubic ice was comparable. It was also observed that

doping the ice samples with 7-azaindole drastically decreased the scrambling of the D_2O during irradiation, and little conversion was observed upon warming the samples to near 130 K. This was explained by the fact that 7-azaindole is a deep trap for protons.

Mobile protons can be introduced into ice at low temperatures by doping the sample with a neutral compound that can be made acidic after the ice sample is deposited. One such compound that has been used successfully for this purpose is 2-naphthol. 2-naphthol behaves as a moderately strong acid in the excited state, with the pK_a of the phenolic OH changing from 9.5 to 2.5 upon the absorption of an ultraviolet photon (117). Thus, upon irradiation with ultraviolet light, 2-naphthol releases a proton, increasing the concentration of protons in the sample. In cubic ice, protons generated in this manner are immobile below about 100 K, but warming to near 120 K generates a near steady-state concentration of protons that decays slowly (14). This is the method that will be used in this study to increase mobile proton concentrations in amorphous ice samples.

Statement of the Problem

Pure amorphous ice converts to cubic ice at a temperature for which the thermal concentration of mobile ionic defects is too low to observe proton exchange. It is for this reason that very little is known about proton mobility or defect activity in amorphous ice. This data is needed for a variety of reasons, one being to help determine the role of orientational defects in phase transformations in hydrogen-bonded solids. In this study, ionic and orientational defect activity in amorphous ice will be studied. It has been observed that protons in amorphous ice are approximately as mobile as they are in cubic ice (16). An attempt will be made at increasing the concentration of mobile protons in

amorphous ice to the point that isotopic exchange can be observed spectroscopically in samples of D_2O decoupled in H_2O amorphous ice. This exchange will be used to probe the point defect activity in amorphous ice. The concentration of mobile protons in the samples will be increased by the ultraviolet photolysis of 2-naphthol. The photolysis will be done at a temperature for which orientational defects are not active in amorphous ice. This should result in the formation of $(HOD)_{cp}$ in the sample upon irradiation. By warming the sample to a temperature at which orientational defects become active, the decoupling of the $(HOD)_{cp}$ is then studied. An attempt will be made at determining the Arrhenius activation energies for the proton transfer and turn steps in amorphous ice. This data will hopefully yield insights into processes that occur at the molecular level that explain many of the peculiar properties of ice.

CHAPTER II

EXPERIMENTAL SETUP, SAMPLE PREPARATION, AND DATA COLLECTION

An Overview of the Experimental Setup

Thin films of amorphous ice were prepared by co-deposition of dilute vapor beams of D_2O and H_2O onto a cold CsI substrate. In order to maintain the substrate at low temperatures, the substrate was mounted on the tip of an Air Products CSA-202 closed cycle helium refrigerator. During deposition, the sample chamber housing the substrate was attached to a vacuum system. The vacuum provided thermal insulation of the cold substrate from the environment and evacuated the system of vapors that could condense on the substrate during sample preparation and analysis. The vacuum system also enabled delivery of H_2O and D_2O vapors into the sample chamber. The sample chamber and vacuum system was constructed primarily of glass, and a small amount of stainless steel. These materials are relatively non-porous and do not readily trap potential contaminants that could diffuse out of the materials during sample preparation and analysis. This is important, since a small concentration of contaminants (in particular, compounds that can function as bases) can greatly affect the proton transfer process being investigated. Likewise, a liquid nitrogen trap was installed on the vacuum line between the sample cell and the vacuum pumps (a Welch Duo-Seal Model 1402 in combination

with an oil diffusion pump, capable of producing a vacuum of $\sim 10^{-5}$ torr). By maintaining the trap at liquid nitrogen temperatures, vapor phase contaminants from the pumps (primarily volatile and semi-volatile compounds dissolved in the pump oil) condense in the trap and are excluded from the sample cell.

Two glass bulbs are mounted on the vacuum system. These are loaded with D_2O and H_2O vapor prior to sample preparation. In order to load a bulb, it is first evacuated by pulling a vacuum on the bulb. A reservoir containing either liquid D_2O or H_2O at room temperature is then attached to the vacuum system. By opening the appropriate combination of valves, the lines between the liquid reservoir and bulb are evacuated. Once evacuated, the pumps are isolated from the system and the valves to the reservoir and bulb are opened. Vapor produced by the liquid in the reservoir then fills the bulb. After allowing the vapor in the system to reach equilibrium, the bulb and reservoir are closed. The liquid reservoir is then removed from the vacuum system. The loaded bulb is left on the vacuum system for use during sample deposition. This loading procedure fills the bulb with adequate sample vapor to prepare many samples. The procedure was then repeated in order to load the second bulb.

Each of the glass bulbs is attached to the sample chamber via glass delivery lines and the necessary valves to control flow through the system. Vapor flow into the sample cell is regulated using a micrometer valve installed in each delivery line. In this way it was possible to adjust the flow rate of the vapors individually and reproducibly. The flow of D_2O was adjusted so that it was significantly less than that of the H_2O sample stream in order to produce samples that consisted of D_2O isolated in a predominantly H_2O matrix. In practice, other deuterated species were trapped in the matrix during the

deposition process. These species were produced as a consequence of isotopic exchange processes that occurred prior to deposition. Glass is hydrophilic, and as such it is difficult to remove the last traces of water vapor from the walls of the sample apparatus, even by pulling a strong vacuum on the system. This residual water can participate in isotopic exchange reactions during the loading, storage, and vapor delivery steps. Hence, a small amount of isolated HOD was observed in samples. It is possible that some isotopic exchange occurred once the vapor beams were mixed immediately prior to quenching onto the cold substrate. However, the concentration of deuterated species in the vapor beams is very low (deposition for 25 minutes produces a film only 2 microns thick). In addition, the vapors mix immediately prior to quenching on the cold substrate (the tips of the individual vapor inlets are less than 2 cm from the substrate oriented so that the beams impinge on the substrate at its center). Finally, the films are amorphous rather than crystalline ice, suggesting that the vapors are very rapidly quenched upon contact with the substrate before the molecules have sufficient time to orient themselves into a crystalline arrangement. These factors suggest that the possibility for significant isotopic exchange to occur during deposition is low. Accordingly, upon spectroscopic investigation samples immediately after deposition are found to consist primarily of D₂O and HOD isolated in an H₂O matrix.

A third vapor inlet was also incorporated into the sample cell in order to introduce vapors of dopant molecules into the sample matrix. Incorporation of 2-naphthol into the sample matrix was necessary in order to enhance the concentration of mobile protons via a photochemical reaction. The need for and procedure for increasing the concentration of mobile protons in the samples is discussed later. 2-Naphthol vapor was introduced into

samples through an auxiliary inlet was positioned alongside the D₂O and H₂O vapor inlets. The 2-naphthol reservoir was heated so that the concentration of 2-naphthol produced could be varied.

The sample cell is designed so that the substrate can be rotated without breaking vacuum on the cell. This rotation is necessary in order to facilitate both sample preparation and subsequent analysis by Fourier Transform Infrared Spectroscopy (FTIR). During the deposition process, the substrate is perpendicular to the impinging vapor beams, but for acquisition of infrared spectra the substrate is rotated so that it is parallel to the faces of two spectroscopic windows attached on opposite faces of the cell. Figure 19 illustrates the position of the windows on the cell and the ability to rotate the substrate relative to the windows and vapor beams. After sample deposition, the substrate is rotated to allow the beam of the FTIR to pass through the sample cell, enabling acquisition of spectra.

KBR is commonly used as a window for infrared spectroscopic cells because of its excellent transmission of mid-infrared radiation. One window on the cell is made of KBR. The second window is constructed of Suprasil, a material that transmits mid-infrared and ultraviolet radiation. Transmission of ultraviolet light into the cell is necessary to facilitate photolysis of the 2-naphthol.

The sample cell is equipped with the necessary valves to isolate it from the vacuum system. The sample cell is pumped down before sample preparation, and is then isolated from the vacuum line during sample deposition. These valves also enable the removal of the entire cell from the vacuum and vapor delivery system while maintaining vacuum on the cell. The cell must be leak-proof to enable placement in the FTIR for

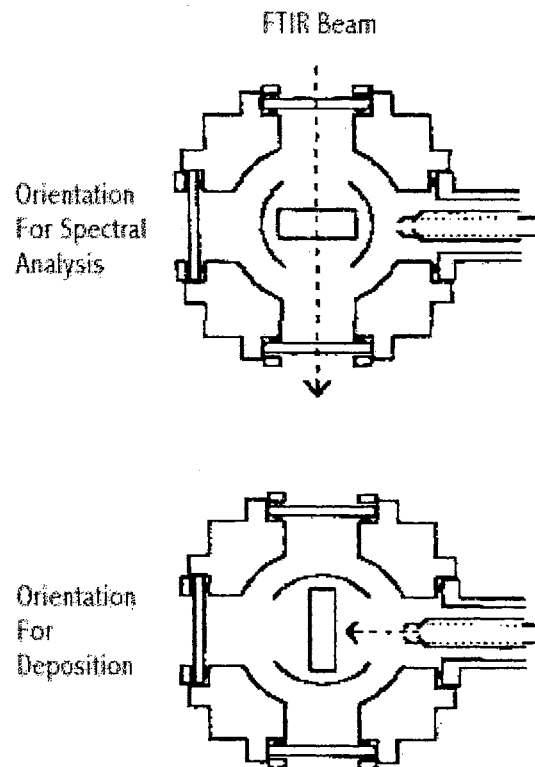


Figure 19. Orientation of substrate during spectral analysis and sample deposition.

hours without the need for attachment to the vacuum system. Once detached from the vacuum system, the sample cell and cryocooler system is transferred to the FTIR for spectral data acquisition.

Sample Preparation

The three vapor beams described above are concurrently deposited onto the substrate, which is maintained at 80K for the duration of sample deposition. The settings of the micrometer valves regulating the flow rates of the vapor streams were determined by trial and error during preparation of several test samples. The temperature of the 2-naphthol reservoir was also maintained in order to generate the proper concentration of dopant. Once these values were determined, the temperature and micrometer valves were adjusted to the desired settings during sample deposition. Total deposition time was approximately 25 minutes.

Once sample deposition was complete, the sample was annealed for one hour at a temperature of 125K. Vapor-deposited amorphous ice prepared as described here has a relatively low density. This is because rapid quenching of the sample matrix during deposition freezes in a significant amount of molecular disorder. Annealing the samples results in structural relaxation of the sample to a more ordered configuration and a corresponding increase in sample density. It was determined that annealing the sample at a temperature in excess of 125K resulted in slow conversion of the amorphous sample into crystalline ice. Although not quantified in this study, annealing at temperatures in excess of 135K resulted in significant crystallization in a matter of a few minutes.

Annealing of the samples was necessary in order to relax the structure of the ice prior to kinetic studies. During kinetic studies, a sample is maintained for hours at a temperature in excess of the deposition temperature but less than the phase transition temperature for amorphous to crystalline ice (up to $\sim 125\text{K}$). If the sample is not annealed prior to initiating the kinetic measurements, structural relaxation occurs during the measurements. If this occurs, it significantly complicates interpretation of spectral data. Significant changes in the local molecular environment occur during annealing, and these changes are quite evident in the infrared spectra. Kinetic studies on unannealed samples would be greatly complicated because changes in the spectrum due to annealing would be difficult to separate from spectral changes due to isotopic exchange reactions taking place in the sample. Hence, samples were always annealed prior to kinetic studies.

Once the sample was annealed, the substrate was rotated into position for spectral data acquisition. The sample cell was carefully positioned into the beam of a Digilab FTS-40 FTIR for sample collection. Sixteen scans at a resolution of 2 cm^{-1} were averaged for each sample. Averaging more scans would have improved the signal-to-noise ratio, but the number of scans was limited to sixteen. This was due to the fact that during kinetic measurements the spectrum is evolving with time. Hence, data acquisition times were limited so that the spectrum remained essentially constant during a series of sixteen scans.

Proton Enrichment of Samples

Amorphous ice contains a very low concentration of mobile protons relative to that of crystalline ices at comparable temperatures. It is presumed that this is due to a

relative abundance of shallow and possibly deep traps in amorphous ice compared to that found in crystalline ices. The higher number of proton traps in amorphous ice could be attributed to a number of factors. As discussed earlier, in crystalline ice a given water molecule on average forms four hydrogen bonds with four neighboring water molecules. In vapor deposited amorphous ice, water molecules are more likely to participate in fewer or a greater number of hydrogen bonds (78). Disorder in the oxygen atom positions also leads to a variety of strengths of hydrogen bond interactions. Hence, it could be argued that the inherent disorder in amorphous ice could lead to structural features that serve as traps for protons.

Isotopic scrambling of samples during the annealing process was observed to be negligible. If there were a significant concentration of mobile protons in amorphous ice below the glass transition temperature, it could be argued that proton hopping in the samples would convert isolated D_2O molecules into coupled HOD units during the annealing process. This effect was not observed in the present work, nor was it observed previously. Hence, it was concluded that there were a sufficient number of proton traps of sufficient depth in amorphous ice to greatly decrease the rate of hopping of naturally occurring free protons. Hence, an attempt was made to increase the concentration of mobile protons in amorphous ice samples in hopes of stimulating observable proton mobility on reasonable laboratory time scales. As mentioned in the literature review, this has been done previously by a number of methods including electron beam radiolysis (16), laser photolysis, and by incorporation of dopant molecules in the ice lattice that release protons upon photolysis (14). By incorporating low concentrations of 2-naphthol into samples, it was possible to enrich the concentration of mobile protons in amorphous

ice. Upon irradiation with a mercury vapor lamp, 2-naphthol is photolyzed, producing naphtholate ions and protons. This reaction is depicted in Figure 20.

Collection of Data For Kinetic Studies

After annealing the samples and collecting an initial spectrum at 80K, the sample was removed from the FTIR and placed back on the vacuum system. A mercury vapor lamp was positioned adjacent to the Suprasil window on the cell, and the sample was irradiated through the window for three hours. During irradiation, the sample was held at a temperature of 80K. After irradiation was completed, the sample was placed back in the FTIR, and a spectrum was collected at a temperature of 80K. As will be discussed later, these samples contained vibrationally coupled HOD pairs and a corresponding reduction in the concentration of D₂O. This conversion is presumably facilitated by the passage of protons liberated from the 2-naphthol during irradiation. After collection of the 80K spectrum after irradiation, the temperature of the substrate was increased to a previously selected temperature for the purpose of study of the kinetics of the isotopic exchange process. A spectrum was collected immediately after the cell reached the target temperature, followed by collection of spectra at selected time intervals. Once this series of data was collected, it was deconvolved into pure component spectra (D₂O, vibrationally coupled HOD units, and separated (decoupled) HOD units). The concentration of each species was estimated, enabling the change in concentration with respect to time for each component to be monitored. Models describing the isotopic exchange reaction were developed and fit to the observed data in an attempt to determine rate constants and activation energies for key processes in the isotopic exchange process.

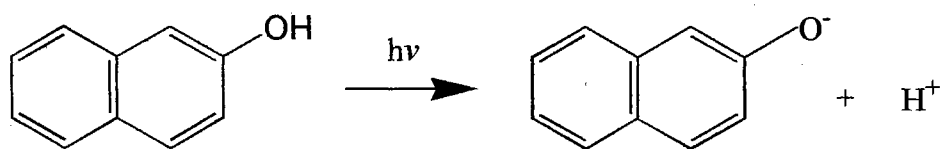


Figure 20. Photolysis of 2-Naphthol

CHAPTER III

DATA ANALYSIS AND MODEL DEVELOPMENT

Band Fitting

Because of the large distribution of hydrogen bond environments in amorphous ice, the vibrational bands attributed to decoupled OD stretching vibrations in amorphous ice are broad. In addition, the individual bands heavily overlap. This makes deconvolution of the bands due to the various deuterated species found in the samples prepared during this study very difficult. Since the integrated intensities of these bands were used to estimate concentrations of the various deuterated species produced during the isotopic scrambling process, it was important that deconvolution of the OD stretching band complex be performed reproducibly and accurately. Traditional spectral subtraction methods could have been employed for this purpose. However, pure component spectra for each isotopomer were needed, and the spectrum of only one isotopomer (isolated HOD) was available. Hence, because the pure spectra were not available, and because the bands were broad and overlapped, the subtraction process was highly subjective.

As mentioned, samples containing only one isotopomer could not be generated except for isolated HOD. Because samples containing only D₂O could not be prepared (the samples always contained some isolated HOD), the spectrum of isolated HOD could be subtracted from the D₂O / isolated HOD band complex to obtain the D₂O spectrum.

In practice this was almost impossible to do with any degree of confidence in the results because of the large degree of overlap of the bands. In the case of the crystalline ices, the bands are much sharper, making it easier to determine when the appropriate concentration of isolated HOD has been subtracted.

For this reason, pure component spectra were derived by fitting bandshapes to experimental data. This approach has the advantage of being less subjective because the computer algorithms converge on the solution in a consistent manner. However, this approach is not without problems. The fitting algorithm simply converges on the best fit by adjusting fitting parameters to values that yield the best fit to the data. Unfortunately, the 'best fit' to the data may make no physical sense. Hence, fitting bands to the data must be performed with certain constraints applied in order to force the solution to a reasonable conclusion.

Because bands due to OD stretching vibrations are asymmetric, fitting functions that account for this asymmetry were utilized. A skewed product function was selected for this purpose. The function has both Gaussian and Lorentzian components. The skewed product function is given by

$$I_v = \frac{I_0 \exp \left[-f^2 \left(\frac{v-v_0}{Y} \right)^2 A \right]}{1 + (1-f)^2 \left(\frac{v-v_0}{Y} \right)^2 A} \quad 2.1$$

$$A = 1 + a(v-v_0) + a^2(v-v_0)^2 / 2$$

where v_0 is the band center, I_0 is the peak height at v_0 , f is the fraction of the peak that is Gaussian, Y is related to the band half-width, and a is an asymmetry parameter (118).

Clarke and Glew (119) were able to fit the infrared stretch of decoupled HOD with one,

two, or four skewed product bands. Two bands were used in the present study. A single band fit the peak well, but did not adequately fit the wings of the band. Addition of a second band resulted in a good fit to the experimental data.

Background Correction

Before the OD stretch band complex was deconvolved, the H₂O background was fit and then subtracted from each spectrum. Samples of H₂O amorphous ice were prepared according to the procedure previously outlined. The infrared spectrum from 4000 cm⁻¹ to 500 cm⁻¹ was then collected at 80 K, and at two to three degree Kelvin increments ranging from 100 K to 125 K. The spectrum was then parameterized using a total of 12 skewed product functions and a cubic polynomial baseline to fit the region from 4000 cm⁻¹ to 1500 cm⁻¹. Once these reference H₂O background spectra were fit at each temperature, these were used as reference parameter sets for background correction. The skewed product peak intensities were adjusted using a common scale factor across all peaks. The cubic polynomial function was used to account for differences in baseline from sample to sample. For samples containing deuterated species, the spectral data in the range from 2700 cm⁻¹ to 2250 cm⁻¹ was excluded from the fit. This was necessary because the reference background samples contained no deuterated species. Once the background parameter sets were fit to samples, the baseline (cubic polynomial) was subtracted resulting in the baseline corrected infrared spectrum of the sample. A representative spectrum corrected for baseline in this manner is illustrated in Figure 21. If desired, the cubic polynomial and the scaled parameterized H₂O background could be

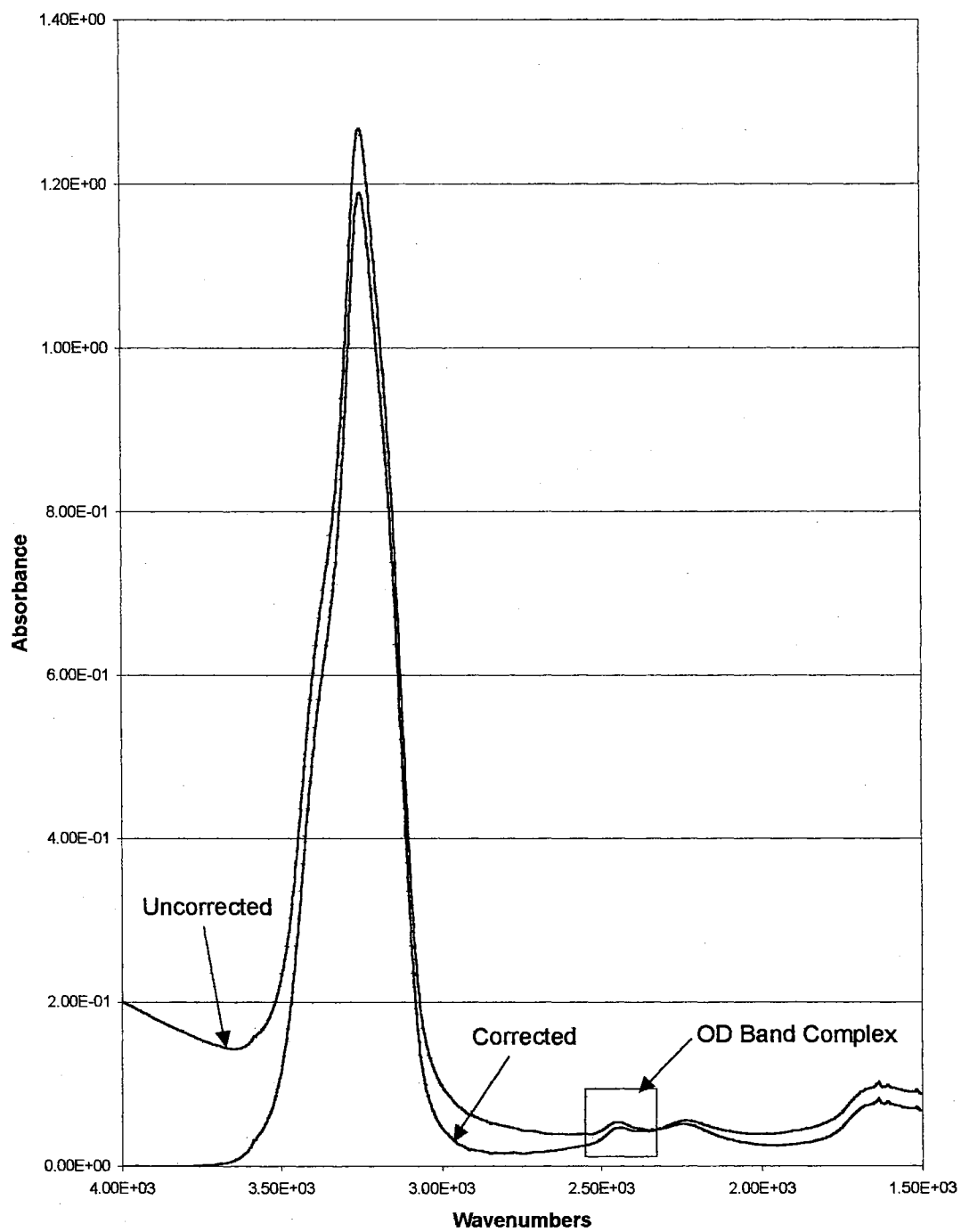


Figure 21. Baseline corrected data set.

subtracted, yielding the spectrum of the OD band complex. Figure 22 is a representative data set illustrating the results of the background subtraction process. The figure compares the baseline corrected data, H₂O combination band + OD band complex, and the OD band complex.

Isolated HOD Spectrum

The pure component spectrum of isolated HOD was relatively straightforward to obtain. Three solutions of D₂O in H₂O were prepared. Solutions containing 0.5% D₂O, 5% D₂O, and 10% D₂O by mass were prepared. Assuming complete isotopic exchange of the D₂O occurs upon mixing, solutions of 1%, 10%, and 20% HOD result. The gas bulb normally loaded with D₂O was loaded with vapor from the HOD solutions as previously described. This gas mixture (HOD + H₂O) was vapor deposited as described before. Since H₂O was in the mixture, the H₂O vapor beam that normally forms the sample matrix was not required. After annealing the samples for one hour at 125 K, the infrared spectrum of isolated HOD was collected at 80 K, 100 K, 102 K, 105 K, 108 K, 110 K, 112 K, 115 K, 118 K, 120 K, 122 K, and 125 K. These were the target temperatures for the kinetic studies, enabling isolated HOD spectra to be acquired at each temperature in the process. The process was repeated for all three solutions.

After baseline correction a parameterized water background subtraction was completed as described before, the resulting spectra were fit using two skewed product functions. The fits to the 1% and 10% HOD sample were virtually identical except for the corresponding linear increase in integrated peak intensity. However, weak shoulders were observed on both sides of the peak maximum for the 20% HOD samples. These

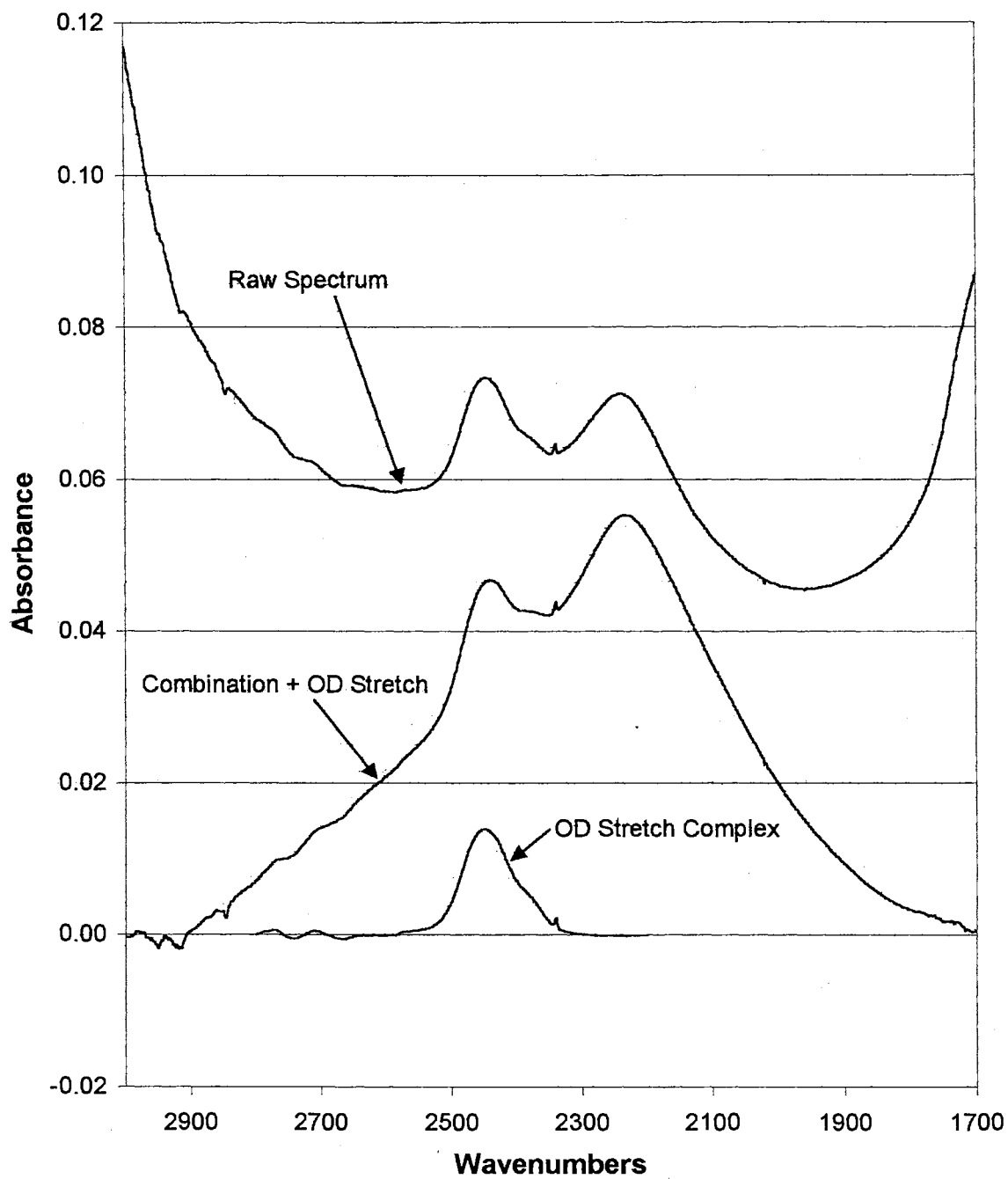


Figure 22. Subtraction of water background and baseline to yield OD stretch band complex.

shoulders are likely due to the presence of vibrationally coupled HOD in the 20% sample. Figure 23 contrasts the pure component spectra for the 1%, 10%, and 20% HOD samples at 80 K.

The position of the peak maximum for isolated HOD is temperature dependent, shifting to higher wavenumbers with increasing temperature. This is also true of the other deuterated species in this study. The temperature dependence of the position of the peak maximum for isolated HOD was readily available from this data. Figure 24 is the plot of peak position versus temperature. The temperature of the peak maximum shifts approximately 0.12 wavenumbers per degree Kelvin.

Determination of Sample Concentrations

The integrated intensities of the three isolated HOD samples discussed in the previous section were used to construct a calibration line for determination of the total concentration of OD oscillators in each sample. The integrated intensity of the H₂O combination band was determined for each of the three HOD samples. The ratio of the total integrated intensity for the OD band complex was then divided by the integrated intensity of the H₂O combination band for a given sample. The data obtained is listed in Table VII. This ratio was then plotted as a function of % HOD in each sample. The calibration line obtained is depicted in Figure 25. The concentrations in terms of % HOD were then converted to molar OD concentrations, and the result was plotted in Figure 26.

For this calibration curve to be valid, it is necessary that the infrared absorbance for an OD oscillator be independent of the isotopomer it was a part of. In order to check

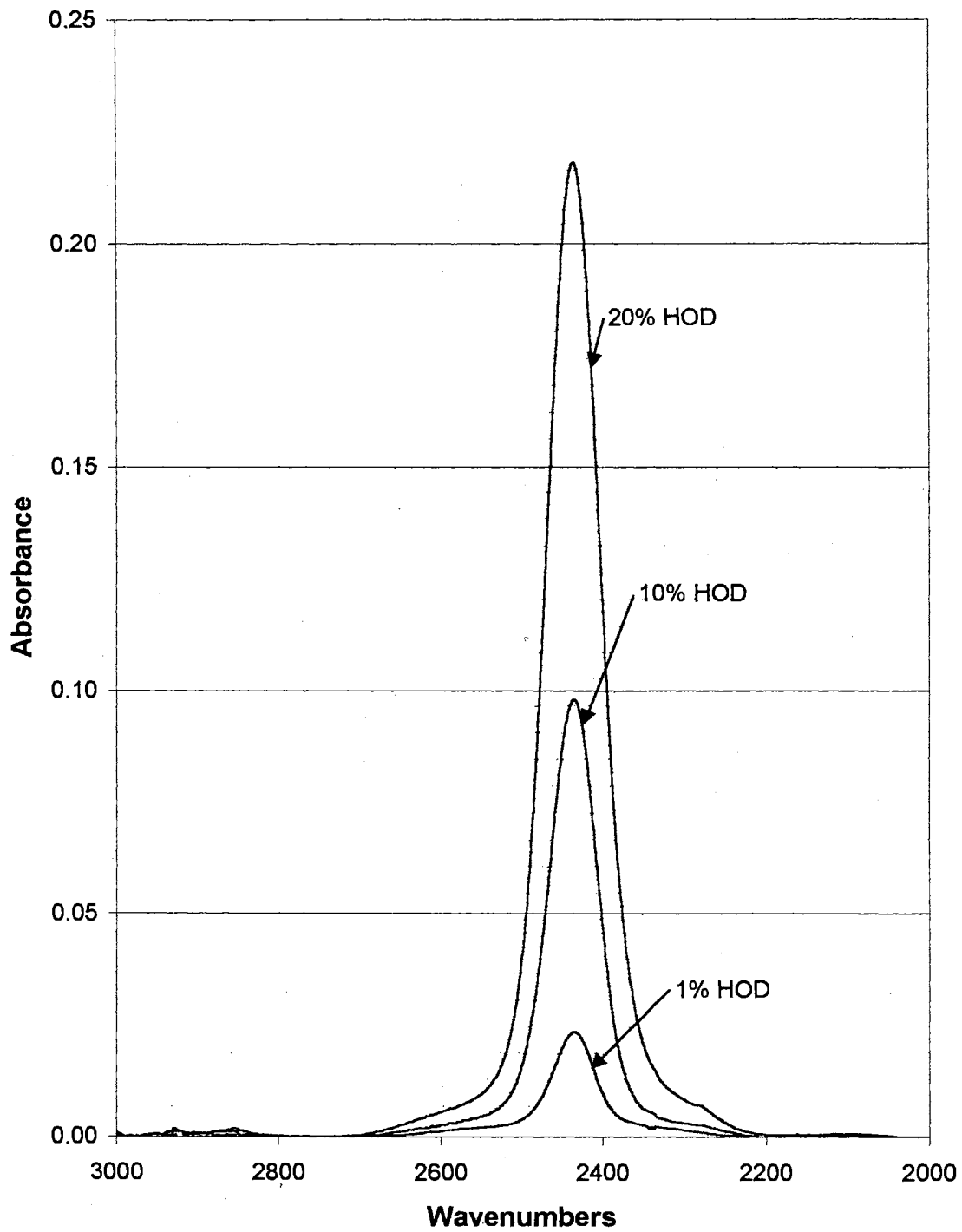


Figure 23. 80K isolated HOD spectra for several HOD concentrations.

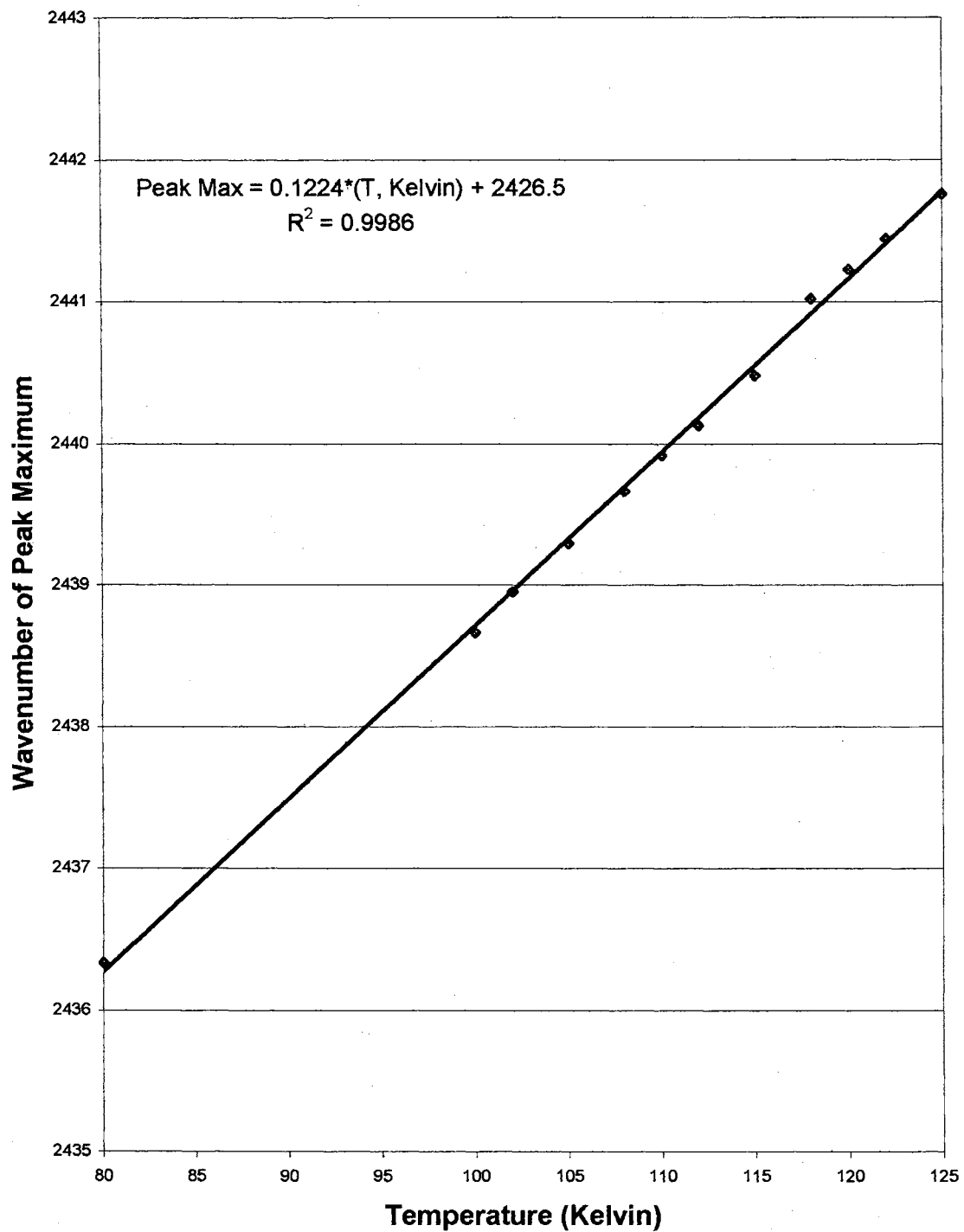


Figure 24. Isolated HOD peak position as a function of temperature.

TABLE VII

RATIO OF INTEGRATED INTENSITIES
FOR OD BAND COMPLEX TO H₂O
COMBINATION BAND AS A FUNCTION
OF HOD CONCENTRATION

% HOD	Molar OD Concentration	OD/Comb
1	0.526	0.031
10	5.263	0.389
20	10.526	0.689

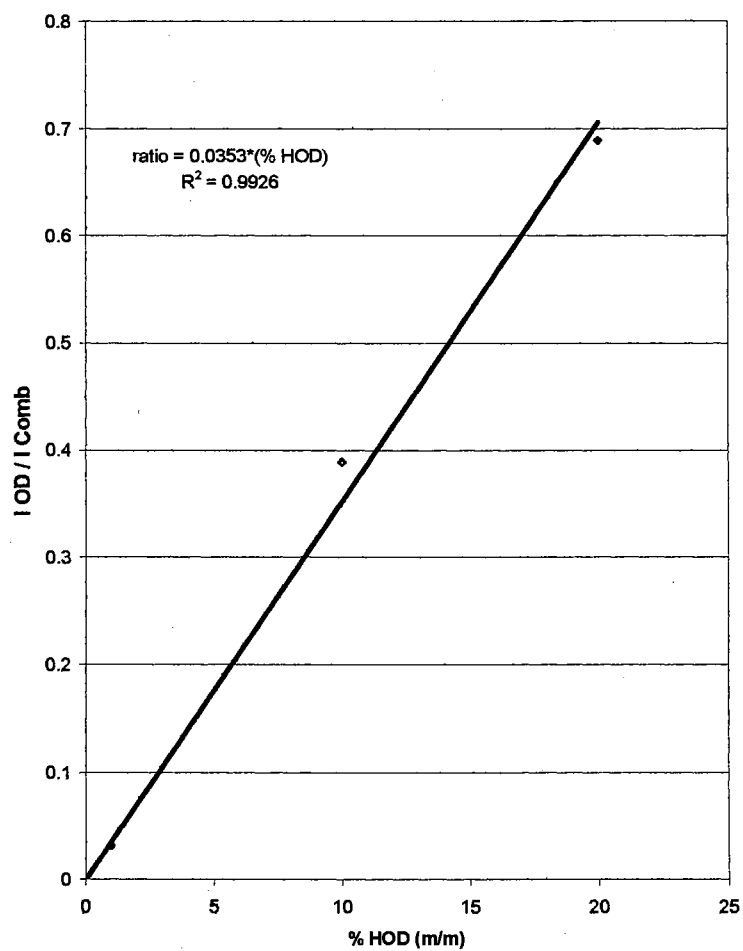


Figure 25. Percent OD Calibration Line

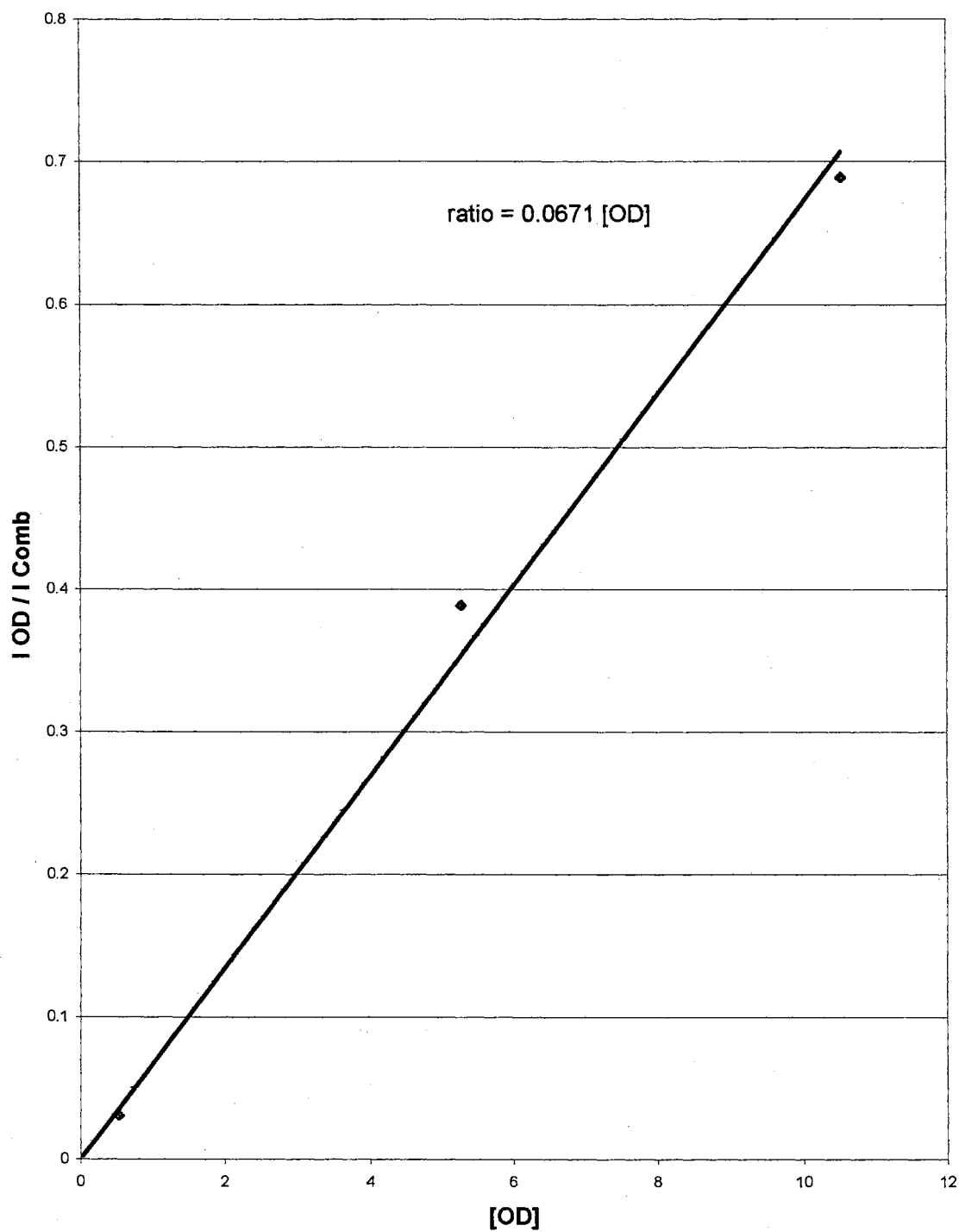


Figure 26. Calibration line for molar concentration of OD oscillators.

this assumption, the total integrated intensity of the OD band complex was determined for several series of kinetic data. During a kinetic run, samples were collected over a 13 hour period as isotopic scrambling of a sample was ongoing. Hence, the concentration of individual deuterated species was changing with time. If there were a significant difference in OD oscillator absorbance depending on the deuterated species the oscillator was incorporated into (i.e., D_2O , coupled HOD, or isolated HOD), it would be reasonable to assume that the total integrated intensity of the OD band complex over time would change. For example, if OD oscillators in D_2O exhibited stronger absorbance than those in isolated HOD, as D_2O were converted to the more weakly absorbing coupled HOD, the total integrated intensity of the band complex would decrease. As can be seen from the data in Table VIII, this is not the case. In this table the integrated intensity of each deuterated isotopomer was computed, and the results were totaled. As can be seen from the table, the total integrated intensity remained fairly constant throughout the run. The average integrated intensity was 23.96 with a standard deviation of 0.34 over the course of the run. During this time, the concentration of D_2O decreased by 40% while the concentration of isolated HOD increased by almost 50%. The data set selected for this analysis was one in which a significant amount of isotopic exchange occurred during the course of the experiment, which should amplify the effect relative to a data set at lower temperature in which the isotopic scrambling of the sample was minimal. This data, which is representative for the data obtained, could be argued as evidence supporting the assumption that OD oscillator absorbance is independent of deuterated specie in question. The calibration curve generated as described above was then applied to the data for each

TABLE VIII
TOTAL INTEGRATED INTENSITY OF OD BAND COMPLEX
DURING A KINETIC RUN

Time, Hours	Integrated Intensity			Sum
	D2O	(HOD)is	(HOD)cp	
0	14.891	6.256	1.551	22.699
0.0822	14.450	7.399	0.892	22.741
0.1644	14.199	7.898	0.714	22.810
0.2469	13.959	8.225	0.619	22.803
0.4961	13.453	8.829	0.673	22.955
0.7453	13.044	9.212	0.832	23.087
0.9944	12.701	9.528	0.941	23.170
1.2436	12.413	9.752	1.073	23.238
1.4928	12.162	9.946	1.193	23.301
1.7419	11.967	10.115	1.250	23.332
1.9911	11.846	10.256	1.371	23.474
2.4906	11.437	10.558	1.372	23.367
2.9892	11.239	10.741	1.479	23.459
3.4878	11.029	10.916	1.550	23.496
3.9864	10.827	11.073	1.611	23.511
4.9853	10.520	11.315	1.724	23.558
5.9842	10.251	11.529	1.817	23.596
6.9828	10.046	11.697	1.885	23.628
7.9814	9.842	11.841	1.961	23.644
8.9803	9.659	11.983	2.001	23.643
9.9792	9.520	12.117	2.029	23.667
10.9781	9.400	12.200	2.104	23.704
11.9767	9.262	12.302	2.132	23.696
12.9753	9.167	12.354	2.229	23.751
13.9739	9.039	12.466	2.231	23.737
Max Intensity	14.891	12.466	2.231	
Min Intensity	9.039	6.256	0.619	
% Change	39.297	49.814	72.242	
Average				23.36
Standard Deviation				0.34

TABLE IX
TOTAL OD CONCENTRATION FOR SAMPLES

Temperature	Run #	I OD / I Comb	% HOD	[HOD]
105	3	0.060	1.69	0.89
105	2	0.101	2.85	1.50
112	3	0.113	3.21	1.69
110	1	0.119	3.37	1.77
105	1	0.150	4.24	2.23
102	1	0.153	4.33	2.28
102	2	0.159	4.49	2.36
120	1	0.207	5.85	3.08
100	1	0.221	6.25	3.29
122	3	0.233	6.60	3.47
118	1	0.233	6.61	3.48
112	1	0.269	7.61	4.00
100	3	0.290	8.22	4.33
102	3	0.302	8.55	4.50
110	2	0.303	8.59	4.52
120	3	0.310	8.79	4.63
125	3	0.315	8.92	4.69
125	2	0.331	9.37	4.93
118	2	0.350	9.92	5.22
120	2	0.365	10.34	5.44
108	2	0.398	11.29	5.94
108	3	0.409	11.59	6.10
112	2	0.412	11.66	6.14
115	3	0.413	11.71	6.16
100	2	0.421	11.92	6.28
110	3	0.436	12.36	6.50
122	2	0.457	12.94	6.81
122	1	0.463	13.11	6.90
108	1	0.562	15.92	8.38
118	3	0.599	16.97	8.93
115	1	0.696	19.70	10.37
115	2	0.870	24.66	12.98

kinetic run in order to determine the concentrations of deuterated species in the sample. The results of this analysis are presented in Table IX. Most of the samples contained less than a 10% equivalent of HOD (i.e., OD oscillators). Hence, most deuterated species present in the sample before isotopic exchange is initiated are distributed in such a way that the probability of deuterated species being adjacent to each other in the ice lattice due to random distribution as a consequence of the vapor deposition process is low. This is evidenced further by the absence of coupled HOD units in samples before irradiation.

Spectrum of D₂O

The spectrum of D₂O was obtained from the 80K spectra collected before sample irradiation. Since orientational defect activity and proton mobility in amorphous ice samples is largely absent at 80K, conversion of D₂O into coupled HOD units is not likely. Hence, the samples should contain little coupled HOD. Consequently, the parameterized spectrum of isolated HOD can be utilized along with bands fit to ν_3 and ν_1 of D₂O.

Fitting of the spectra were performed subject to two constraints. The first constraint was to force the full width at half max (FWHM) for ν_3 and ν_1 of D₂O to be identical. From data for cubic ice, the FWHM are not identical, but are similar. The second constraint is to force the bandshapes for the two bands to be identical. Infrared data for the OD stretch region is routinely fit using combinations of symmetric Gaussian or Lorentzian bandshapes. The difference here is that the function used incorporates

asymmetry. The isolated HOD parameters were held constant at the values previously determined except for inclusion of an intensity scale factor.

Data was initially fit to the 80K spectra obtained before irradiation. In order to limit the possibility of coupled HOD interfering with the analysis, samples containing more than 10% OD oscillators were not included in the analysis at this stage. An additional constraint was also introduced at this stage. The ratio of intensities of ν_3 and ν_1 of D₂O were held constant during iteration of the remaining parameters. Once the fit converged, the ratio of intensities was incremented, and the data was again fit at the new ratio. Figure 27 is a plot of chi-squared versus the ν_3 to ν_1 ratio for one of the D₂O spectra. The minimum in chi-squared, which represents the best fit to the data, occurs when the ratio of intensities is 1.86. This compares favorably to the ratio of 1.84 reported by Whalley and Klug (120).

Once the average value of 1.86 for the ratio of peak intensities for D₂O was determined, the ratio was fixed at 1.86 for all data sets, and all the spectra were again fit. Once the fit converged, constraints were systematically relaxed to obtain the final fit to the experimental data. Parameters for ν_3 were relaxed, while parameters for other bands were fixed at their previously 'optimized' values. After convergence, the parameters for ν_3 and isolated HOD were fixed, and the parameters for ν_1 were relaxed. The final optimized peak intensity ratios, FWHM, and band positions for each sample are tabulated in Tables X, XI, and XII. A representative spectrum of D₂O and isolated HOD obtained from one of the samples is given in Figure 28.

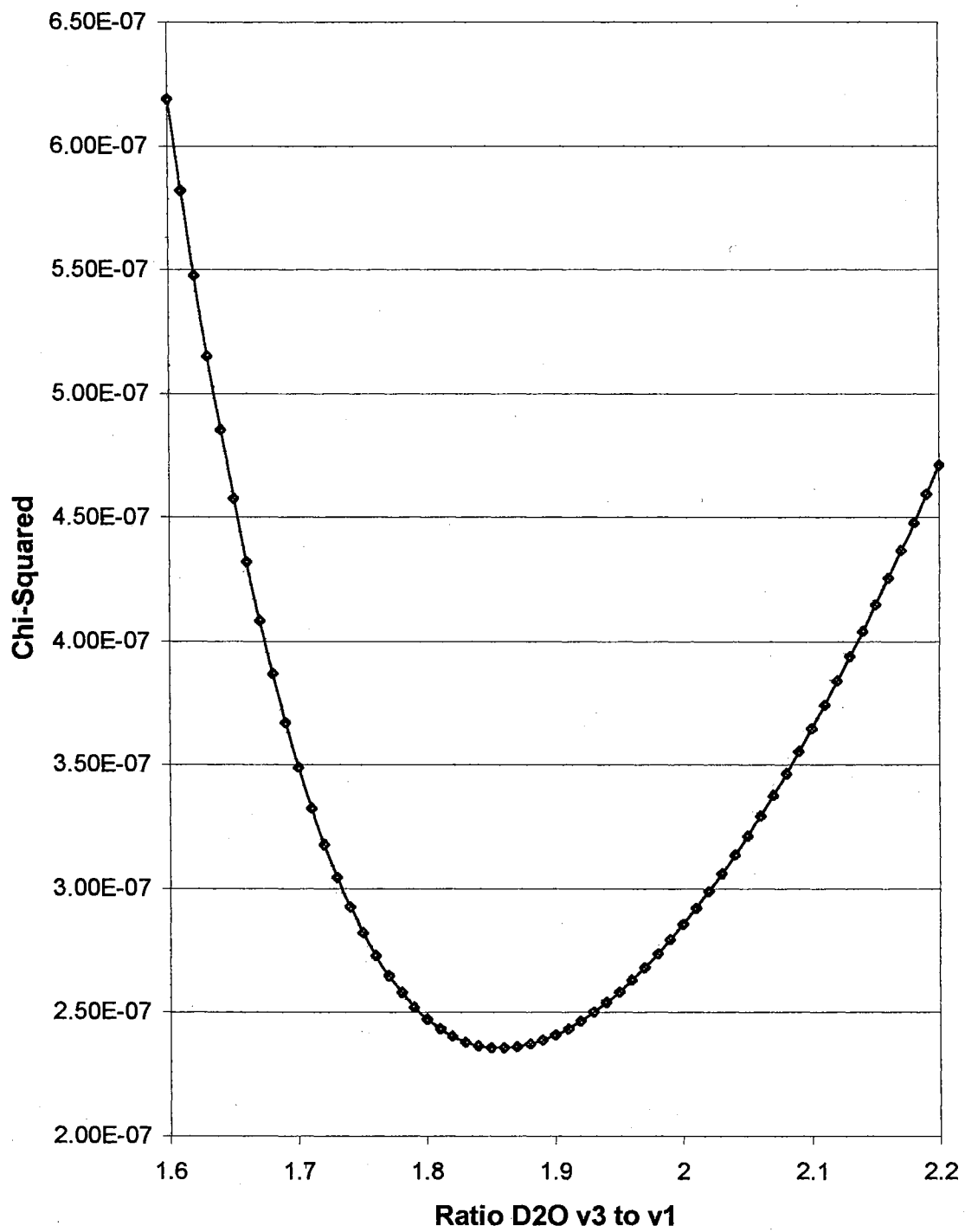


Figure 27. Goodness of fit for v_3 to v_1 ratio for D_2O .

TABLE X
REFINED V_3 TO V_1 INTENSITY RATIOS FOR D_2O

File	% OD	Ratio v_3 / v_1	Chi Squared
C726.FDT	1.69	1.88	5.34E-09
B703.FDT	2.85	1.87	1.36E-08
C1161.FDT	3.21	2.13	4.09E-08
A1189.FDT	3.37	1.93	2.12E-08
A678.FDT	4.24	1.95	8.90E-09
A599.FDT	4.33	1.85	1.56E-08
B628.FDT	4.49	1.78	1.49E-08
A1558.FDT	5.85	1.79	3.39E-08
A1841.FDT	6.25	1.68	2.14E-08
C1727.FDT	6.60	1.81	4.60E-08
A1474.FDT	6.61	1.63	3.02E-08
A1105.FDT	7.61	2.00	7.90E-08
C1897.FDT	8.22	1.76	1.88E-07
C654.FDT	8.55	1.89	1.68E-08
B1219.FDT	8.59	1.82	3.92E-08
C1643.FDT	8.79	1.82	3.61E-08
C1811.FDT	8.92	1.97	1.30E-07
B1783.FDT	9.37	1.94	1.72E-07
B1502.FDT	9.92	1.85	7.24E-08
B1586.FDT	10.34	1.70	5.66E-08
B833.FDT	11.29	1.83	5.16E-08
C859.FDT	11.59	1.84	5.73E-08
B1133.FDT	11.66	1.82	5.31E-08
C1331.FDT	11.71	1.82	6.49E-08
B1869.FDT	11.92	1.71	4.49E-08
C1247.FDT	12.36	1.75	5.83E-08
B1699.FDT	12.94	1.89	2.29E-07
A1671.FDT	13.11	1.75	7.62E-08
A752.FDT	15.92	1.82	7.56E-08
C1530.FDT	16.97	1.84	1.84E-07
A1275.FDT	19.70	1.67	7.52E-08
B1303.FDT	24.66	1.67	1.15E-07
Average, All Sets		1.83	
Std dev		0.11	
Average, <10% OD		1.86	
Std dev		0.11	

TABLE XI

REFINED FWHM FOR V_3 AND V_1 OF D_2O AND
ISOLATED HOD IN WAVENUMBERS

File	v3 D2O	v1 D2O	HOD
A599.FDT	65.1	65.8	66.6
B628.FDT	64.2	64.9	65.4
C654.FDT	67.4	69.0	69.3
A678.FDT	64.1	64.0	65.2
B703.FDT	62.8	62.3	63.8
C726.FDT	60.0	60.7	61.7
A752.FDT	72.2	75.6	75.2
B833.FDT	69.0	71.8	71.2
C859.FDT	71.6	73.9	74.2
A1105.FDT	67.7	71.3	70.8
B1133.FDT	69.6	73.8	72.6
C1161.FDT	66.6	74.6	70.8
A1189.FDT	66.3	68.0	68.6
B1219.FDT	69.4	71.3	71.9
C1247.FDT	71.9	74.7	74.9
A1275.FDT	77.4	82.6	81.4
B1303.FDT	78.1	84.0	82.2
C1331.FDT	71.5	74.1	74.2
A1474.FDT	70.8	75.5	75.3
B1502.FDT	70.2	72.3	73.0
C1530.FDT	73.1	76.3	76.0
A1558.FDT	67.2	67.3	68.9
B1586.FDT	73.1	74.8	76.1
C1643.FDT	69.3	69.7	71.1
A1671.FDT	74.6	80.2	79.4
B1699.FDT	70.1	70.6	71.6
C1727.FDT	68.1	68.3	69.7
A1755.FDT	70.0	72.8	74.7
B1783.FDT	70.2	71.8	72.9
C1811.FDT	69.3	70.7	72.0
A1841.FDT	69.1	72.0	73.3
B1869.FDT	72.7	78.6	78.0
C1897.FDT	67.6	72.4	70.5
Average	69.4	72.0	72.2
Std Dev	3.8	5.3	4.7

TABLE XII
REFINED POSITIONS OF PEAK MAXIMA FOR
D₂O AND ISOLATED HOD IN WAVENUMBERS

File	v3 D2O	v1 D2O	HOD
A599.FDT	2467.2	2384.8	2436.3
B628.FDT	2468.1	2385.1	2436.3
C654.FDT	2467.3	2384.8	2436.3
A678.FDT	2467.7	2385.7	2436.3
B703.FDT	2468.1	2385.9	2436.3
C726.FDT	2468.9	2385.9	2436.3
A752.FDT	2467.6	2384.4	2436.3
B833.FDT	2467.5	2383.7	2436.3
C859.FDT	2467.2	2384.4	2436.3
A1105.FDT	2466.8	2384.2	2436.3
B1133.FDT	2467.3	2383.4	2436.3
C1161.FDT	2466.0	2382.5	2436.3
A1189.FDT	2467.1	2384.2	2436.3
B1219.FDT	2467.7	2383.5	2436.3
C1247.FDT	2467.4	2383.3	2436.3
A1275.FDT	2467.3	2383.1	2436.3
B1303.FDT	2467.5	2383.1	2436.3
C1331.FDT	2467.5	2384.0	2436.3
A1474.FDT	2466.9	2383.7	2436.3
B1502.FDT	2467.5	2384.9	2436.3
C1530.FDT	2467.7	2385.4	2436.3
A1558.FDT	2467.7	2385.3	2436.3
B1586.FDT	2467.9	2385.3	2436.3
C1643.FDT	2467.6	2386.1	2436.3
A1671.FDT	2467.0	2384.5	2436.3
B1699.FDT	2467.4	2387.0	2436.3
C1727.FDT	2467.4	2385.9	2436.3
A1755.FDT	2466.9	2383.5	2436.3
B1783.FDT	2467.4	2386.3	2436.3
C1811.FDT	2467.4	2386.6	2436.3
A1841.FDT	2466.9	2383.6	2436.3
B1869.FDT	2466.8	2384.0	2436.3
C1897.FDT	2468.0	2383.6	2436.3
Average	2467.4	2384.6	2436.3
Std Dev	0.5	1.2	0.0

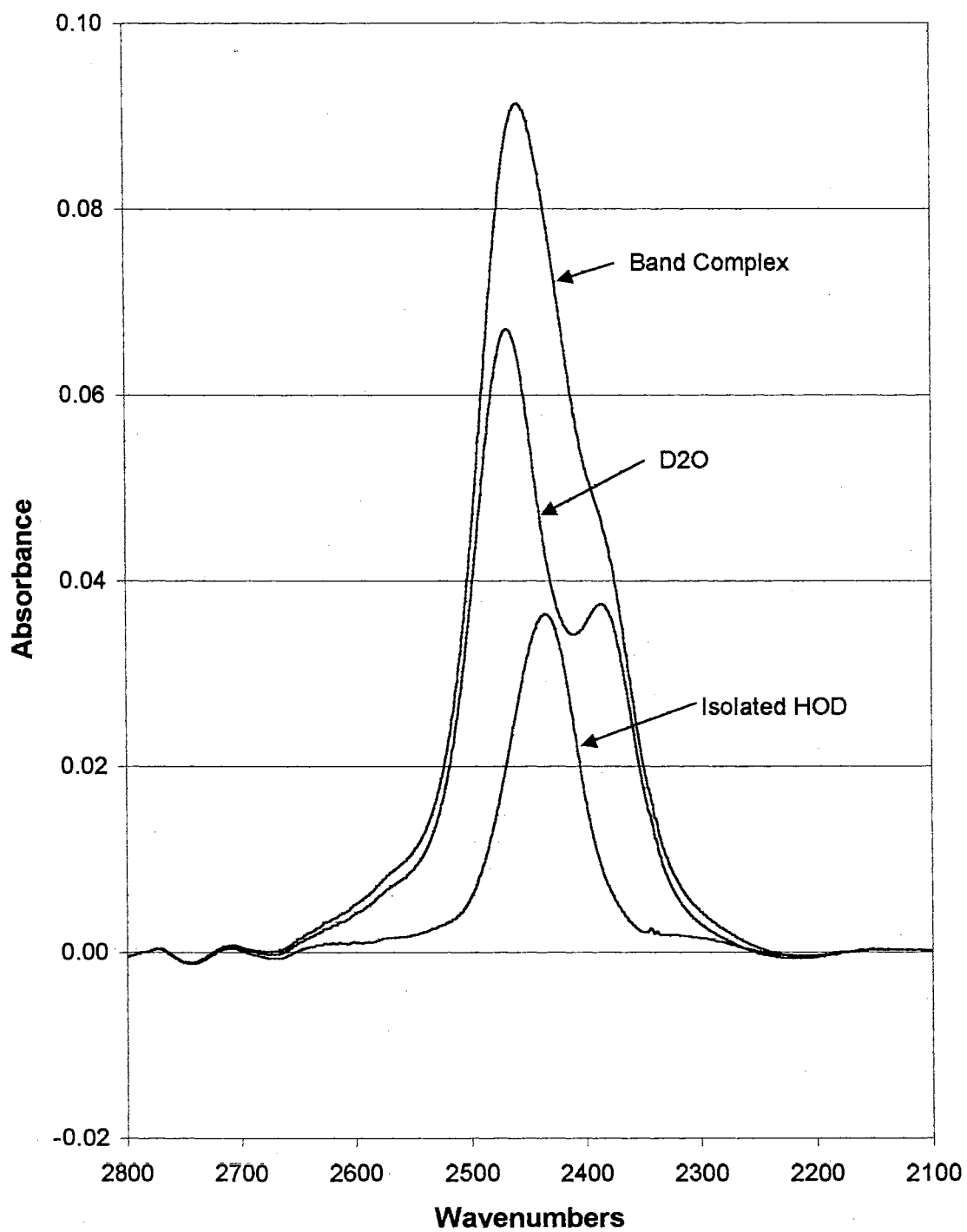


Figure 28. Pure component spectra derived from samples before irradiation.

Spectrum of Vibrationally Coupled HOD

The spectrum of coupled HOD was obtained by deconvolution of the 80K spectra collected after sample irradiation. Mobile protons generated by photolysis of 2-naphthol converted a portion of the D₂O in the initial sample into coupled HOD units. A corresponding decrease in the D₂O concentration was noted, with little change in the isolated HOD concentration.

Fitting of the coupled HOD spectrum was performed subject to the same constraints as was imposed for the fitting of the D₂O spectrum. An additional constraint was imposed on the positions of the band maxima for ν^- and ν^+ of the coupled HOD units. The positions of these bands should be approximately split about the band center for isolated HOD. The magnitude of the splitting was not constrained. As during the determination of the D₂O spectrum, the ratio of the intensities of ν^- and ν^+ was constrained to a given value, and the fit was determined. This ratio was iterated as before, yielding a ratio of intensities for each spectrum. A minimum in chi-squared was observed when the ratio of intensities (ν^+ / ν^-) was approximately 1.66 (see Figure 29). This is again in good agreement with the value of 1.66 for this ratio for cubic ice reported by Whalley and Klug (102).

Values for the ratio of intensities of (ν^+ / ν^-) for individual samples are listed in Table XIIIV. The values of the band maxima and FWHM are given in Tables XIV and XV respectively. Finally, the deconvolved spectra of isotopomers are illustrated in Figure 30.

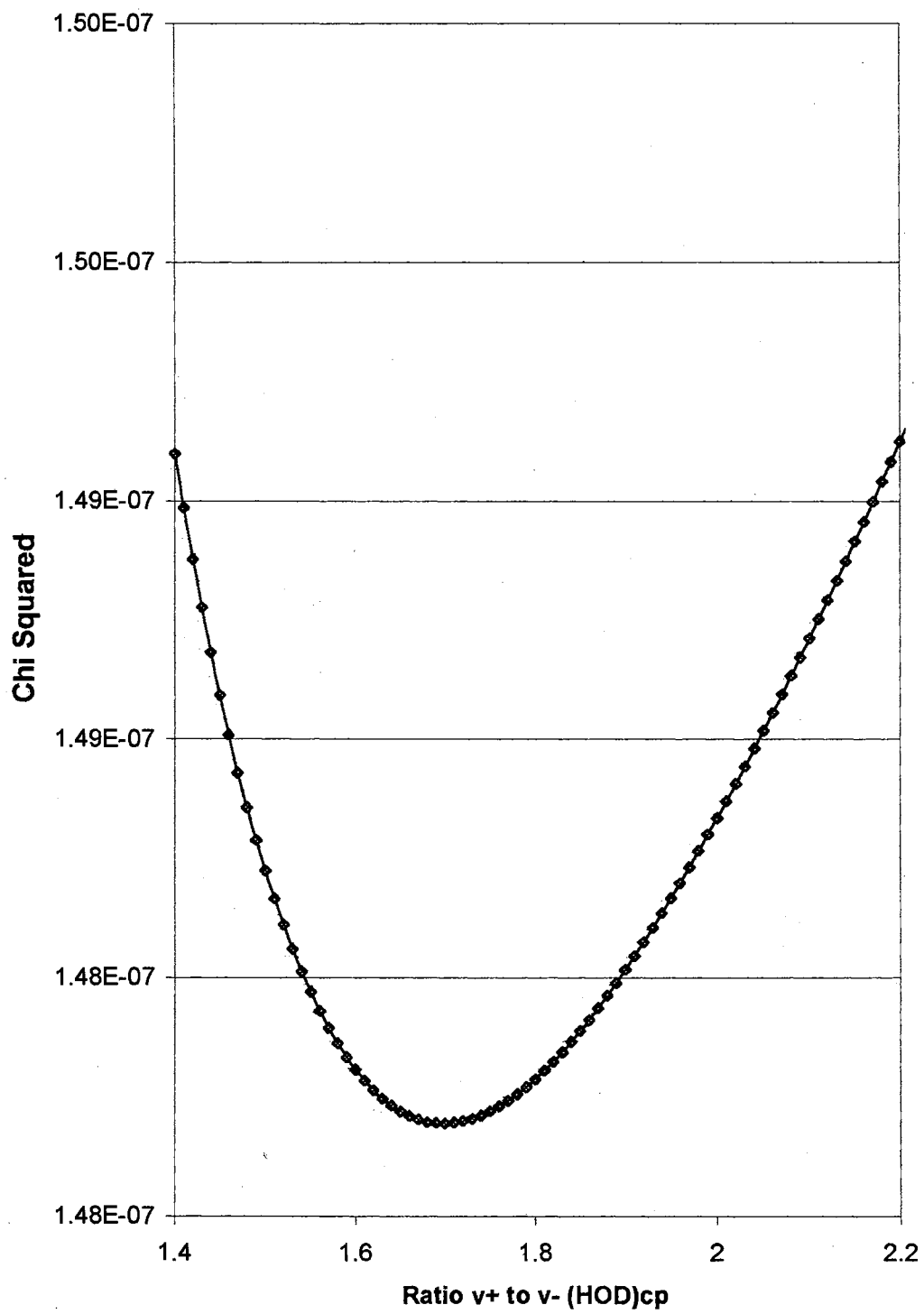


Figure 29. Goodness of fit for v+ to v- ratio of (HOD)_{cp}.

TABLE XIII
 RATIO OF V- TO V+ FOR (HOD)_{cp}

File	v- (HOD) _{cp}	v+ (HOD) _{cp}	v- / v+
A600.FDT	0.28	0.47	1.66
B629.FDT	0.24	0.40	1.63
C655.FDT	0.42	0.70	1.67
A679.FDT	0.14	0.23	1.64
B704.FDT	0.09	0.15	1.58
C728.FDT	0.08	0.13	1.58
A753.FDT	0.94	1.52	1.63
B834.FDT	0.59	1.01	1.70
C860.FDT	0.58	0.98	1.69
A1106.FDT	0.37	0.61	1.64
B1134.FDT	0.82	1.29	1.58
C1162.FDT	0.17	0.28	1.68
A1190.FDT	0.18	0.29	1.61
B1220.FDT	0.44	0.74	1.67
C1248.FDT	0.68	1.12	1.65
A1276.FDT	1.30	2.13	1.64
B1304.FDT	1.77	2.92	1.65
C1332.FDT	0.74	1.21	1.63
A1475.FDT	0.65	1.00	1.54
B1503.FDT	0.81	1.32	1.63
C1531.FDT	1.62	2.65	1.64
A1559.FDT	0.40	0.66	1.65
B1587.FDT	0.80	1.33	1.66
C1644.FDT	0.42	0.74	1.74
A1672.FDT	0.85	1.49	1.75
B1700.FDT	0.87	1.53	1.77
C1728.FDT	0.45	0.76	1.69
A1756.FDT	0.19	0.35	1.81
B1784.FDT	0.93	1.60	1.73
C1812.FDT	0.77	1.29	1.68
A1842.FDT	0.40	0.66	1.65
B1870.FDT	0.79	1.36	1.72
C1898.FDT	0.55	0.92	1.67
Average			1.66
Std dev			0.057

TABLE XIV
POSITIONS OF BAND MAXIMA IN WAVENUMBERS FOR SAMPLES
AFTER IRRADIATION

File	v3 D2O	v1 D2O	HOD	v- (HOD)cp	v+ (HOD)cp
A600.FDT	2467.4	2385.0	2436.3	2467.5	2408.8
B629.FDT	2468.5	2386.2	2436.5	2466.6	2408.3
C655.FDT	2467.5	2385.2	2436.4	2467.5	2409.0
A679.FDT	2467.8	2386.3	2436.3	2467.2	2408.6
B704.FDT	2468.3	2387.1	2436.3	2464.9	2406.8
C728.FDT	2468.8	2387.8	2436.5	2466.2	2406.5
A753.FDT	2467.1	2385.3	2436.4	2466.2	2408.7
B834.FDT	2467.7	2384.0	2436.4	2468.1	2409.4
C860.FDT	2466.5	2385.5	2436.3	2467.4	2409.5
A1106.FDT	2466.4	2384.2	2436.5	2466.8	2408.7
B1134.FDT	2466.6	2384.0	2436.7	2465.1	2408.1
C1162.FDT	2465.8	2384.6	2436.4	2467.9	2408.9
A1190.FDT	2467.0	2384.3	2436.4	2466.3	2408.1
B1220.FDT	2467.4	2384.1	2436.4	2467.3	2409.0
C1248.FDT	2467.1	2383.2	2436.4	2466.8	2408.9
A1276.FDT	2466.7	2383.4	2436.4	2465.9	2409.2
B1304.FDT	2466.9	2382.9	2436.4	2465.9	2409.3
C1332.FDT	2467.0	2384.2	2436.4	2466.1	2408.8
A1475.FDT	2466.5	2383.3	2436.4	2464.8	2407.6
B1503.FDT	2467.1	2385.3	2436.4	2466.1	2408.7
C1531.FDT	2467.2	2385.8	2436.5	2466.1	2409.0
A1559.FDT	2467.6	2386.4	2436.3	2467.4	2408.6
B1587.FDT	2468.1	2385.3	2436.2	2467.2	2408.9
C1644.FDT	2467.7	2386.7	2436.2	2469.5	2409.9
A1672.FDT	2467.0	2384.5	2436.1	2468.7	2410.0
B1700.FDT	2466.8	2388.2	2436.3	2469.5	2410.3
C1728.FDT	2467.5	2387.1	2436.3	2468.3	2409.2
A1756.FDT	2468.1	2385.7	2435.7	2471.2	2410.4
B1784.FDT	2467.3	2387.1	2436.2	2468.4	2409.8
C1812.FDT	2467.3	2387.2	2436.4	2467.4	2409.3
A1842.FDT	2466.9	2384.3	2436.4	2466.9	2408.7
B1870.FDT	2467.0	2384.0	2436.2	2468.3	2409.5
C1898.FDT	2468.1	2384.4	2436.3	2466.9	2409.1
Average	2467.3	2385.2	2436.3	2467.2	2408.9
Std Dev	0.6	1.4	0.2	1.4	0.8

TABLE XV
FWHM OF BANDS IN WAVENUMBERS FOR
SAMPLES AFTER IRRADIATION

File	v3 D2O	v1 D2O	HOD	v- (HOD)cp	v+ (HOD)cp
A600.FDT	64.6	65.1	66.7	66.6	67.5
B629.FDT	63.9	63.9	65.6	65.4	66.2
C655.FDT	67.3	68.6	69.5	69.3	70.1
A679.FDT	63.3	63.3	65.2	65.2	66.1
B704.FDT	62.6	60.1	63.6	63.8	64.6
C728.FDT	59.2	59.2	61.6	61.7	62.4
A753.FDT	71.3	75.3	75.7	75.2	76.2
B834.FDT	68.8	71.2	71.3	71.2	72.1
C860.FDT	70.2	74.6	74.2	74.2	75.1
A1106.FDT	66.7	70.6	70.8	70.8	71.7
B1134.FDT	68.6	73.8	72.5	72.7	73.6
C1162.FDT	66.4	71.8	70.8	70.8	71.7
A1190.FDT	65.9	67.6	68.6	68.6	69.5
B1220.FDT	68.5	70.3	71.9	71.9	72.8
C1248.FDT	71.0	74.2	74.9	74.9	75.9
A1276.FDT	76.7	82.7	81.1	81.5	82.5
B1304.FDT	77.2	84.7	81.9	82.3	83.4
C1332.FDT	70.6	73.9	74.1	74.2	75.2
A1475.FDT	70.5	74.9	74.9	75.3	76.3
B1503.FDT	69.8	72.4	73.1	73.0	74.0
C1531.FDT	72.8	76.3	76.0	76.1	77.0
A1559.FDT	67.1	66.3	68.7	68.9	69.7
B1587.FDT	73.5	74.4	75.9	76.2	77.1
C1644.FDT	69.4	69.2	71.2	71.1	72.0
A1672.FDT	74.5	80.8	79.4	79.5	80.5
B1700.FDT	69.5	70.1	71.5	71.6	72.5
C1728.FDT	67.9	67.3	69.6	69.7	70.6
A1756.FDT	70.6	72.3	75.4	74.7	75.6
B1784.FDT	70.0	71.7	73.0	73.0	73.9
C1812.FDT	69.2	70.5	72.2	72.0	72.9
A1842.FDT	69.1	71.3	73.2	73.3	74.2
B1870.FDT	72.8	78.3	77.7	78.0	79.0
C1898.FDT	67.6	71.8	70.5	70.5	71.4
Average	69.0	71.5	72.2	72.2	73.1
Std Dev	3.8	5.7	4.6	4.7	4.8

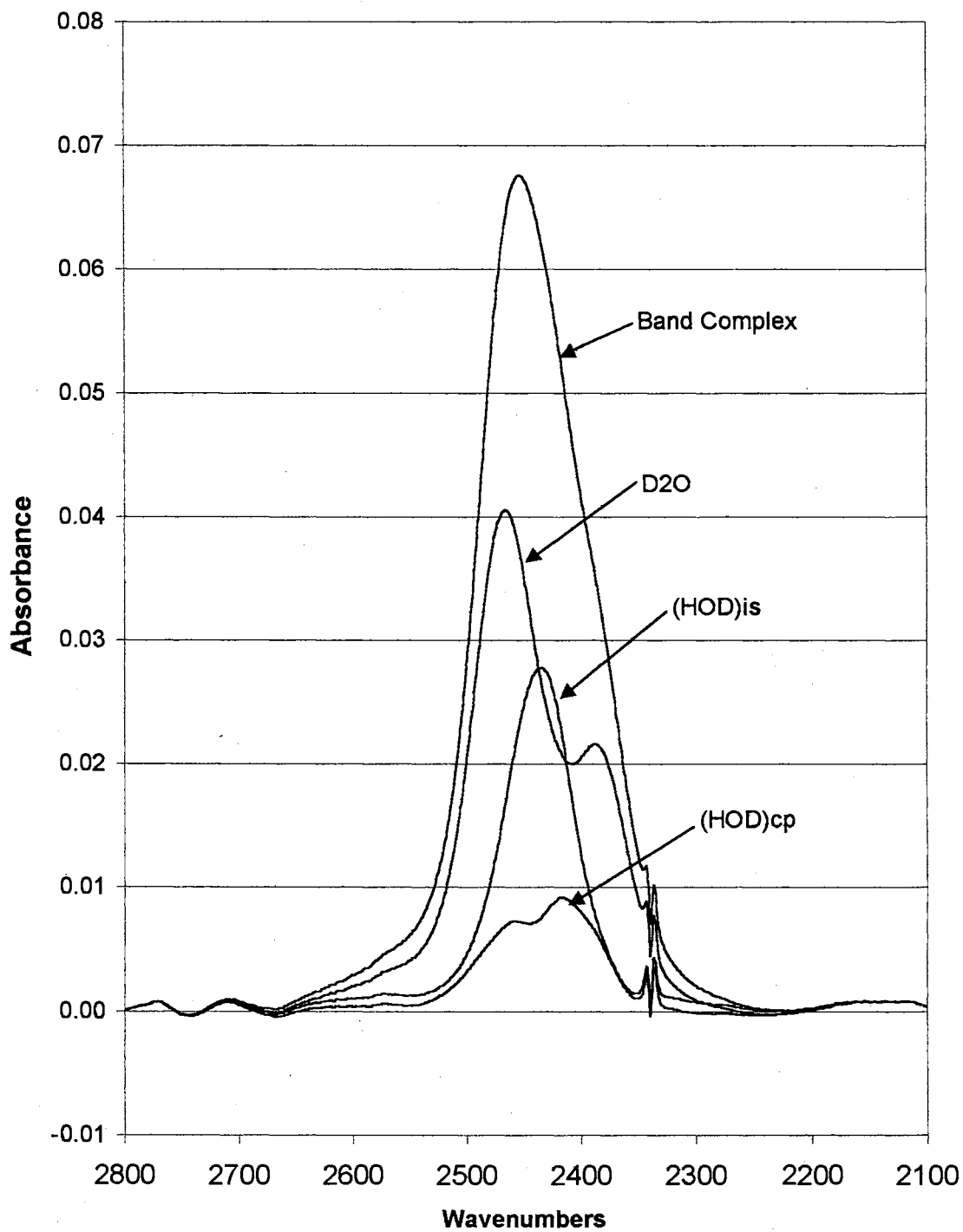


Figure 30. Pure component spectra derived from samples after irradiation.

Fitting of Spectral Data For Kinetic Runs

Fitting of the spectra during kinetic runs was straightforward once the pure component spectra for D₂O, coupled HOD, and isolated HOD were available. Each of the parameterized pure component spectra for each sample set were fit to each spectrum in a given time series using only an intensity scale factor for each of the three component spectra. Prior to fitting, the positions of the bands were shifted to compensate for temperature differences between the pure component spectra (determined at 80K) and the temperature maintained during the kinetic run. The magnitude of the shift in peak position was determined for HOD from the shift observed in the isolated HOD spectra as a function of temperature. It was assumed that the shifts due to temperature for D₂O and coupled HOD were determined by including an adjustable parameter to allow similar in magnitude to that of isolated HOD. Once the spectra for a given run were fit, the integrated intensities for each component were converted to concentrations as previously described. This data was then input into the kinetic models that will now be described.

Kinetic Model Development

Figure 31 illustrates the mechanism used to model the isotopic exchange process in amorphous ice. As can be seen from the figure, six different OD species can be produced by the systematic passage of protons and L-defects through the various OD sites in the ice lattice. The infrared spectra of D₂O, coupled HOD (i.e., (HOD)_{cp}), and isolated HOD (i.e., (HOD)_{sep}) all isolated in H₂O cubic ice, have been previously reported by workers in this laboratory in a study of the proton exchange process in cubic

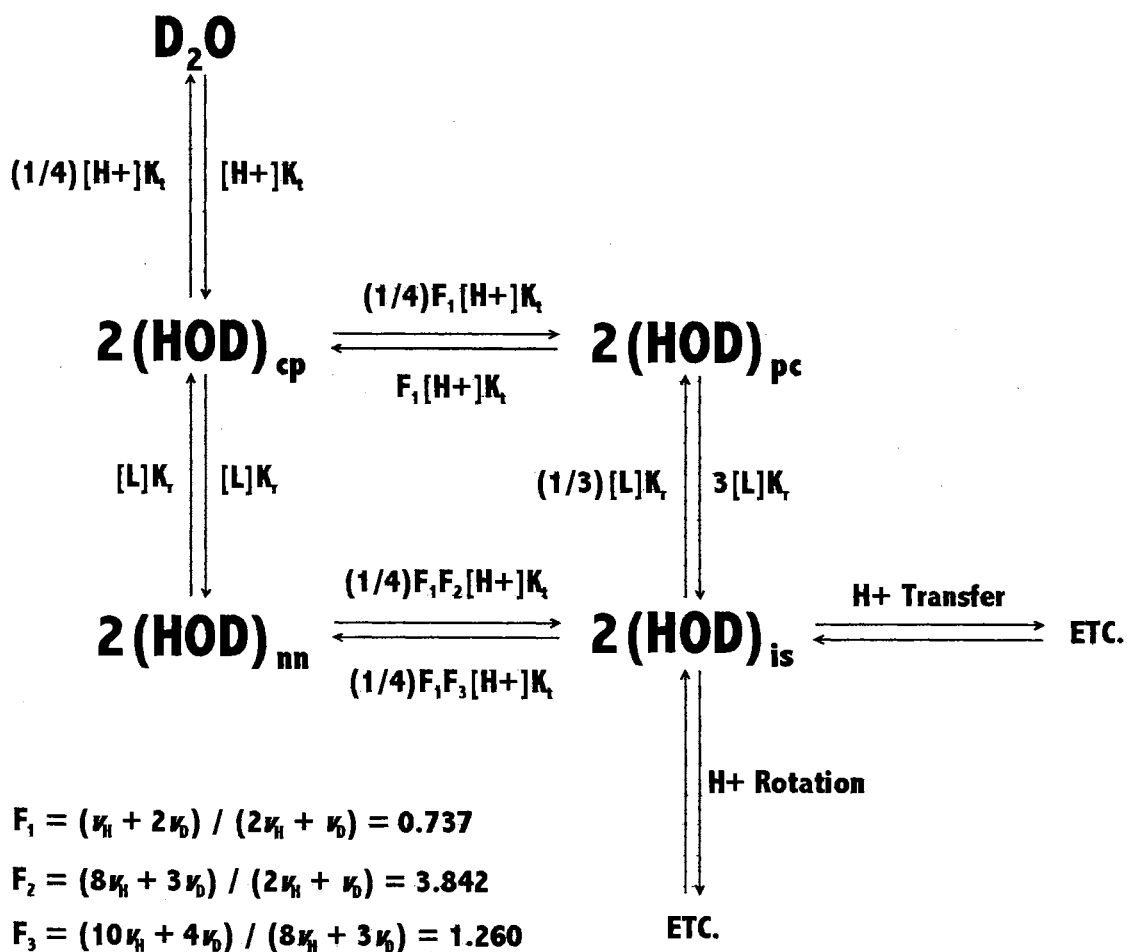


Figure 31. Proposed isotopic exchange mechanism.

ice. In the previous study, the infrared spectra of $(\text{HOD})_{\text{nn}}$, $(\text{HOD})_{\text{pc}}$, $(\text{HOD})_{\text{is}}$, and $(\text{HOD})_{\text{sep}}$ were assumed to be indistinguishable from one another based on the assumption that any intra-molecular coupling between the HOD units making up these species is very weak. If this is true, it would follow that the spectra of $(\text{HOD})_{\text{nn}}$, $(\text{HOD})_{\text{pc}}$, and $(\text{HOD})_{\text{is}}$ should more closely resemble that of $(\text{HOD})_{\text{sep}}$ than that of $(\text{HOD})_{\text{cp}}$. In the present study, it was assumed that the spectra of $(\text{HOD})_{\text{nn}}$, $(\text{HOD})_{\text{pc}}$, $(\text{HOD})_{\text{is}}$, and $(\text{HOD})_{\text{sep}}$ are indistinguishable. Hence, the spectrum of the OD band complex was separated into the spectra of D_2O , $(\text{HOD})_{\text{cp}}$, and $(\text{HOD})_{\text{sep}}$, where the $(\text{HOD})_{\text{sep}}$ spectrum is actually a sum of the absorbance due to $(\text{HOD})_{\text{nn}}$, $(\text{HOD})_{\text{pc}}$, $(\text{HOD})_{\text{is}}$, and $(\text{HOD})_{\text{sep}}$.

The kinetic model illustrated in Figure 31 will now be discussed in more detail. The passage of a proton or L-defect through a given site in the ice lattice does not necessarily produce the desired outcome, since several different outcomes are possible. For this reason it was necessary to introduce constants representing the probability of a desirable outcome relative to a given reaction. Each reaction was analyzed as an attack, transfer, and leaving step. Using the reaction in which D_2O is converted to $(\text{HOD})_{\text{cp}}$ as an example (refer to Figure 32), a mobile proton can attack a D_2O molecule by hopping from an adjacent water molecule. Before this proton hop step occurs, the adjacent water molecule is more correctly referred to as an H_3O^+ ion due to the mobile proton associated with the water molecule. Any one of the three protons can leave the ion adjacent to the D_2O molecule, so the probability that the desired proton will hop to the D_2O site is one in three. In equation form, the probability factors can be expressed as the ratio of

favorable outcomes to the total number of possible outcomes. Since only one out of three possible proton hopping reactions produces a favorable outcome, the probability factor is given by $v_H / 3v_H$. Since there are two possible approach channels for conversion of D_2O to coupled HOD, the attack probability factor must be multiplied by 2. If a given step involves moving a deuteron, the frequency of deuteron hopping (v_D) is used rather than the frequency of proton hopping (v_H). For the transfer step, favorable outcomes involve moving one of two deuterons onto adjacent water molecules. The total number of outcomes for the transfer step also includes hopping of the proton moved in the attack step back to the water molecule it originally transferred from. Hence, the total number of outcomes is the sum of the two deuteron hop steps (both favorable) and a single undesirable proton hop step. Similar logic is employed for the leaving step. The probability factor for the overall reaction is then the product of the attack, transfer, and leaving probability factors.

As implied in the previous analysis for the conversion of D_2O to $(HOD)_{cp}$, for a change in the configuration of a site in the lattice containing an OD species to occur, both protons and deuterons must move. This is taken into account in the model, as the probability factors (designated F_1 , F_2 , and F_3 in Figure 31) include values for the frequency of proton (v_H) and deuteron (v_D) hopping.

The relative probability factors for steps involving L-defect migration were also deduced. The rate of each reaction step also depends on mobility and concentration of either protons or L-defects, and either a rate constant for proton hopping (K_p) or a rate constant for L-defect motion (K_r), depending on which reaction is being considered. A

graphical derivation of the probability factors for each step outlined in Figure 31 are tabulated in Figures 32 through 46.

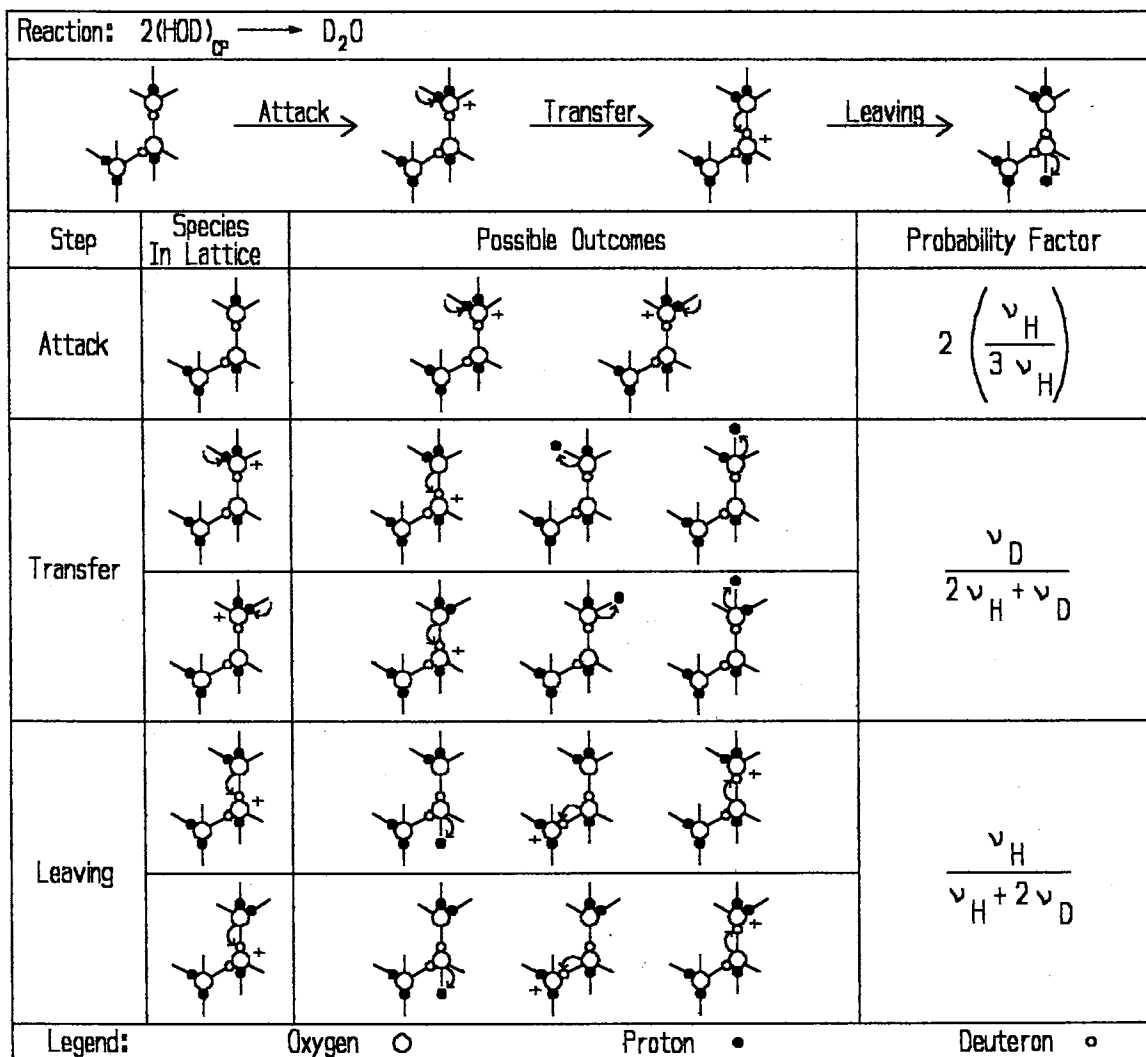
Kunst and Warman (115) have published values for the frequency of hopping for protons and deuterons. These frequencies are temperature dependent. However, they noted that these values seem to change uniformly with temperature, resulting in a relatively constant ratio for $(\nu_H) / (\nu_D)$ with respect to temperature. Rather than include both (ν_H) and (ν_D) as fitting parameters, the relationship $(\nu_D) = (\nu_H) * R_{HD}$ was used to simplify the probability terms F_1 , F_2 , and F_3 , resulting in relationships in terms of the single fitting parameter R_{HD} , rather than in terms of (ν_D) and (ν_H) . The initial value of R_{HD} was set equal to 1.65, a best estimate from the work of Kunst and Warman. Substitution of this value into the probability factors previously tabulated, followed by appropriate algebraic manipulation, yielded the numerical values for probability factors included in the model.

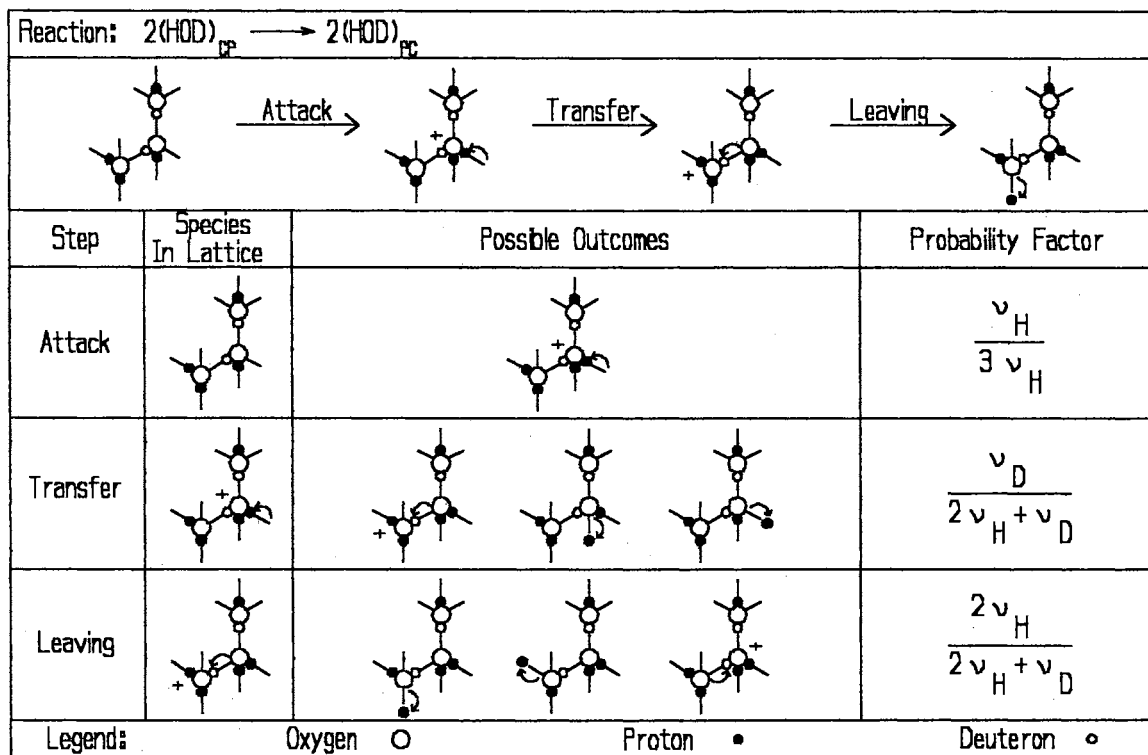
A number of simplifying assumptions were made to the original model. First, as previously discussed the infrared spectra of $(HOD)_{nn}$, $(HOD)_{pc}$, $(HOD)_{is}$, and $(HOD)_{sep}$ are indistinguishable. Hence, direct spectral measurement of the initial concentrations of each of these species was not possible. It was assumed that the time zero concentrations of $(HOD)_{pc}$ and $(HOD)_{nn}$ were small, and most of the time zero 'uncoupled' isotopomer concentration was in the form of $(HOD)_{sep}$. The reaction for $(HOD)_{is}$ to $(HOD)_{nn}$ was ignored (the probability factor for this reaction was smaller than the forward reaction converting $(HOD)_{nn}$ to $(HOD)_{is}$). Similarly, the reaction converting $(HOD)_{is}$ to $(HOD)_{pc}$ was ignored for the same reason. Since the reactions

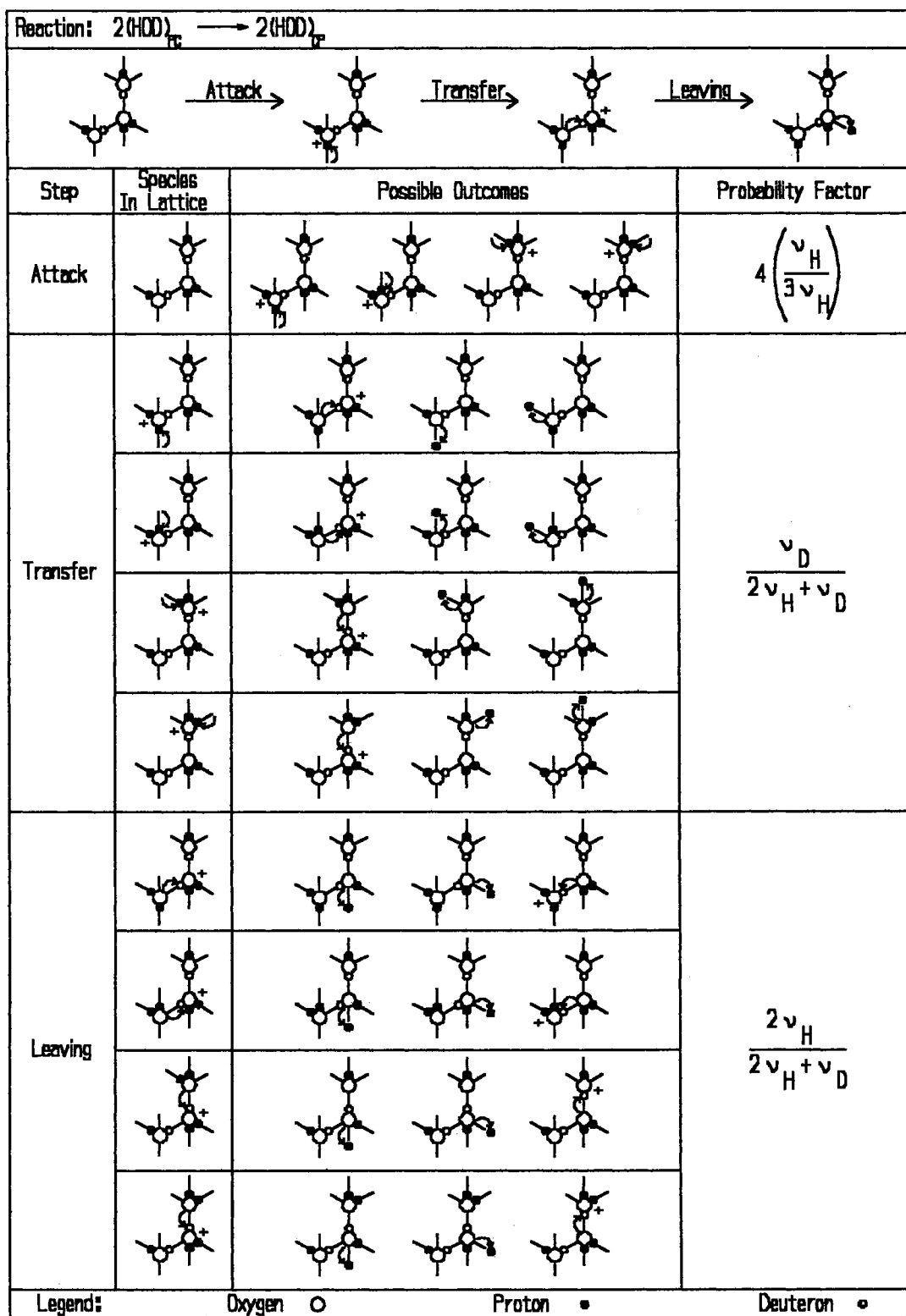
Reaction: $D_2O \longrightarrow 2(HOD)_{cp}$

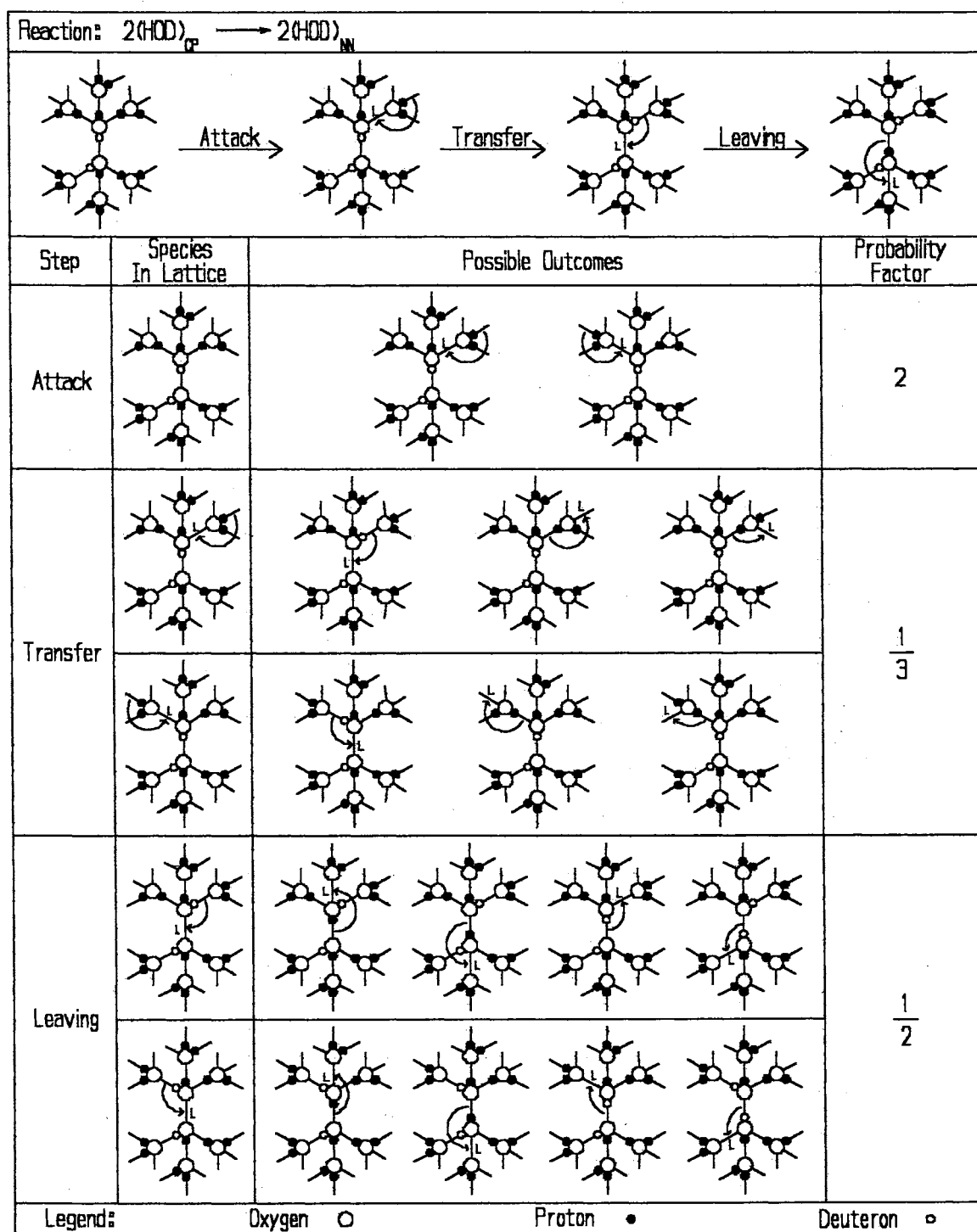
Step	Species In Lattice	Possible Outcomes	Probability Factor
Attack			$2 \left(\frac{\nu_H}{3 \nu_D} \right)$
Transfer			$\frac{2 \nu_D}{\nu_H + 2 \nu_D}$
Leaving			$\frac{2 \nu_H}{2 \nu_H + \nu_D}$
Legend:	Oxygen ○	Proton ●	Deuteron ◐

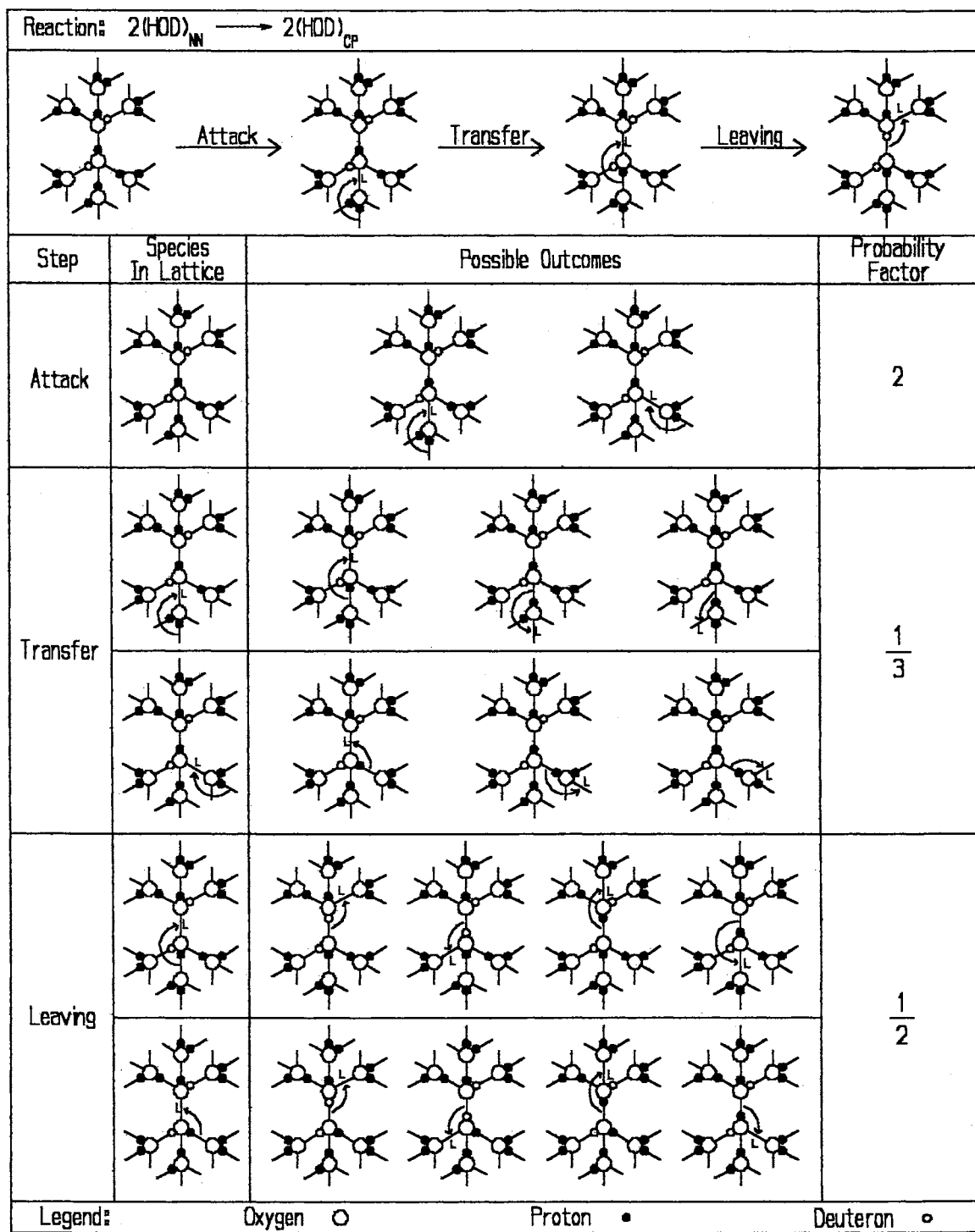
Figure 32. Conversion of D_2O to $(HOD)_{cp}$.

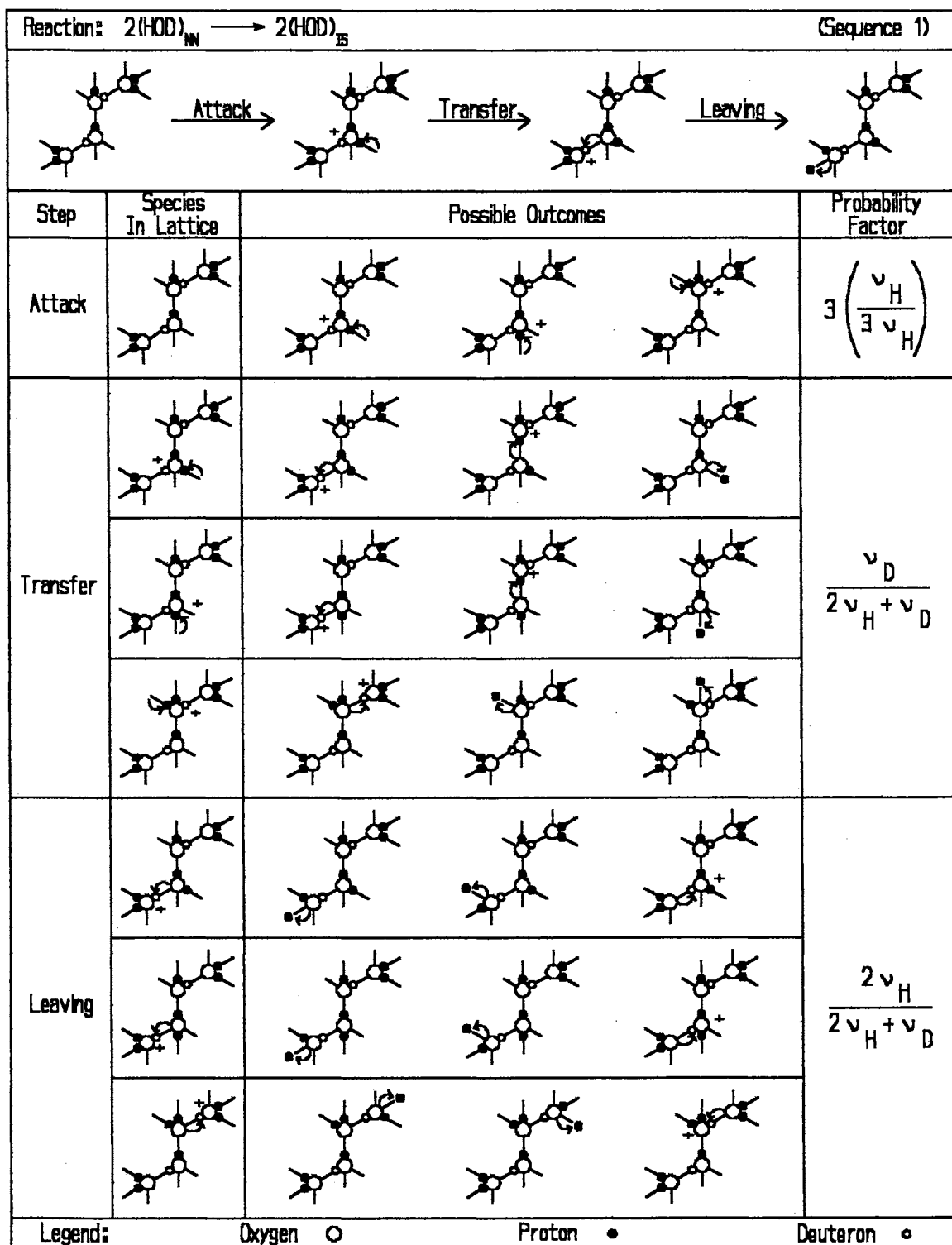
Figure 33. Conversion of $(\text{HOD})_{\text{cp}}$ to D_2O .

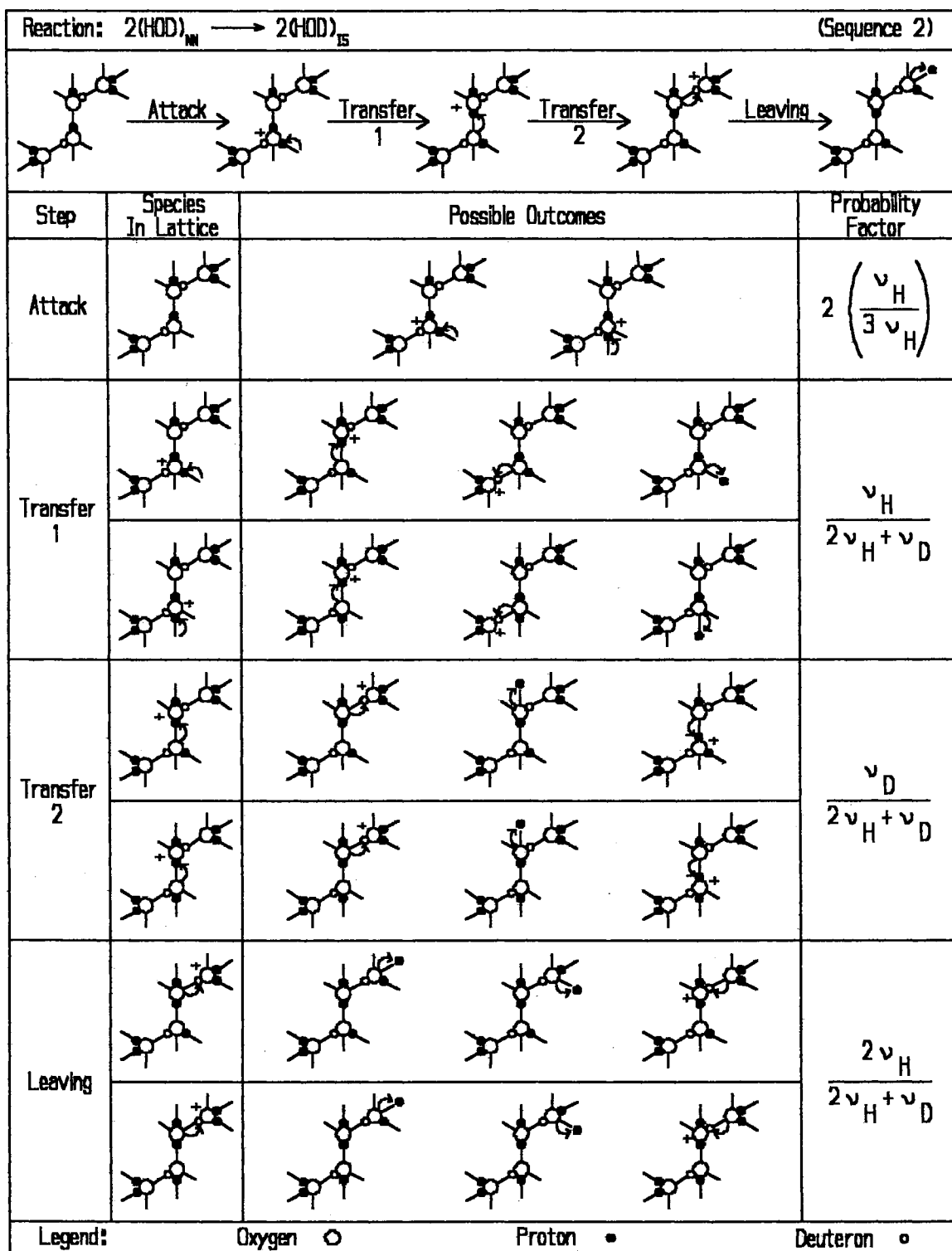
Figure 34. Conversion of $(\text{HOD})_{\text{cp}}$ to $(\text{HOD})_{\text{pc}}$.

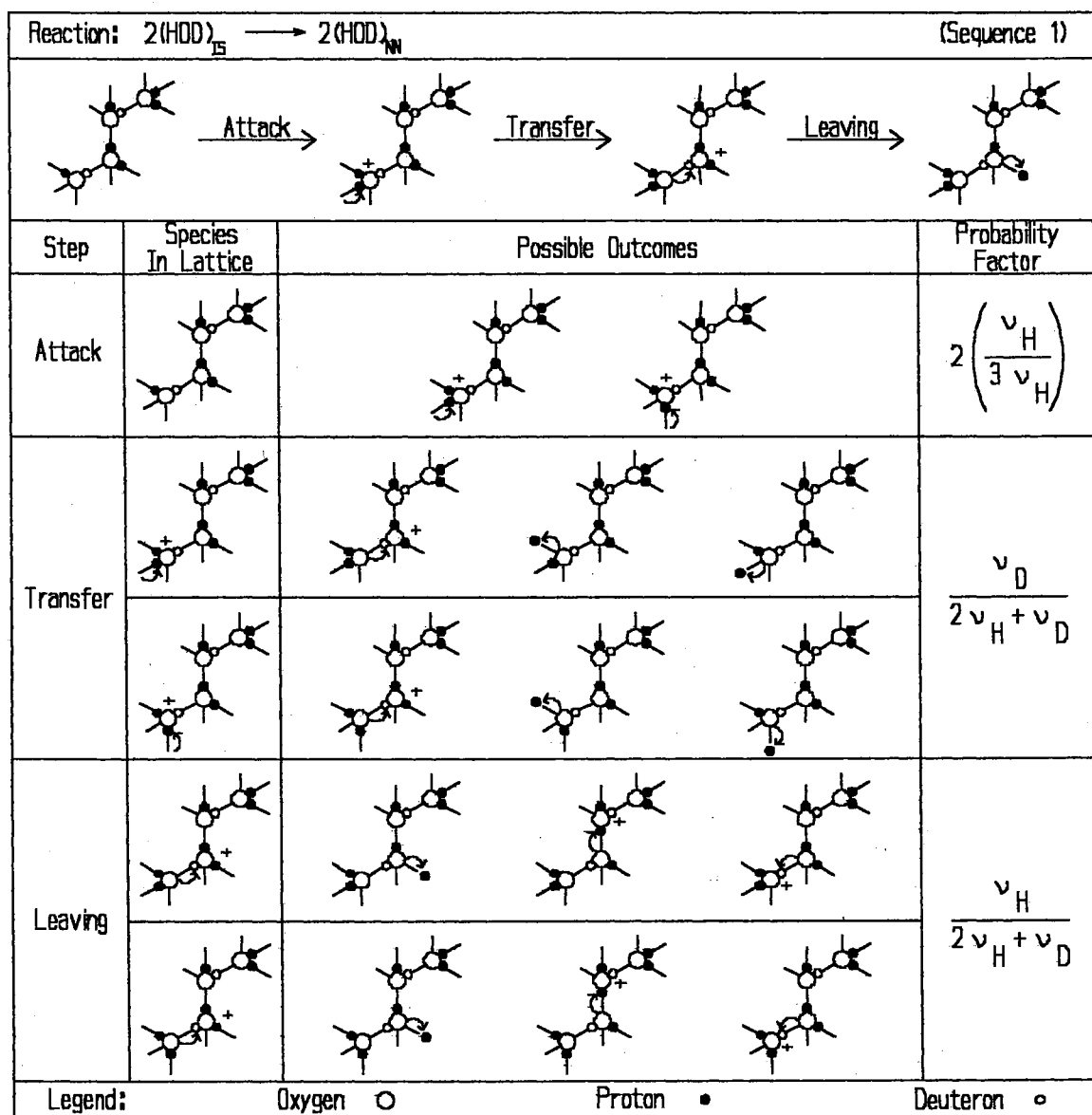
Figure 35. Conversion of $(\text{HOD})_{\text{pc}}$ to $(\text{HOD})_{\text{cp}}$.

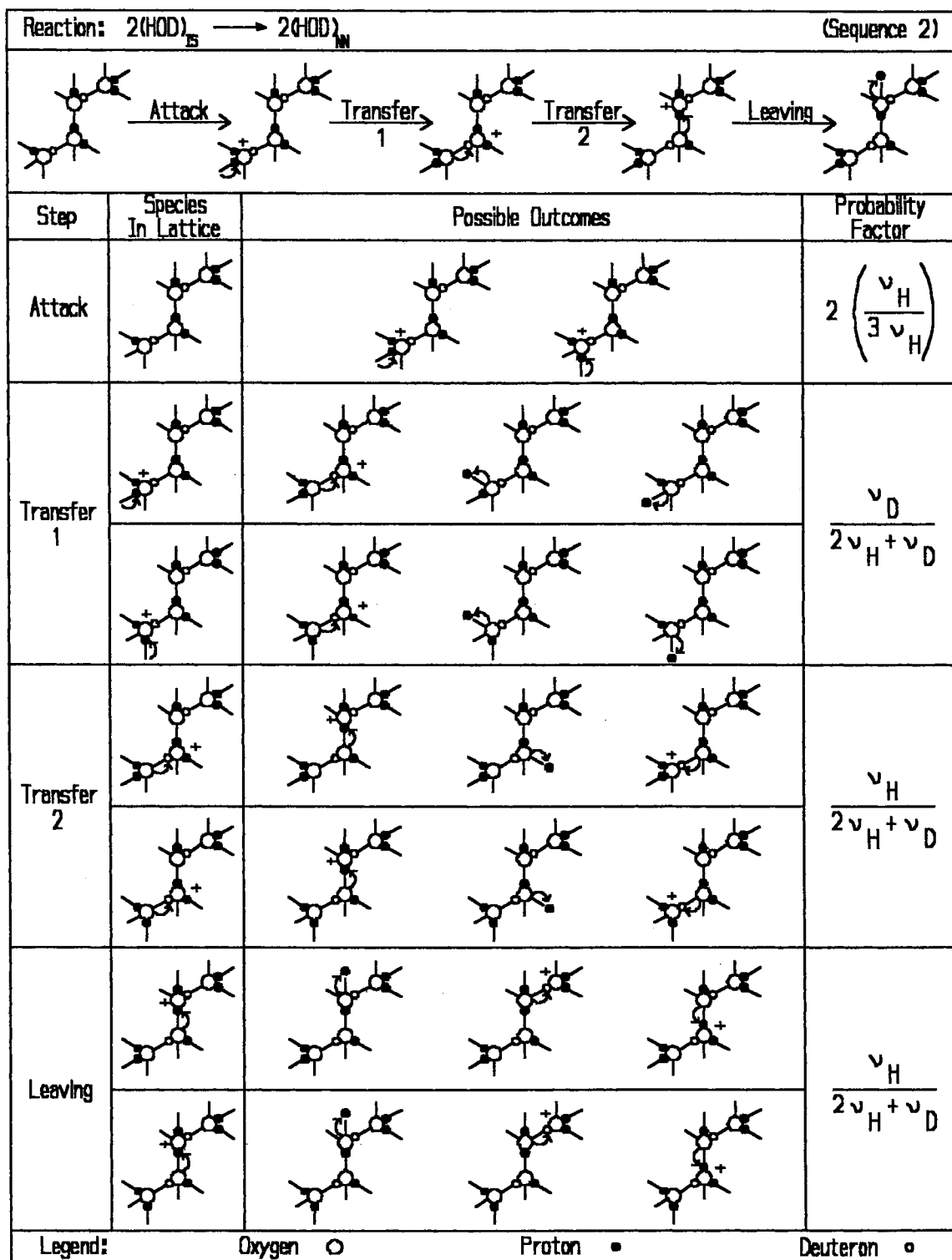
Figure 36. Conversion of $(\text{HOD})_{cp}$ to $(\text{HOD})_{nn}$.

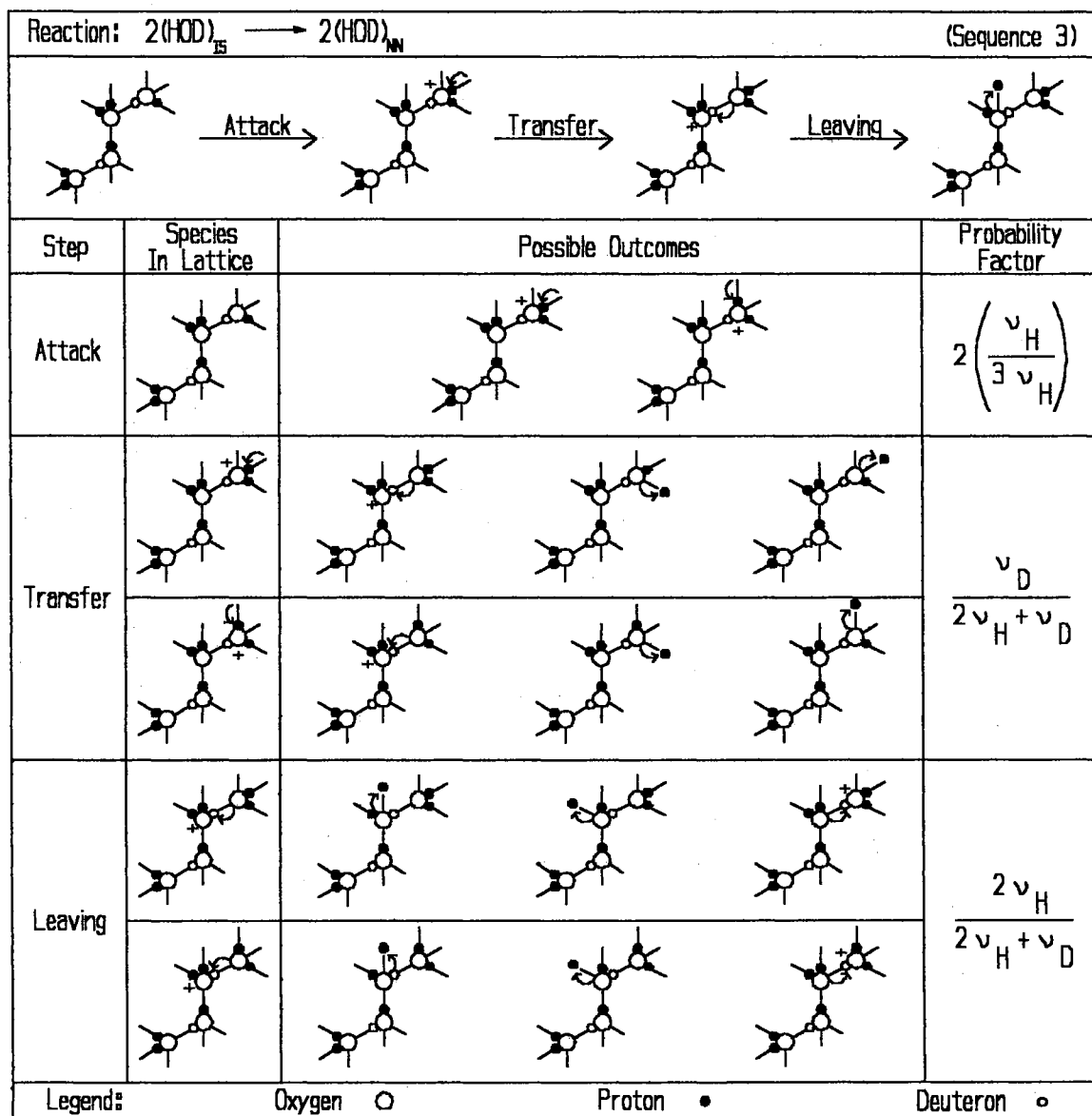
Figure 37. Conversion of $(\text{HOD})_{\text{nn}}$ to $(\text{HOD})_{\text{cp}}$.

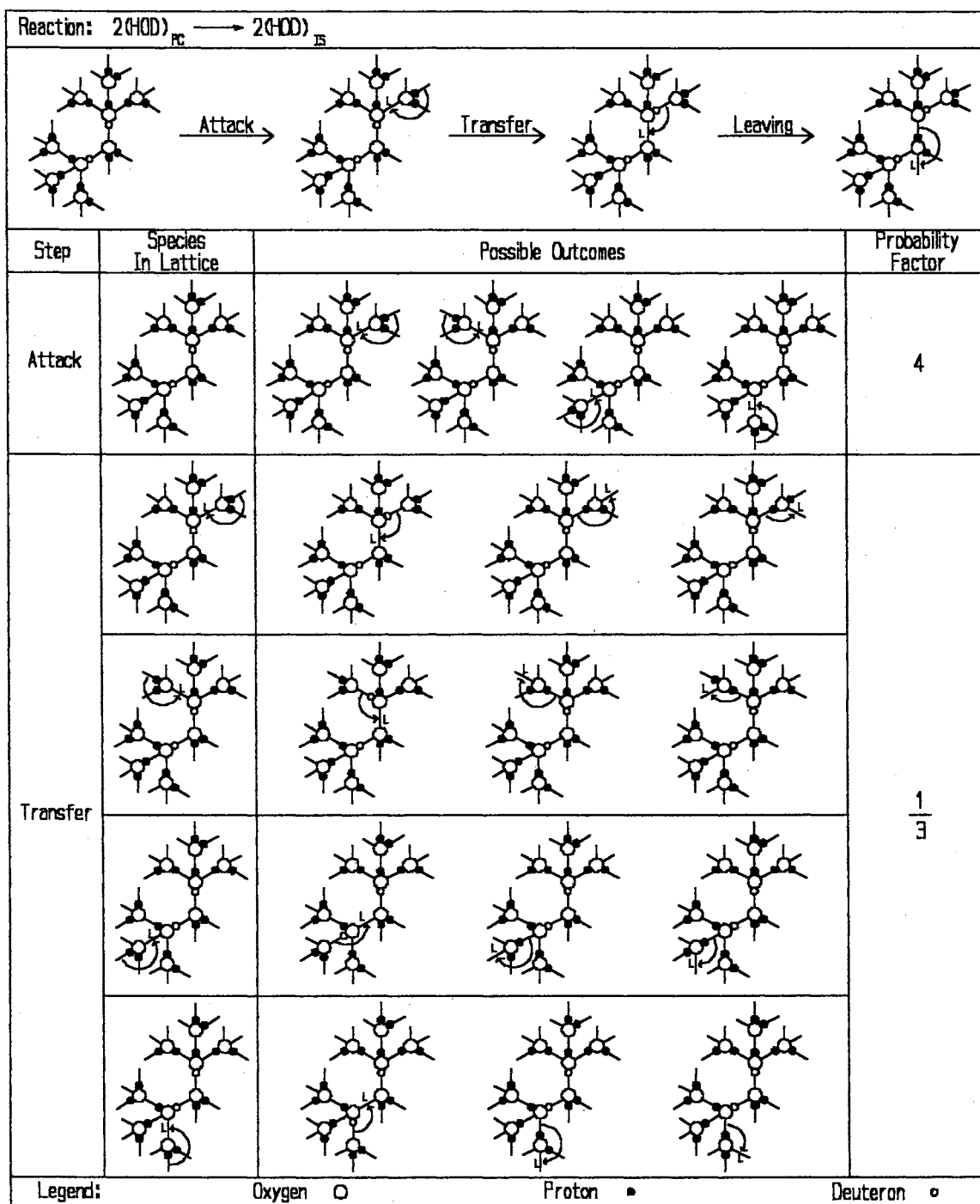
Figure 38. Conversion of $(\text{HOD})_{nn}$ to $(\text{HOD})_{is}$ series 1.

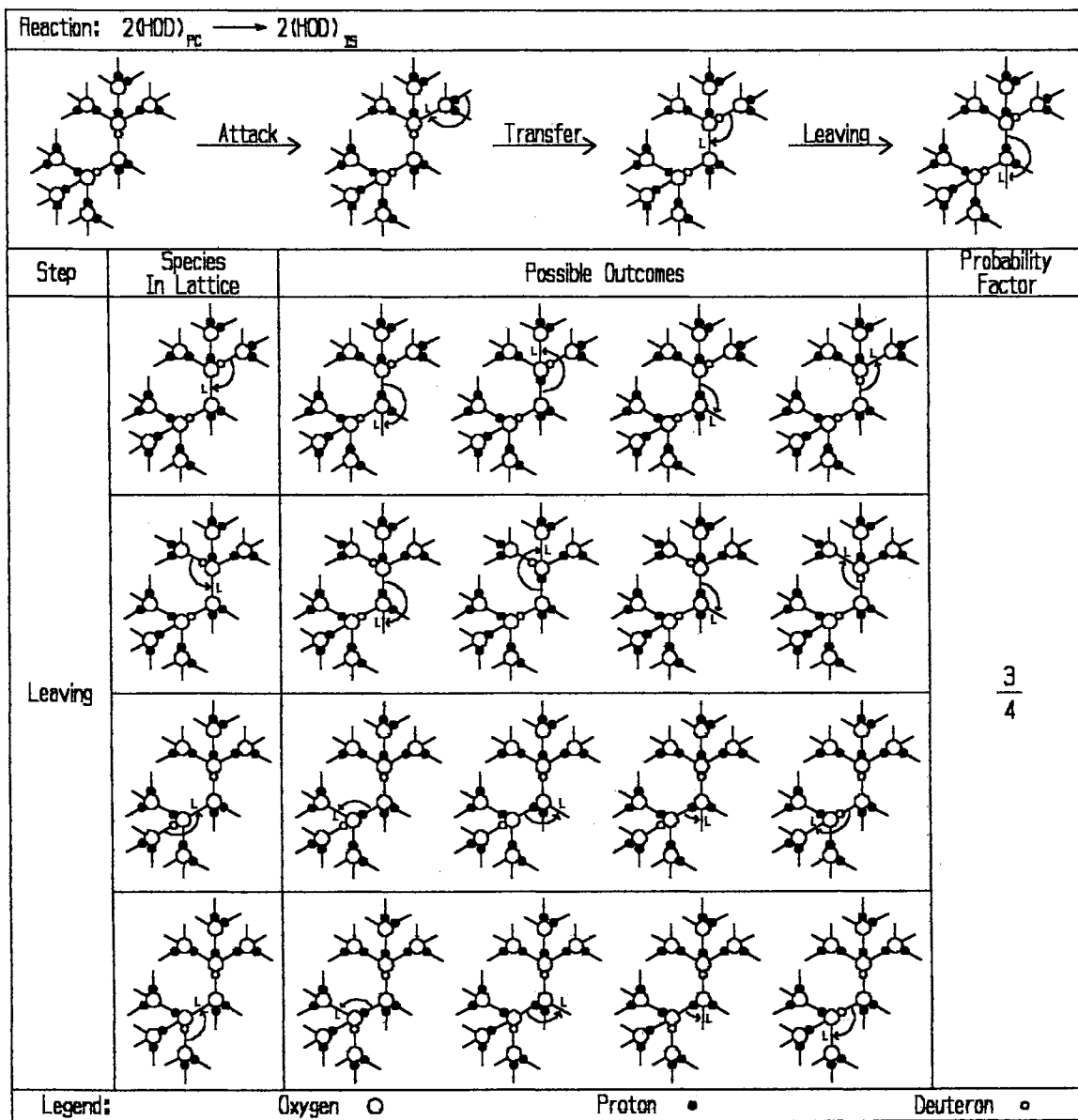
Figure 39. Conversion of $(\text{HOD})_{\text{nn}}$ to $(\text{HOD})_{\text{is}}$ series 2.

Figure 40. Conversion of $(\text{HOD})_{is}$ to $(\text{HOD})_{nn}$ series 1.

Figure 41. Conversion of $(\text{HOD})_{\text{is}}$ to $(\text{HOD})_{\text{nn}}$ series 2.

Figure 42. Conversion of $(\text{HOD})_{is}$ to $(\text{HOD})_{nn}$ series 3.

Figure 43. Conversion of $(\text{HOD})_{\text{PC}}$ to $(\text{HOD})_{\text{IS}}$ series 1.

Figure 44. Conversion of $(\text{HOD})_{\text{pc}}$ to $(\text{HOD})_{\text{is}}$ series 2.

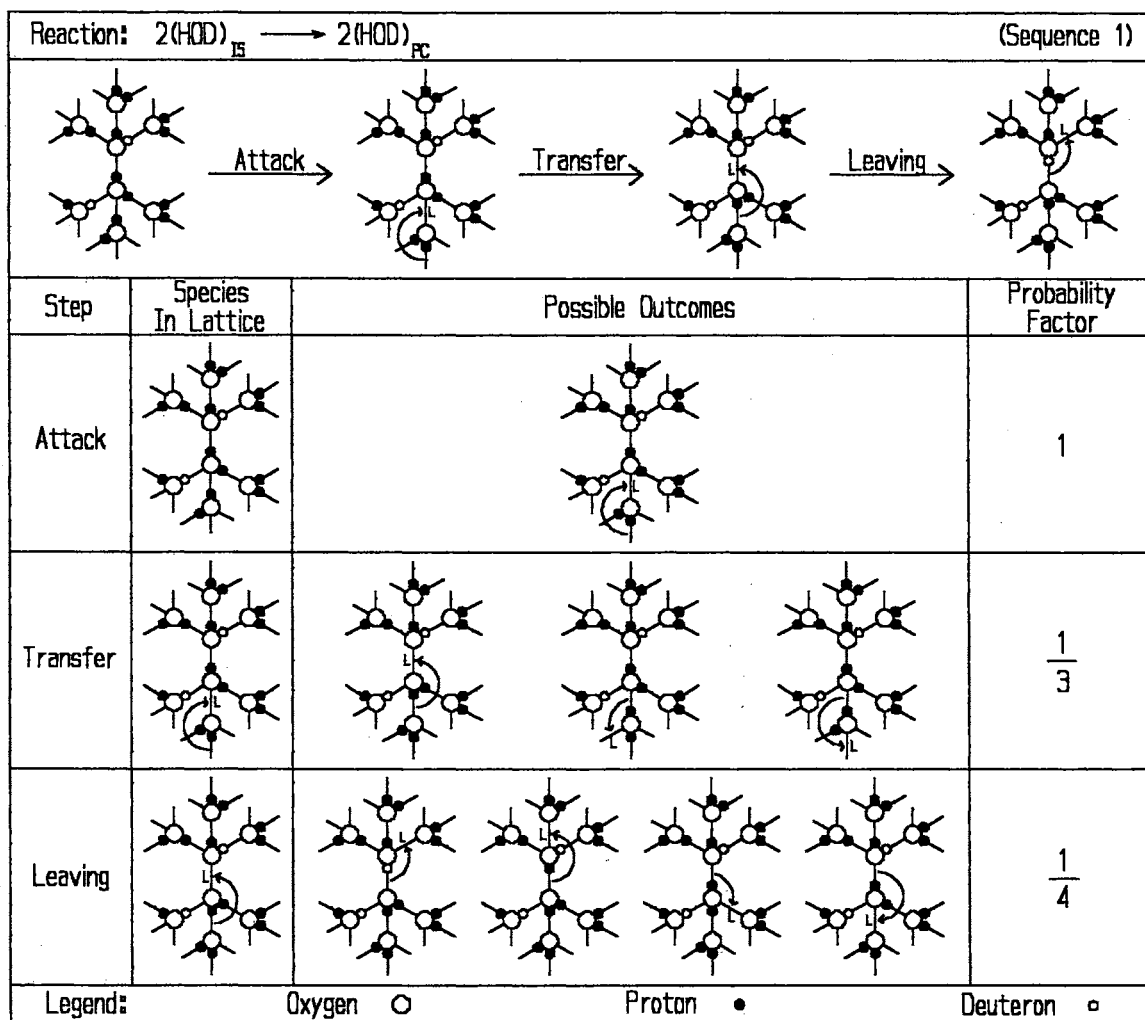
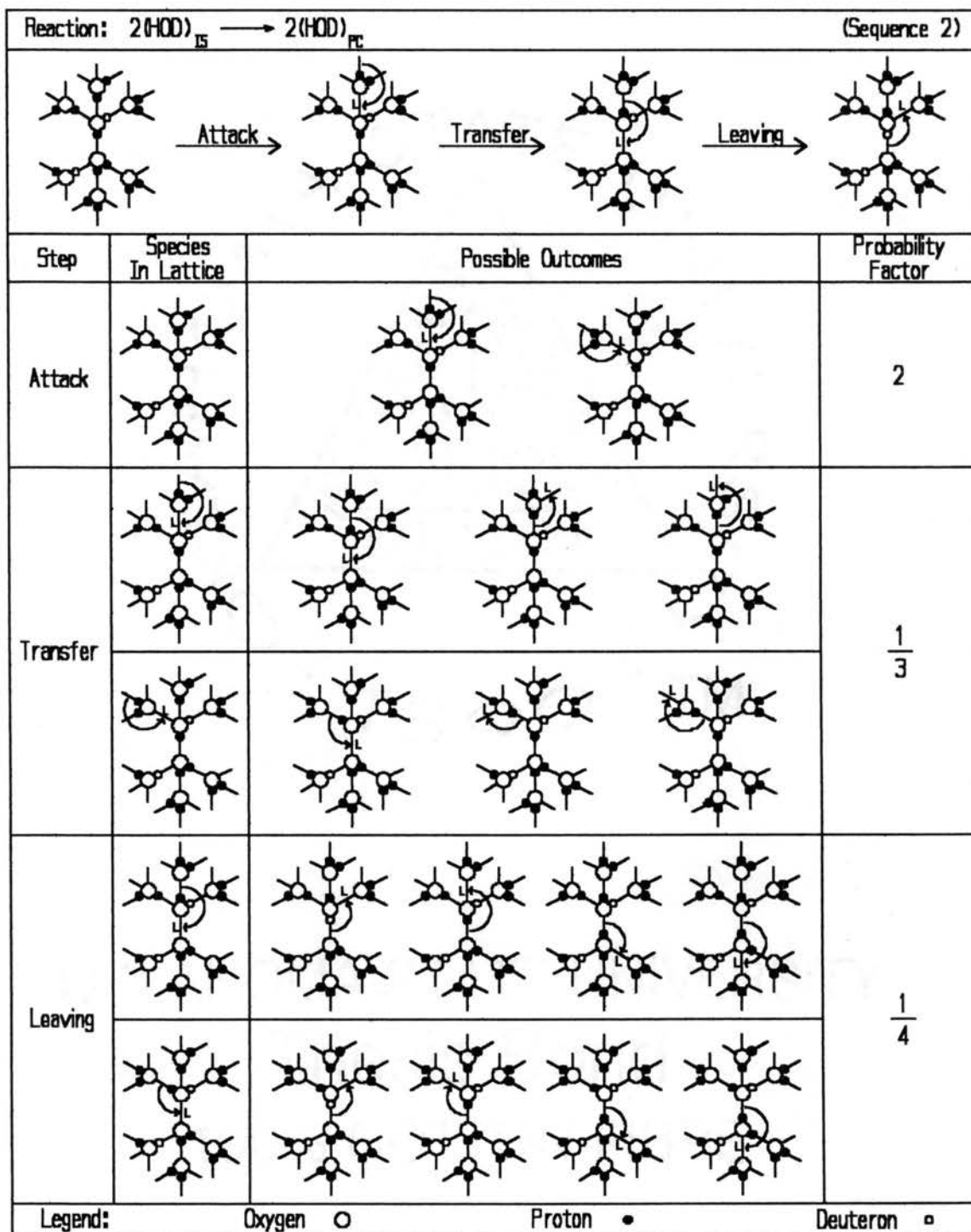
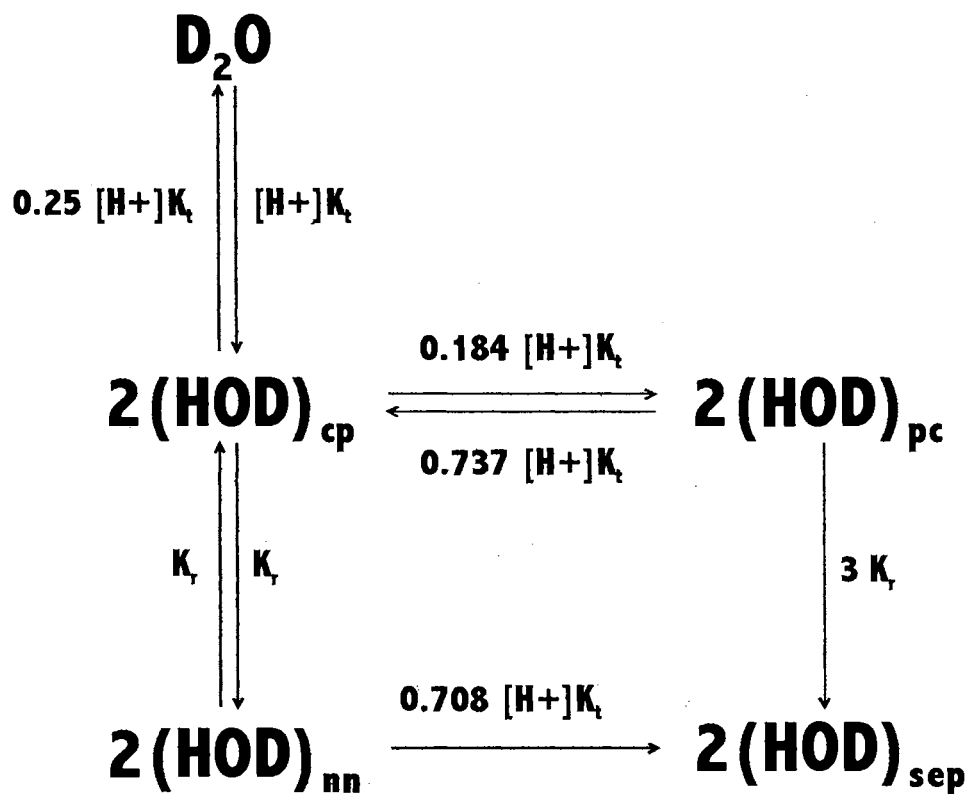
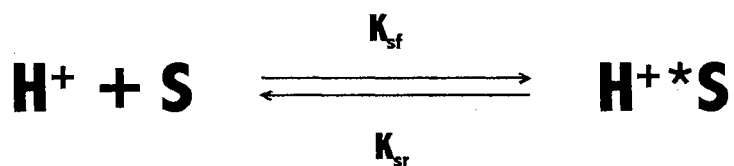


Figure 45. Conversion of $(\text{HOD})_{\text{IS}}$ to $(\text{HOD})_{\text{PC}}$ series 1.

Figure 46. Conversion of $(\text{HOD})_{\text{IS}}$ to $(\text{HOD})_{\text{PC}}$ series 2.



Proton Shallow Trapping



Proton Deep Trapping

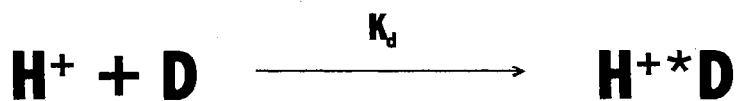


Figure 47. A simplified reaction mechanism.

consuming $(\text{HOD})_{\text{is}}$ were ignored, this also eliminated the pathways enabling $(\text{HOD})_{\text{sep}}$ to feed back into the initial scrambling steps. Hence, $(\text{HOD})_{\text{is}}$ and $(\text{HOD})_{\text{sep}}$ were treated as identical isotopomers, and were referred to in the simplified model as $(\text{HOD})_{\text{sep}}$. The simplified model is depicted in Figure 47 along with the reactions for shallow and deep trapping of protons.

Initial concentrations of the various isotopomers were model input parameters. The time zero concentrations (i.e., the concentrations present at the time of collection of the first spectrum in each kinetic series) for D_2O and $(\text{HOD})_{\text{cp}}$ were available from the experimental data, and were fixed at the experimentally determined values. The concentration of $(\text{HOD})_{\text{sep}}$ was fixed at the concentration determined after sample irradiation. This assumption was made because the isotopic scrambling reactions are slow and the time required to heat the sample to the kinetic experiment temperature is short. Furthermore, $(\text{HOD})_{\text{sep}}$ would have to undergo several reaction steps to convert back into either $(\text{HOD})_{\text{cp}}$ or D_2O , adding validity to the assumption. Hence, little change in $(\text{HOD})_{\text{sep}}$ concentration would be expected in the time interval required to heat the sample to the kinetic run temperature. However, some change in D_2O and $(\text{HOD})_{\text{cp}}$ were observed to occur during the time required to achieve kinetic run temperature, resulting in an increase in concentrations of $(\text{HOD})_{\text{nn}}$ and $(\text{HOD})_{\text{pc}}$. When fitting the data, the experimental HOD concentration was assumed to be a sum of the concentrations of $(\text{HOD})_{\text{sep}}$, $(\text{HOD})_{\text{pc}}$, and $(\text{HOD})_{\text{nn}}$. Hence, the experimentally observed concentration of $(\text{HOD})_{\text{sep}}$ at time zero (denoted as $[(\text{HOD})_{\text{sep}}]_0$) is the sum of $[(\text{HOD})_{\text{nn}}]_0$, $[(\text{HOD})_{\text{pc}}]_0$, and $[(\text{HOD})_{\text{sep}}]$ after irradiation at 80 K). Because the

concentration of $(\text{HOD})_{\text{sep}}$ was assumed to remain constant during heat-up to time zero, the increase in initial concentrations of 'uncoupled' isotopomers is due to an increase in the concentrations of $(\text{HOD})_{\text{nm}}$ and $(\text{HOD})_{\text{pc}}$ that occurred from reactions during heating from 80K to run temperature. Since these are spectrally indistinguishable, the initial concentrations of these isotopomers are included as adjustable parameters, the sum of whose concentrations are equal to the increase in 'uncoupled' isotopomer concentration before kinetic run temperature is reached. In addition, the initial concentrations of deep traps, shallow traps, shallow trapped protons, and mobile protons are included as adjustable parameters. Rate constants included as adjustable parameters include the rate constant for proton hopping (K_t), and the rate constant for L-defect rotation (K_r). The rate constants for deep trapping of protons (K_d), and the forward (K_{sf}) and reverse reactions (K_{sr}) for shallow trapping of protons are also included as adjustable parameters.

It was assumed that the concentration of mobile L-defects rapidly reached a constant value for a given sample upon heating to a given temperature, and that this concentration did not change with time. The rate equations for proton trapping assume that the mobile proton concentration rapidly reach a maximum value and then steadily decayed as deep trapping of the protons proceeded.

An iterative process was used to fit the kinetic model to the experimental data using the previously mentioned adjustable parameters. Differential rate equations were written describing the rate of change of each species in the reaction mechanism with respect to time, with each equation taking into account the appropriate factors discussed above. These equations were then solved numerically using a Runge - Kutta technique. The concentrations calculated by these equations were then fit to the experimental data

using a gradient search least squares fitting technique to adjust the fitting parameters until the best fit to the experimental data was obtained. The best values for the fitting parameters obtained by this cycle were then fed back into the differential equations, which were then re-solved. This entire process was repeated until the calculated concentrations converged to the experimental concentrations as closely as possible. After convergence was achieved, the kinetic parameters were then analyzed.

CHAPTER IV

RESULTS AND CONCLUSIONS

Results From Preparation of Spectra For Kinetic Study

After completion of spectral deconvolution of samples it was possible to compare the concentrations of isotopomers of interest in samples before and after irradiation, and at time zero for kinetic runs. Table XVI lists the change in concentration of D_2O , $(HOD)_{cp}$, and $(HOD)_{sep}$ as a result of generating mobile protons by UV photolysis of 2-naphthol contained in the samples. The concentration of D_2O decreases during irradiation at 80 K, with a corresponding increase in the concentration of $(HOD)_{cp}$. The conversion of D_2O to $(HOD)_{cp}$ is consistent with passage of mobile protons through lattice sites occupied by a D_2O molecule. Of interest is the fact that the concentration of $(HOD)_{sep}$ remained virtually constant during the irradiation process. According to the proposed mechanism (Figure 31), conversion of $(HOD)_{cp}$ to $(HOD)_{nn}$ requires action of mobile orientational defects. Because there was no significant conversion $(HOD)_{cp}$ to $(HOD)_{nn}$ during irradiation, it could be argued that the mobility of orientational defects is absent in ASW at 80 K. This finding (i.e., lack of conversion of $(HOD)_{cp}$ to $(HOD)_{nn}$) is not consistent with molecular translational diffusion during these reactions at 80K. Molecular translational diffusion would result in conversion of D_2O into

TABLE XVI

CHANGE IN ISOTOPOMER CONCENTRATIONS BEFORE
AND AFTER UV PHOTOLYSIS OF 2-NAPHTHOL

Sample #	% Change of Total [OD]			Change in [OD]		
	D2O	(HOD)sep	(HOD)2	D2O	(HOD)sep	(HOD)2
1	-16.7	0.2	16.5	-0.381	0.005	0.377
2	-15.9	0.5	15.4	-0.375	0.012	0.363
3	-13.7	0.1	13.5	-0.615	0.006	0.609
4	-10.3	0.1	10.2	-0.230	0.003	0.228
5	-9.1	0.2	8.8	-0.136	0.003	0.132
6	-13.8	0.1	13.7	-0.123	0.001	0.122
7	-18.5	0.1	18.4	-1.554	0.011	1.543
8	-16.6	0.0	16.6	-0.987	0.002	0.985
9	-15.7	0.0	15.7	-0.955	0.000	0.956
10	-13.4	0.1	13.2	-0.535	0.005	0.530
11	-18.8	0.1	18.8	-1.156	0.005	1.152
12	-13.2	0.3	12.9	-0.222	0.005	0.217
13	-13.9	0.4	13.6	-0.247	0.006	0.241
14	-14.5	0.1	14.4	-0.655	0.003	0.653
15	-16.4	0.0	16.4	-1.067	0.001	1.066
16	-19.0	0.0	19.1	-1.972	-0.005	1.977
17	-21.1	0.0	21.1	-2.733	-0.001	2.733
18	-17.3	0.0	17.2	-1.065	0.002	1.063
19	-18.7	-0.1	18.8	-0.649	-0.004	0.653
20	-16.8	0.1	16.7	-0.878	0.007	0.870
21	-17.6	0.1	17.6	-1.575	0.005	1.570
22	-12.5	-0.1	12.6	-0.384	-0.004	0.388
23	-14.3	-0.1	14.4	-0.779	-0.004	0.784
24	-10.6	0.1	10.5	-0.490	0.003	0.487
25	-11.1	0.0	11.1	-0.763	-0.002	0.765
26	-13.2	-0.1	13.2	-0.898	-0.004	0.902
27	-12.3	-0.1	12.3	-0.426	-0.002	0.428
28	-3.2	0.7	2.5	-0.260	0.061	0.199
29	-13.8	-0.5	14.3	-0.680	-0.023	0.703
30	-13.5	0.1	13.4	-0.631	0.004	0.628
31	-11.1	0.0	11.1	-0.366	0.000	0.366
32	-12.3	-0.1	12.4	-0.774	-0.005	0.779
33	-12.3	0.2	12.2	-0.534	0.008	0.527

(HOD)_{cp}, but the same translational diffusion should have also formed separated (uncoupled) isotopomers. Since this was not observed, we conclude there is no evidence for translational diffusion in ASW at 80 K from this data. Hence, the data suggests that mobile, photo-generated protons converted D₂O to (HOD)_{cp}, without further conversion to (HOD)_{nn}. Conversion of (HOD)_{cp} to (HOD)_{nn} requires mobile L-defects, and at 80 K the concentration of mobile L-defects is very low.

Samples were irradiated with UV light for three hours. Longer exposure times to UV did not result in further isotopic scrambling, suggesting that photo-generated protons traveled a short distance through the ice lattice before becoming trapped, presumably in shallow traps. The kinetic data shows that the protons generated by photolysis of 2-naphthol could be thermally liberated by heating the samples to over 100 K.

Table XVII lists the change in concentration of isotopomeric species upon heating irradiated samples from 80 K up to the temperature for kinetic experiments. The temperatures for kinetic runs ranged from 102 K to 125 K. As can be seen, a limited amount of reaction occurred during heating to temperature. The amount of time to reach the target temperature ranged from between 4 to 7 minutes depending on the target temperature.

Results of Kinetic Study

Data representative of the fit of the kinetic models to the experimental isotopic exchange data is presented in Figures 48 through 57. The solid lines represent the fit to the experimental data. The fit to (HOD)_{sep} is shown as the sum of the concentrations of (HOD)_{nn}, (HOD)_{pc}, and (HOD)_{sep}, which as stated before are spectroscopically

TABLE XVII

CHANGE IN ISOTOPOMER CONCENTRATIONS DURING
HEATING OF SAMPLES TO TEMPERATURE FOR
COLLECTION OF FIRST SPECTRUM OF KINETIC RUN

Sample #	Temperature (Kelvin)	% Change in Total [OD]			Change in [OD]		
		D2O	(HOD)sep	(HOD)2	D2O	(HOD)sep	(HOD)2
1	102	-4.04	4.60	-0.56	-0.092	0.105	-0.013
2	102	-5.21	4.27	0.94	-0.123	0.101	0.022
3	102	-2.70	2.78	-0.08	-0.122	0.125	-0.003
4	105	-3.74	3.32	0.42	-0.083	0.074	0.009
5	105	-7.46	6.04	1.42	-0.112	0.090	0.021
6	105	-6.98	5.18	1.80	-0.062	0.046	0.016
7	108	-2.60	4.33	-1.73	-0.218	0.363	-0.145
8	108	-2.81	3.54	-0.73	-0.167	0.210	-0.043
9	108	-1.73	4.37	-2.64	-0.106	0.267	-0.161
10	112	-3.50	4.71	-1.21	-0.140	0.188	-0.048
11	112	-3.82	6.46	-2.64	-0.234	0.396	-0.162
12	112	0.29	3.79	-4.09	0.005	0.064	-0.069
13	110	0.64	2.31	-2.95	0.011	0.041	-0.052
14	110	0.14	3.02	-3.16	0.006	0.136	-0.143
15	110	-1.59	4.09	-2.50	-0.103	0.266	-0.162
16	115	-2.90	9.51	-6.61	-0.301	0.987	-0.686
17	115	-2.18	8.83	-6.65	-0.283	1.146	-0.864
18	115	-2.71	8.08	-5.37	-0.167	0.498	-0.331
19	118	-5.89	10.63	-4.74	-0.205	0.370	-0.165
20	118	-4.70	10.23	-5.53	-0.245	0.534	-0.289
21	118	-4.89	9.64	-4.75	-0.436	0.861	-0.424
22	120	-5.81	8.48	-2.67	-0.179	0.261	-0.082
23	120	-2.49	8.13	-5.64	-0.135	0.442	-0.307
24	120	-6.59	7.86	-1.26	-0.305	0.364	-0.058
25	122	-7.71	11.97	-4.26	-0.532	0.826	-0.294
26	122	-7.85	11.53	-3.68	-0.535	0.785	-0.251
27	122	-7.55	10.53	-2.99	-0.262	0.366	-0.104
28	125	-10.07	14.19	-4.12	-0.816	1.151	-0.334
29	125	-9.08	16.39	-7.32	-0.447	0.808	-0.361
30	125	-9.90	16.98	-7.08	-0.465	0.797	-0.332
31	100	-1.76	1.55	0.20	-0.058	0.051	0.007
32	100	-1.90	2.05	-0.14	-0.120	0.128	-0.009
33	100	-1.44	1.87	-0.44	-0.062	0.081	-0.019

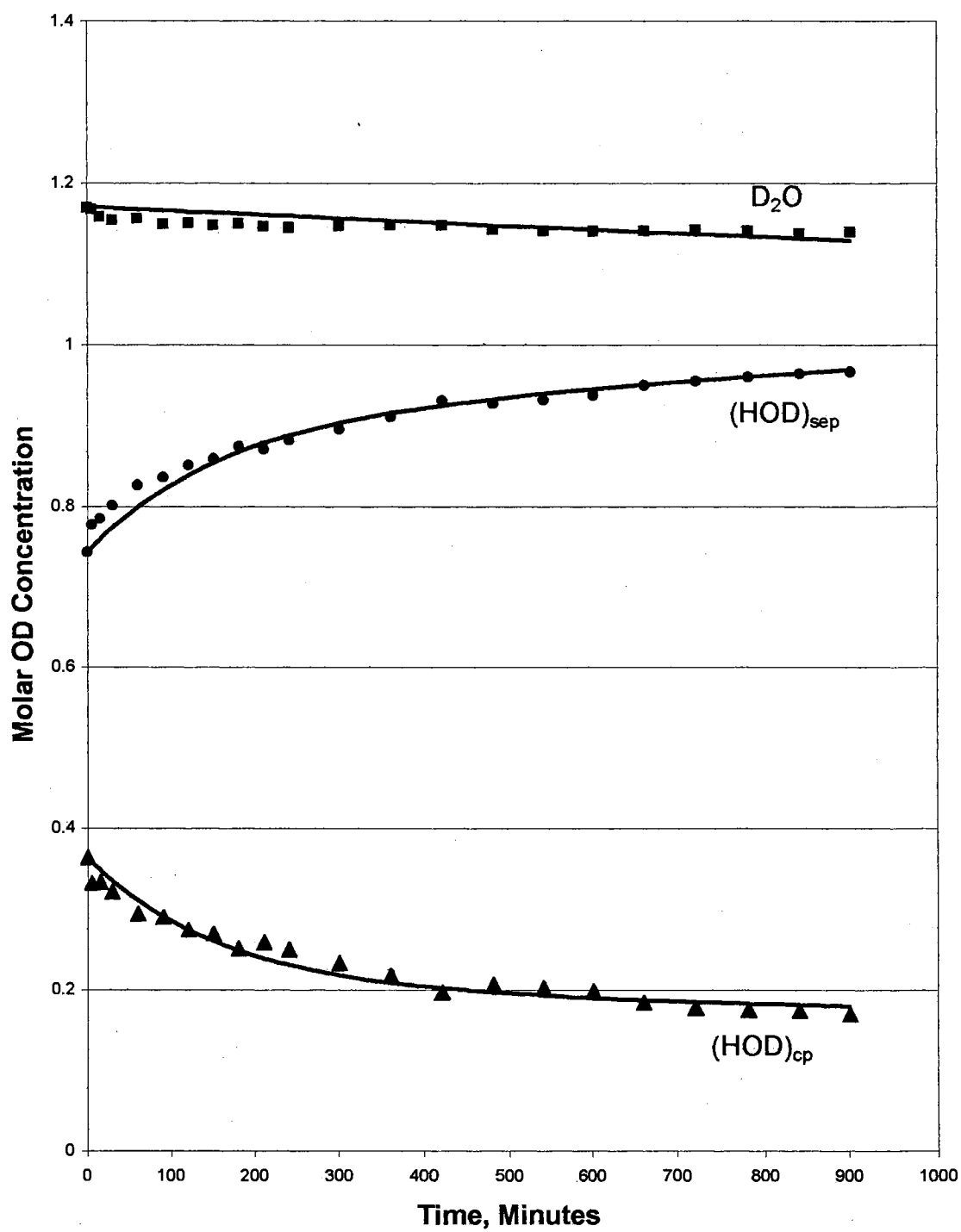


Figure 48. Fit to experimental data for kinetic run 1 at 102 K.

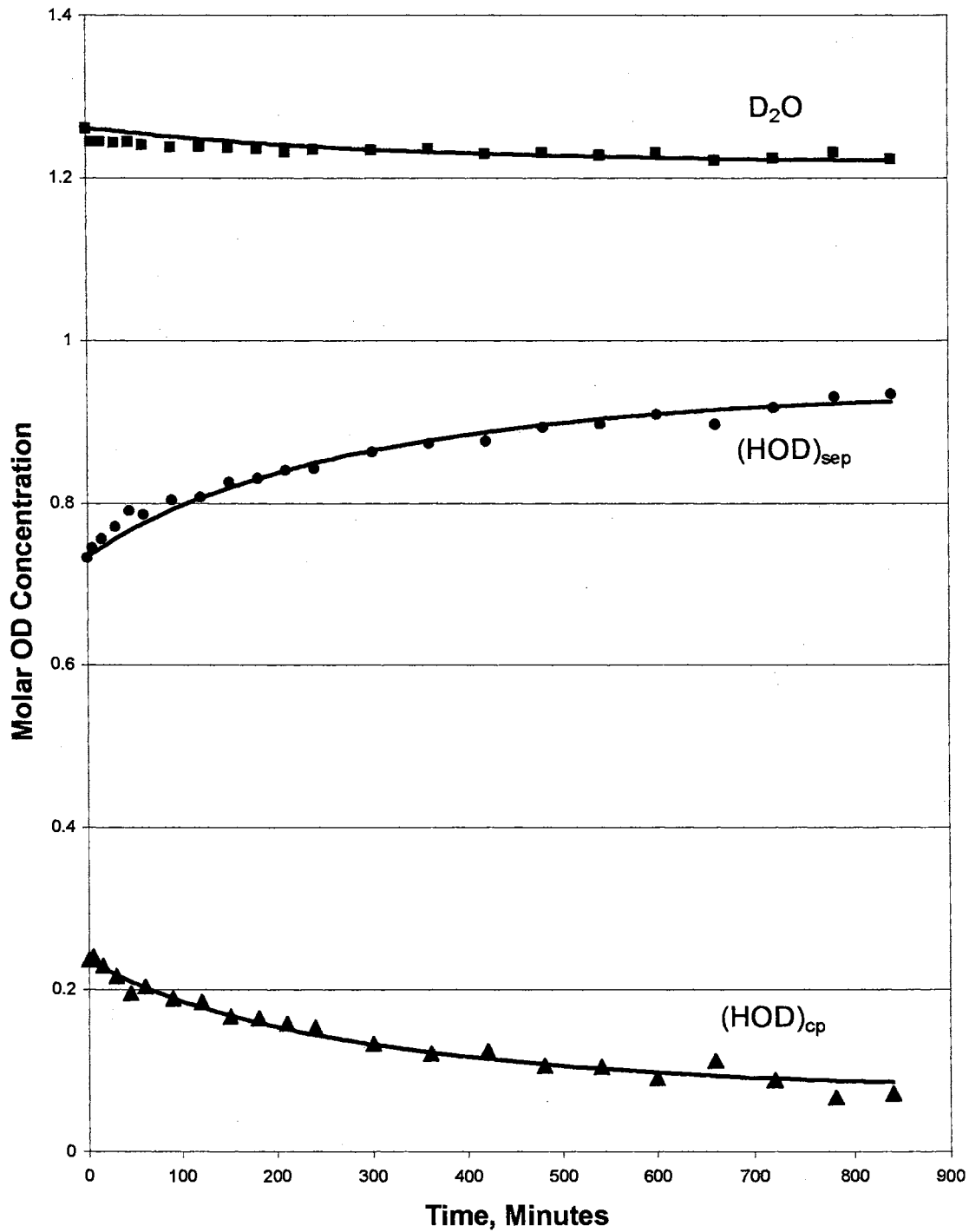


Figure 49. Fit to experimental data for kinetic run 1 at 105 K.

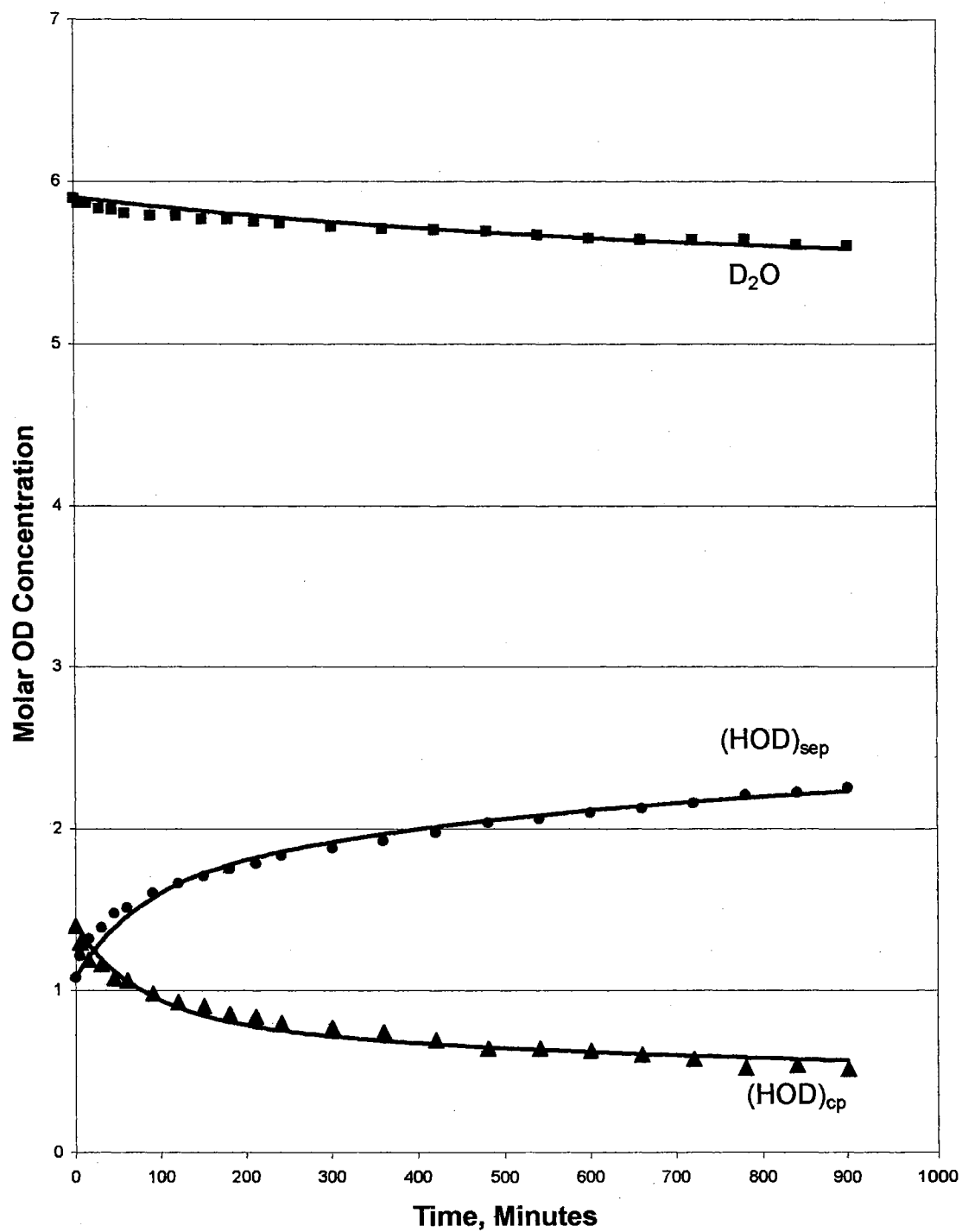


Figure 50. Fit to experimental data for kinetic run 1 at 108 K.

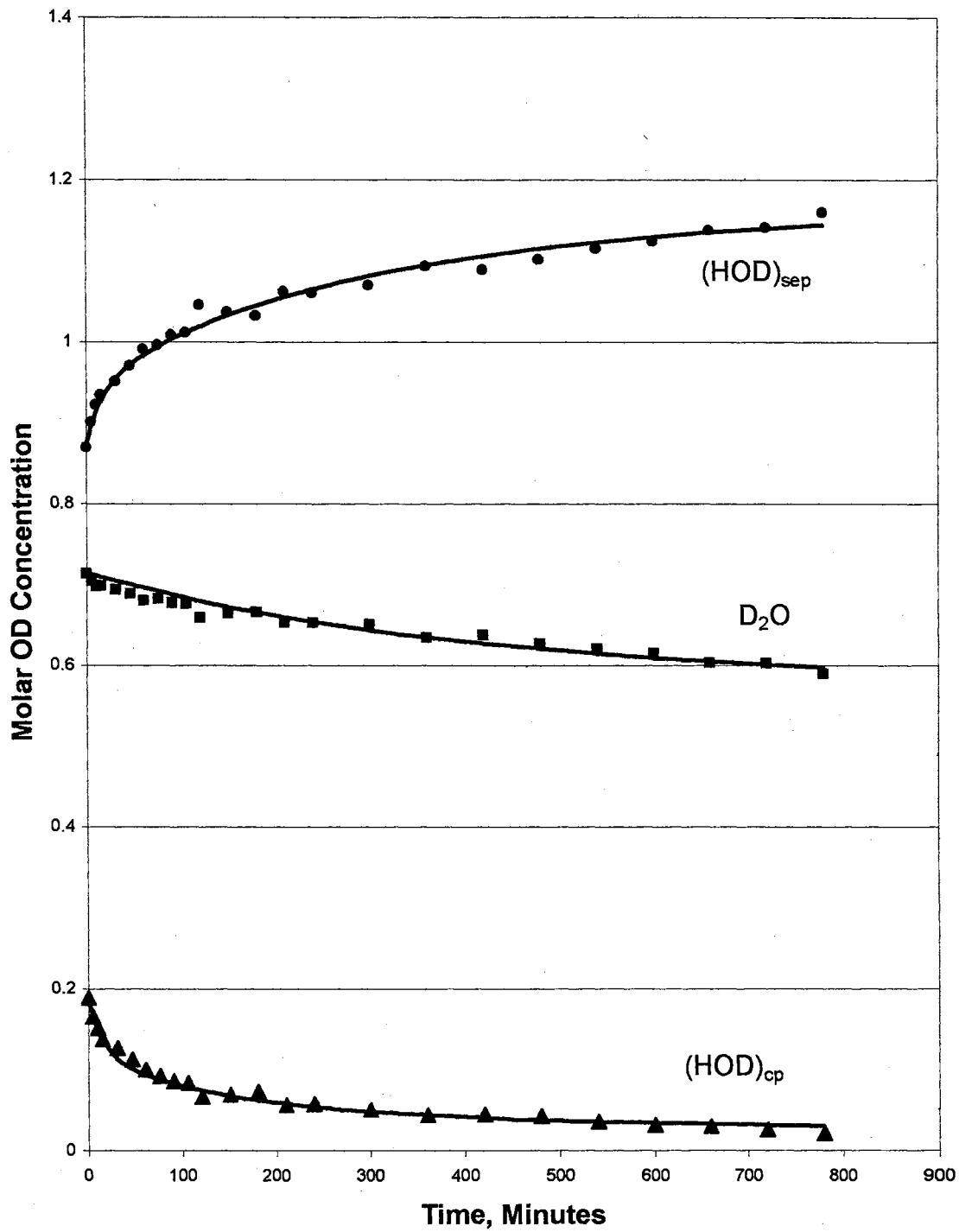
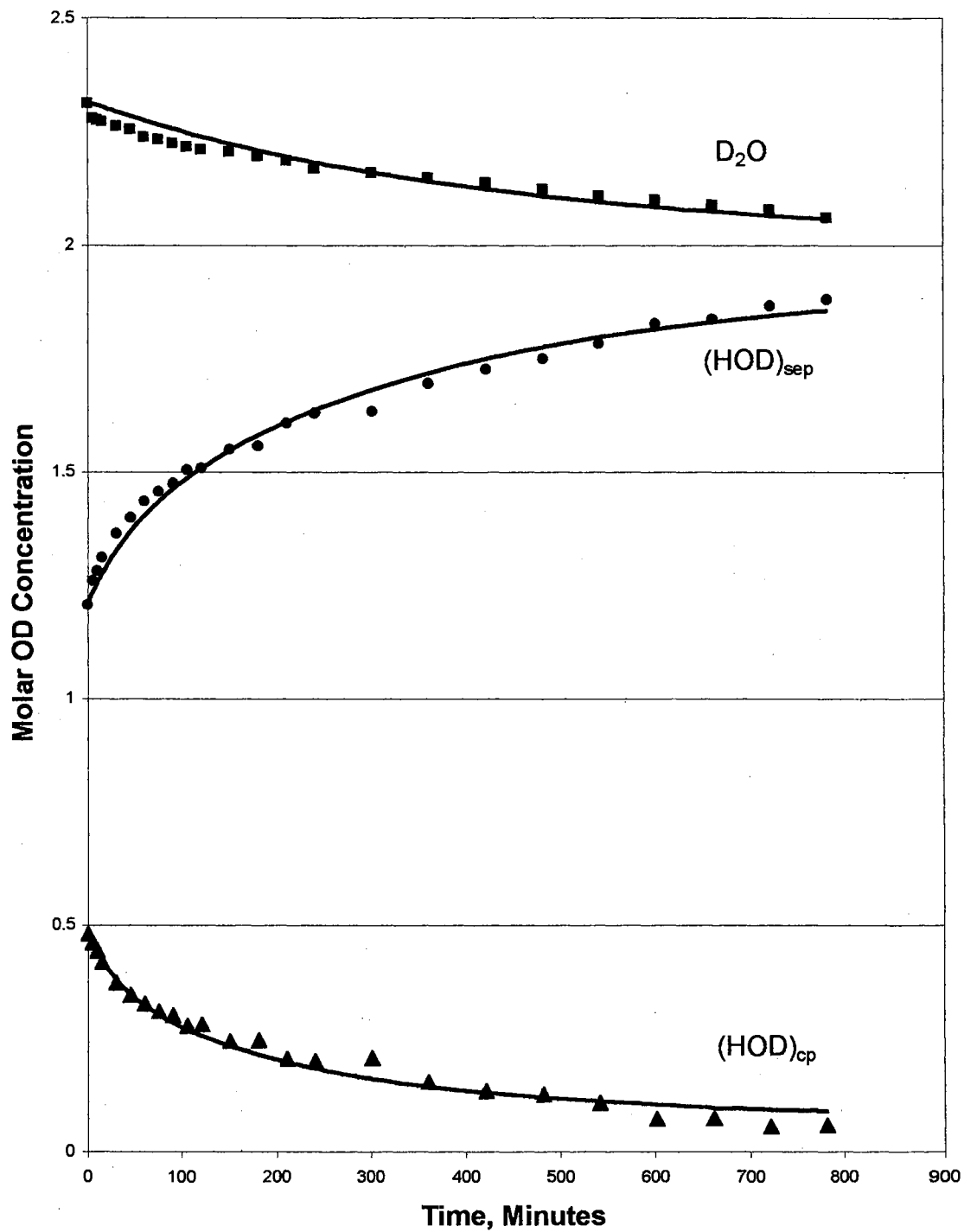


Figure 51. Fit to experimental data for kinetic run 1 at 110 K.



52. Fit to experimental data for kinetic run 1 at 112 K.

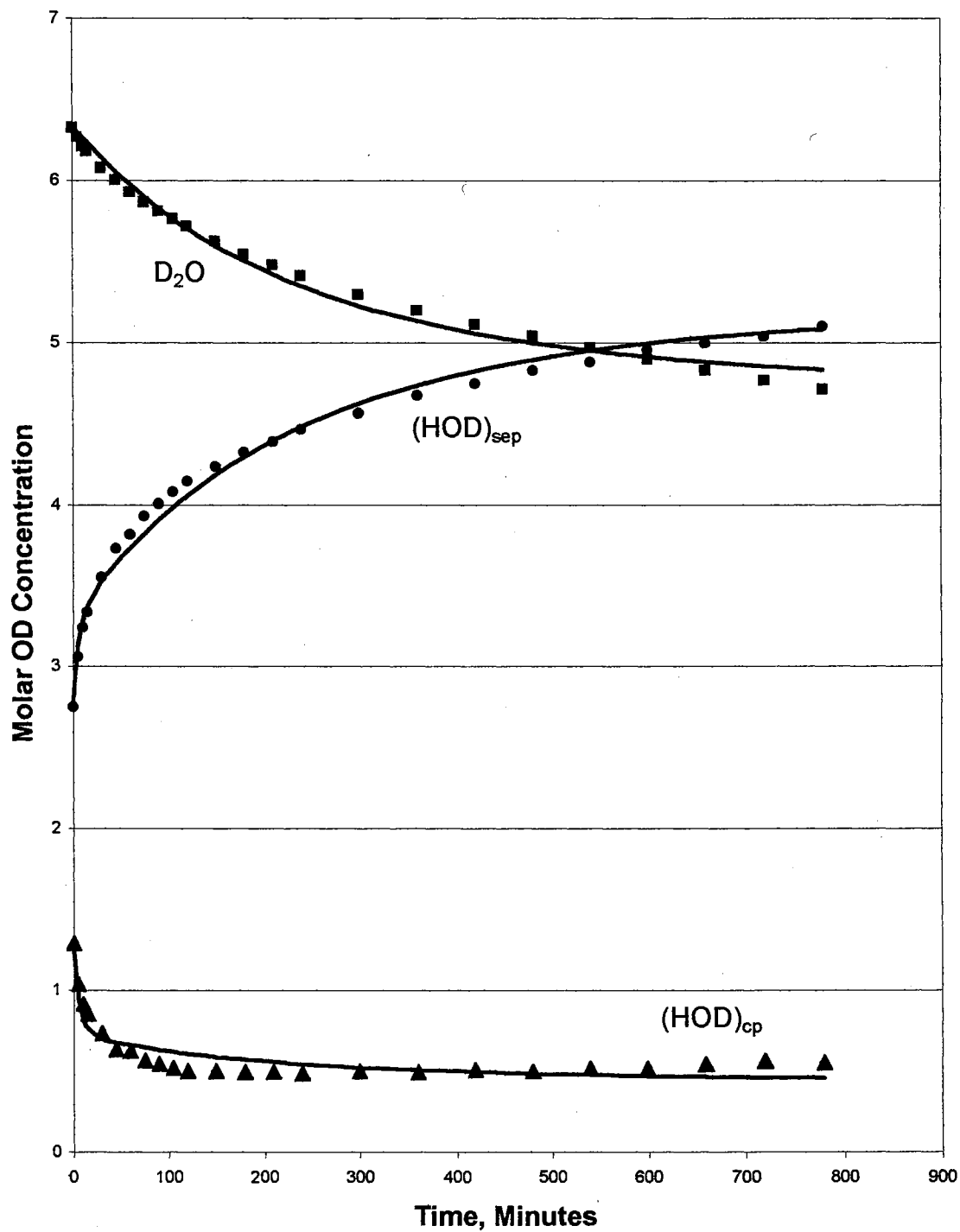


Figure 53. Fit to experimental data for kinetic run 1 at 115 K.

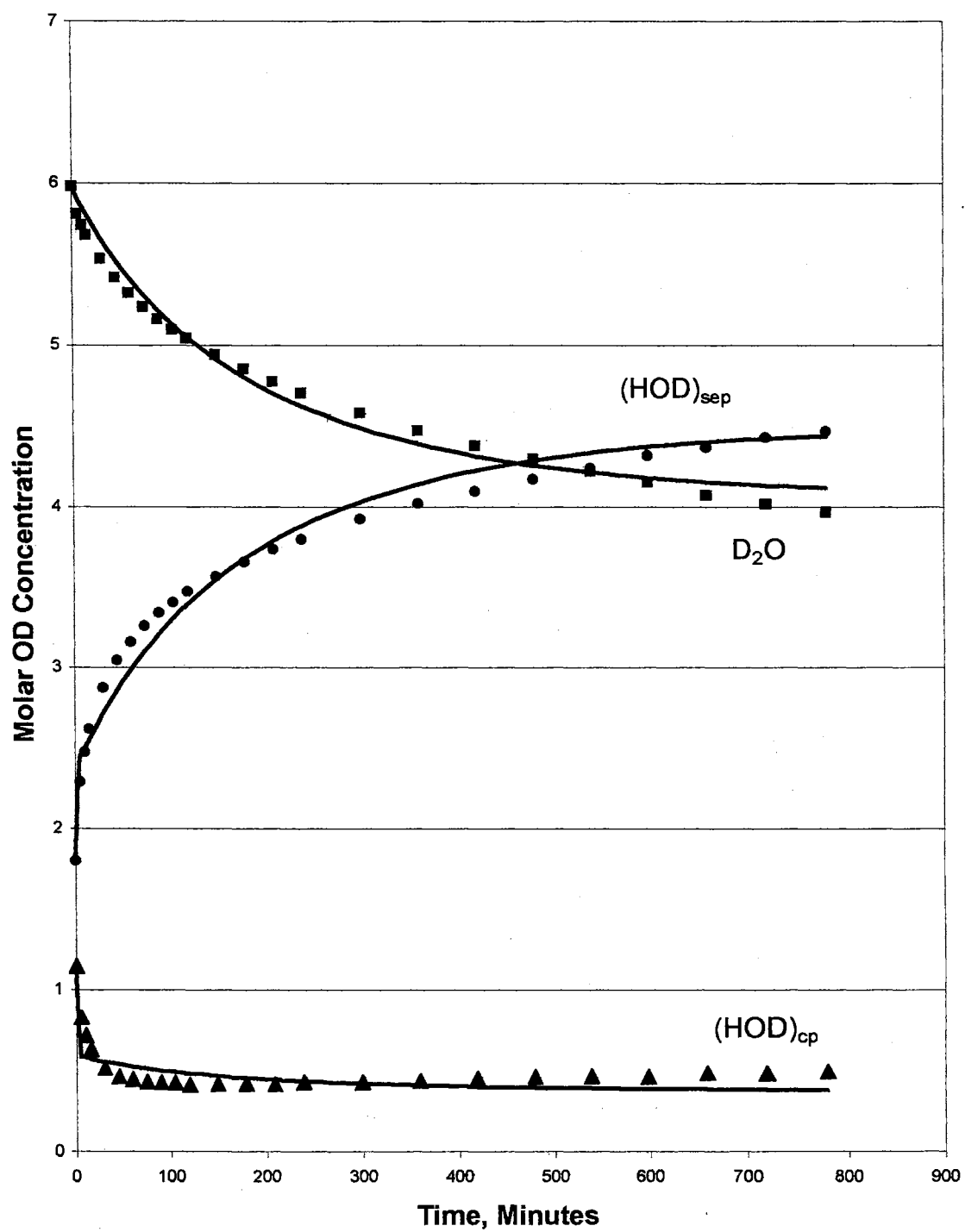


Figure 54. Fit to experimental data for kinetic run 3 at 118 K.

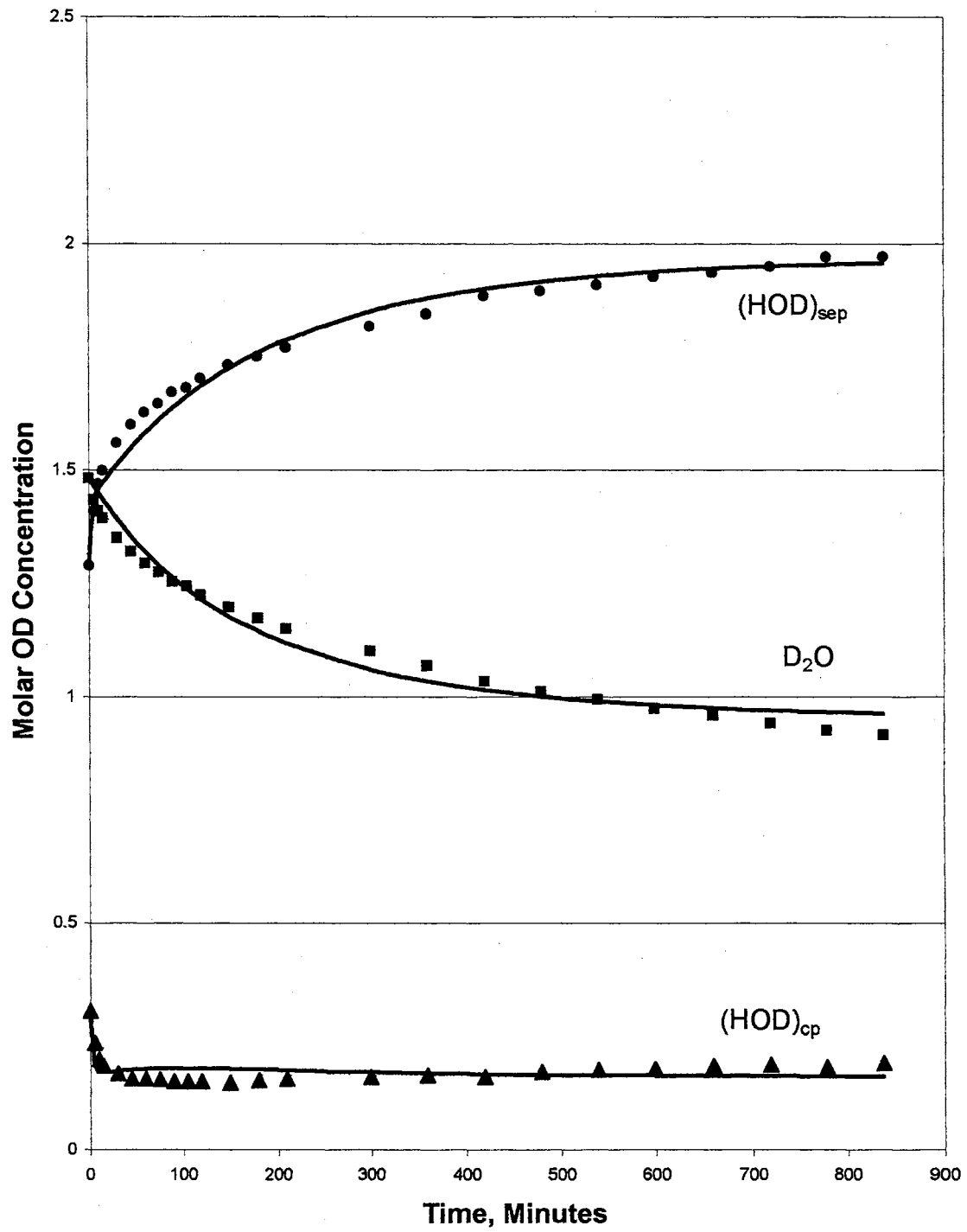


Figure 55. Fit to experimental data for kinetic run 1 at 120 K.

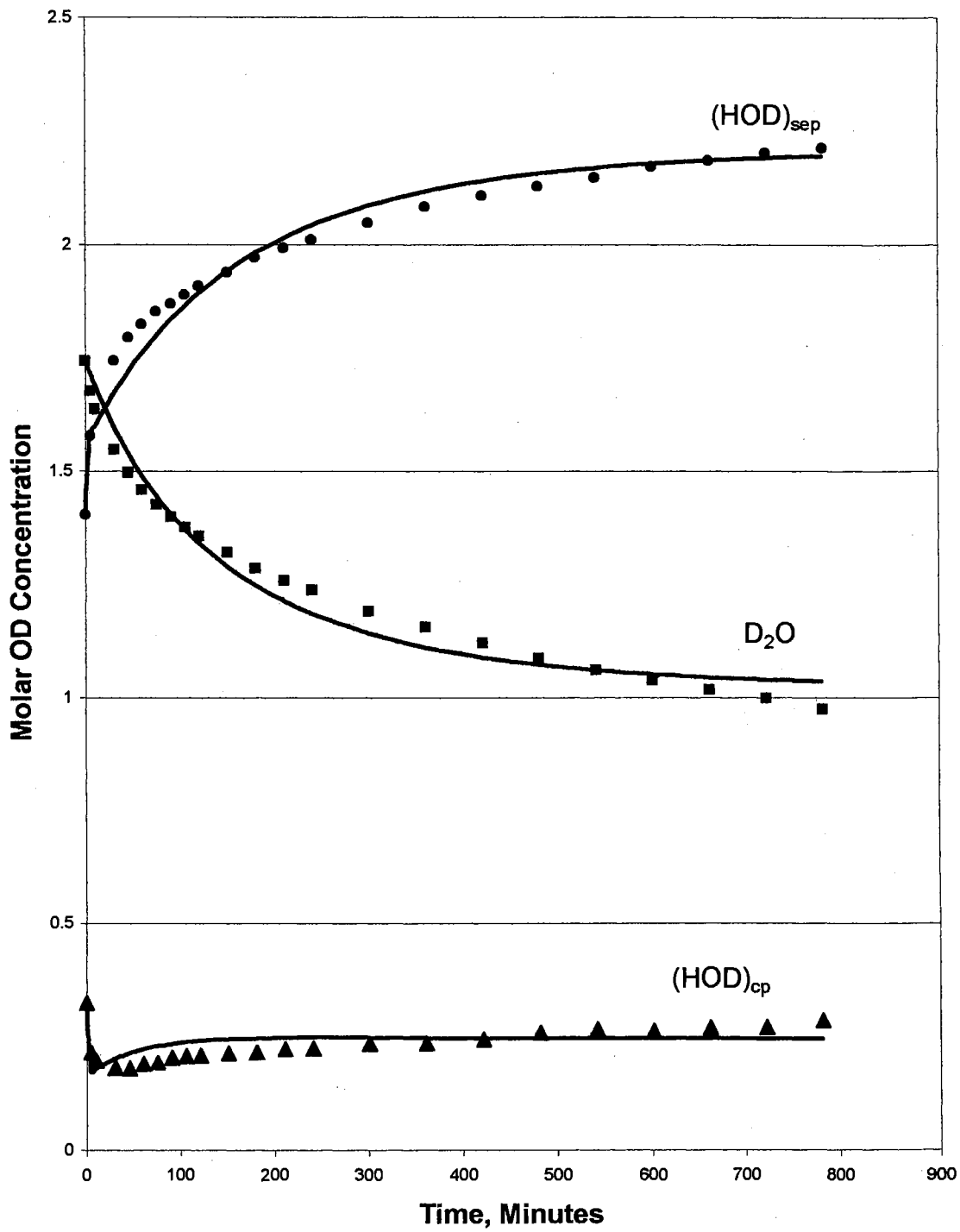


Figure 56. Fit to experimental data for kinetic run 3 at 122 K.

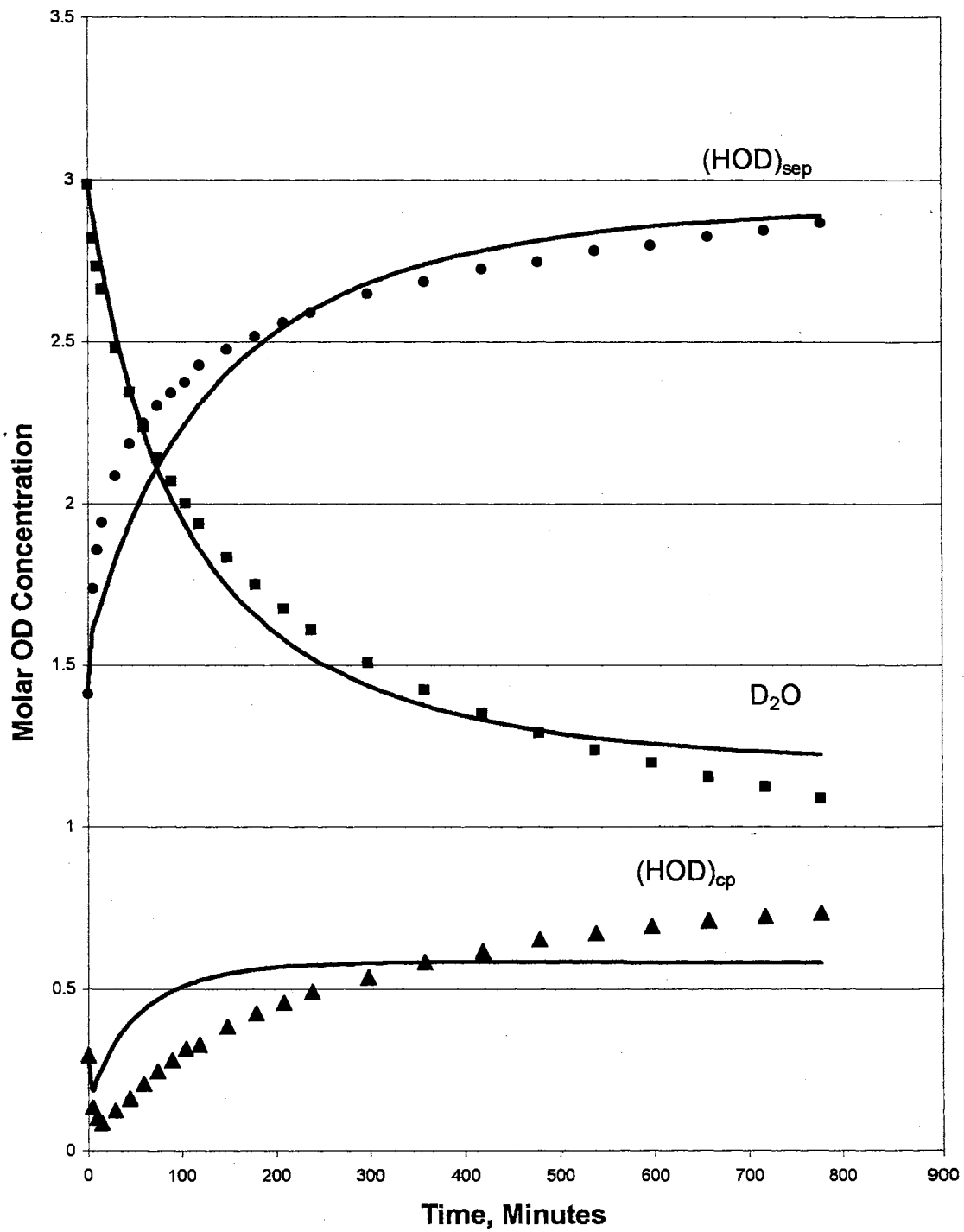


Figure 57. Fit to experimental data for kinetic run 3 at 125 K.

indistinguishable. Figures 58 through 67 represent the calculated concentrations of the individual isotopomers versus time based on the results of the fit of the model to the experimental data. Also included are plots depicting the estimated mobile proton concentration with respect to time. These are plots 68 through 77.

The onset of proton hopping and L-defect activity was observed to occur at a temperature near 102 K. Apparently, even after proton enrichment the concentration of mobile protons is very low in amorphous ice, presumably due to shallow trapping, or possibly deep trapping of protons. As can be seen from figures 68 through 77, the model predicts that protons that are initially shallow trapped are thermally liberated from the traps upon heating to the kinetic run temperature, resulting in an initial increase in mobile proton concentration. However, after only a short period of time the mobile proton concentration begins to drop as protons encounter shallow traps, and apparently, eventually deep traps. Naphtholate ions that are present from the photolysis reaction are a source of deep traps because naphtholate ions will recombine irreversibly with mobile protons. It cannot be determined from this analysis if there are other deep traps beside naphtholate ions. As can be seen from figures 68 through 77, as the temperature increases the rate of loss of mobile protons accelerates. This is presumably due to enhanced proton mobility at higher temperatures. As the rate of proton hopping increases, the protons sample more lattice sites in a shorter time period, decreasing the amount of time required before a mobile proton encounters a deep trap. Hence, the observed behavior is consistent with a mechanism in which protons generated during photolysis are shallow trapped after moving a short distance through the ice lattice. These shallow trapped protons are thermally liberated upon heating, and eventually

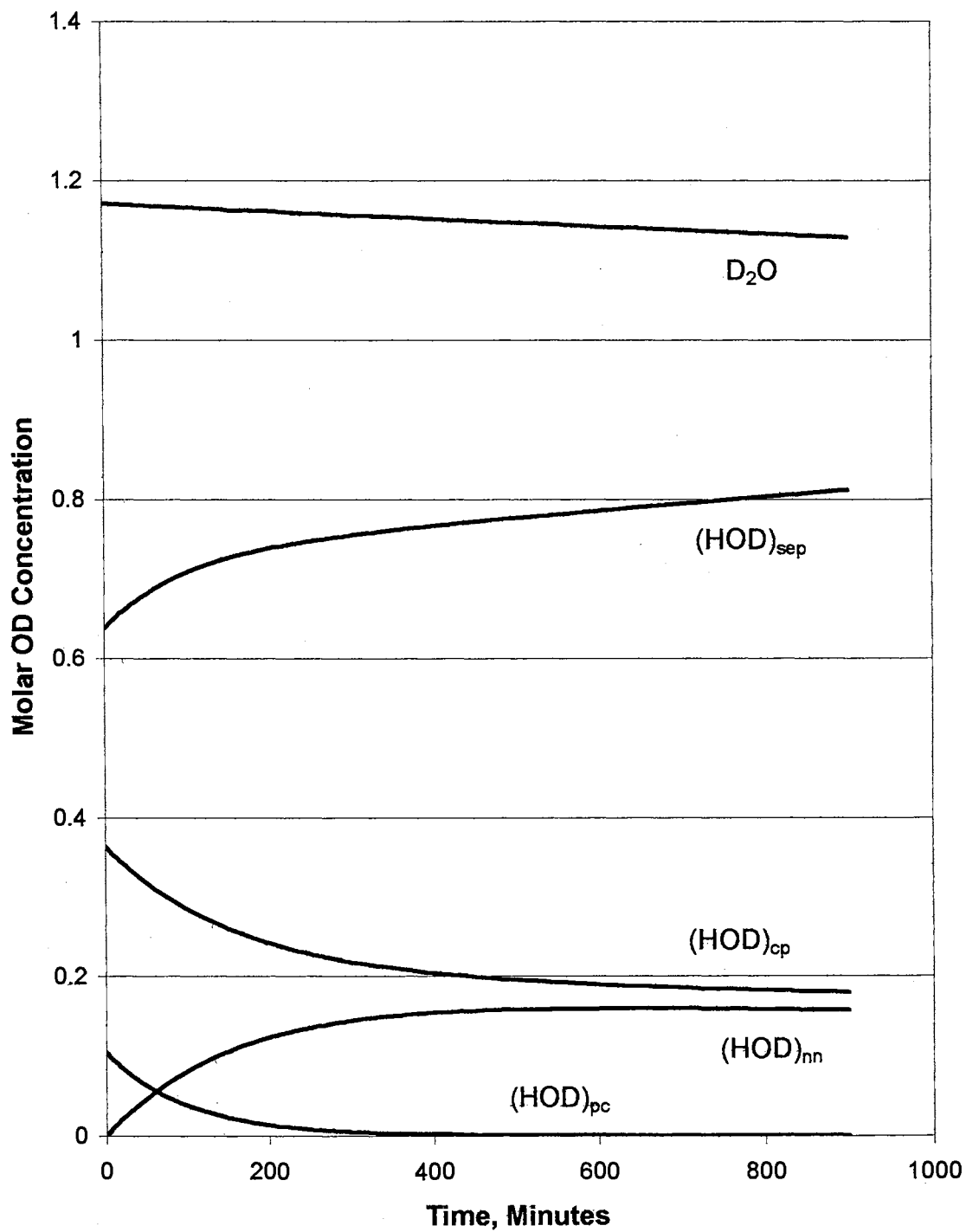


Figure 58. Calculated isotopomer concentrations from fit to experimental data for run 1 at 102 K.

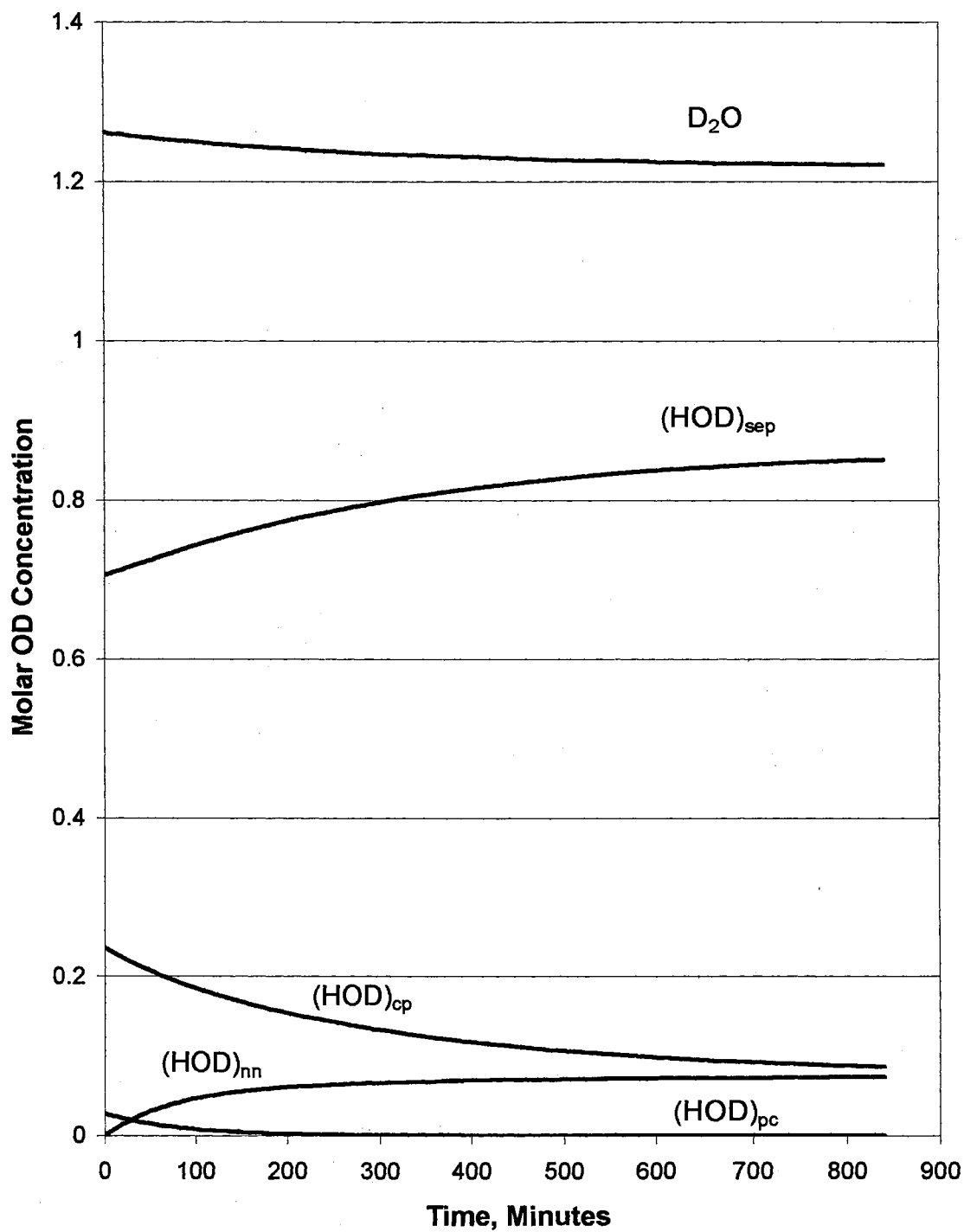


Figure 59. Calculated isotopomer concentrations from fit to experimental data for run 1 at 105 K.

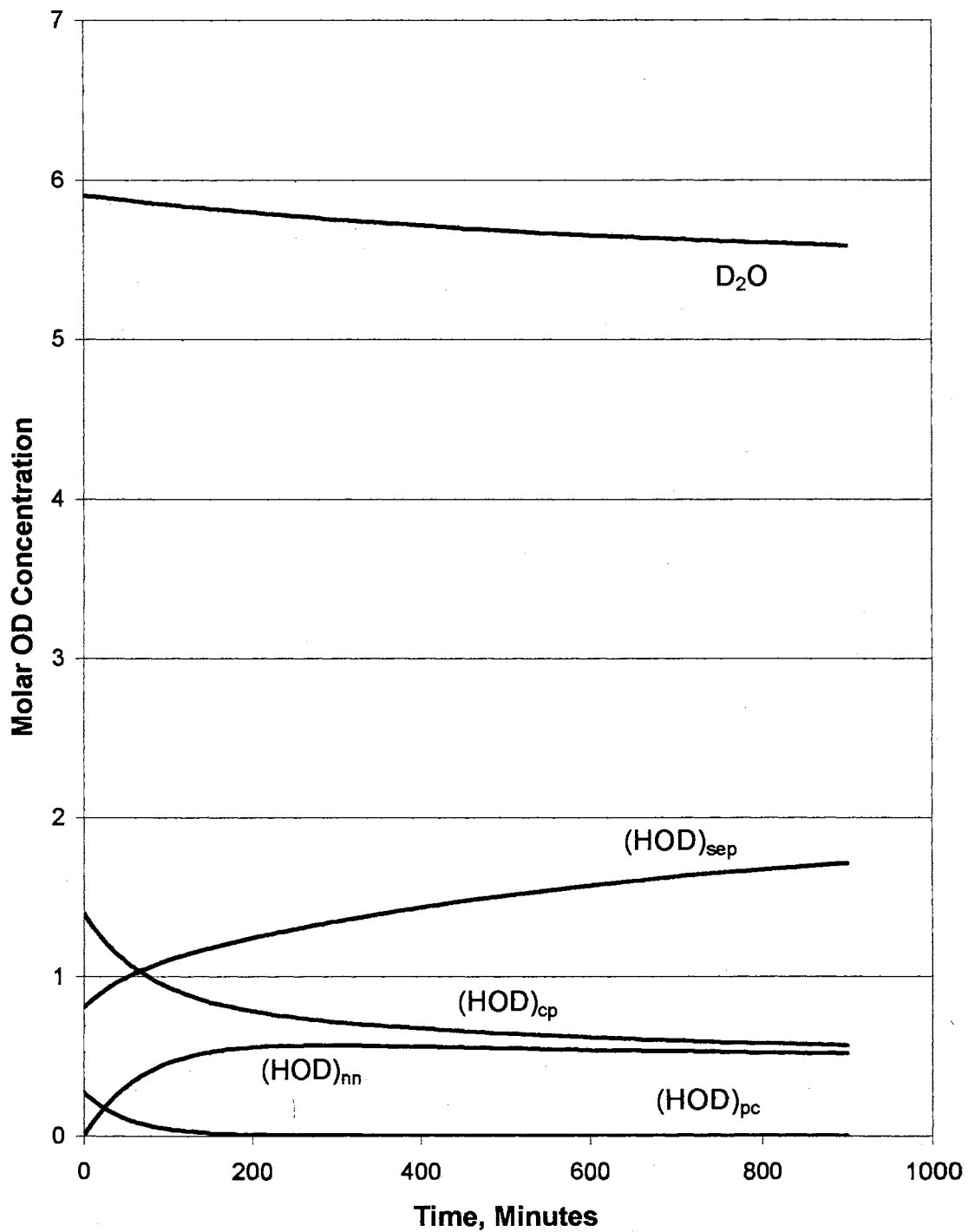


Figure 60. Calculated isotopomer concentrations from fit to experimental data for run 1 at 108 K.

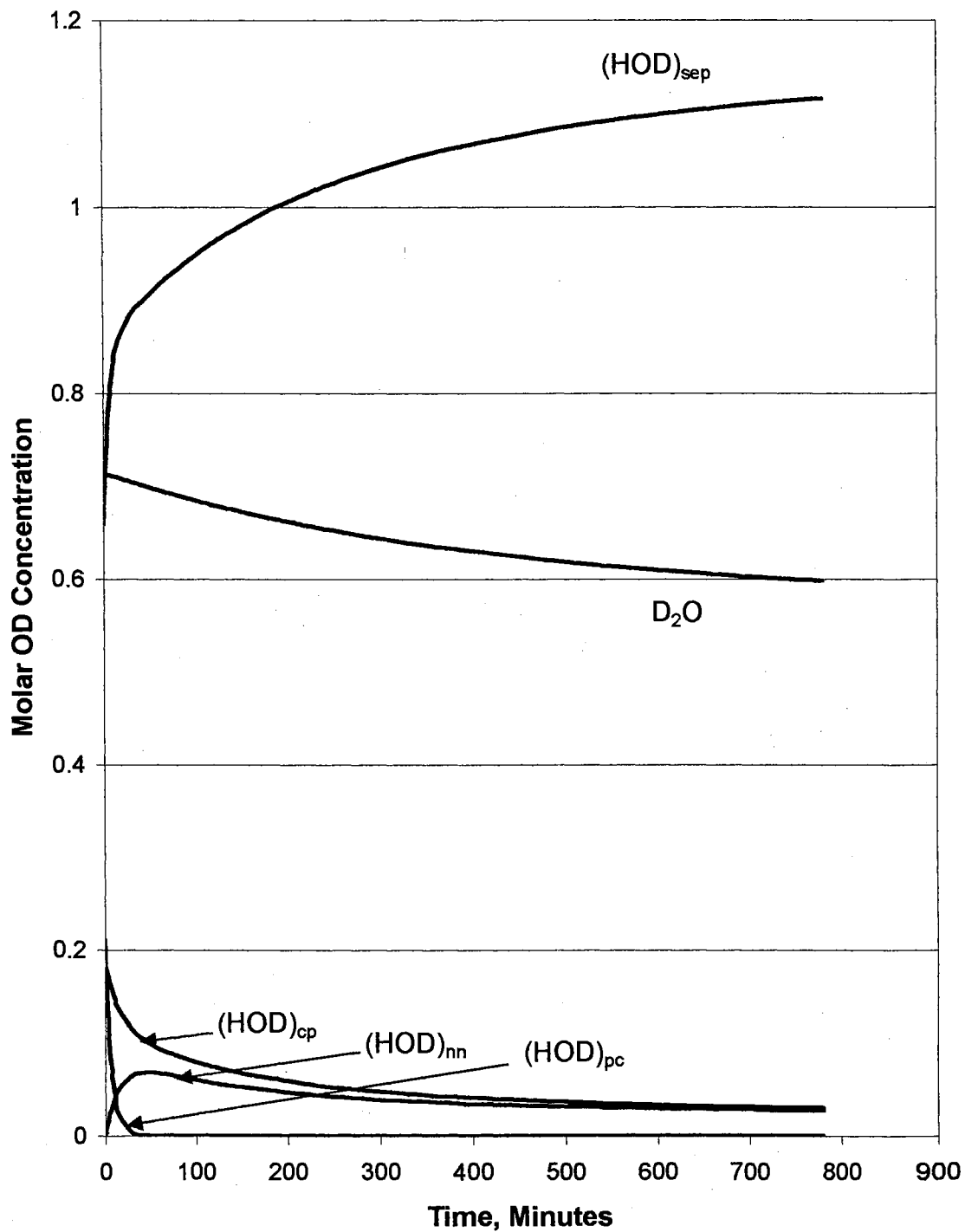


Figure 61. Calculated isotopomer concentrations from fit to experimental data for run 1 at 110 K.

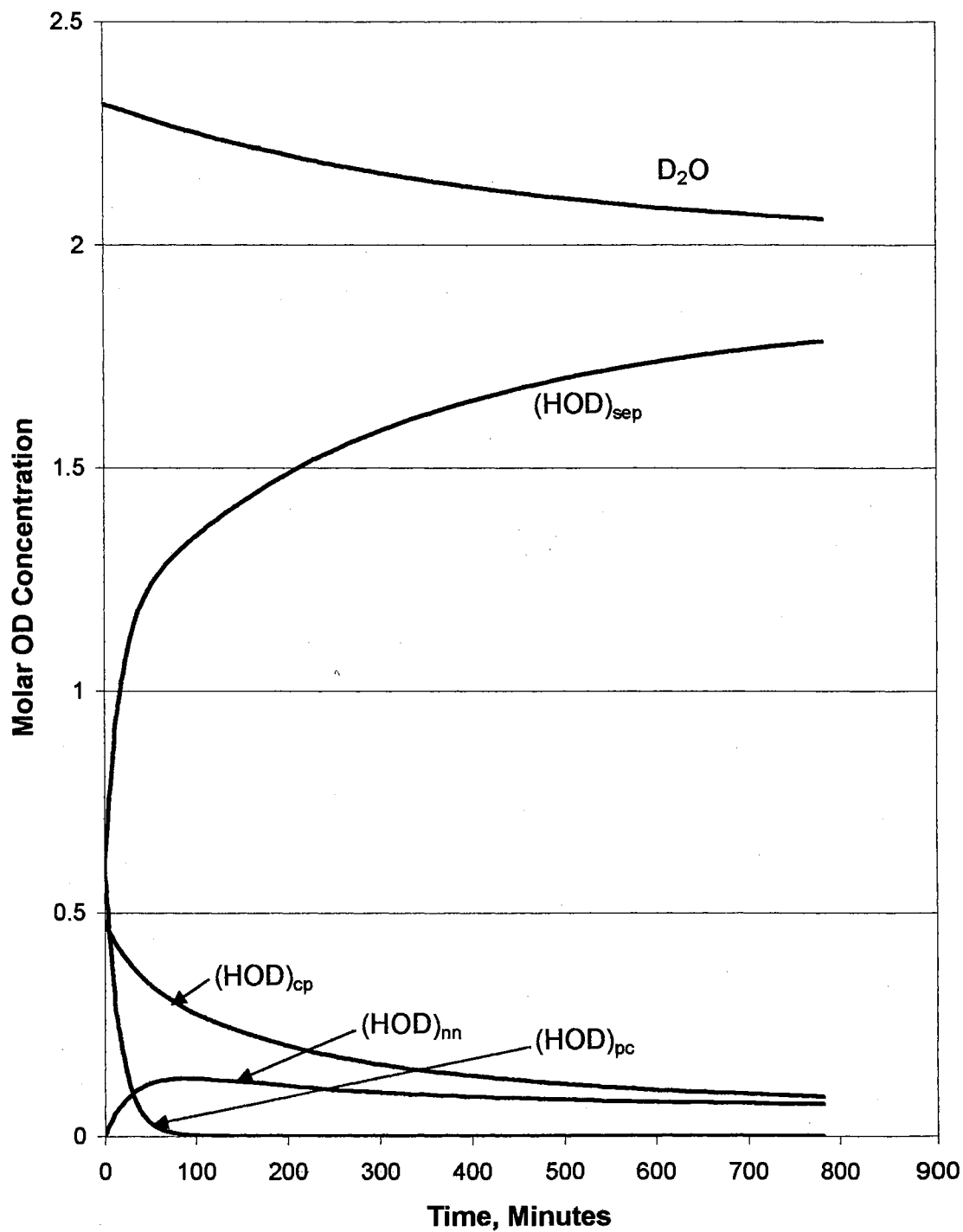


Figure 62. Calculated isotopomer concentrations from fit to experimental data for run 1 at 112 K.

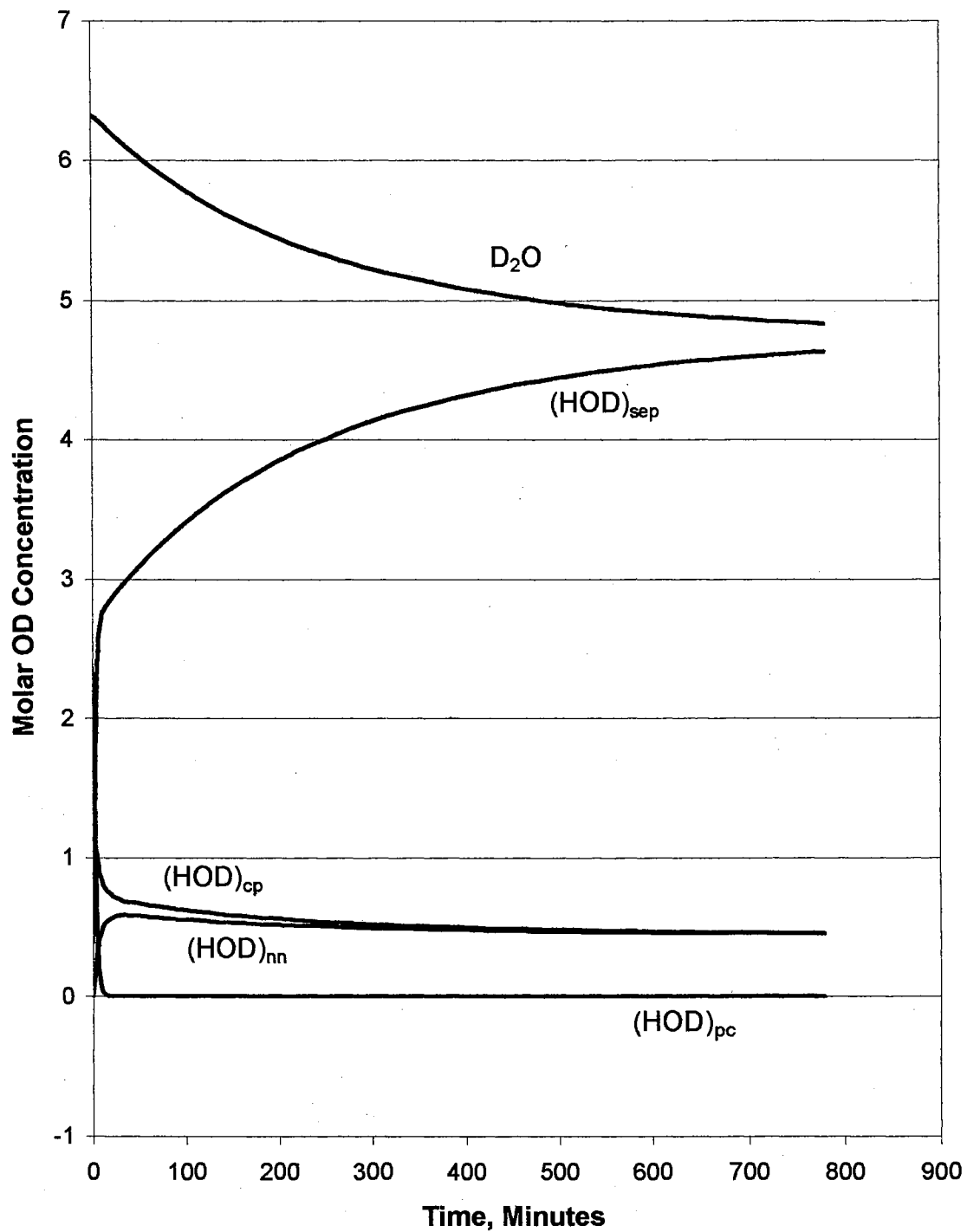


Figure 63. Calculated isotopomer concentrations from fit to experimental data for run 1 at 115 K.

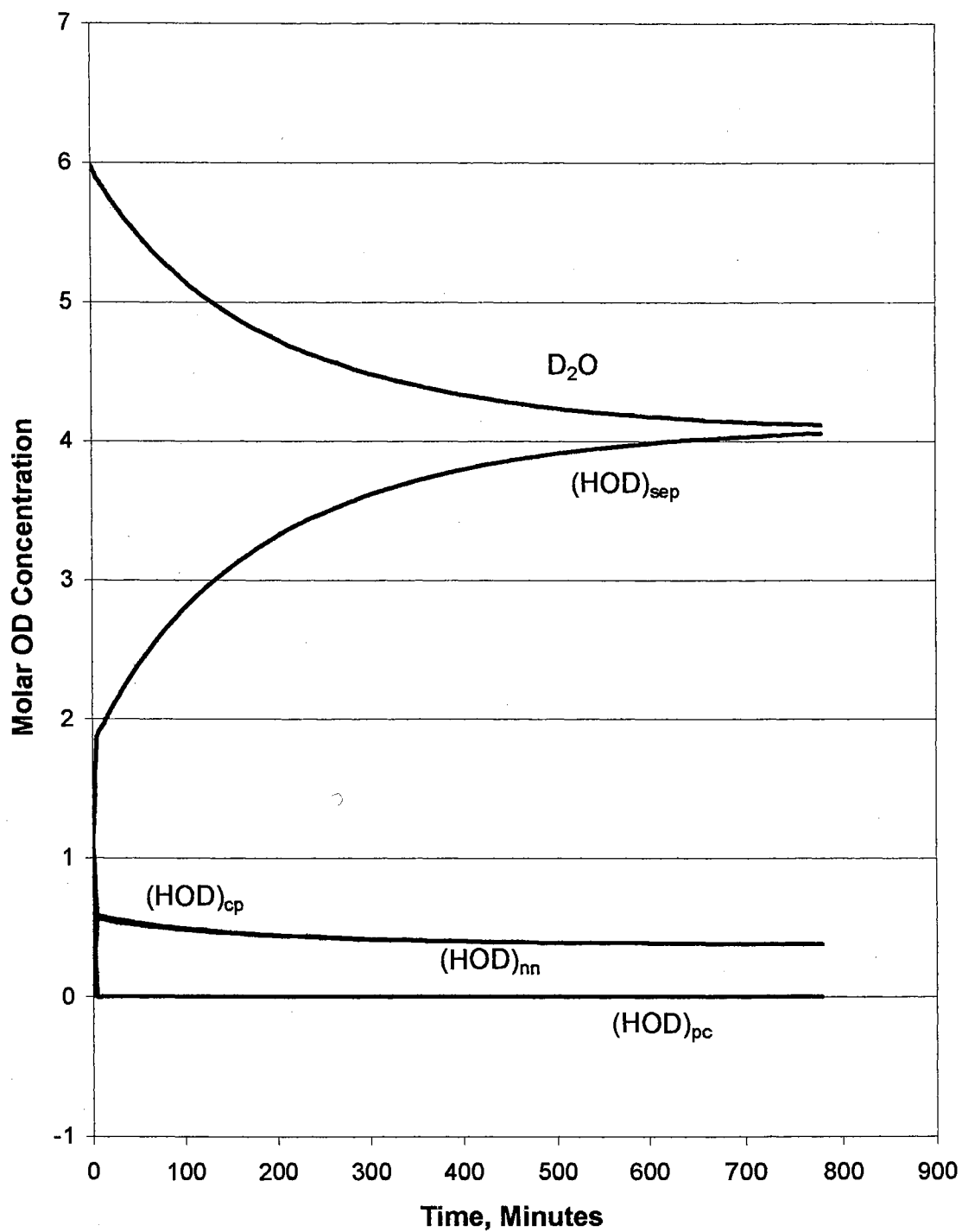


Figure 64. Calculated isotopomer concentrations from fit to experimental data for run 3 at 118 K.

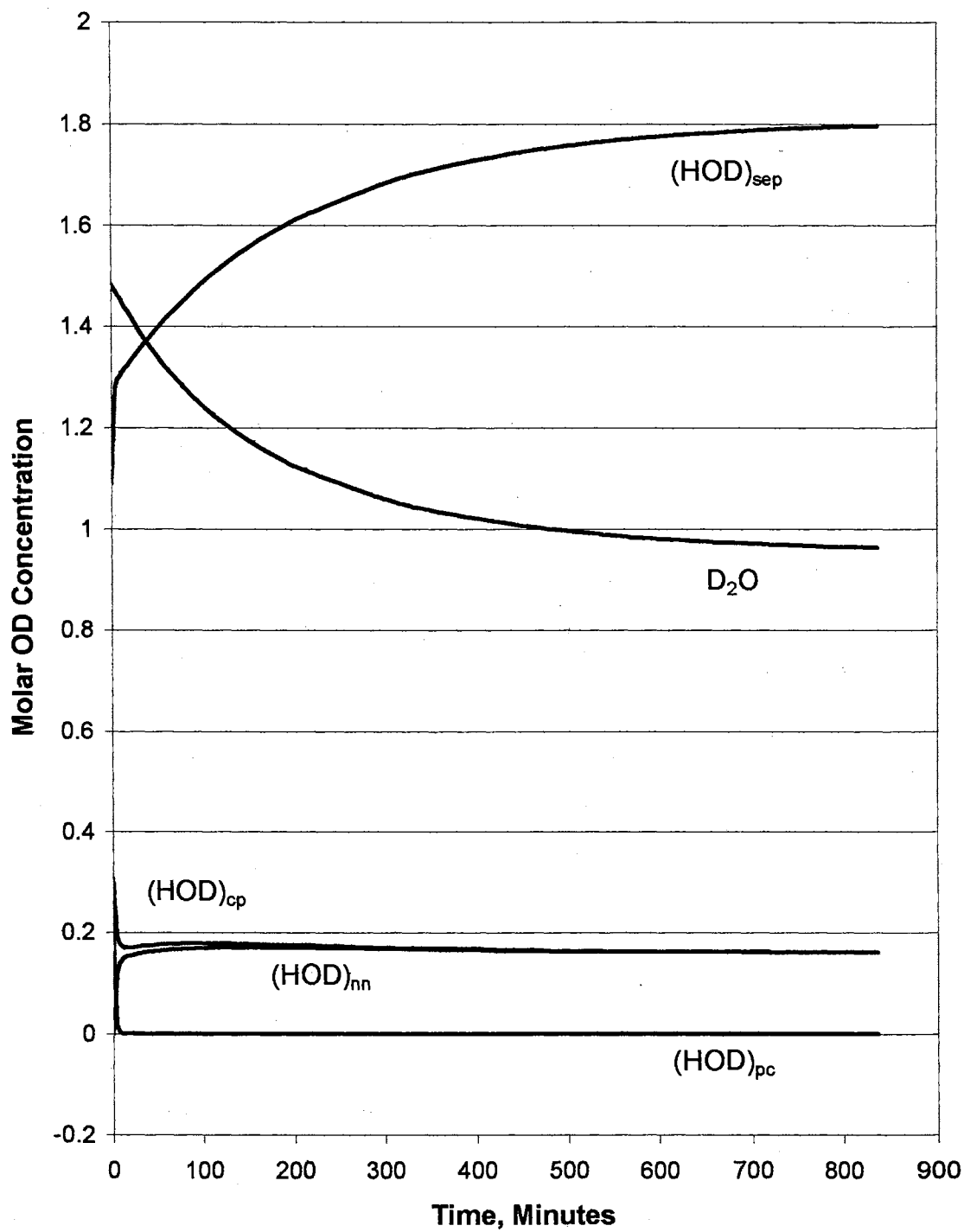


Figure 65. Calculated isotopomer concentrations from fit to experimental data for run 1 at 120 K.

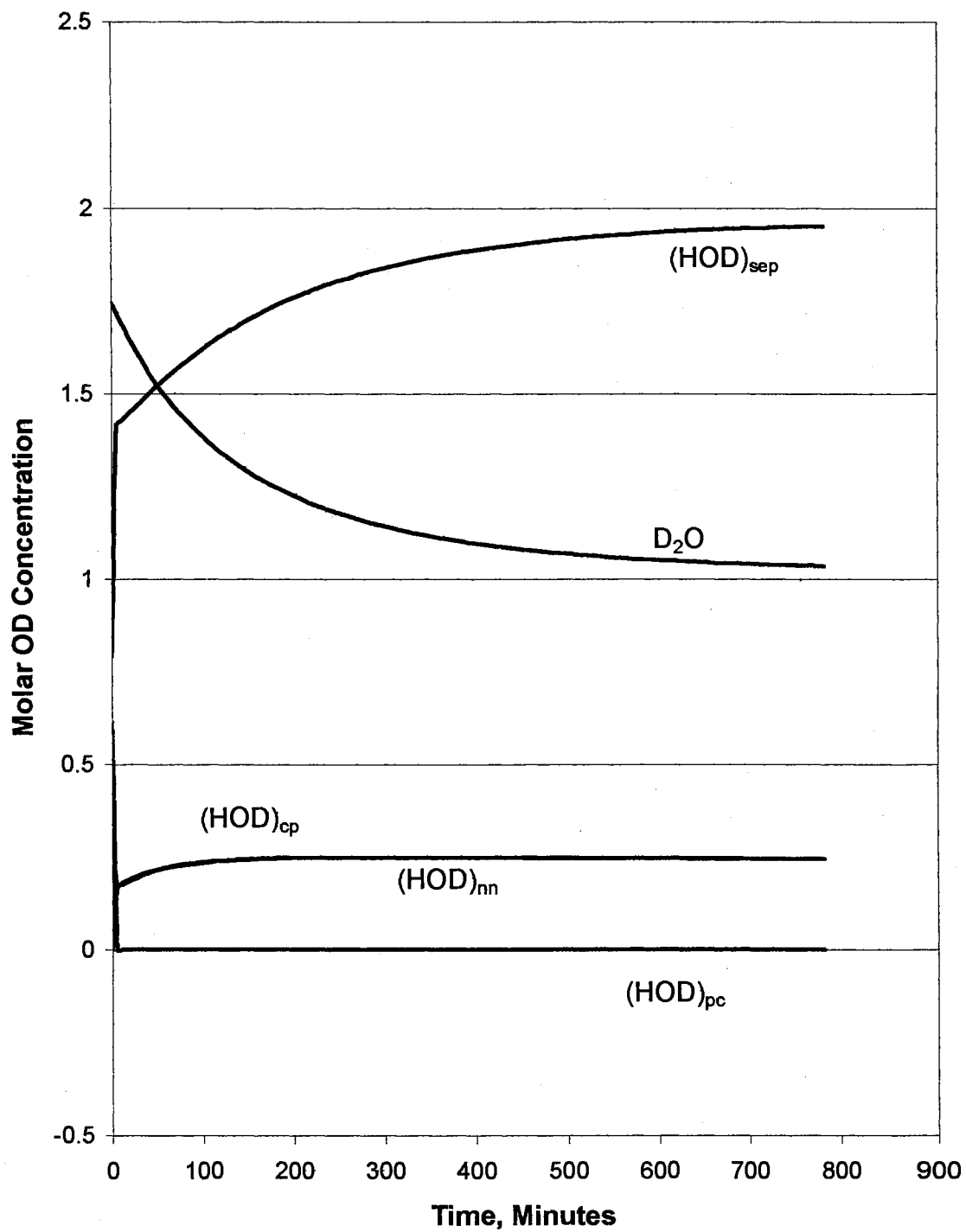


Figure 66. Calculated isotopomer concentrations from fit to experimental data for run 3 at 122 K.

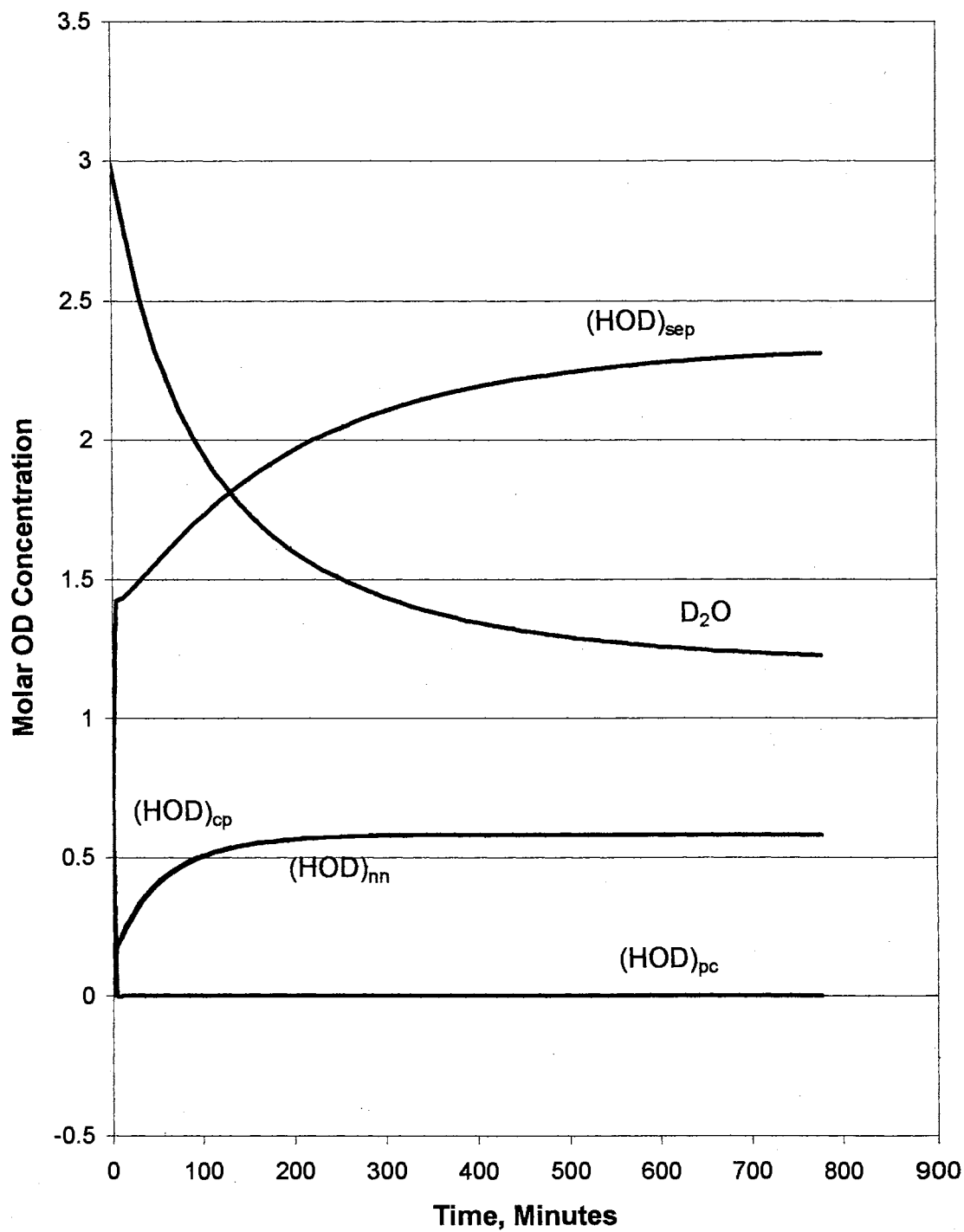


Figure 67. Calculated isotopomer concentrations from fit to experimental data for run 3 at 125 K.

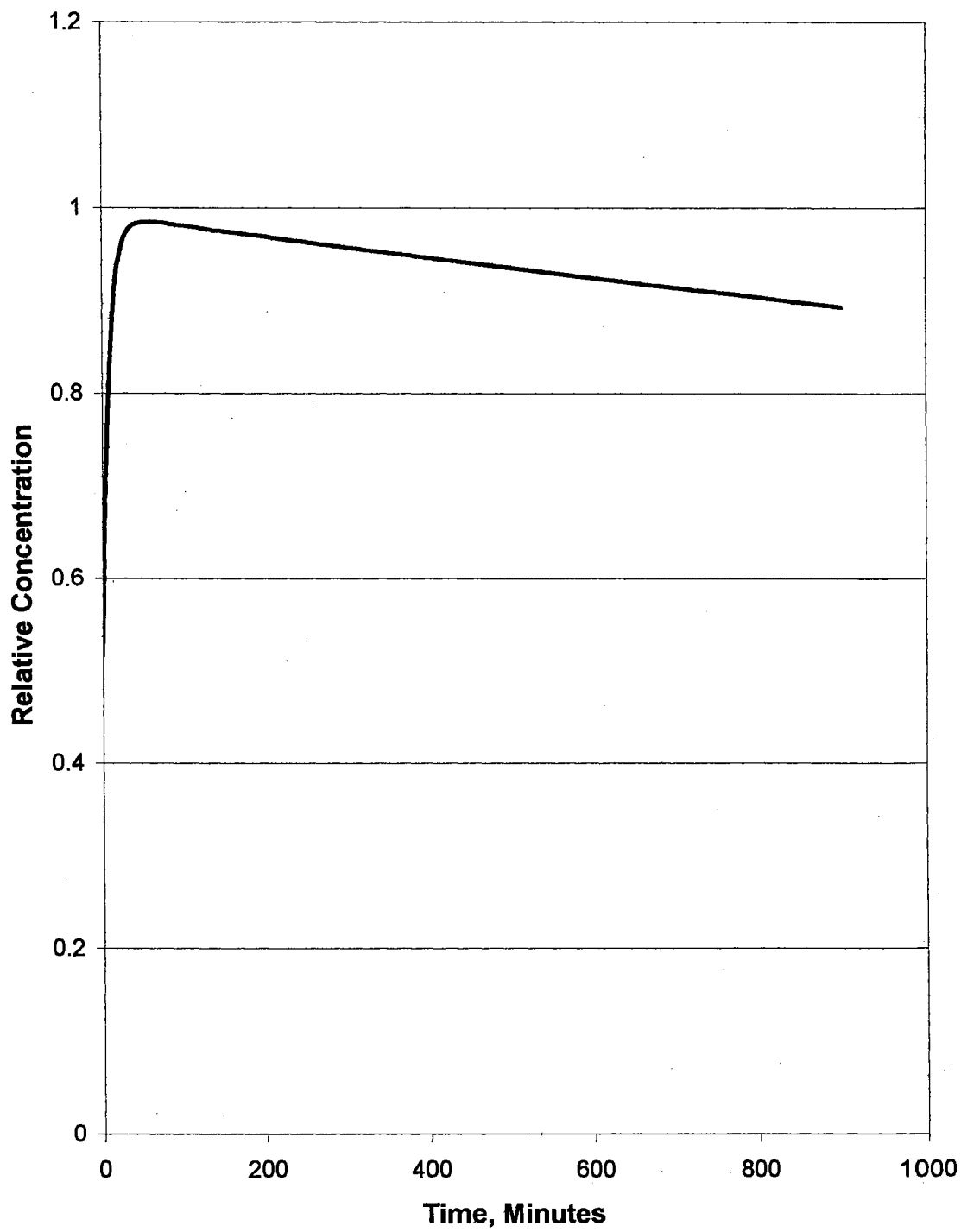


Figure 68. Estimated mobile proton concentration versus time for run 1 at 102 K.

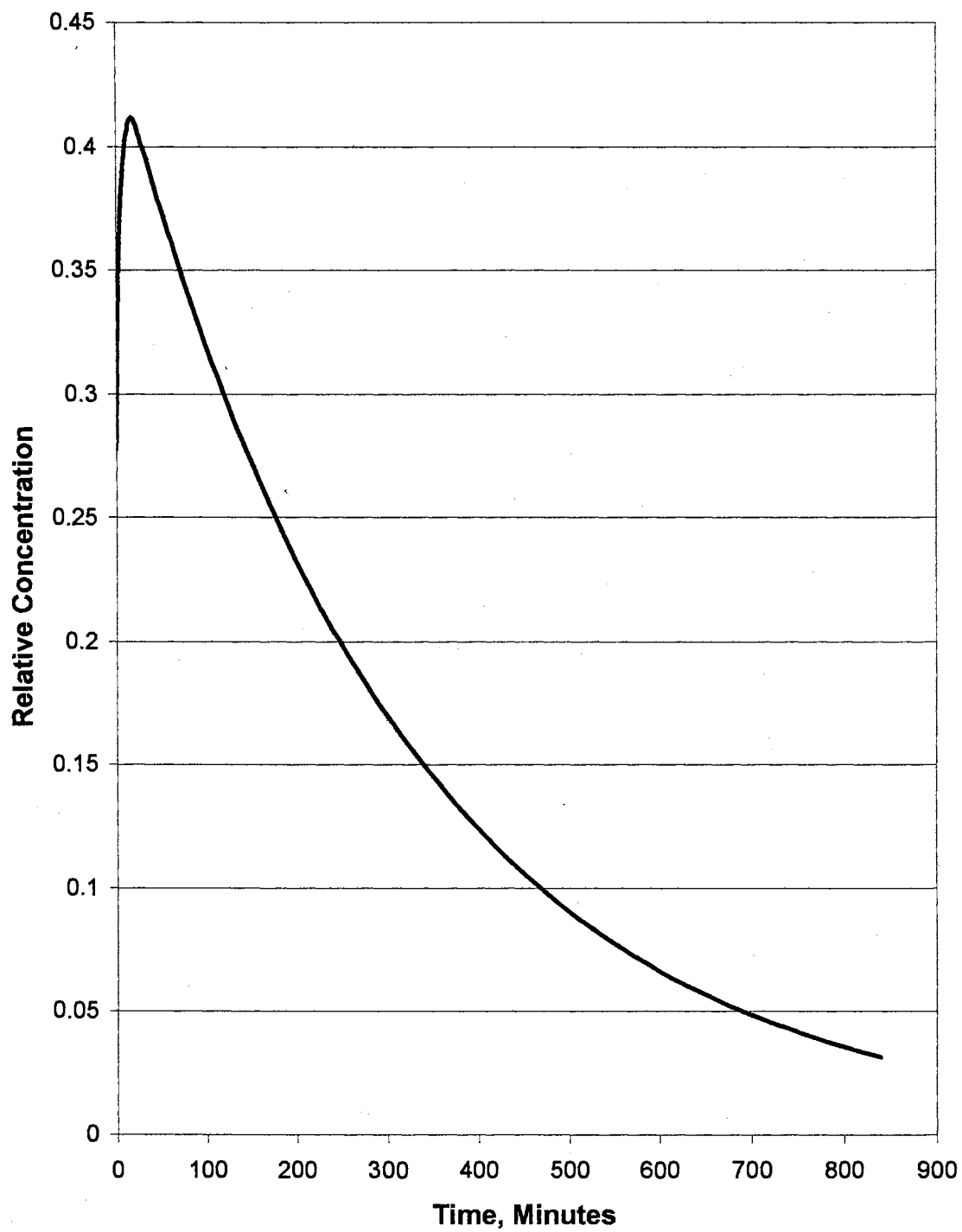


Figure 69. Estimated mobile proton concentration versus time for run 1 at 105 K.

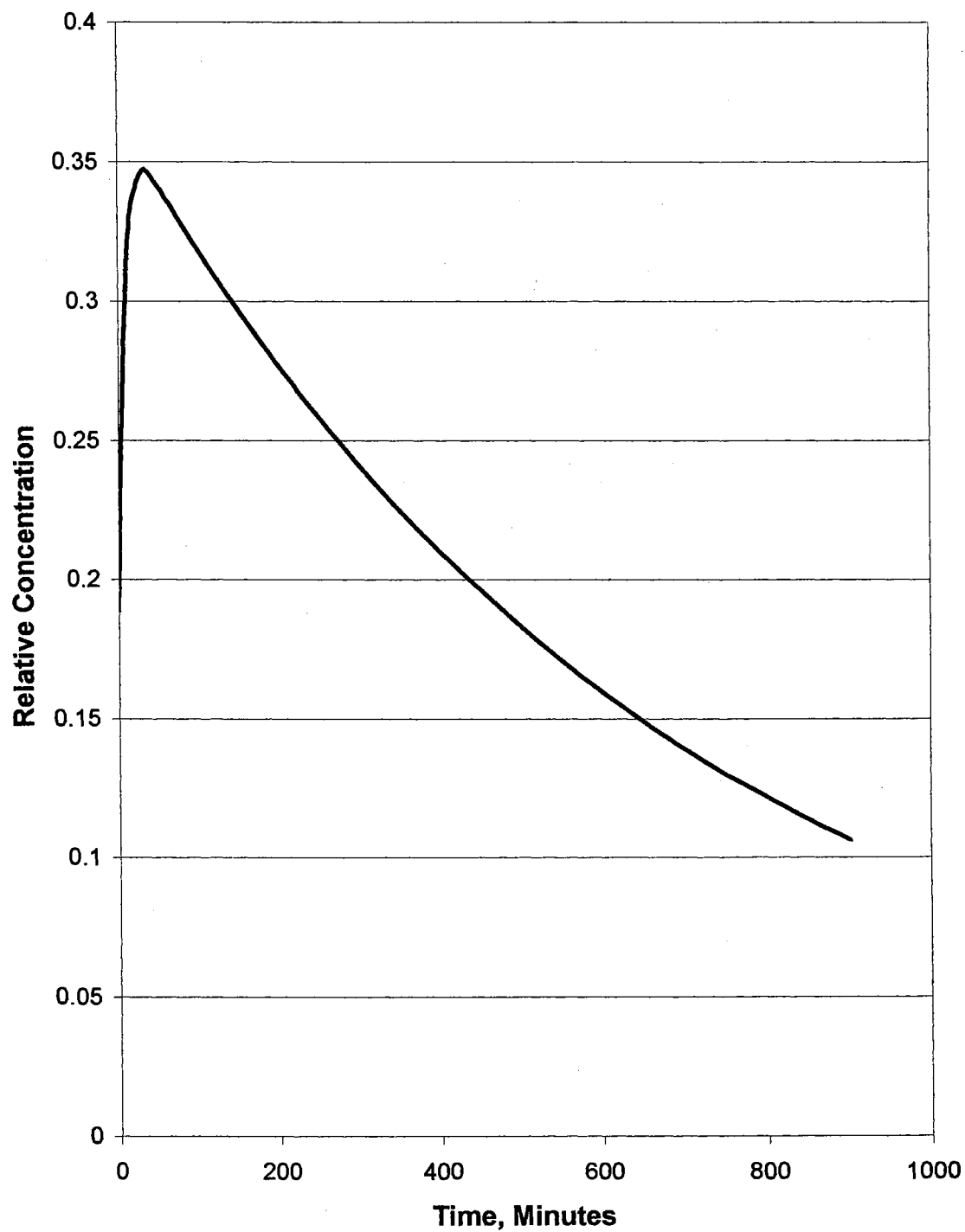


Figure 70. Estimated mobile proton concentration versus time for run 1 at 108 K.

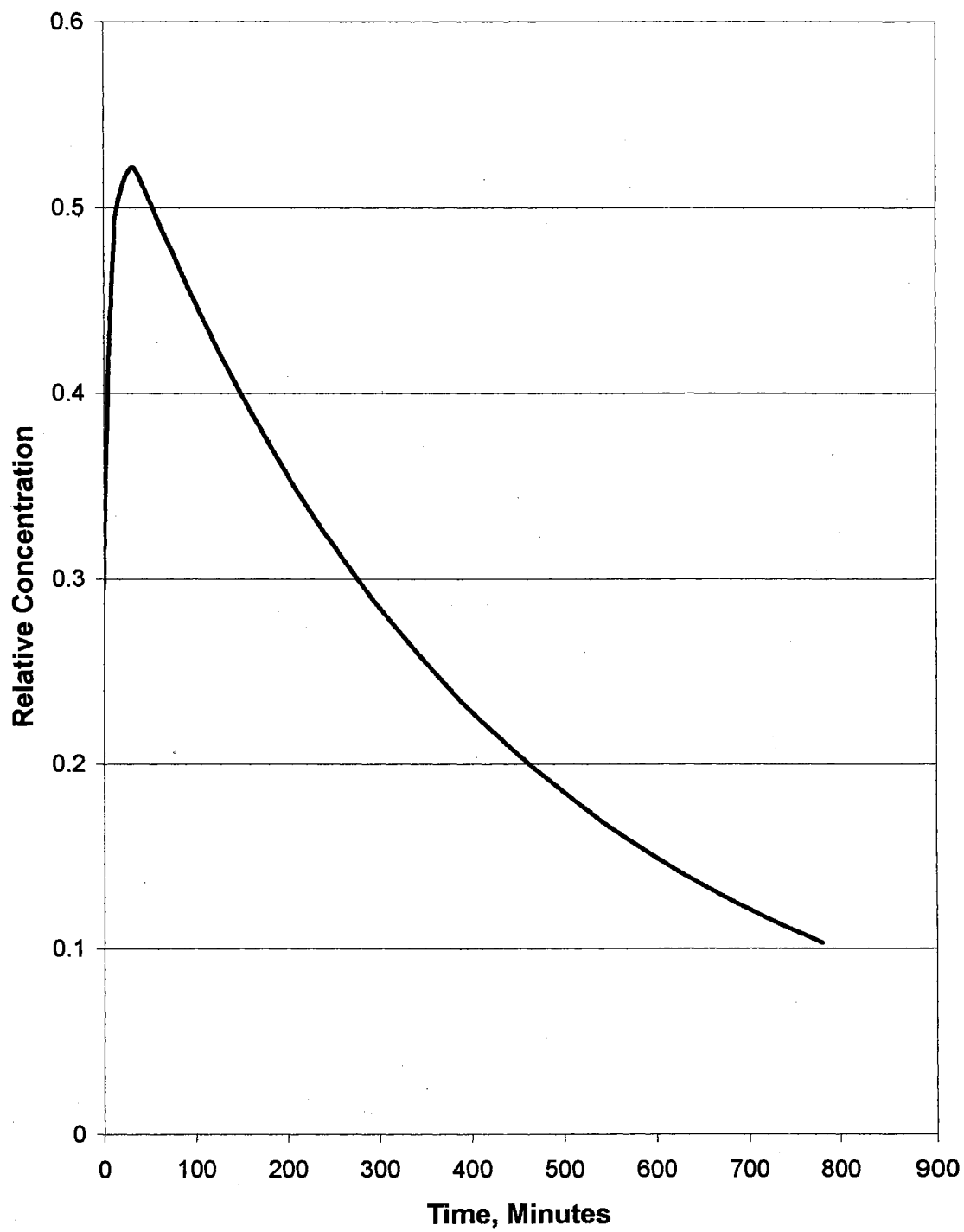


Figure 71. Estimated mobile proton concentration versus time for run 1 at 110 K.

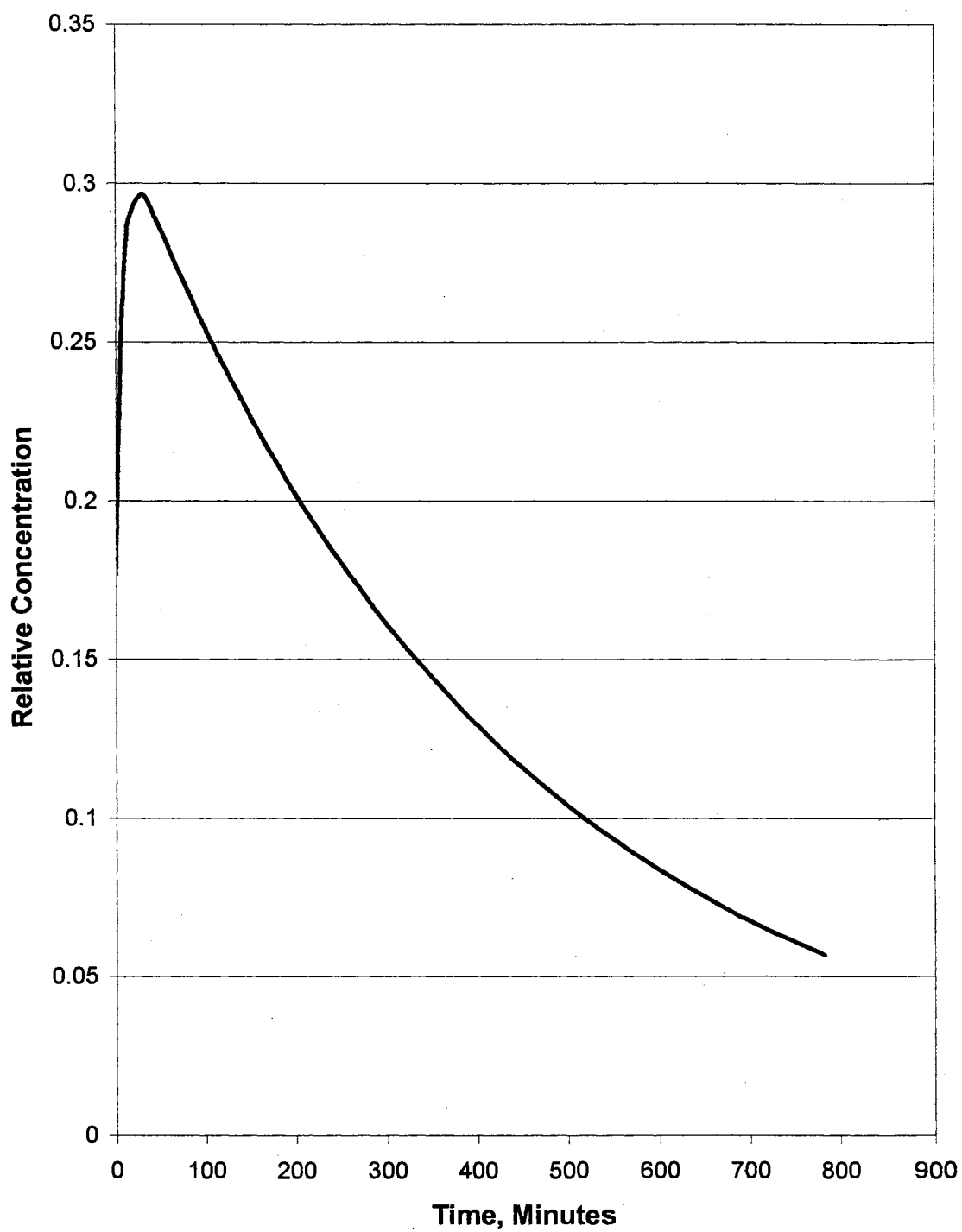


Figure 72. Estimated mobile proton concentration versus time for run 1 at 112 K.

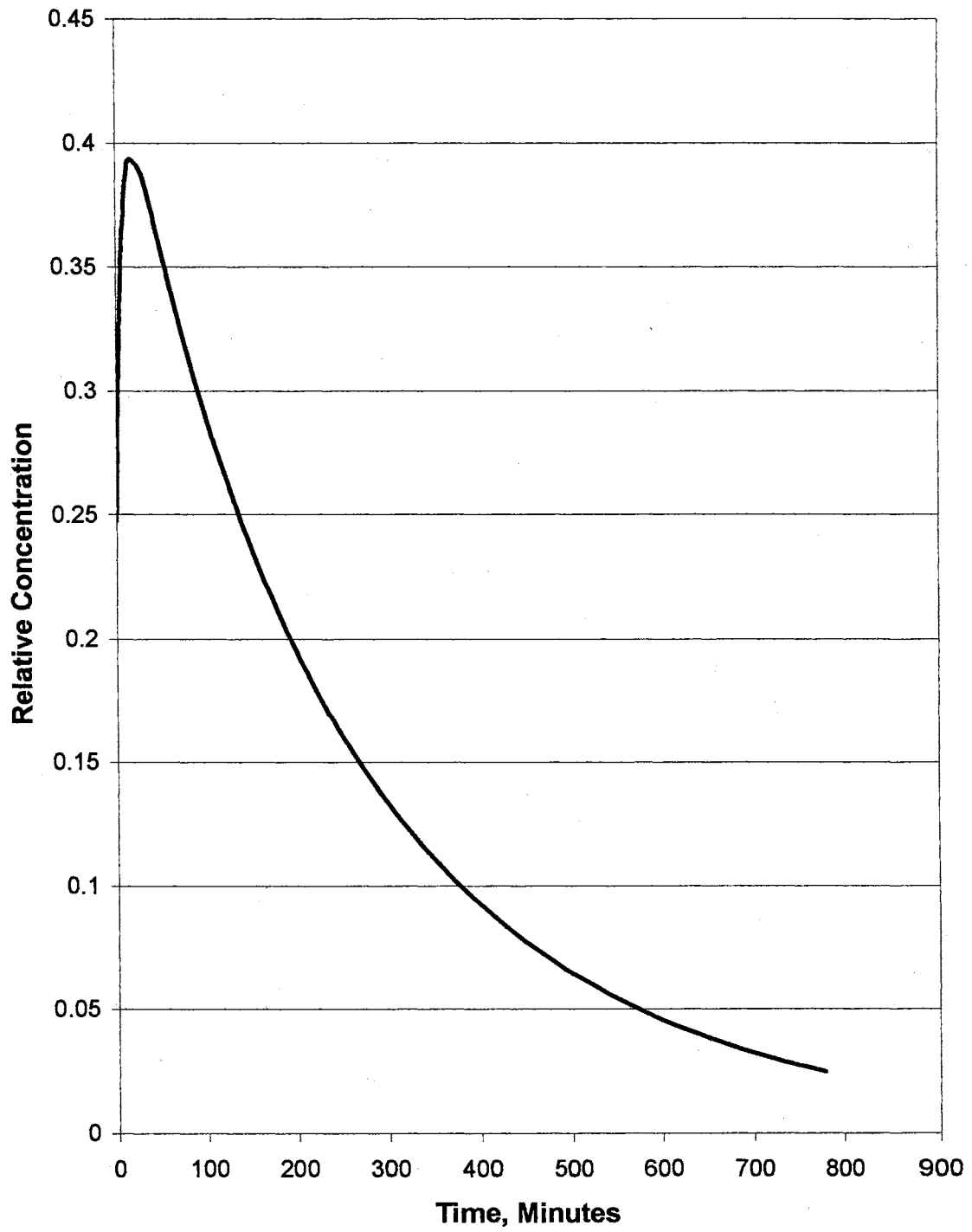


Figure 73. Estimated mobile proton concentration versus time for run 1 at 115 K.

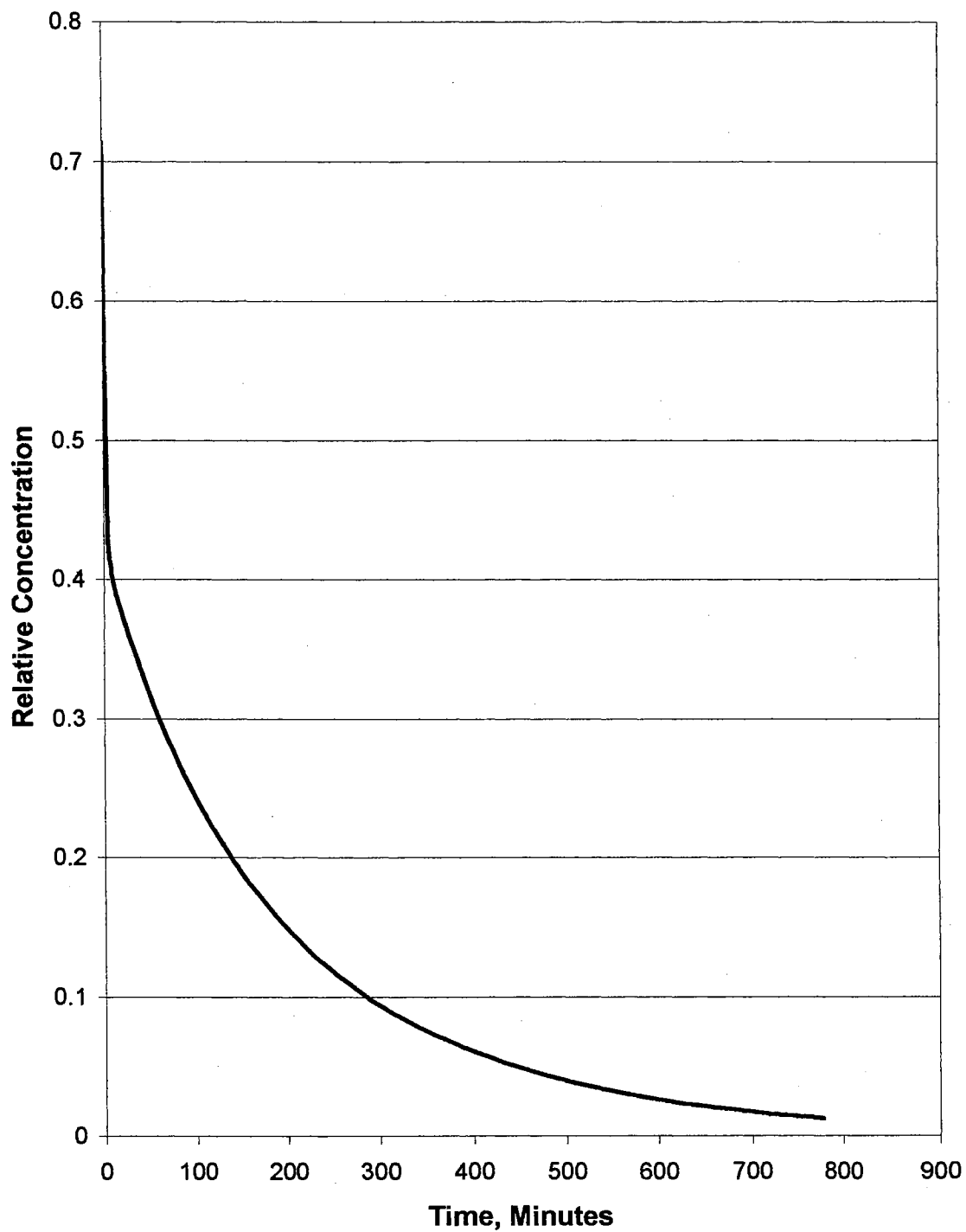


Figure 74. Estimated mobile proton concentration versus time for run 3 at 118 K.

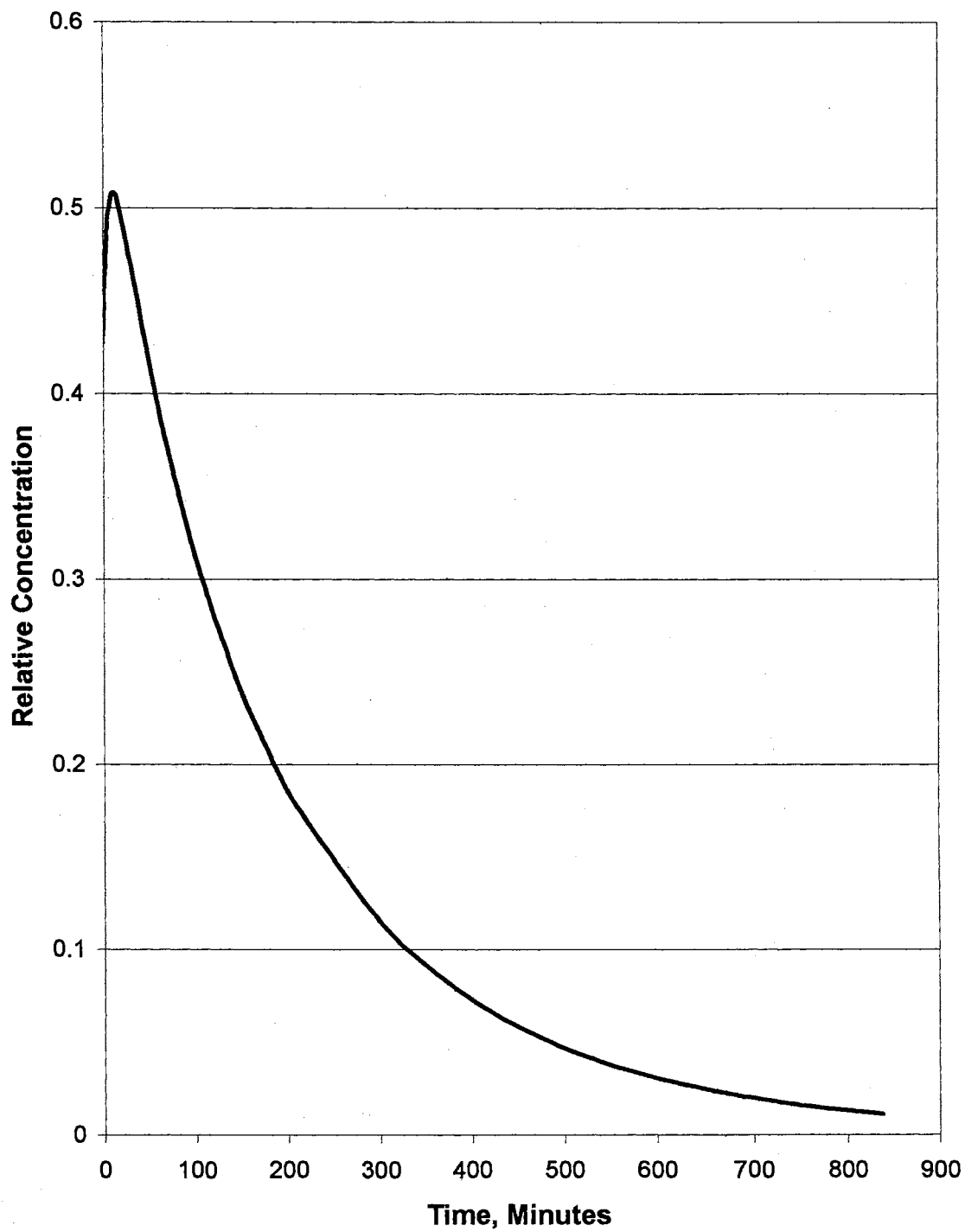


Figure 75. Estimated mobile proton concentration versus time for run 1 at 120 K.

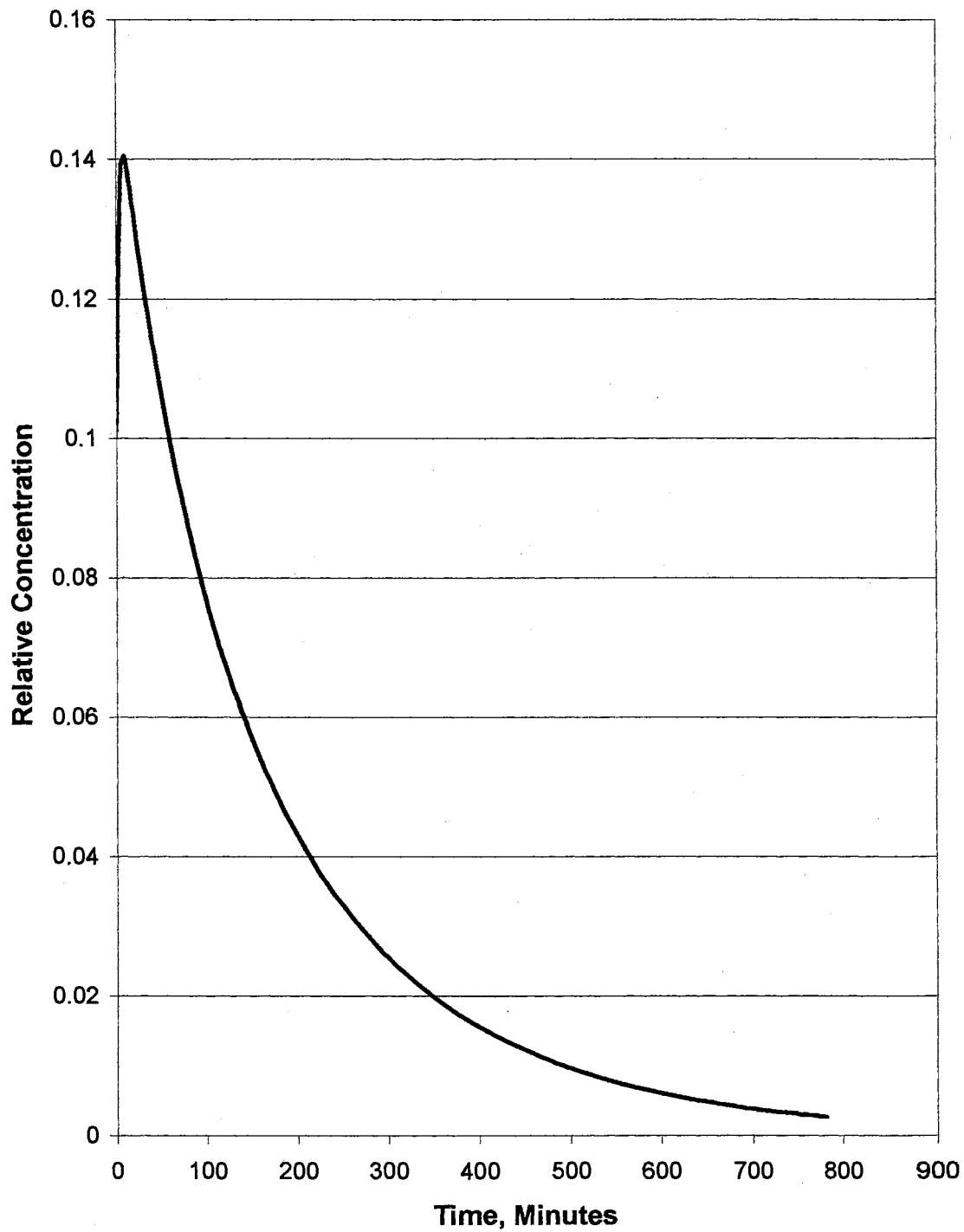


Figure 76. Estimated mobile proton concentration versus time for run 3 at 122 K.

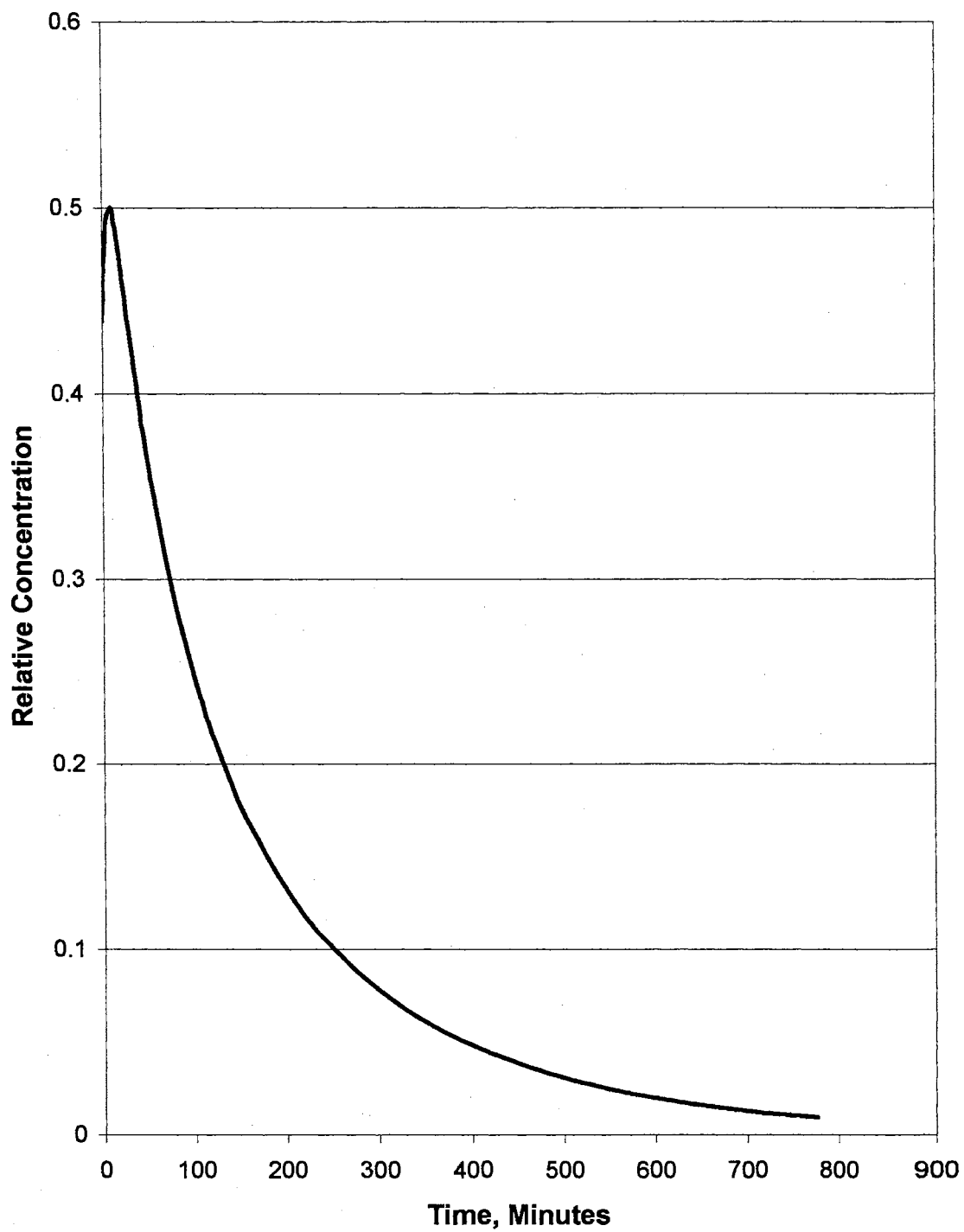


Figure 77. Estimated mobile proton concentration versus time for run 3 at 125 K.

migrate into deep traps, resulting in a decrease in the concentration of mobile protons over time. As the concentration of mobile protons decreases, the proton hopping rate will decrease as well, slowing reaction steps in the mechanism that depend on proton hopping. The primary steps in the mechanism that are affected are the conversion of D_2O to $(HOD)_{cp}$, and conversion of $(HOD)_{nn}$ to $(HOD)_{sep}$.

The steps of the mechanism that depend on L-defect mobility do not appear to experience the same reduction in rate with time. It was assumed that the mobile L-defect concentration in the samples quickly reaches equilibrium at a given temperature and remains constant over time. This situation gives rise to observation of an interesting effect. At higher temperatures, there appears to be an initial rapid decoupling of $(HOD)_{cp}$ into $(HOD)_{nn}$, presumably due to the action of mobile L-defects. However, as the proton hop step that could separate $(HOD)_{nn}$ into isolated HOD units slows with time, the concentration of $(HOD)_{nn}$ begins to increase until a pseudo-equilibrium is established between $(HOD)_{cp}$ and $(HOD)_{nn}$. Note that the rate constants for the forward and reverse reaction are the same, so as pseudo-equilibrium is reached the concentrations of $(HOD)_{cp}$ and $(HOD)_{nn}$ approach each other. This effect can be seen most dramatically by comparing Figures 58 and 67. In figure 58, the concentrations of $(HOD)_{cp}$ and $(HOD)_{nn}$ are approaching each other with time as this step approaches pseudo-equilibrium over several hours. However, in Figure 67 these concentrations approach each other very rapidly because of the enhanced L-defect mobility at 125 K relative to 102 K, and a pseudo-equilibrium is reached within minutes.

If the interpretation of the observed data is correct, it is strongly implied that in ASW near the reported glass transition temperature there is no evidence of translational

molecular diffusion. If translational diffusion were present, it is difficult to conceive how the pseudo-equilibrium between $(\text{HOD})_{\text{cp}}$ and $(\text{HOD})_{\text{nn}}$ could be reached. Diffusion of water molecules could account for conversion of $(\text{HOD})_{\text{cp}}$ directly into isolated HOD units. However, the reverse reaction is difficult to explain if translational molecular diffusion occurring. An isotopic scrambling mechanism relying on proton hopping and molecular diffusion should cause the concentration of D_2O and $(\text{HOD})_{\text{cp}}$ to decrease monotonically with time, eventually producing a more or less random distribution of isolated HOD molecules throughout the ice lattice. At the concentrations of isotopomers present in these samples, most isotopomer molecules would be separated by one or more water molecule if they were randomly dispersed by the action of diffusion. Hence, it would be difficult to explain the observed increase in concentration of $(\text{HOD})_{\text{cp}}$ that occurs with time, especially for the higher temperature samples. For this increase to occur, it would require occupation of a significant number of lattice sites in the ice by HOD molecules, and that the adjacent molecules be oriented so that the molecules are vibrationally coupled.

The data presented here does not appear to be consistent with a mechanism in which ASW passes through a diffusing liquid phase before crystallizing. If translational diffusion of water molecules in ASW near the proposed glass transition temperature occurred on a similar time scale as orientational defect motion, conversion of $(\text{HOD})_{\text{nn}}$ to $(\text{HOD})_{\text{is}}$ and $(\text{HOD})_{\text{sep}}$ would occur at a rate similar to the conversion of $(\text{HOD})_{\text{cp}}$ to $(\text{HOD})_{\text{nn}}$. If this were occurring, $(\text{HOD})_{\text{nn}}$ would be quickly converted to $(\text{HOD})_{\text{sep}}$, greatly slowing the rate of conversion of $(\text{HOD})_{\text{nn}}$ to $(\text{HOD})_{\text{cp}}$. Again, this would make it extremely unlikely that the concentration of $(\text{HOD})_{\text{cp}}$ would increase over time.

Hence, we conclude that the rate of translational molecular diffusion near the proposed glass transition temperature is not competitive with the orientational diffusion rate (90). This is in contrast to the rapid translational diffusion rate in ASW reported by Kay that was used to argue the presence of a viscous, but liquid-like phase prior to crystallization of samples (89). If the experimental data for isotopic scrambling with time are correct, the data presented here is consistent with the proposed model based on proton hopping and Bjerrum orientational defect activity.

An attempt to study the isotopic exchange at higher temperatures was undertaken, but at temperatures slightly above 125 K the samples began to slowly crystallize. It may not be coincidental that the onset of rapid orientational defect activity and the rate of crystallization of ASW to cubic ice both occur in the same temperature range.

Furthermore, it is interesting that the rate of orientational defect activity in ice I at 140 K is similar to the rate observed for ASW in this study (87). Orientational defect motion is thought to connect numerous nearly degenerate proton configurations at the "glass transition" of ice I and the clathrate hydrates (121, 122). It could be argued that the origin of the endotherms observed upon heating ASW that have been reported as glass transitions (81, 124) may be due to relaxation of the large number of nearly degenerate proton configurations into a crystalline structure, and that this is facilitated by the onset of rapid orientational defect activity. This would preclude the direct observation of the glass transition, which would occur at a higher temperature. More investigation into the glass transition of water is warranted, as many questions still remain unanswered (123).

The rate constants for proton hopping and L-defect activity were determined. An Arrhenius plot of the natural logarithm of the rate constants as a function of the inverse of

the absolute temperature of the sample was prepared for both the proton hopping and L-defect rate constants (Figures 78 and 79). The slope of the best-fit line to this data was then used to estimate the activation energy for defect mobility. The proton hopping activation energy was 1.61 kcal/mol, and the activation energy for L-defects was found to be 6.8 kcal/mol.

The experimentally determined value for the activation energy for proton hopping in amorphous ice is surprisingly low. Amorphous ice contains a range of shallow trap configurations, and naphtholate ions that are generated during the photolysis of 2-naphthol are deep traps. Mobile protons that encounter a naphtholate ion will likely recombine, annihilating the mobile proton. In addition, the incorporation of 2-naphthol into the lattice generates defects because the hydrogen bond network in the vicinity of naphthol molecules is disrupted. Hence, it is difficult to ascertain with any certainty exactly how the mobile proton concentration is attenuated in these samples. Likewise, these complexities make it difficult to comment with any degree of certainty on the magnitude of the activation energy for proton mobility since so many poorly defined processes may be contributing to the experimentally determined value.

The value of the activation energy for L-defects is comparable to that of the mobilization of pre-existing L-defects. This may be due to the fact that amorphous ice is rich in L-defects relative to other phases of ice. The corresponding value for cubic ice is 12.8 kcal/mol. Because cubic ice is much more ordered than amorphous ice, the concentration of pre-existing L-defects would be low. Hence, L-defect activity in cubic ice requires energy for the formation of the L-defect, and energy to mobilize the defect. In the case of

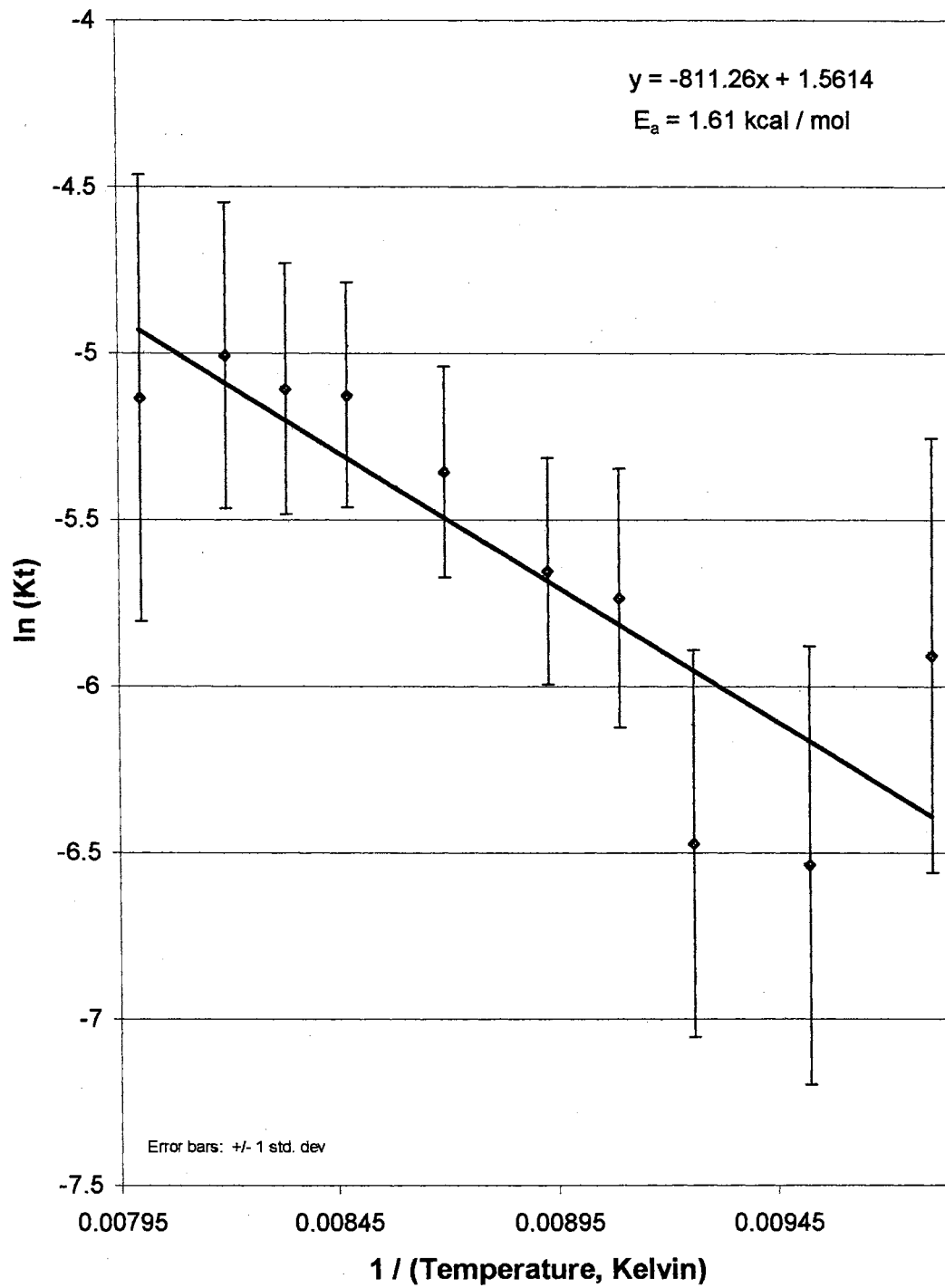
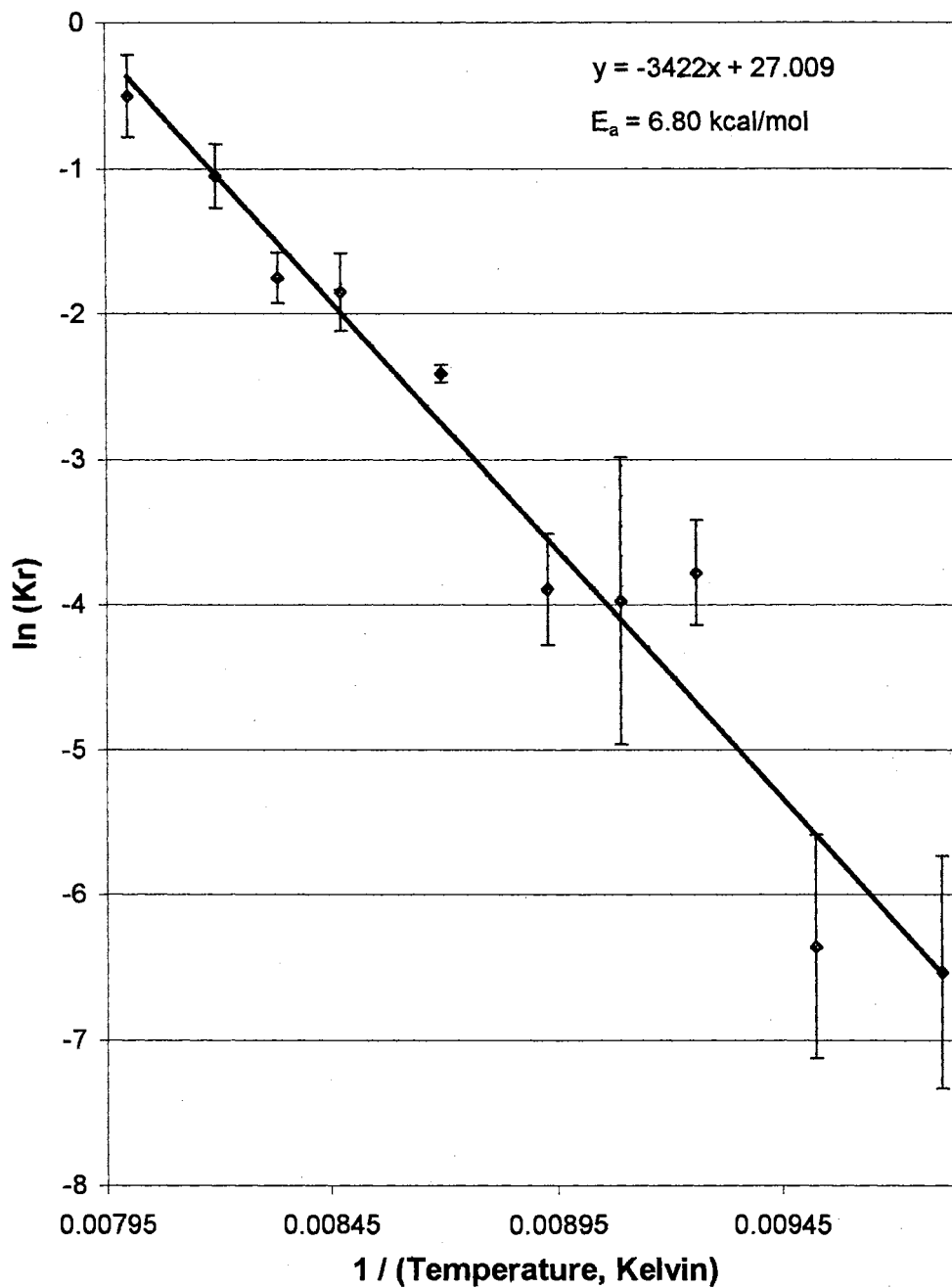


Figure 78. Arrhenius plot for proton hopping reactions.



79. Arrhenius plot for L-defect activity.

amorphous ice, there are likely more pre-existing defects that only require energy for activation to become mobile.

Conclusions and Summary

In this study we were able to demonstrate that isotopic scrambling in vapor-deposited proton-enriched samples of amorphous solid water appears to occur by a mechanism very similar to that previously reported for crystalline ices. The model is based on proton mobility via two mechanisms: proton hopping and Bjerrum orientational defect mobility. The onset of the proton hop step and orientational (L-defect) mobility occurs at temperatures in excess of 100 K. Pure amorphous ice exhibits a very low mobile proton concentration, so it was necessary to enrich the samples with mobile protons by photolysis of 2-naphthol included in the ice matrix at low concentrations. Upon photolysis, the protons liberated migrated a short distance through the ice lattice converting D_2O into vibrationally coupled HOD units before finally becoming trapped. The low mobile proton concentration in pure ASW is presumably due to an abundance of shallow and deep proton traps in ASW. Upon heating proton-enriched samples, protons generated during photolysis were thermally liberated from shallow traps, but quickly recombined with deep traps. Hence, the mobile proton concentration fell with time, and a corresponding decrease in the rates of isotopic scrambling steps relying on proton hopping was observed. At temperatures above 112 to 115 K, the accelerating rate of L-defect activity combined with a low mobile proton concentration were sufficient to cause a pseudo-equilibrium to be established between coupled HOD units and nearest neighbor HOD units, a reaction that is facilitated by mobile orientational defects. The fact that this

pseudo equilibrium was established, and that the concentration of coupled HOD increased with time is cited as evidence that translational molecular diffusion was absent in ASW at temperatures near 130 K. It is suggested that the results are consistent with ASW undergoing a structural relaxation facilitated by orientational defect mobility that results in crystallization of ASW to cubic ice before a true glass transition occurs. This position is weakly supported by the observation that amorphous ice converts to cubic ice on a laboratory time scale at temperatures above which orientational defect mobility is significant. More investigation into the glass transition in water is needed, as many issues remain unresolved.

REFERENCES

1. Hobbs, P. V., Ice Physics, Clarendon Press, Oxford (1974).
2. Bountis, T. ed., Proton Transfer in Hydrogen-Bonded Systems, NATO ASI Series B: Physics Vol. 291, Plenum Press, New York (1992).
3. Denchner, N. A., Buldt, G., Heberle, J., Holtje, H., and Holtje, M., in Proton Transfer in Hydrogen-Bonded Systems, Bountis, T. ed., NATO ASI Series B: Physics Vol. 291, Plenum Press, New York (1992).
4. Heberle, J., and Denchner, N. A., in Proton Transfer in Hydrogen-Bonded Systems, Bountis, T. ed., NATO ASI Series B: Physics Vol. 291, Plenum Press, New York (1992).
5. Nagle, J. F., and Tristram-Nagle, S., *J. Membrane Biol.*, 74, 1 (1983).
6. Chowdry, U., Barkley, J. R., English, A. D., and Sleight, A. W., *Mater. Res. Bull.*, 17, 917 (1982).
7. Gross, G. W., *J. Geophys. Res.*, 87, C9, 7170 (1982).
8. Tajima, Y., Matsuo, T., and Suga, H., *Nature*, 299, 810 (1982).
9. Matsuo, T., Tajima, Y., and Suga, H., *J. Phys. Chem. Solids*, 47, 165, (1986).
10. Wooldridge, P. J., Richardson, H. H., and Devlin, J. P., *J. Chem. Phys.*, 87, 4126 (1987).
11. Murase, N., Gonda, K., and Watanabe, T., *J. Phys. Chem.*, 90, 5420 (1986).
12. Dharmawardhana, P. B., Parrish, W. R., and Sloan, E. D., *Ind. Eng. Chem. Fundam.*, 19, No. 4, 411 (1980).
13. Collier, W. B., Ritzhaupt, G., and Devlin, J. P., *J. Phys. Chem.*, 88, 363 (1984).
14. Wooldridge, P. J., and Devlin, J. P., *J. Chem. Phys.*, 88, 3086 (1988).
15. Devlin, J. P., Wooldridge, P. J., and Ritzhaupt, G., *J. Chem. Phys.*, 84, 6095 (1986).

16. Devlin, J. P., and Richardson, H. H., *J. Chem. Phys.*, 81, 3250 (1984).
17. Richardson, H. H., Wooldridge, P. J., and Devlin, J. P., *J. Phys. Chem.*, 89, 3552 (1985).
18. Scheiner, S., in Proton Transfer in Hydrogen-Bonded Systems, Bountis, T. ed., NATO ASI Series B: Physics Vol. 291, Plenum Press, New York (1992).
19. Mayer, Erwin, and Pletzer, Rudolf, *Nature*, 319, 298 (1986).
20. Kouchi, Akira, *Nature*, 330, 550 (1987).
21. Whalley, E., *J. Phys. Chem.*, 87, 4174 (1983).
22. Fletcher, N. H., The Chemical Physics of Ice, Cambridge University Press, London (1970).
23. Tammann, G., *Ann. Phys.*, 2, 1 (1900).
24. Bridgman, P., *Proc. Am. Acad. Arts Sci.*, 47, 441 (1912).
25. Bridgman, P., *J. Chem. Phys.*, 3, 597 (1935).
26. Bridgman, P., *J. Chem. Phys.*, 5, 964 (1937).
27. Whalley, E., and Davidson, D., and Heath, J. B. R., *J. Chem. Phys.*, 45, 3976 (1966).
28. Whalley, E., Heath, J. B. R., and Davidson, D., *J. Chem. Phys.*, 48, 2362 (1968).
29. Polian, A., and Grimsditch, M., *Phys. Rev. Lett.*, 52, 1312 (1984).
30. Sirota, N. N., and Bizhigitov, T. B., *Russ. J. Phys. Chem.*, 62, 134 (1988).
31. Kuhs, W., and Lehmann, M., in Water Science Reviews 2, Franks, F. ed., Cambridge University Press, Cambridge (1986).
32. Whalley, E., in Physics of Ice, Riehl, N., Bullemer, B., and Engelhardt, H. ed., Plenum Press, New York (1969).
33. Savage, Hugh, in Water Science Reviews 2, Franks, F. ed., Cambridge University Press, Cambridge (1986).
34. Kamb, B., *Acta Cryst.*, 17, 1437 (1964).
35. Hamilton, W. C., Kamb, B., Laplaca, S. J., and Prakash, A., in Physics of Ice, Riehl, N., Bullemer, B., and Engelhardt, H. ed., Plenum Press, New York (1969).

36. Bragg, W. H., Proc. Phys. Soc., 34, 98 (1922).
37. Rinne, F., Ber. Verh. Sachs Acad. Wiss., Math.-Phys. K1, 69, 57 (1917).
38. St. John, A., Proc. Natn. Acad. Sci. U.S.A, 4, 193 (1918).
39. Dennison, D. M., Phys. Rev., 17, 20 (1921).
40. Barnes, W. J., Proc. Roy. Soc. Lond. A, 125, 670 (1929).
41. Kinsey, E. L., and Sponsler, O. L., Proc. Phys. Soc., 45, 768 (1933).
42. Bernal, J. D., and Fowler, R. H., J. Chem. Phys., 1, 515 (1933).
43. Pauling, L., J. Am. Chem. Soc., 57, 2680 (1935).
44. Debye, P., Polar Molecules, Reprinted 1945, Dover Press, New York (1929).
45. Flubacher, P., Leadbetter, A. J., and Morrison, J. A., J. Chem Phys., 33, 1751 (1960).
46. Wollan, E. O., Davidson, W. L., and Shull, C. G., Phys. Rev., 75, 1348 (1949).
47. Peterson, S. W., and Levy, H. A., Acta Cryst., 10, 70 (1957).
48. Kuhs, W. F., and Lehmann, M. S., Acta Cryst. A (1986).
49. Lonsdale, K., Proc. R. Soc. A., 247, 424 (1958).
50. Owston, P. G., Adv. Phys., 7, 171 (1958).
51. Laplaca, S., and Post, B., Acta Cryst., 13, 503 (1960).
52. Brille, R., and Tippe, A., Acta Cryst., 23, 343 (1967).
53. Kamb, B., in Structural Chemistry and Molecular Biology, Rich, A., and Davidson, N. ed., Freeman, San Fransisco (1968).
54. Shimaoka, K., J. Phys. Soc. Japan, 15, 106 (1960).
55. Rabideau, S., Finch, E., and Denison, A., J. Chem. Phys., 49, 4660 (1968).
56. Whalley, E., Mol. Phys., 28, 1105 (1974).
57. Baianu, I., Boden, N., Lightowers, D., and Mortimer, M., Chem. Phys. Lett., 54, 169 (1987).
58. Bertie, J., and Whalley, E., J. Chem. Phys., 40, 1637 (1964).

59. Sivakumar, T., Rice, S., and Sceats, M., *J. Chem. Phys.*, **69**, 3468 (1978).
60. Dewar, J., *Chem. News*, **91**, 216 (1905).
61. Burton, E. F., and Oliver, W. F., *Proc. R. Soc. London, Ser. A*, **153**, 166 (1935).
62. Konig, H., *Z. Kristallogr.*, **105**, 279 (1943).
63. Blackmann, M., and Lisgarten, N. D., *Proc. R. Soc. A*, **239**, 93 (1957).
64. Honjo, G., and Shimaoka, K., *Acta Cryst.*, **10**, 710 (1957).
65. Gough, S. R., and Davidson, D. W., *J. Chem. Phys.*, **52**, 5442 (1970).
66. Narten, A. H., Venkatesh, C. G., and Rice, S. A., *J. Chem. Phys.*, **64**, 1106 (1976).
67. Bertie, J. E., Calvert, L. D., and Whalley, E., *J. Chem. Phys.*, **38**, 840 (1963).
68. Bertie, J. E., Calvert, L. D., and Whalley, E., *Can. J. Chem.*, **42**, 1373 (1964).
69. Pilcher, C., Ridgway, S., and McCord, T., *Science*, **178**, 1087 (1972).
70. Erickson, E., Knacke, R., Tokunaga, A., and Haas, M., *Astrophys. J.*, **245**, 148 (1981).
71. Kobayashi, T., Furukawa, Y., and Takahashi, T., *J. Cryst. Growth*, **35**, 262 (1976).
72. Pryde, J. A., and Jones, G. O., *Nature*, **170**, 685 (1952).
73. Olander, D. S., and Rice, S. A., *Proc. Nat. Acad. Sci. USA*, **69**, 98 (1972).
74. Mishima, O., Calvert, L. D., and Whalley, E., *Nature*, **310**, 3935 (1984).
75. Mishima, O., Calvert, L. D., and Whalley, E., *Nature*, **314**, 76 (1985).
76. Bizid, A., Bosio, L., Defrain, A., and Oumezzine, M., *J. Chem. Phys.*, **87**, 2225 (1987).
77. Bellissent-Funel, M.-C., Teixeira, J., and Bosio, L., *J. Chem. Phys.*, **87**, 2231, (1987).
78. Zhang, Q., and Buch, V., *J. Chem. Phys.*, **92**, 1512 (1990).
79. Stillinger, F. H., *Science*, **209**, 451 (1980).
80. Handa, Y., Klug, D., and Whalley, E., *J. Chem. Phys.*, **84**, 7009 (1986).

81. Johari, G., Hallbrucker, A., and Mayer, E., *Nature*, **330**, 552 (1987).
82. Johari, G. P., *Phys. Chem. Chem. Phys.*, **2**, 1567-1577 (2000)
83. Velikov, V., Borick, S., and Angell, C.A., *Science*, **294**, 5550, 2335-2338 (2001).
84. Handa, J. P., and Klug, D. D., *J. Phys. Chem.*, **92**, 3323 (1988).
85. Hallbrucker, A., Mayer, E., and Johari, G. P., *J. Phys. Chem.*, **93**, 7751 (1989).
86. Hallbrucker, A., and Mayer, E., *J. Phys. Chem.*, **91**, 503 (1987).
87. Johari, G., Hallbrucker, A., and Mayer, E., *J. Chem. Phys.*, **95**, 2955 (1991).
88. Speedy, R., *J. Phys. Chem.*, **96**, 2322 (1992).
89. Smith, R. S., Huang, C., and Kay, B., *J. Phys. Chem. B*, **101**, 6123-6126 (1997).
90. Fisher, M., and Devlin, J. P., *J. Phys. Chem.*, **99**, 11584 (1995).
91. Lippincott, E. R., and Schroeder, R., *J. Chem. Phys.*, **23**, 1099 (1955).
92. Weissmann, M., and Cohan, N. V., *J. Chem. Phys.*, **43**, 119 (1965).
93. Eigen, M., and De Maeyer, L., *Proc. Roy. Soc. Lond. A*, **247**, 505 (1958).
94. Bjerrum, N., *K. danske Vidensk. Selsk. Skr.*, **27**, 1 (1951).
95. Bilgram, J. H., Roos, J., and Granicher, H., *Z. Phys. B*, **23**, 1 (1976).
96. Sceats, M. G., Stavola, M., and Rice, S. A., *J. Chem. Phys.*, **71**, 983 (1979).
97. Sceats, M. G., and Rice, S. A., in Water, a Comprehensive Treatise, Vol. 7, Franks, F. ed., Plenum Press, New York (1982).
98. Devlin, J. P., *Int. Rev. Phys. Chem.*, **9**, No. 1, 29 (1990).
99. Walrafen, G. E., *J. Chem. Phys.*, **40**, 3249 (1964).
100. Nakagawa, I., and Shimanouchi, T., *Spectrochim. Acta*, **20**, 429 (1964).
101. Haas, C., and Hornig, D. F., *J. Chem. Phys.*, **32**, 1763 (1960).

102. Whalley, E., and Klug, D. D., *J. Chem. Phys.*, 86, 7244 (1987).
103. Ritzhaupt, G., and Devlin, J. P., *J. Chem. Phys.*, 67, 4779 (1977).
104. Ritzhaupt, G., Thornton, C., and Devlin, J. P., *Chem. Phys. Lett.*, 59, 420 (1978).
105. Ritzhaupt, G., Collier, W. B., Thornton, C., and Devlin, J. P., *Chem. Phys. Lett.*, 70, 294 (1980).
106. Camp, P. R., in *Physics of Ice*, Riehl, N., Bullemer, B., and Engelhardt, H. ed., Plenum Press, New York (1969).
107. Riehl, N., Bullemer, B., and Engelhardt, H., in *Physics of Ice*, Riehl, N., Bullemer, B., and Engelhardt, H. ed., Plenum Press, New York (1969).
108. Decroly, J. C., Granicher, H., and Jaccard, C., *Helv. Phys. Acta*, 30, 465 (1957).
109. Granicher, H., *Phys. Condens. Mater.*, 1, 1 (1963).
110. Steinmann, A., *Helv. Phys. Acta*, 30, 581 (1957).
111. Onsager, L., and Dupuis, M., *Rc. Scu. Int. Fis. 'Enrico Fermi'*, Corso x (1960).
112. Jaccard, C., *Helv. Phys. Acta*, 32, 89 (1959).
113. Jaccard, C., *Phys. Kondens. Materie.*, 3, 99 (1964).
114. Jaccard, C., *Ann. New York Acad. Sci.*, 125, 390 (1965).
115. Kunst, M., and Warman, J. M., *J. Phys. Chem.*, 87, 4093 (1983).
116. Devlin, J. P., *J. Phys. Chem.*, 92, 6867 (1988).
117. Weller, A., in *Progress in Reaction Kinetics*, Vol. 1, Porter, G. ed., Pergamon Press, New York (1961).
118. Scherer, J. R., in *Advances in Infrared and Raman Spectroscopy*, Vol. 5, Clark, R. J. H., and Hester, R. E. ed., Heyden and Son Ltd., London (1978).
119. Clarke, E. C. W., and Glew, D. N., *Can. J. Chem.*, 50, 1655 (1972).
120. Whalley, E., and Klug, D. D., *J. Chem. Phys.*, 84(1), 78 (1986).

121. Suga, H., Matsuo, T., and Yamamuro, O., *Supramol. Chem.*, 1, 221 (1993).
122. Devlin, J. P., *J. Geophys. Res. - Planets*, 106(E2), 3333 (2001).
123. Klug, D. D., *Science*, 294, 2305 (2001).
124. Hallbrucker, A., Mayer, E., and Johari, G. P., *J. Phys. Chem.*, 93, 4986 (1989).

VITA 2

Mark Edwin Fisher

Candidate for the Degree of

Doctor of Philosophy

Thesis: A SPECTROSCOPIC INVESTIGATION OF PROTON TRANSFER AND
BERRUM DEFECT ACTIVITY IN AMORPHOUS ICE

Major Field: Chemistry

Biographical:

Personal Data: Born in Frederick, Oklahoma on May 10, 1962, the son of Carl Edwin and Elwana Fisher.

Education: Graduated from Chattanooga High School in May 1980; received the Bachelor of Science degree in Chemistry from Cameron University in May 1985; received the Master of Science degree with a major in Chemistry from Oklahoma State University in July 1989. Completed the requirements for the Doctor of Philosophy degree with a major in Chemistry at Oklahoma State University in August, 2002.